



THE UNIVERSITY

of ADELAIDE

**Directing Selectivity of Carbon Dioxide Reduction Reaction via
Heteroatom Doping**

Xing Zhi

School of Chemical Engineering and Advanced Materials
Faculty of Engineering, Computer and Mathematical Science

A thesis submitted for the degree of Doctor of Philosophy

The University of Adelaide

January 2021

Table of Contents

Abstract	1
Declaration	3
Acknowledgements	5
Chapter 1: Introduction	7
1.1 Project Significance.....	7
1.2 Research objectives	7
1.3 Thesis outline	8
1.4 References	9
Chapter 2: Literature Review	11
2.1 Introduction	11
2.2 Role of oxygen-bound reaction intermediates in selective electrochemical CO ₂ reduction.....	11
Chapter 3: Impact of Interfacial Electron Transfer on Electrochemical CO₂ Reduction on Graphitic Carbon Nitride/Doped Graphene	53
3.1 Introduction and Significance	53
3.2 Impact of interfacial electron transfer on electrochemical CO ₂ reduction on graphitic carbon nitride/doped graphene.....	54
Chapter 4: Selectivity Roadmap for Electrochemical CO₂ Reduction on Copper-based Alloy Catalysts	98
4.1 Introduction and Significance	98
4.2 Selectivity roadmap for electrochemical CO ₂ reduction on copper-based alloy catalysts	98
Chapter 5: Kinetic Insights into Selective C-C Coupling for Electrochemical CO₂ Reduction on Copper Alloy Surfaces	122
5.1 Introduction and Significance	122
5.2 Kinetic insights into selective C-C coupling for electrochemical CO ₂ reduction on copper alloy surfaces	122
Chapter 6: Directing Selectivity of CO₂ Electroreduction to Target C₂ Products via Non-metal Doping on Cu Surfaces	141
6.1 Introduction and Significance	141

6.2 Directing selectivity of CO ₂ electroreduction to target C ₂ products via non-metal doping on Cu surfaces	141
Chapter 7: Conclusions and Perspectives	167
Appendix I: Publications during PhD Candidature	170

Abstract

The electrochemical CO₂ reduction reaction (CRR) presents a promising route to convert CO₂ into valuable chemicals and fuels from renewable energy sources. However, this process is complex in nature with multiple reaction pathways and numerous possible intermediates. Due to various C₁-C₃ products being produced during CO₂ electroreduction, directing selectivity to a target product remains a challenging task. Heteroatom doping in catalytic materials provides an achievable method to modify reaction energetics and control selectivity distributions for the CRR. Despite the research efforts in selective CO₂ reduction, greater understanding is needed regarding the catalytic mechanisms and key reaction intermediates at the atomic level. Therefore, this Thesis aims to develop some heteroatom doped catalytic materials for directing the CRR selectivity to certain products by using density functional theory (DFT) calculations.

In this Thesis, the recent research progress of CRR pathway selection is firstly summarized by identifying the important role of key intermediates in directing selectivity to target products (Chapter 2). This section points out that the development of selective CRR electrocatalysts relies on optimizing reaction energetics of critical elementary steps in the preferred pathway to a specific product.

The first aspect of this Thesis focuses on graphitic carbon nitride/doped graphene with and without heteroatom doping in graphene substrate (C₃N₄/XG) for CO₂ reduction by using computational methods (Chapter 3). It is demonstrated that a higher catalytic activity originates from increased interfacial electron transfer among different doping cases. A low overpotential is estimated from a volcano-type CRR activity trend for the selective production of methane on C₃N₄/XG, indicating the applicability of heteroatom doping to achieve improved CRR activity and selectivity.

The second aspect of this Thesis is about copper-based catalytic materials for electrochemical CO₂ reduction (Chapters 4 - 6). Copper has shown its unique ability to generate energy dense products during CRR. However, the moderate adsorption strength of key reaction intermediates on Cu lead to its poor CRR selectivity. Therefore, engineering Cu-based catalysts with optimized reaction energetics is important to address the selectivity

issue. In the first part (Chapters 4 and 5), Cu-based alloys (M@Cu) are modelled to explore their CRR selectivity trends by using DFT calculations. The heteroatom doping of secondary metals in Cu substrate provides a feasible strategy to tailor multiple active sites and mediate adsorption energies. The different hydrogen and oxygen affinities of the secondary metals in the M@Cu catalysts are found to be effective descriptors in determining CRR selectivity. Furthermore, the reaction kinetics of C-C coupling steps are evaluated on some Cu alloy surfaces by using the Nudged Elastic Band (NEB) method. We discovered that the OC-COH coupling is kinetically more favorable than the OC-CHO coupling to direct CRR selectivity toward multi-carbon products. The linear energy relations for C-C coupling and its reverse dissociation reactions on Cu-based alloy catalysts provides a route to estimate kinetic barriers from reaction energies. In the second part (Chapter 6), heteroatom doping of non-metal elements on Cu surfaces (Cu-X) is applied to modulate C₂ products (including ethylene, ethane and ethanol) selectivity during CRR. The thermodynamically derived selectivity amongst competing reaction pathways is demonstrated through the evaluation of adsorption energetics of key post-C₂-coupling intermediates on Cu-X model catalysts. The oxygen affinities of the dopant atom site and the Cu site on Cu-X catalysts can serve as useful descriptors for C₂ product selectivity. The electron transfer through Bader charge analyses and electronegativity analyses of non-metal dopant atoms are identified as the underlying electronic properties that impact selectivity through oxygen affinity. From these computational studies, we demonstrated heteroatom doping to electrocatalysts can affect reaction energetics and direct the CRR selectivity to a target product.

Declaration

I certify that this work contains no material which has been accepted for the award of any other degree or diploma in my name, in any university or other tertiary institution and, to the best of my knowledge and belief, contains no material previously published or written by another person, except where due reference has been made in the text. In addition, I certify that no part of this work will, in the future, be used in a submission in my name, for any other degree or diploma in any university or other tertiary institution without the prior approval of the University of Adelaide and where applicable, any partner institution responsible for the joint-award of this degree.

I acknowledge that copyright of published works contained within this thesis resides with the copyright holder(s) of those works.

I also give permission for the digital version of my thesis to be made available on the web, via the University's digital research repository, the Library Search and also through web search engines, unless permission has been granted by the University to restrict access for a period of time.

I acknowledge the support I have received for my research through the provision of an Australian Government Research Training Program Scholarship.

Signed:

Date: 08 Apr. 2021

Acknowledgements

This Thesis would not come to fruition without the kind help and support from many people. I would like to extend my sincere appreciation to all of them.

First and foremost, I would like to express my deepest gratitude to my supervisors, Prof. Shizhang Qiao, Dr. Yan Jiao and Dr. Yao Zheng for their ongoing support and encouragement throughout my PhD study. I own my sincere thanks to Prof. Shizhang Qiao for his continuous guidance and professional supervision. I am motivated by his enormous devotion to his research career. In particular, I sincerely appreciate Dr. Yan Jiao for her patience, encouragement, and trust during this research period. She inspires me with her enthusiasm, dedication, and immense knowledge. I also would like to acknowledge Dr. Yao Zheng for his insightful suggestions and academic support.

I am deeply indebted to all colleagues in Prof. Qiao's group. It has been a great pleasure working alongside them. I would like to thank Xin Liu, Dr. Anthony Vasileff, Dr. Chaochen Xu, Dr. Fangxi Xie, Dr. Xuesi Wang, Dr. Yongqiang Zhao, Dr. Huanyu Jin, Yang Shi, Dr. Ke Zhang, Jieqiong Shan, Dr. Chao Ye, Xianlong Zhou, Huan Li, Laiquan Li, Bingquan Xia, Dazhi Yao, Xin Xu, Yanzhao Zhang, Dr. Dongdong Zhu, Dr. Jinlong Liu, Dr. Jingjing Duan, Dr. Jingrun Ran, Dr. Cheng Tang, Dr. Dongliang Chao, Dr. Bo You for all the enlightening discussions and technological assistance during the last four years.

To many research and technical staff, I would like to thank them all for their generous help. My special thanks go to Prof. Sheng Dai for his help with the application of my PhD scholarship, Prof. David Lewis for supporting my conference travel, Dr. Kenneth Davey for his valuable comments and suggestions in my research, Officers Michelle Fitton and Sue Earle for their administrative help, Analytical Services Coordinator Dr. Qihong Hu for her technical support, and IT Support Manager David Bowler for his professional assistance.

I would also like to acknowledge China Scholarship Council (CSC), The University of Adelaide and the Australia Research Council (ARC) for their financial support; the National Computational Infrastructure (NCI) supported by the Australian Government and

the Phoenix High Performance Compute (HPC) service at The University of Adelaide for their assistance of computational resources and services.

Finally, I am forever grateful to all my families and friends in China and Australia for their love and support. This PhD would not be possible without them. To my parents, thank you for always being there for me through the good times and bad, and giving me your support, trust, and unconditional love. To Fangxi, thank you for your wonderful companion and continual love.

Chapter 1: Introduction

1.1 Background

The excessive emission of CO₂ from the burning of fossil fuels leads to severe environmental impacts, such as global climate change and ocean acidification.¹⁻³ In addition, the current dependence of chemical industries on fossil fuels is not conducive to the sustainable development, which therefore induces the requirement to exploit renewable energy sources.^{4, 5} The electrochemical CO₂ reduction reaction (CRR) using renewable electricity enables clean energy storage in chemical bonds by converting CO₂ into valuable chemicals and fuels.⁶⁻⁹ However, the complexity of reaction network in the CRR process leads to selectivity issues.¹⁰⁻¹³ Given this, development of efficient electrocatalysts is required to direct the CRR selectivity to a target product amongst competing reaction pathways. Moreover, an atomic-level understanding of reaction mechanism is necessary to elucidate CRR pathway selection. Nowadays, computational modelling has emerged as a powerful technique to identify possible reaction intermediates and their interaction with catalyst surfaces at the atomic level.¹⁴ Therefore, fundamental understanding of CRR reaction mechanism in relation to the control of product distribution through using computational methods provides significant insights for addressing the selectivity issues.

1.2 Research objectives

The main goal of this Thesis is to use heteroatom doping as an engineering strategy for developing efficient electrocatalysts for the CRR and to explore the inherent effects of doping elements on the selectivity distribution of this process. Using computational modelling, detailed reaction energetics and electronic properties are evaluated to illustrate the mechanistic aspects of competing reaction pathways for the CRR. The specific objectives of this Thesis are:

- To establish a **roadmap** to estimate the CRR selectivity trends by identifying the role of key intermediates in the preferred reaction pathways.
- To model a range of **heteroatom-doped catalysts** to evaluate their reaction activity and selectivity for certain products during the CO₂ reduction.

- To identify **key reaction intermediates** in the favorable pathways toward target products based on adsorption thermochemistry.
- To utilize Nudged Elastic Band method to calculate the **activation barriers** of C-C coupling steps and determine associated kinetic preference.
- To study descriptor-based approach to predict the **selectivity** of copper-based catalysts through doping secondary metal elements or non-metal elements.
- To explore the **inherent properties** of heteroatom-doped catalysts to determine the CRR selectivity.

1.3 Thesis outline

This Thesis presents the outcomes of my PhD research and is presented in the form of journal publications. The Chapters in this Thesis are presented in the following sequence:

- **Chapter 1** introduces the significance of developing efficient catalysts for electrochemical CO₂ reduction. In addition, it outlines mechanistic understanding of CRR reaction pathways in relation to selectivity distribution.
- **Chapter 2** reviews the recent research development of CRR reaction mechanisms in both computational and experimental studies. The identification of key reaction intermediates and underlying CRR mechanisms provides a framework for controlling selectivity toward target products.
- **Chapter 3** studies graphitic carbon nitride/doped graphene hybrid structures as electrocatalysts for CRR with improved catalytic performance originating from electron transfer modulation.
- **Chapter 4** reports the CRR selectivity roadmap on copper-based alloy catalysts and introduces the hydrogen and oxygen affinity of the secondary metals as effective descriptors in determining CRR selectivity.
- **Chapter 5** employs copper-based bimetallic materials as model catalysts to investigate the reaction kinetics of C-C coupling steps and the linear energy relations.
- **Chapter 6** develops a range of non-metal doped copper surfaces in directing CRR selectivity to target C₂ products based on oxygen affinities of different active sites.

- **Chapter 7** presents the conclusions and perspectives for future work on the study of efficient electrocatalysts for CO₂ reduction reaction.

1.4 References

1. S. Solomon, G.-K. Plattner, R. Knutti and P. Friedlingstein, *Proc. Natl. Acad. Sci. U. S. A.*, 2009, 106, 1704.
2. M. R. Allen, D. J. Frame, C. Huntingford, C. D. Jones, J. A. Lowe, M. Meinshausen and N. Meinshausen, *Nature*, 2009, 458, 1163-1166.
3. J. P. Gattuso, A. Magnan, R. Billé, W. W. L. Cheung, E. L. Howes, F. Joos, D. Allemand, L. Bopp, S. R. Cooley, C. M. Eakin, O. Hoegh-Guldberg, R. P. Kelly, H. O. Pörtner, A. D. Rogers, J. M. Baxter, D. Laffoley, D. Osborn, A. Rankovic, J. Rochette, U. R. Sumaila, S. Treyer and C. Turley, *Science*, 2015, 349, aac4722.
4. S. Chu, Y. Cui and N. Liu, *Nat. Mater.*, 2017, 16, 16-22.
5. N. S. Lewis, *Science*, 2016, 351, aad1920.
6. Q. Lu and F. Jiao, *Nano Energy*, 2016, 29, 439-456.
7. J. H. Montoya, L. C. Seitz, P. Chakthranont, A. Vojvodic, T. F. Jaramillo and J. K. Nørskov, *Nat. Mater.*, 2017, 16, 70-81.
8. O. S. Bushuyev, P. De Luna, C. T. Dinh, L. Tao, G. Saur, J. van de Lagemaat, S. O. Kelley and E. H. Sargent, *Joule*, 2018, 2, 825-832.
9. A. Vasileff, Y. Zheng and S. Z. Qiao, *Adv. Energy. Mater.*, 2017, 7, 1700759.
10. R. Kortlever, J. Shen, K. J. Schouten, F. Calle-Vallejo and M. T. Koper, *J. Phys. Chem. Lett.*, 2015, 6, 4073-4082.
11. L. R. L. Ting and B. S. Yeo, *Curr. Opin. Electrochem.*, 2018, 8, 126-134.
12. Q. Fan, M. Zhang, M. Jia, S. Liu, J. Qiu and Z. Sun, *Mater. Today Energy*, 2018, 10, 280-301.
13. Y. Zheng, A. Vasileff, X. Zhou, Y. Jiao, M. Jaroniec and S. Z. Qiao, *J. Am. Chem. Soc.*, 2019, 141, 7646-7659.
14. J. K. Nørskov, T. Bligaard, J. Rossmeisl and C. H. Christensen, *Nat. Chem.*, 2009, 1, 37-46.

Chapter 2: Literature Review

2.1 Introduction

This Chapter presents a review of recent research progress for CRR pathway selectivity in relation to reaction intermediates that bind to the catalysts via oxygen atom(s). These oxygen-bound intermediates play a key role in elucidating mechanistic aspects of competing reaction pathways and determining selectivity distribution. This Chapter provides an in-depth understanding of critical elementary steps in directing selectivity toward desired products, from both computational and experimental studies. Here, we highlight the favorable CRR pathways to specific products controlled by oxygen-bound species, with consideration of theoretical computations, electrochemical observations and operando spectroscopy observations. A comprehensive understanding of CRR reaction mechanisms regarding the oxygen-bound intermediates provides a roadmap for governing product distribution and enhancing selectivity.

2.2 Role of oxygen-bound reaction intermediates in selective electrochemical CO₂ reduction

This chapter is included as it appears as a journal paper in preparation for publication by Xing Zhi, Anthony Vasileff, Yao Zheng, Yan Jiao, Shi-Zhang Qiao, Role of oxygen-bound reaction intermediates in selective electrochemical CO₂ reduction, **2021**, submitted for publication.

Statement of Authorship

Title of Paper	Role of Oxygen-Bound Reaction Intermediates in Selective Electrochemical CO ₂ Reduction
Publication Status	<input type="checkbox"/> Published <input type="checkbox"/> Accepted for Publication <input checked="" type="checkbox"/> Submitted for Publication <input type="checkbox"/> Unpublished and Unsubmitted work written in manuscript style
Publication Details	Xing Zhi, Anthony Vasileff, Yao Zheng, Yan Jiao, Shi-Zhang Qiao, Role of oxygen-bound reaction intermediates in selective electrochemical CO ₂ reduction, 2021 , submitted for publication.

Principal Author

Name of Principal Author (Candidate)	Xing Zhi		
Contribution to the Paper	Proposed the idea of the paper with supervisors, collected information and wrote the majority of the paper		
Overall percentage (%)	70%		
Certification:	This paper reports on original research I conducted during the period of my Higher Degree by Research candidature and is not subject to any obligations or contractual agreements with a third party that would constrain its inclusion in this thesis. I am the primary author of this paper.		
Signature	_____	Date	31 Mar. 2021


Co-Author Contributions

By signing the Statement of Authorship, each author certifies that:

- i. the candidate's stated contribution to the publication is accurate (as detailed above);
- ii. permission is granted for the candidate to include the publication in the thesis; and
- iii. the sum of all co-author contributions is equal to 100% less the candidate's stated contribution.

Name of Co-Author	Anthony Vasileff		
Contribution to the Paper	Collected related information, wrote some sections and helped to revise the paper		
Signature	_____	Date	31 Mar. 2021

Name of Co-Author	Yao Zheng		
Contribution to the Paper	Discussed the idea of the paper, supervised the project and revised the paper.		
Signature	_____	Date	31 Mar. 2021

Name of Co-Author	Yan Jiao		
Contribution to the Paper	Discussed the idea of the paper, supervised the project and revised the paper.		
Signature		Date	31 Mar. 2021

Name of Co-Author	Shi-Zhang Qiao		
Contribution to the Paper	Discussed the idea of the paper, supervised the project and revised the paper.		
Signature		Date	31 Mar. 2021

Role of Oxygen-Bound Reaction Intermediates in Selective Electrochemical CO₂ Reduction

Xing Zhi⁺, Anthony Vasileff⁺, Yao Zheng, Yan Jiao*, Shi-Zhang Qiao*

Centre for Materials in Energy and Catalysis (CMEC)

School of Chemical Engineering and Advanced Materials

The University of Adelaide, SA 5005, Australia

* Correspondence: s.qiao@adelaide.edu.au; yan.jiao@adelaide.edu.au

⁺X.Z. and A.V. contributed equally to this work.

Abstract: The electrochemical CO₂ reduction reaction (CRR) is intrinsically complex given the multiple possible reaction pathways and end products. Consequently, selectivity is a persistent challenge for the design and operation of CRR electrocatalysts. A detailed understanding of key elementary steps and surface-bound species involved in the C₁-C₃ pathways is important for directing the reaction to a target product. However, there has been limited success in fully explaining the selectivity of CO₂ reduction, such as the competing production of oxygen-free hydrocarbons and oxygen-containing alcohols. Recently, oxygen-bound intermediates have been identified as essential species to help explain the full reaction roadmap for CO₂ reduction. This Review explores the important role of oxygen-bound intermediates in affecting CRR selectivity to the many reduction products, ranging from two-electron products to higher reduced products. These oxygen-bound intermediates have a big influence on addressing mechanistic aspects of competing reaction pathways, based on extensive analysis of adsorption behaviour, reaction thermodynamics and reaction kinetics. Considering available theoretical calculations, electrochemical measurements and operando spectroscopy observations, we highlight the preferred reaction pathways to certain products

when regulated by oxygen-bound species. The geometries of these oxygen-bound intermediates and their binding on a catalyst surface dictate the breakage or preservation of C-O bonds, which has a significant effect on directing selectivity toward a final product. Based on this mechanistic evaluation, we summarize practical techniques for probing the evolution of intermediates and propose possible strategies for promoting the selectivity of electrocatalysts.

Keywords: selectivity, electrocatalysis, CO₂ reduction reaction (CRR), density functional theory (DFT), *in situ*/operando spectroscopy

Broader context: The global consumption of fossil fuels has massive environmental ramifications and is unsustainable in the long term. The electrochemical CO₂ reduction reaction (CRR) provides a promising route to resource sustainability because it can convert CO₂ into valuable chemicals and fuels and enable a closed carbon cycle when powered by renewable electricity. However, this process is complex in nature due to the existence of multiple possible reaction pathways, leading to a multitude of different C₁-C₃ products. While some key intermediates, mainly carbon-bound species, have been studied to identify favorable reaction pathways, the ability to tune CRR selectivity is still far from satisfactory. Recently, the involvement of oxygen-bound intermediates in the CRR mechanism was found to be more significant than previously thought and has hence gained considerable attention. This perspective highlights the important role of oxygen-bound reaction intermediates in directing CRR selectivity by considering the current theoretical calculations, electrochemical measurements and operando spectroscopy observations. Mechanistic aspects of competing reaction steps involving oxygen-bound species are discussed in detail to advance the understanding of selective CO₂ electrocatalysis.

1. Introduction

The electrochemical conversion of CO₂ to valuable chemicals and fuels via the CO₂ reduction reaction (CRR) enables clean energy storage in chemical bonds when used in conjunction with renewable electricity.¹⁻⁴ However, CO₂ reduction involves a complex reaction network with numerous possible intermediates and pathways to different products. This is accompanied by an increasing number of proton/electron transfer steps and C-C bond formation processes as the complexity of the products increases.⁵⁻⁷ Therefore, control of selectivity and product distribution is a persistent challenge surrounding this reaction. Therefore, it is important to identify favorable reaction pathways and the key intermediates in order to target a specific product. Early experimental studies found that electrochemical conversion of CO₂ and CO feed stocks produces a common product distribution, indicating that the CRR shares a similar reaction mechanism with CO reduction.⁸⁻¹² Given this, the CO species is a key reaction intermediate in the CRR. This is also evidenced by spectroscopic observations and theoretical analysis.¹³⁻¹⁸ The combination of operando spectroscopy and computational techniques provides an effective method for identifying the adsorption behaviour of key surface-bound intermediates and for determining selectivity during CO₂ reduction. Although substantial research effort has been devoted to developing a CRR roadmap, mechanistic details of the preferred pathways to desired products, especially to C₂₍₊₎ hydrocarbons and oxygenates, are still far from settled.

In the past, extensive theoretical calculations based on density functional theory (DFT) have been conducted, and these studies enabled atomic-level understandings of the thermodynamic and kinetic reaction energetics.¹⁹⁻²⁵ In these studies, the reaction mechanism and pathway selectivity were obtained by analysing multiple reaction steps. From a theoretical standpoint, feasible pathways toward desired products are proposed by identifying surface-bound species with favorable reaction energetics. Related to the binding energies of these various

intermediates, the development of descriptors based on the intrinsic catalyst properties has contributed significantly to our understanding of product distribution.²⁶⁻³¹ The binding energies of some carbon-bound intermediates, such as *CO, have been proposed as effective descriptors to rationalize the preferred formation of certain products.³²⁻³⁴ However, carbon-bound intermediates might not be the only intermediates that can steer CRR selectivity. In recent years, oxygen-bound intermediates have shown a significant impact on CRR selectivity. For example, Feaster et al. indicated that the binding energy of the oxygen-bound *OCHO intermediate is affected by the oxygen affinity of metal surfaces.³⁵ Our group highlighted that the hydrogen and oxygen affinity of the secondary metals in Cu-based alloys can serve as descriptors for CRR selectivity.³⁰ Therefore, understanding the importance of oxygen-bound reaction intermediates in directing CRR selectivity is a significant endeavour in this research field.

Apart from theoretical investigations, spectroscopic analysis of the reaction interface has become increasingly important in the study of CRR pathways, evidenced by the increasing number of reports using these tools.³⁶ The most common techniques used to study the reaction intermediates are surface enhanced infrared absorption spectroscopy (SEIRAS),^{15, 18, 37, 38} generally using attenuated total reflection (ATR) accessories, and surface enhanced Raman spectroscopy (SERS).³⁹⁻⁴² These techniques have shown great utility due to the surface enhancement effects afforded by nanostructured surfaces which can amplify the signals of mono and sub-monolayer adsorbates to detectable levels.⁴³ Because of this enhancement, meaningful data regarding the nature of the reaction intermediates can be obtained *in situ*. This is particularly important for the CRR where the reaction mechanism is complicated due to the existence of multiple possible reaction intermediates, including oxygen-bound species.^{36, 44} Other spectroscopy techniques like X-ray absorption spectroscopies (XAS) are also proving useful for the operando determination of catalyst structural evolution,⁴⁵ but have also been used to detect coordination of intermediates.⁴⁶

The combination of experimental and computational approaches provides a promising way to refine our mechanistic understanding of product selectivity during CO₂ electrocatalysis. Among competing reaction pathways, oxygen-bound intermediates have been identified as essential species for explaining these selectivity phenomena, yet their role has not been comprehensively evaluated in the literature. In this Review, we aim to present a crucial assessment of pathway selection for CO₂ reduction to specific products and underline the effects of oxygen-bound intermediates on directing CRR selectivity. We first provide the fundamentals of CRR reaction mechanisms that control the product distribution. Then, we discuss in detail the reaction pathways to a variety of products and highlight key elementary steps involving oxygen-bound species at a full range of reaction stages. The identification of these key oxygen-containing intermediates are comprehensively reviewed from a range of examples covering computational modelling, electrochemical measurements and operando spectroscopy. Balance of the C-O bond breakage/preservation in oxygen-bound species contributes significantly to achieving high selectivity towards a target product. We also propose some possible strategies that can be used to optimize the energetics of oxygen-containing species on the surface of the electrocatalyst to improve its selectivity.

2. Fundamental Mechanisms of the CRR

2.1 Complex Reaction Network

The electrochemical CO₂ reduction reaction occurs through multiple proton and electron transfer steps involving many possible intermediates. Various pathways to C₁-C₃ products from the electroreduction of CO₂ or CO reactant feeds have been proposed by identifying intermediates in key reaction steps. Advances in operando spectroscopy and computational techniques provide significant scope for exploring the evolution of surface-bound species and for rationalizing a pathway to the desired product. As shown in Figure 1, reaction pathways of

CO₂ reduction to C₁-C₃ products are summarized schematically, with oxygen-bound intermediates highlighted.

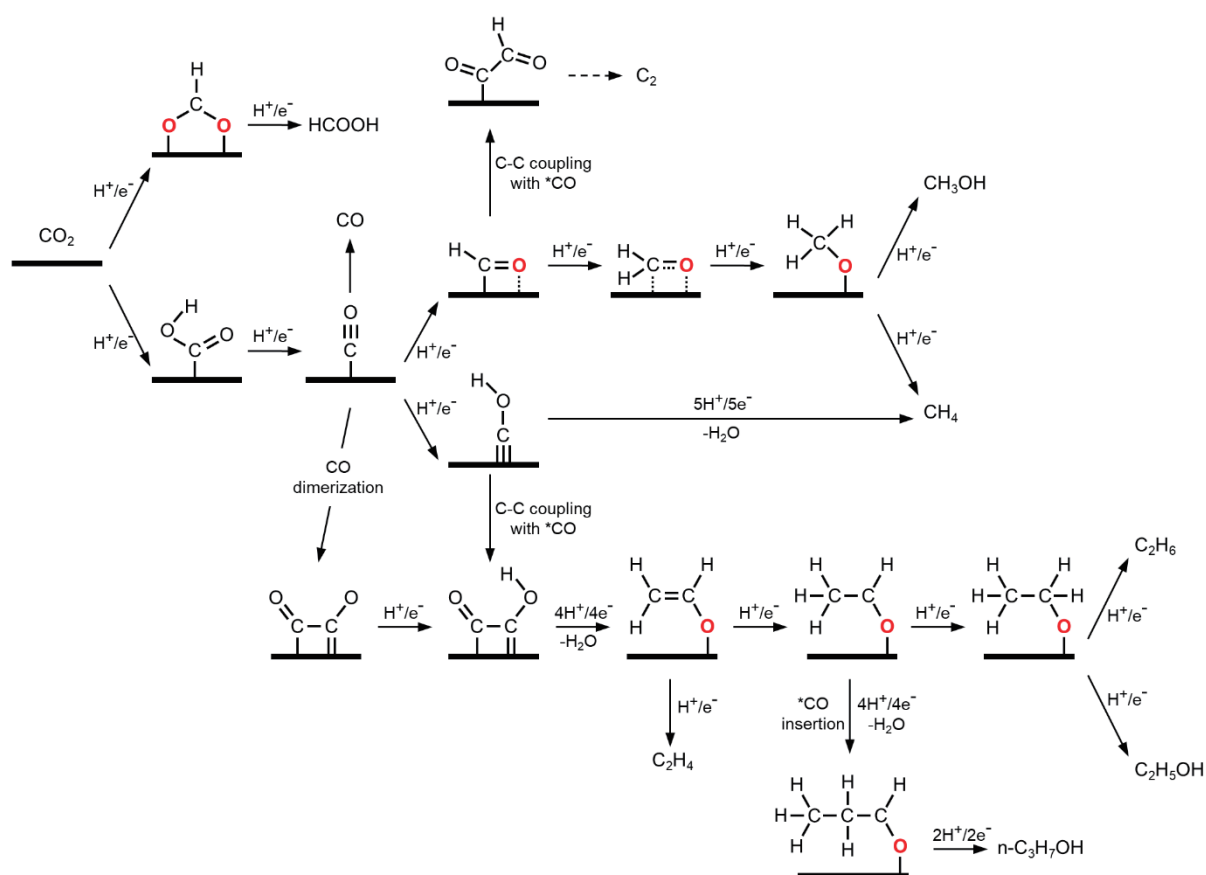


Figure 1. Reaction pathways of CO₂ reduction to various C₁-C₃ products involving oxygen-bound intermediates. The O atoms binding to the catalysts are highlighted in red. The dashed arrow indicates consecutive proton/electron transfer steps toward different C₂ products.

The reaction pathways for the formation of C₁ products are well-established in the literature. The conversion of CO₂ to CO or formate proceeds through an initial selectivity-determining step with distinct adsorption behaviour of the first hydrogenated reaction intermediate (i.e. *COOH or *OCHO).³⁵ While the formate pathway is considered a dead-end, *CO is generally accepted as a key intermediate for further electroreduction to higher reduced products.⁵ For the reduction of CO₂ to methane or methanol, it was suggested that the hydrogenation of *CO to *CHO or *COH is a key reaction step in determining the reaction activity and selectivity.^{21, 32,}
⁴⁷ Additionally, the hydrogenation of the oxygen-containing CH₃O* intermediate at the late

stage of the C₁ pathways is considered a selectivity-determining step for the production of methane and methanol.⁴⁸

In the C₂ pathway, *CO is a key intermediate for C-C coupling, whereby the formation of the *CO dimer, *COCO₂H, or *COCHO occurs. *CO dimerization is the most widely accepted rate-determining step to C₂ products.⁵ This has been evidenced by theoretical calculations and *in situ* spectroscopic observations.^{20, 49, 50} After the initial C-C coupling step, further reduction proceeds through branching pathways to a range of multi-carbon products. At the late stages of the C₂ pathway, oxygen-bound intermediates show marked effects in directing selectivity to different C₂ products, such as ethylene, ethanol, ethane, etc. For example, it was found that CH₂CHO* can serve as a key intermediate in determining the selectivity to ethylene or ethanol.^{7, 27, 51} Acetaldehyde (CH₃CHO) has been proposed as an important precursor to the production of ethanol and *n*-propanol,^{52, 53} while recently, an ethane pathway via the oxygen-bound ethoxy (CH₃CH₂O*) intermediate was supported by *in situ* spectroscopy studies.⁴⁶ It should be noted that the *CO insertion mechanism has also been suggested to explain the formation of certain C₂ and C₃ products.^{9, 54-56} Being a complex reaction network, the engineering of multiple active sites has also provided interesting mechanistic insights, such as the tandem catalysis mechanism, into the C₂₊ pathway reaction chemistry.⁵⁷⁻⁵⁹

2.2 Activity Descriptors

In many electrocatalytic reactions, theoretical descriptors have been used extensively to indicate reaction activity. For example, the volcano-type plot based on the Sabatier principle provides guidance for the rational design of more efficient catalysts for the hydrogen evolution reaction (HER), oxygen evolution reaction (OER) and oxygen reduction reaction (ORR).⁶⁰⁻⁶⁴ The greater complexity of CO₂ reduction requires a number of descriptors to explain catalytic activity and selectivity and to define the product distribution. The findings of a combined experimental and theoretical investigation indicated that the binding energies of *OCHO can

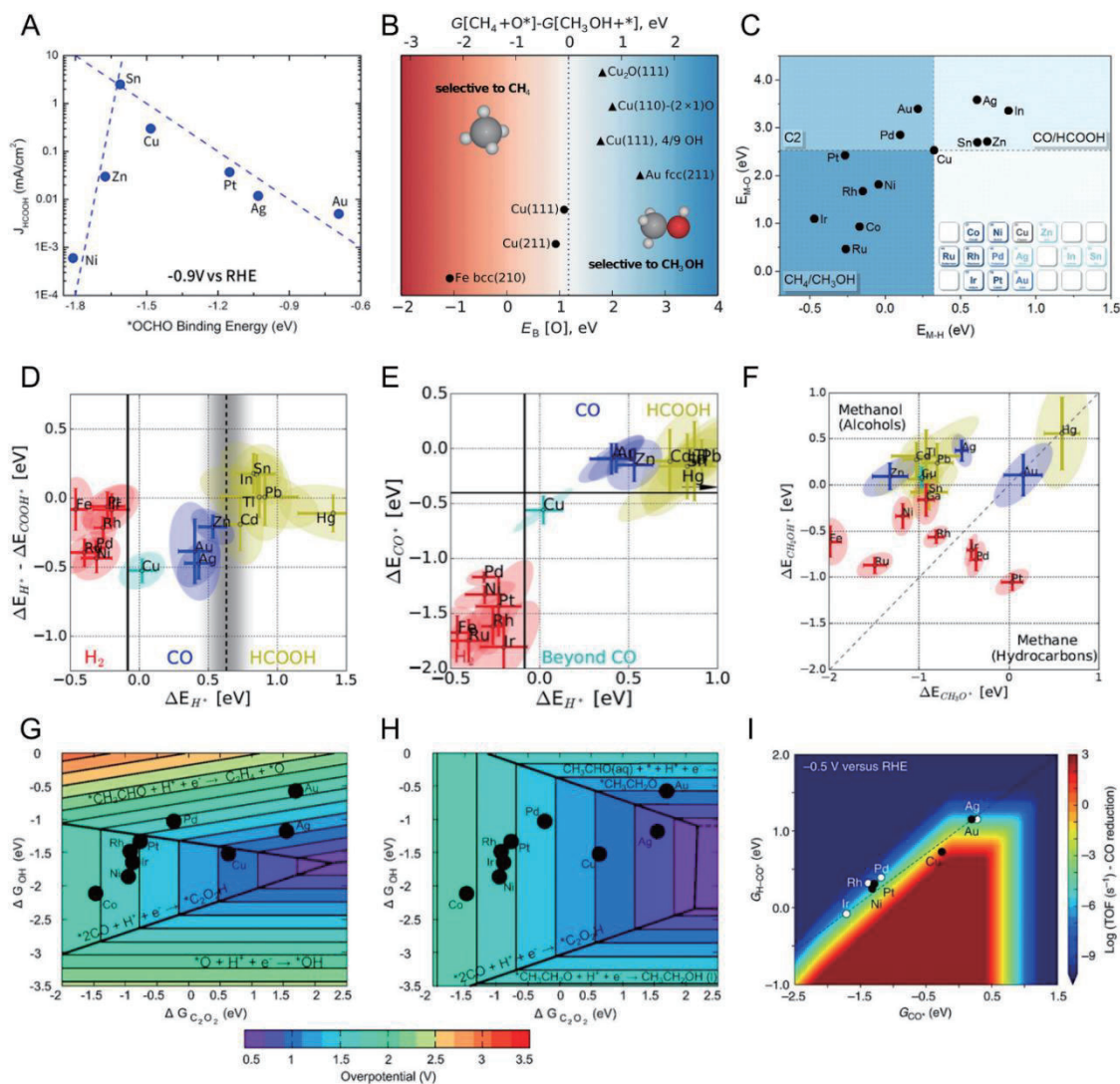


Figure 2. Theoretical Descriptors for CRR Selectivity and Activity. (A) Binding energy of *OCHO as a descriptor for formate partial current density. Reproduced with permission from ref. ³⁵ Copyright 2017, American Chemical Society. (B) Oxygen binding energy as an activity descriptor for selectivity to methane/methanol. Reproduced with permission from ref. ⁴⁸ Copyright 2015, Royal Society of Chemistry. (C) Hydrogen and oxygen affinities of the secondary metal in Cu-based bimetallic electrocatalysts as descriptors for CRR product grouping. Reproduced with permission from ref. ³⁰ Copyright 2020, Elsevier. (D) The experimental product classification of H_2 , CO, and HCOOH using binding energy of H^* as a descriptor. (E) The binding energies of CO^* and H^* as descriptors for categorizing metal catalysts into three distinct groups. (F) The binding energies of CH_2OH^* and CH_3O^* as descriptors for the production of methanol or methane from carbon-oxygen compounds. (D) to (F) are reproduced with permission from ref. ²⁶ Copyright 2017, Wiley-VCH. (G-H) Two-dimensional volcano plots using *C_2O_2 and *OH binding energies as descriptors for ethylene (G) and ethanol (H) production. Reproduced with permission from ref. ²⁷ Copyright 2018, American Chemical Society. (I) Two-dimensional map of the rate of CO reduction based on H-CO transition state energy and CO binding energy. Reproduced with permission from ref. ³⁴ Copyright 2017, Nature Publishing Group.

be assigned to the selectivity toward formate (Figure 2A).³⁵ Another computational study demonstrated that the oxygen binding strength may be a useful descriptor for predicting the selective production of methane and methanol from a methoxy (CH_3O^*) intermediate (Figure 2B).⁴⁸ As proposed by our group, the hydrogen and oxygen affinities of the secondary metal in Cu-based bimetallic electrocatalysts plays an important role in determining the CRR selectivity.²⁸ Using DFT calculations, we found that the hydrogen and oxygen affinity of the secondary metal in Cu-based alloy catalysts can be used as descriptors to categorize the product grouping for the CRR, as shown in Figure 2C.³⁰

On the basis of scaling relations, sets of descriptors have been developed to predict activity trends in limiting potentials and to derive selectivity distribution for different products. Activity volcano plots were built to dictate the overpotential requirement for methane production using $^*\text{CO}$ and $^*\text{OH}$ binding energies as descriptors.³² In another study, binding energies of $^*\text{CO}$ and $^*\text{OH}$ on pure metal surfaces were used to describe the selectivity for CO_2 conversion to CO and formate.³¹ As shown in Figure 2D-F, DFT calculations by Bagger et al. showed that binding energies of $^*\text{H}$, $^*\text{COOH}$, $^*\text{CO}$, and CH_3O^* intermediates can be used to describe product classification for the CRR.²⁶ Specifically, the oxygen-bound CH_3O^* intermediate was used for methanol formation (Figure 2F). Elsewhere, the binding energies of $^*\text{C}_2\text{O}_2$ and $^*\text{OH}$ were identified as descriptors for the production of ethylene and ethanol (Figure 2G and H).²⁷ In addition to thermodynamic models, Liu et al. reported scaling relations involving transition state energies in a kinetic model.³⁴ They found that the $^*\text{CO}$ adsorption energy and transition state energy for CO hydrogenation limited the CO_2 reduction activity (Figure 2I). In brief, these descriptive models help to understand the underlying reaction mechanism for certain products and facilitate the screening of CRR catalysts.

3. Directing Selectivity through Oxygen-Bound Intermediates

3.1 Mechanisms toward Two-Electron Products

3.1.1 Pathways and Intermediates for Two Electron Products

The reduction of CO₂ on an electrocatalyst is a complex process given the multitude of possible pathways and intermediates involved. Coupled with the inherent sensitivity between the catalyst surface and activity/selectivity, the nature of the initial reaction intermediates has been the subject of much contention.⁶⁵ As such, there has been significant research into the formation and coordination of these intermediates. One aspect which remains relatively certain is the existence of two distinct pathways: one to CO and one to formate. This claim is fairly well backed up by experiments and computations which show that formate cannot be reduced further and is regarded as a dead-end pathway.^{11, 19} In contrast, CO is known as a key intermediate in the pathway to more reduced products. It is believed that the reaction activity and selectivity for two electron products depend on the adsorption geometries of the initial intermediates. The conversion of CO₂ to CO proceeds mainly through a C-bound *COOH intermediate. Experimental and computational works provide mechanistic insights into the formate pathway and evidence suggests it is an oxygen-bound intermediate that is responsible for the production of formate.^{35, 66} Therefore, it is important to study how these initial reaction intermediates are formed on a catalyst and the binding preference for oxygen-containing groups.

3.1.2 Role of Oxygen-Bound Intermediates for Two Electron Products

To tune the CO₂ reduction selectivity for two electron products, it is critical to control the adsorption behaviour of the oxygen-containing intermediates in competing reaction pathways. As discussed above, the early oxygen-bound intermediate plays a significant role in determining the selectivity towards formate. Theoretical studies have shown that formate selectivity via the HCOO* intermediate was more viable (Figure 3A).⁶⁷ In this study, a strong linear scaling relation was found between the free energies of *COOH and *H, while little

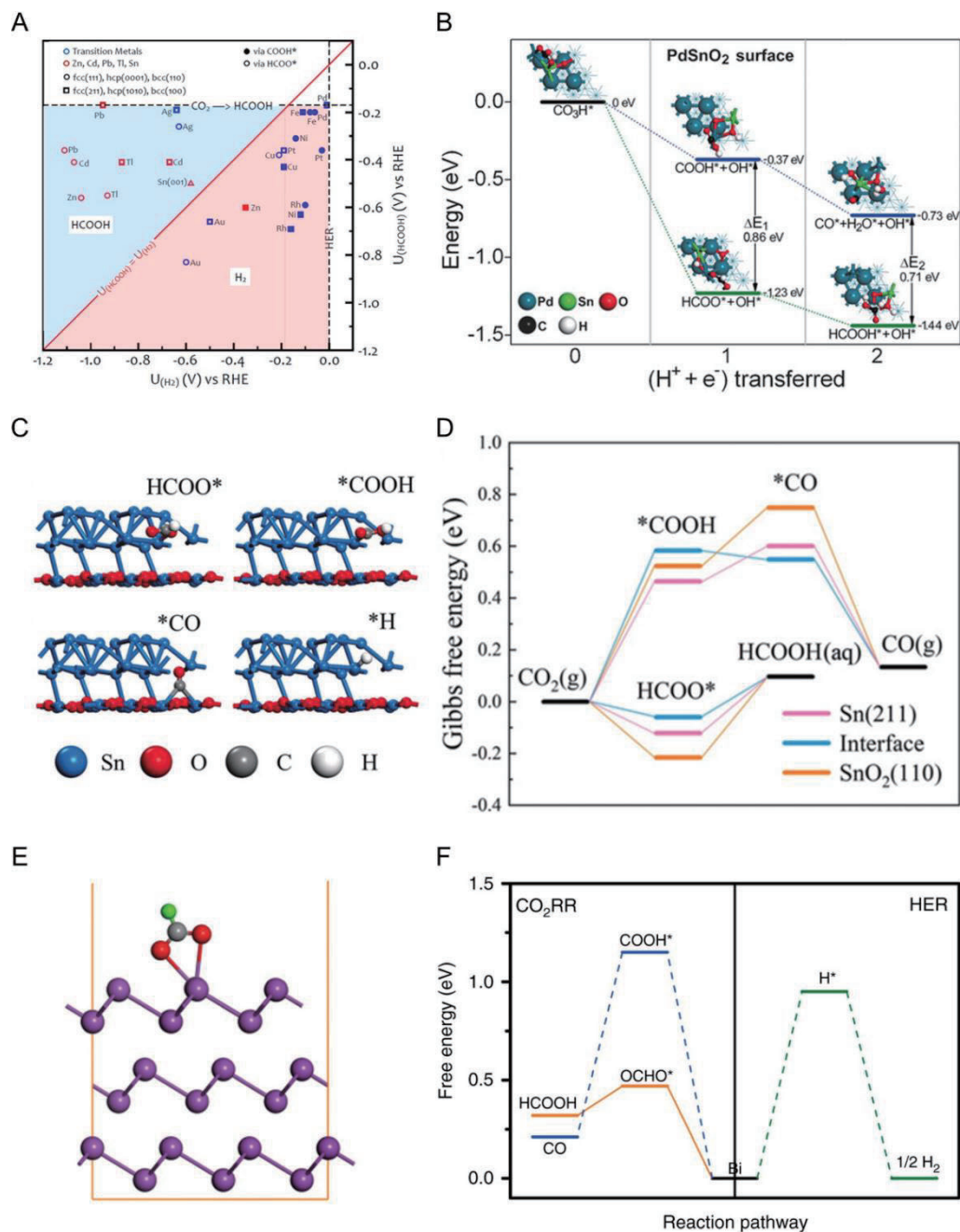


Figure 3. Role of oxygen-bound intermediates in directing CRR selectivity to two electron products based on computational techniques. (A) Theoretical limiting potentials for CO₂ electroreduction to HCOOH and the HER. Reproduced with permission from ref. ⁶⁷ Copyright 2016, Wiley-VCH. (B) Calculated reaction energy profiles for CO₂ electroreduction to CO and HCOOH on the PdSnO₂ surface. Reproduced with permission from ref. ⁶⁸ Copyright 2017, Wiley-VCH. (C) Optimized adsorption configurations for reaction intermediates at the *in situ* reconstructed Sn/SnO_x interface. (D) Calculated Gibbs free energy diagrams for CO₂ reduction to CO and HCOOH. (C) and (D) are reproduced with permission from ref. ⁷⁰ Copyright 2020, Wiley-VCH. (E) Optimized geometric structure of OCHO* adsorbate on Bi (001) plane. (F) Free energy diagrams for HCOOH, CO, and H₂ formation on Bi (001) plane. (E) and (F) are reproduced with permission from ref. ⁸⁰ Copyright 2018, Nature Publishing Group.

correlation between the free energies of *OCHO and *H existed. As a result, it was unlikely that CO₂ reduction to formate occurred through the *COOH intermediate, as the HER would be a strongly competing side reaction. Additionally, a separate study about CO₂ reduction on various metal electrodes suggested that the oxygen-bound *OCHO intermediate was the key intermediate for selective CO₂ reduction to formate, while *COOH was the key intermediate for CO₂ conversion to CO.³⁵ An optimal *OCHO binding strength on Sn leads to its high selectivity toward formate. DFT computations on Cu-based alloy catalysts (M@Cu) indicated that different metal hydrogen (M-H) and metal oxygen (M-O) affinities had a marked effect on adsorption configurations of the initial intermediates.³⁰ The formation of formic acid (HCOOH) via *OCHO was facilitated on M@Cu alloys with weak M-O affinity, while the *COOH pathway to HCOOH was favoured on M@Cu catalysts with weak M-H affinity. Bai et al. reported high Faradaic efficiency for HCOOH production on a Pd-Sn alloy electrocatalyst.⁶⁸ DFT calculations suggested that the formation of HCOO* intermediate and the generation of HCOOH were facilitated by the optimal surface Pd-Sn-O configuration, where both CO formation and hydrogen evolution were suppressed (Figure 3B).

Many other studies also report that optimizing adsorption energetics for the initial oxygen-bound intermediate can facilitate the conversion of CO₂ to formate in various catalyst systems including materials based on copper,⁶⁹ tin,⁷⁰⁻⁷² palladium,^{73, 74} and bismuth.⁷⁵⁻⁸⁰ For example, Ye et al. demonstrated that a SnO_x shell covering a Sn_{2.7}Cu catalyst exhibited high C₁ (formate and CO) Faradaic efficiency. DFT calculations indicated that the Sn/SnO_x interface promoted the production of HCOOH by optimizing the adsorption energy of HCOO* (Figure 3C and D).⁷⁰ In another study, ultrathin bismuth nanosheets (BiNS) showed high selectivity and activity for electrochemical CO₂ reduction to formate. This was further rationalized by DFT calculations, which indicated that the *OCHO intermediate was better stabilized on the Bi (001) surface compared to *COOH or *H (Figure 3E and F).⁸⁰

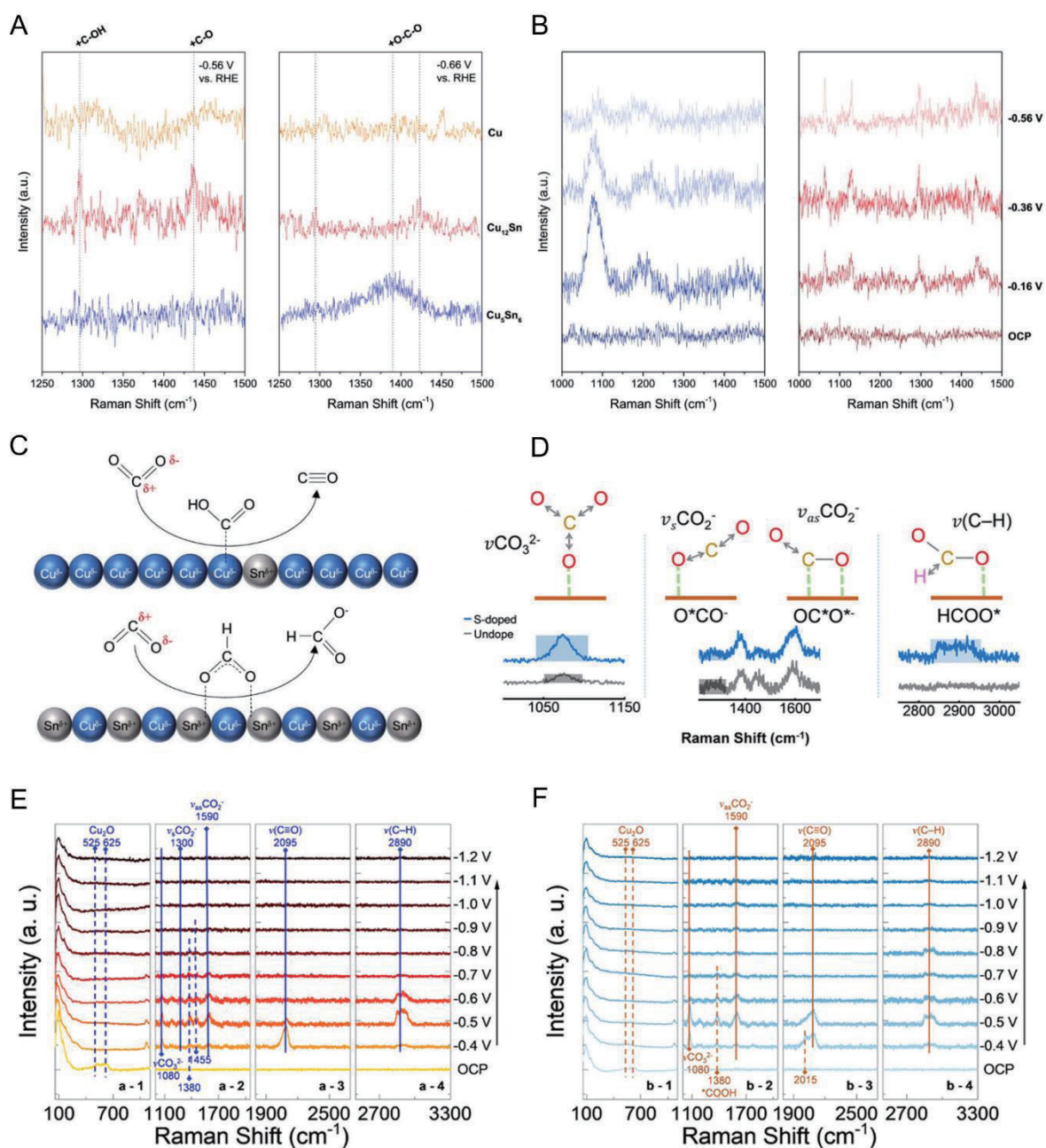


Figure 4. Role of oxygen-bound intermediates in directing CRR selectivity to two electron products based on experimental techniques. (A) *In situ* Raman spectroscopy study on the carboxyl/formate intermediate vibrational range for Cu, Cu₁₂Sn and Cu₅Sn₆ samples at -0.4 V vs RHE (left) and at -0.5 V vs RHE. (B) Potential-dependent Raman spectra in CO₂-saturated 0.1 M KHCO₃ electrolyte for Cu₅Sn₆ (left) and Cu₁₂Sn (right). (C) Proposed CRR pathway to CO and formate in the Cu-Sn alloy system. (A) to (C) are reproduced with permission from ref. ⁸¹ Copyright 2019, American Chemical Society. (D) *In situ* Raman spectroscopy and adsorption structure of the intermediates. (E-F) *In situ* Raman spectra with the static scanning subsection of CuOD (E) and CuODS (F). Reproduced with permission from ref. ⁴² Copyright 2020, American Chemical Society.

CO and formate can be formed concurrently on metallic catalysts, such as copper, which adds a layer of complexity to determining the nature of oxygen-bound intermediates. One SERS study on copper provides evidence that both CO and formate are formed through a carboxylate intermediate ($^*\text{COO}^-$) which is initially bound at the carbon.⁴⁰ However, formate is only produced at larger overpotentials where the Cu-C bond is weakened, and the C-O bond is stabilised on the surface. In our lab, we have shown that introducing a secondary metal plays a significant role in tuning the selectivity of copper-based alloys.⁸¹ By alloying Cu with Sn, the selectivity toward CO and formate was finely tuned, which fundamentally stems from a change in binding preference from $^*\text{COOH}$ to $^*\text{OCHO}$.^{81, 82} This was confirmed using *in situ* Raman spectroscopy. For high Sn content alloys, only the symmetric stretching band of formate ($^*\text{OCHO}$ or $^*\text{OCO}^-$) was observed while bands associated with carboxylate ($^*\text{COOH}$) were observed on low Sn content alloys (Figure 4A and B). The CRR pathway to CO and formate in the Cu-Sn alloy system was proposed based on the presence of localized positive charge on the Sn site (Figure 4C). In another study using oxygen-derived Cu (OD-Cu), it was found that S-doping enhanced formate selectivity (Figure 4D).⁴² Again evidenced from Raman spectroscopy, the S-doped sample showed better stabilization of the C-O bond in the CO_2^- intermediate, exhibiting increased $\nu_{\text{as}}\text{CO}_2^-$ band intensities, as shown in Figure 4E and F. Subsequently, the $\nu(\text{C-H})$ band of formate was observed over a wider potential range.

On the other hand, CO is formed via a proton and electron transfer to adsorbed CO_2 to form $^*\text{COOH}$.⁸³ It is generally thought that this $^*\text{COOH}$ intermediate is bound via the carbon atom and the second electron and proton transfer act to remove the -OH group to yield $^*\text{CO}$.⁸³ Smith's group has done significant investigation into the CRR on Ag films from which several key points regarding the initial reaction intermediates can be gleaned. In an earlier ATR-SEIRAS study,³⁸ they predominantly observed bands related to carboxylate and bands related to $-\text{COO}^-$ symmetric and asymmetric stretching only appeared at more negative potentials.

They reason that COO^- bound by the oxygen atoms only shows symmetric stretching. Therefore, COO^- and $^*\text{COOH}$ is bound via the carbon in the Ag system. However, they later found that oxygen-bound $^*\text{OCHO}$ may play a role in the mechanism on Ag.⁴¹ Using DFT, they found that $^*\text{OCHO}$ should readily form on Ag through a Tafel reaction between CO_2 and $^*\text{H}$. From SERS, they then found that $^*\text{OCHO}$ may be present as a spectator and act to promote $^*\text{COOH}$ formation by weakening $^*\text{H}$ binding. Therefore, a balance between C-binding and O-binding may be key to driving the reaction through the CO pathway and to higher reduction products. This is also dictated by the pathway given that many intermediates (e.g. in the ethanol pathway) are oxygen-bound.⁴⁴

3.2 $^*\text{CO}$ Hydrogenation and Further Reduction

3.2.1 Pathways and Intermediates for Deeply Reduced C_1 Products

In the late C_1 pathways, i.e. hydrocarbons and alcohols beyond CO, the hydrogenation of $^*\text{CO}$ to $^*\text{CHO}$ or $^*\text{COH}$ is considered to be the selectivity- and potential-determining step. Early DFT calculations on the Cu (211) surface by Peterson et al. proposed that a pathway to methane through the hydrogenation of $^*\text{CO}$ to $^*\text{CHO}$ (formyl) intermediate was thermodynamically favourable.¹⁹ Subsequent hydrogenation of $^*\text{CHO}$ leads to formaldehyde (CH_2O^*) and methoxy (CH_3O^*). The oxygen-bound CH_3O^* intermediate is then further reduced to methane through breaking of the C-O bond, with an adsorbed $^*\text{O}$ remaining on the surface. This study also showed that the hydrogenation of CH_3O^* to methane was favoured by 0.27 eV (on the basis of reaction free energies) over the hydrogen addition to the oxygen end of CH_3O^* to form methanol. A differential electrochemical mass spectrometry (DEMS) study by Javier et al. showed that the reduction of pre-adsorbed HCHO can lead to methane production, with no methanol detected.⁸⁴ This demonstrated that HCHO was an intermediate for the production of methane and is in good agreement with the theoretically proposed pathway by Peterson et al.¹⁹

It should be noted that other studies suggested that the methane pathway proceeds through *CHO to *CH_x species.^{34, 85}

Nie et al. proposed a different reaction mechanism for methane selectivity compared to methanol on Cu electrocatalysts based on a combination of thermodynamic and kinetic analysis.²¹ They found that the reaction pathway through the *CHO intermediate preferences the production of methanol over methane from CH₃O* reduction. This reconciles the experimental observations that direct electroreduction of formaldehyde (CH₂O) mainly produces methanol and methanol is not reduced to methane on Cu electrodes.⁸⁵ Alternatively, a different pathway through the *COH intermediate was proposed for methane production. It was shown that the kinetic barrier for *COH formation from *CO reduction was 0.18 eV lower than that for *CHO at a potential of -1.15 V vs. RHE (reversible hydrogen electrode). The *COH intermediate is further reduced to an adsorbed *C intermediate and then hydrogenated to *CH_x species, which eventually results in the formation of methane. It has also been proposed that ethylene formation shares this *COH pathway and proceeds via dimerization of *CH₂ species. Additionally, the combination of DFT calculations and observations from experimental literature by Tang et al. have indicated the pathway through *COH to methane via the *C adsorbate.³¹

3.2.2 Role of Oxygen-Bound Intermediates for Deeply Reduced C₁ Products

As discussed in Section 3.2.1, *CO hydrogenation to *CHO was identified as the potential-determining step in the *CHO pathway to methane production.¹⁹ Scaling relations between the binding energies of *CO and *CHO on transition metal catalysts restrict the catalytic activity for CO₂ electroreduction to methane.³² In order to reduce the large overpotentials for methane production (Figure 5A), Hansen et al. demonstrated that *CHO should be stabilized on catalyst surfaces relative to *CO. It was proposed that alloying with an element with high O affinity is likely a feasible strategy to improve activity and selectivity to more reduced C₁ products by

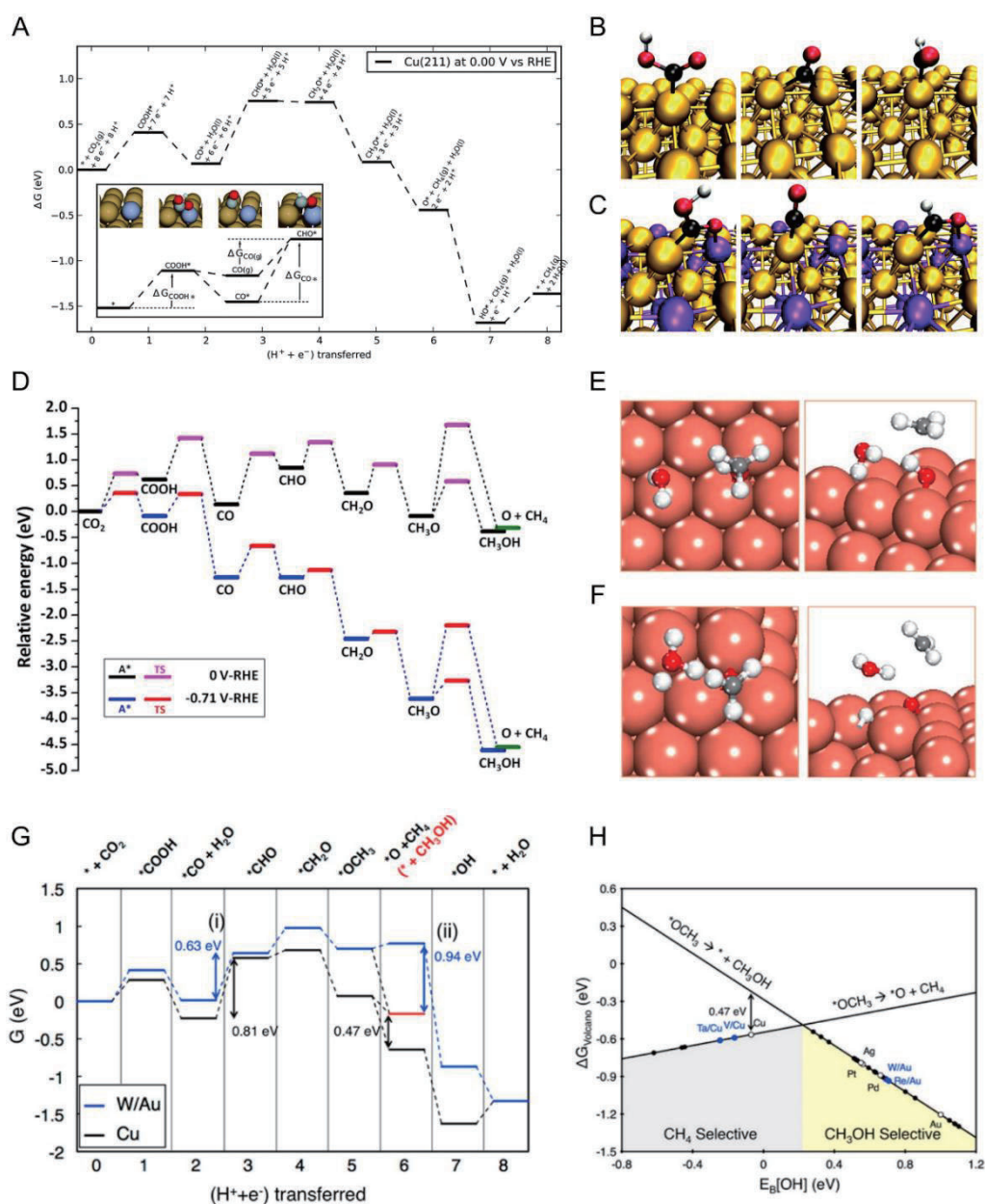


Figure 5. Role of oxygen-bound intermediates in directing CRR selectivity to methane and methanol based on computational techniques. (A) Free energy diagram for CO₂ reduction to methane on Cu (211) surface. (B-C) Intermediates, including COOH* (left), CO* (middle) and CHO* (right), in CO₂ reduction on Au (211) surface (B) and Au₃Zn (211) surface (C). (A) to (C) are reproduced with permission from ref. ⁸⁶ Copyright 2016, Royal Society of Chemistry. (D) Free energy diagrams for CRR reaction pathways through a CHO* intermediate to methane and methanol. (E-F) Optimized structures of the transition states associated with the elementary step of CH₃O* reduction to methane with one H₂O in the water-solvated (E) and H-shuttling (F) models. (D) to (F) are reproduced with permission from ref. ⁴⁷ Copyright 2014, Elsevier. (G) Free energy diagram for the CO₂ electroreduction to methane or methanol on Cu and W/Au. (H) Predicted Gibbs free energy changes in the selectivity-determining step for methane vs. methanol production as a function of OH binding energy. (G) and (H) are reproduced with permission from ref. ⁸⁷ Copyright 2015, American Chemical Society.

decoupling the binding energies of *CO and *CHO. DFT calculations on model alloy catalysts showed preferential stabilization of *CHO over *CO by increased interaction between the *O end of *CHO and alloy surfaces (Figure 5B and C).⁸⁶

In late stages of the CRR pathway to higher C₁ products, the reduction of CH₃O* is proposed to determine the selectivity between methane and methanol. It was found that CH₃O* was an oxygen-bound intermediate with its methyl end away from the catalyst surface.¹⁹ DFT calculations of kinetic barriers for CH₃O* reduction indicated that the production of methanol was favoured over methane in a solvated environment.²¹ Figure 5E and F show the reduction of CH₃O* to methane in transition states with various orientations. As a result, the production of methane through C-O bond breakage coupled with C-H bond formation incurred high kinetic barriers (Figure 5D).⁴⁷ Kuhl et al. studied electrocatalytic CO₂ conversion on a range of transition metal surfaces and observed the production of either methane, methanol, or both.³³ They proposed that the O binding affinity of the catalyst surface can play an important role in directing reaction pathways toward methane or methanol. They indicate that the breakage of the second C-O bond in CO₂ might be facilitated on catalysts with high O binding energies, leading to the production of hydrocarbons. In contrast, surfaces with weak O affinity would likely preserve this C-O bond and favor production of alcohols such as methanol.

After the production of methane from CH₃O* reduction, an adsorbed *O is left on the surface, which is further reduced to H₂O through an *OH intermediate. The binding energy of *OH was proposed as a feasible descriptor in determining the activity and selectivity for CO₂ electroreduction to methanol or methane.^{32, 87} It was shown that a high *OH binding energy increases the elementary limiting potential for *OH removal on transition metals.³² Given this, the oxygen-bound *OH intermediate may have a marked effect on limiting the catalytic activity for CO₂ reduction to methane. In addition, DFT calculations on transition metal near-surface alloys by Back et al. showed that the OH binding energy was a selectivity-determining

descriptor for the production of methanol and methane through the key CH_3O^* protonation step (Figure 5G).⁸⁷ Methanol generation was favored on catalysts with weak $^*\text{OH}$ binding energies, while the opposite was true for methane (Figure 5H).

Despite the many computational studies investigating the $^*\text{CO}/^*\text{CHO}$ or $^*\text{CO}/^*\text{COH}$ process and the methane and methanol pathways,^{19, 21, 32, 47} very few related spectroscopic studies have been established. In an early SERS study on copper, bands in the $-\text{C}-\text{H}$ stretching region around 2900 cm^{-1} were attributed to $^*\text{CH}_x$ species involved in the pathway to methane as carbene intermediates.⁸⁸ However, as noted by an earlier paper on Ag, formate exhibits a $-\text{C}-\text{H}$ stretching mode around 2870 cm^{-1} .⁸⁹ Given formate is also a product formed on copper, assignment of bands in this region becomes more difficult. In a recent paper, the $-\text{C}-\text{H}$ bending mode of an oxygen-bound CH_3O^* intermediate (around 1390 cm^{-1}) was predicted using DFT and detected using SEIRAS, as shown in Figure 6A and B.⁹⁰ Detection of this methoxy intermediate provides some experimental evidence for the pathway proposed and developed by Nørskov and co-workers.^{19, 91} Here, scission of the O-C bond leads to methane while scission of the Cu-O bond leads to methanol.⁹⁰ We determined a similar result for selectivity between ethane and ethanol.⁴⁶ Apart from O-binding, a SEIRAS study on Pt studied the effect of H-binding on the production of methane.⁹² It was found that methane could be produced at the equilibrium potential through the assistance of adsorbed $^*\text{H}$ on the Pt surface. H_{OPD} on the atop position was able to facilitate the hydrogenation of linear-bonded CO (CO_L) while bridge-bonded CO (CO_B) was bound more strongly and not reduced further (Figure 6C and D). Other spectroscopy studies on CRR catalysts have investigated how the structural evolution of catalysts affect methane selectivity. Using a copper phthalocyanine (CuPc) starting catalyst and copper MOFs, operando XAS was able to determine that the Cu^{II} species are fully converted to Cu^0 species and the initial coordination environment controls the final morphology (Figure

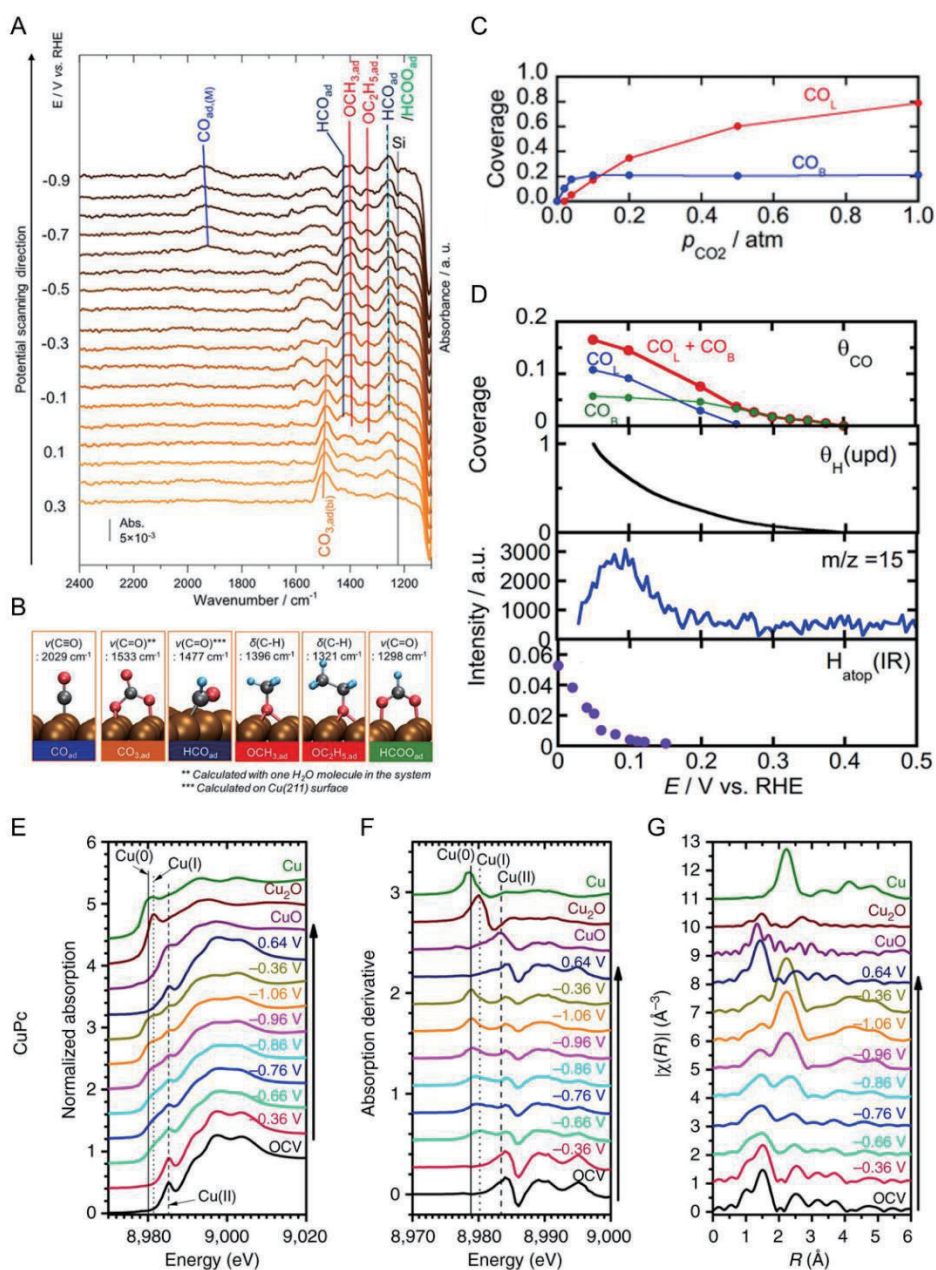


Figure 6. Role of surface-bound intermediates and catalyst structural evolution in directing CRR selectivity to methane based on experimental techniques. (A) *In situ* ATR-SEIRA spectra obtained during linear sweep voltammetry in a potential window from 0.3 V vs. RHE to -0.9 V vs. RHE in 1 M KHCO_3 . (B) Calculated infrared-active vibrational frequencies of possible adsorbed intermediates on Cu (111) and Cu (211) and their schematic structures. (A) and (B) are reproduced with permission from ref. ⁹⁰ Copyright 2019, American Chemical Society. (C) Coverages of adsorbed CO_L and CO_B calculated from the oxidation charges of CO adlayers established at various p_{CO_2} . (D) Relationship between H adsorption and the generation of CO_{ads} and methane. (C) and (D) are reproduced with permission from ref. ⁹² Copyright 2020, American Chemical Society. (E-G) *In situ* XAS measurements under electrocatalytic reaction conditions. Cu K-edge XANES spectra (E), first-order derivatives of the XANES spectra (F) and Fourier-transformed Cu K-edge EXAFS spectra (G) for CuPc. Reproduced with permission from ref. ⁹³ Copyright 2018, Nature Publishing Group.

6E-G).⁹³ The CuPc material was converted into small metallic clusters that exhibited the highest methane selectivity out of the samples tested.

3.3 C-C Coupling Mechanisms toward Multi-Carbon Products

3.3.1 Possible Pathways and Intermediates for Multi-Carbon Products

Mechanisms for the generation of multi-carbon products have been widely explored and many different reaction pathways have been proposed. It is known that *CO is a key intermediate for C-C coupling processes and C-C bond formation mainly occurs through three C₂ pathways which involve *CO and its hydrogenated derivatives (i.e. *CHO and *COH). *CO dimerization is the most widely accepted C-C coupling mechanism in C₂ pathways.^{20, 50, 94} The adsorbed *CO dimer is further hydrogenated to *COCO₂H through decoupled electron and proton transfer steps via a negatively charged *COCO⁻ intermediate, which is an important precursor for producing multi-carbon products. Alternatively, the *CO dimer can be hydrogenated to a *COCHO intermediate by forming a C-H bond.^{49, 95-97} In the other two C-C coupling mechanisms, C-C bond formation proceeds either between *CO and *COH directly to *COCO₂H or between *CO and *CHO directly to *COCHO. DFT calculations on Cu (111) demonstrated that *CO-COH coupling is energetically favorable compared to *CO dimerization, which arises from the radical character of *COH.²³ At high applied potentials, *CO dimerization becomes less favorable due to a large activation barrier and it was suggested that C-C bond formation occurs through *CO and *CHO coupling.⁹⁵ The reaction energetics of these initial C-C coupling steps are influenced by the experimental conditions and catalyst properties, such as crystal facets, applied potentials, local pH, ions in electrolyte, etc. Detailed reviews of these effects can be found elsewhere.^{44, 66, 98, 99}

After a sequence of proton and electron transfer steps, the hydrogenated *CO dimer forms a key C₂ intermediate CH₂CHO* at the later stages of the C₂ pathway. This oxygen-bound CH₂CHO* is likely a selectivity-determining intermediate (SDI) for some C₂ products.^{7, 51} The

hydrogenation of CH_2CHO^* can lead to branching pathways to either ethylene or acetaldehyde/ethanol. It was indicated that acetaldehyde is a key intermediate in the ethanol formation pathway.^{52, 100} In addition, a CO insertion mechanism has been proposed for the production of ethanol.^{9, 54-56} In this mechanism, a $^*\text{COCH}_2$ intermediate is proposed to form through CO insertion with adsorbed $^*\text{CH}_2$ species, which is further reduced to ethanol. Generally, a minor product during CO_2 electroreduction, ethane has been proposed to form through hydrogenation of ethylene or dimerization of $^*\text{CH}_3$.¹⁰¹⁻¹⁰³ Alternatively, another ethane pathway was proposed to occur through the hydrogenation of $\text{CH}_3\text{CH}_2\text{O}^*$ by breaking of the C-O bond.^{46, 104} Regarding the wider range of C_2 products detected experimentally, theoretical studies by Garza et al. proposed a mechanism of CO_2 reduction to seven C_2 products by identifying elementary steps in possible pathways.⁹⁶ Interestingly, they showed that an early bifurcation occurred at the $^*\text{COCHO}$ intermediate, leading to distinct pathways for ethylene or ethanol.

The formation of C_3 products has been proposed to take place through C-C coupling between C_1 and C_2 intermediates.^{9, 53, 105-108} The findings of some electrochemistry and spectroscopy experiments indicate that C-C coupling between C_2 intermediates and $^*\text{CO}$ can lead to the formation of *n*-propanol ($n\text{-C}_3\text{H}_7\text{OH}$) via a key $\text{CH}_3\text{CH}_2\text{CHO}$ species.^{9, 53} DFT calculations on copper ad-particles suggest that enhanced CO adsorption and stable surface-bound C_2 intermediates can facilitate $\text{C}_1\text{-C}_2$ coupling to form *n*- $\text{C}_3\text{H}_7\text{OH}$.¹⁰⁵ In addition, confinement and extended retention of C_2 species (e.g. $^*\text{COCO}$) is desired to direct selectivity to C_3 production.¹⁰⁶

3.3.2 Role of Oxygen-Bound Intermediates for Multi-Carbon Products

Early studies on the CRR pathway suggested that the main C-C coupling mechanism occurred through the coupling of $^*\text{CH}_x$ groups which are formed after the hydrogenation of $^*\text{CO}$.^{8, 47} However, work by Koper's group and more recent spectroscopic evidence suggests that the

key C-C coupling mechanism occurs through coupling of two adsorbed *CO to produce *OCCO.^{50, 109, 110} Using this mechanism, many pathways in the literature show that higher order products (C₂₊) are formed through various oxygen-bound intermediates.^{44, 66} In the late stages of the C₂ reaction pathway, oxygen-bound intermediates play an important role in determining product selectivity. The oxygen binding strength of reactive sites can lead to different selectivity trends. Herein, we focus on elementary steps involving oxygen-bound intermediates that control selectivity to different multi-carbon products.

Ethylene and ethanol are the most widely reported C₂ products from CO₂ electroreduction and have been produced at significant Faradaic efficiencies. It is proposed that these products share common reaction intermediates along a pathway originating from the rate-determining C-C coupling step at the early stages of CO₂ electroreduction.²⁰ Possible pathways leading to ethylene and ethanol have been summarized extensively to distinguish the key intermediates, which determine relative selectivity.^{20, 25, 27, 66, 96, 111} A late bifurcation in the pathway at the CH₂CHO* intermediate has been proposed to form intermediates that can bind to the catalyst via the oxygen.^{20, 27} The hydrogenation of CH₂CHO* leads to either ethylene oxide (*CH₂CH₂O*) or acetaldehyde (CH₃CHO*) intermediates. The reduction to ethylene proceeds through breaking of the C-O bond, leaving an *O adsorbate. Alternatively, ethanol formation proceeds after a further hydrogenation step to oxygen-bound ethoxy (CH₃CH₂O*) intermediates where the C-O bond is maintained. Zhuang et al. studied the effects of core-shell vacancies on the selectivity to multi-carbon alcohols. DFT calculations found that selectivity control for ethylene and ethanol can be achieved by modifying the energetics of post-C-C coupling reaction intermediates.¹¹² Both ethylene and ethanol formation pathways proceeded with similar thermodynamic barriers on copper at -0.5 V applied potential (Figure 7A). After introducing a vacancy on the copper surface, the energy barrier for ethylene production slightly increased, while the energetics for ethanol generation were barely affected (Figure 7B).

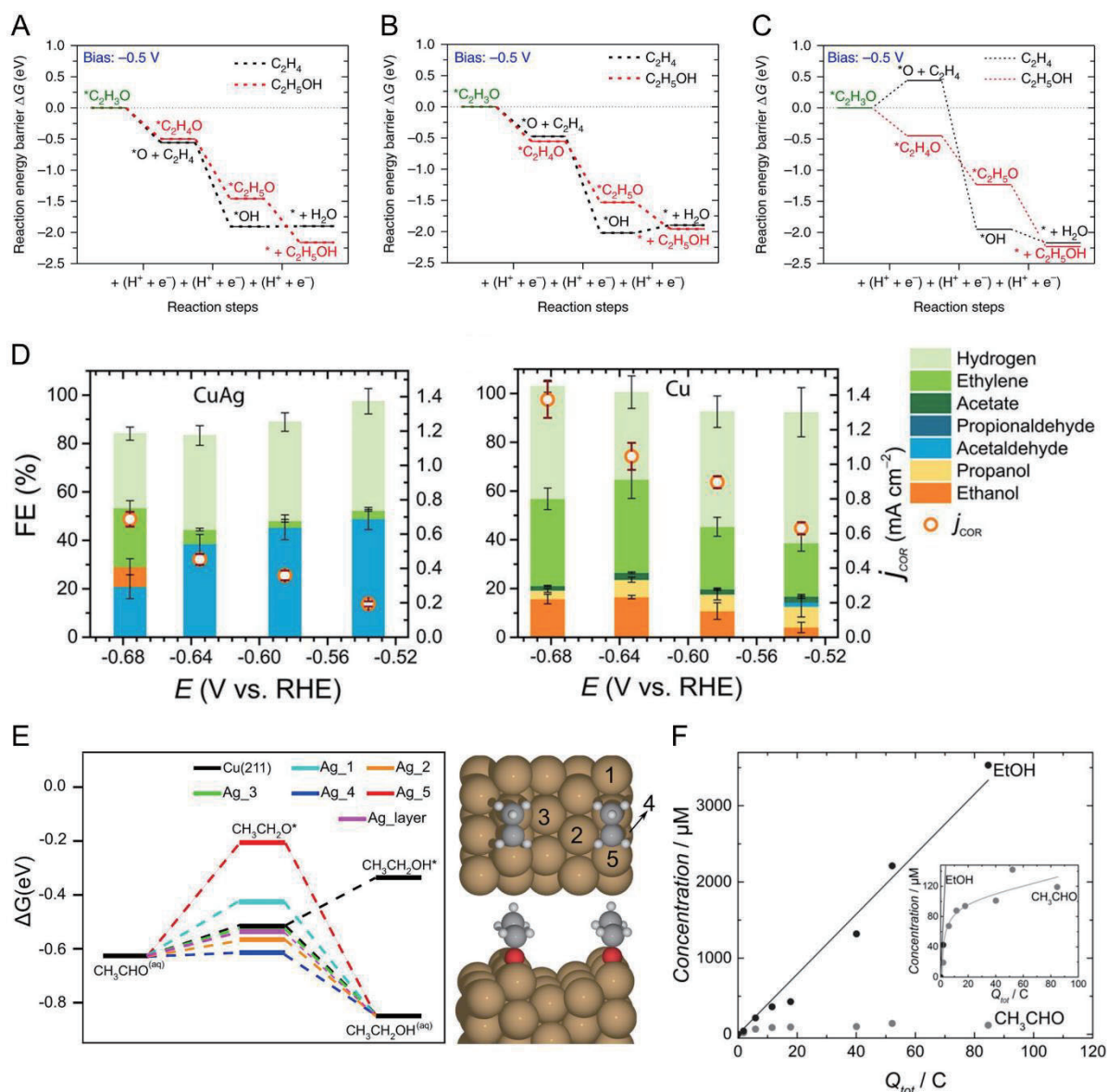


Figure 7. Role of oxygen-bound intermediates in directing CRR selectivity to multi-carbon products based on computational techniques. (A-C) Reaction Gibbs free energy diagram from the adsorbed C_2H_3O intermediate to ethylene and ethanol for Cu (A), Cu with Cu vacancy (B) and Cu with Cu vacancy and subsurface S (C) slab models at -0.5 V bias potential. Reproduced with permission from ref. ¹¹² Copyright 2018, Nature Publishing Group. (D) Selective reduction of CO on CuAg (left) and Cu (right) electrodes. (E) Free energy diagram (left) for CH_3CHO^* reduction to ethanol on the Cu (211) surface with Ag doped at different sites. The free energy of CH_3CHO^* on the pristine Cu (211) surface is taken as an energy reference. The adsorption structure of $CH_3CH_2O^*$ is shown from the top and side view (right). Ag_n denotes when Cu(n) on the surface is replaced by Ag. Ag_{layer} means the subsurface layer of Cu is replaced by Ag. (D) and (E) are reproduced with permission from ref. ¹¹⁵ Copyright 2020, National Academy of Sciences. (F) Acetaldehyde and ethanol concentration from CO reduction at -0.33 V shown as a function of the charge involved in each measurement. Reproduced with permission from ref. ⁵² Copyright 2016, Wiley-VCH.

However, the incorporation of surface vacancies and subsurface sulphur in a copper model system induced a significant increase of the energy barrier in the ethylene pathway, while the ethanol pathway still remained unaffected (Figure 7C). These findings suggested that the thermodynamics of the oxygen-bound CH_2CHO intermediate might shift the selectivity balance from ethylene to ethanol. Engineering synergistic active centers with improved oxygen affinity also provides a feasible route to modify the adsorption behaviour and reaction energetics of intermediates. DFT calculations found that the carbon species in the graphitic carbon nitride (g- C_3N_4) scaffold of a Cu- C_3N_4 catalyst showed strong binding toward oxygen-bound reaction intermediates, while the carbon-bound intermediates strongly adsorbed on the Cu site.¹¹³ This intramolecular synergistic catalysis showed favorable thermodynamics for the production of C_2 products and was further validated by experimental evidence.

As mentioned above, acetaldehyde is a key C_2 species and has been suggested as a precursor for ethanol production in CO_2 and CO reduction on Cu surfaces.^{9, 85, 114} Hori et al. showed that the electroreduction of acetaldehyde on a Cu electrode mainly led to the production of ethanol.⁹ Theoretical investigations demonstrated that ethylene, acetaldehyde, and ethanol share a common pathway during CO reduction on Cu (100) electrodes.²⁰ Additionally, a mechanistic study on oxide-derived copper showed that acetaldehyde was a minor product but key intermediate in the electroreduction of CO to ethanol (Figure 7F).⁵² DFT calculations showed that there was lower free energy for acetaldehyde compared to its counterparts, which was in agreement with the detection of acetaldehyde from headspace analysis. However, the low current efficiency of acetaldehyde suggested its further reduction to ethanol was preferred. Wang et al. found that acetaldehyde was the major product obtained on CuAg catalysts prepared from the galvanic replacement of Ag on Cu (Figure 7D).¹¹⁵ DFT calculations indicated that the adsorption strength of the reduced acetaldehyde intermediate ($\text{CH}_3\text{CH}_2\text{O}^*$)

was weakened due to Ag ad-atoms on Cu (Figure 7E). As a result, further reduction to ethanol was suppressed on the CuAg electrodes.

Ethane is another important C₂ product with higher energy density than ethylene and ethanol.⁴⁶ However, there is a limited understanding of its reaction pathway and mechanism because of its low yield and selectivity.¹¹⁶⁻¹¹⁹ It has been proposed that ethane formation pathway may proceed through the hydrogenation of ethylene.^{101, 102, 119-121} Chen et al. indicated that efficient reduction of CO₂ to ethane could be achieved on Cu₂O-derived Cu with the assistance of adsorbed PdCl_x, which facilitates the adsorption and hydrogenation of pre-generated ethylene.¹⁰² Alternatively, it was suggested that ethane formation proceeds via the dimerization of *CH₃ intermediates.¹⁰³ The authors demonstrated that the improved stability of *CH₃ intermediates on thick oxide-derived Cu catalysts with a high population of Cu⁺ sites may contribute to the enhanced formation of ethane at low overpotentials. It should be noted that *CH₃ is also a potential intermediate for methane formation.^{21, 85} Ma et al. investigated the electrochemical reduction of CO₂ to hydrocarbons on Cu nanowire arrays.¹⁰⁴ The authors found that ethane formation was always accompanied by ethanol production, while no methane formation was observed on longer Cu nanowires. Therefore, they proposed that the reaction pathway to ethane and ethanol proceeded via the CH₃CH₂O* intermediate through a CO coupling mechanism. Very recently, an *in situ* spectroscopy study by our lab on compound-derived copper electrocatalysts supported this ethane formation mechanism by detection of an oxygen-bound ethoxy (CH₃CH₂O*) intermediate (discussed in detail below).⁴⁶ Despite these reported mechanisms, greater understanding is needed regarding the ethane formation pathways.

While few spectroscopic studies have set out to understand the role of oxygen-bound intermediates in the pathway to C₂₊ products, some interesting insights have still been obtained. In a work by Katayama et al., which used SEIRAS and ambient-pressure X-ray photoelectron

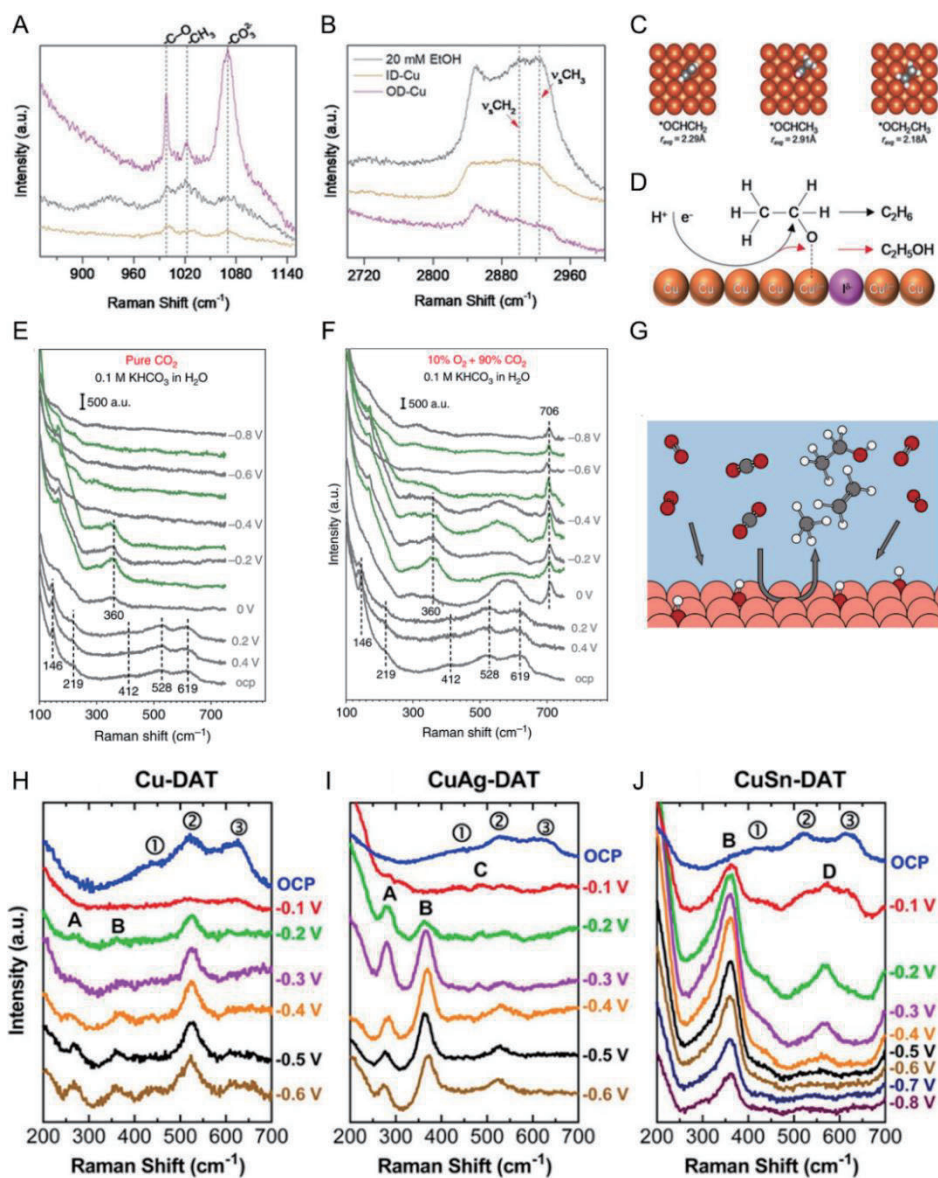


Figure 8. Role of oxygen-bound intermediates in directing CRR selectivity to multi-carbon products based on experimental techniques. (A) *In situ* Raman spectra in CO₂-saturated 0.2 M NaHCO₃ for ID-Cu and OD-Cu samples shown for the region between 850–1150 cm⁻¹ at -1.0 V. (B) The -CH_x stretching region between 2700–3000 cm⁻¹ at -0.8 V. (C) DFT calculated bond lengths for relevant oxygen-bound intermediates in the C₂ pathway. (D) C₂ reaction pathway outlining the selectivity determining ethoxy (CH₃CH₂O*) intermediate between ethane and ethanol. (A) to (D) are reproduced with permission from ref. ⁴⁶ Copyright 2020, Wiley-VCH. (E-F) *In situ* surface-enhanced Raman spectra of Cu electrocatalysts under pure CO₂ gas feed in 0.1 M KHCO₃/ H₂O (E) and 10% O₂ + 90% CO₂ in 0.1M KHCO₃/H₂O (F). (G) Schematic of the CRR on a Cu surface in the presence of hydroxyl groups induced by the ORR. (E) to (G) are reproduced with permission from ref. ¹²² Copyright 2020, Nature Publishing Group. (H-J) Potential-dependent *in situ* SERS spectra obtained from Cu-DAT (H), CuAg-DAT (I) and CuSn-DAT (J) in a Raman flow cell with 1 M KOH electrolyte flow rate of 1 mL min⁻¹ and a CO₂ flow rate of 7 sccm. Reproduced with permission from ref. ¹²⁴ Copyright 2020, American Chemical Society.

spectroscopy (APXPS), the authors investigated the selectivity dependence on carbon- and oxygen-bound intermediates for Cu, Pt, and Au.⁹⁰ Of the metals tested, Cu alone exhibited vibrational bands related to C₂ products. Attributed to the relatively strong oxygen binding of Cu, -C–H bending of oxygen-bound CH₃CH₂O* intermediates was detected at 1340 cm⁻¹ under CRR potentials. In this study, they do not attribute the CH₃CH₂O* intermediate to any observed product (ethylene being the only C₂ product observed). However, their total Faradaic efficiencies were below 100 % (~80 % for all reduction products) which may be attributed to undetected products. As our group and others have found, the CH₃CH₂O* intermediate is consistent with the production of ethanol, which is a commonly observed product on Cu.^{46, 52,}
¹⁰⁴ Using *in situ* Raman spectroscopy and in-situ X-ray absorption fine structure, we detected this ethoxy intermediate on an iodide-derived copper which showed higher selectivity and faster kinetics towards ethane production compared to OD-Cu (Figure 8A and B). From this study, we reasoned that ethane follows the same pathway to ethylene and ethanol and better stabilization of the late stage ethoxy intermediate can steer the reaction to ethane over ethanol (Figure 8C and D). Again, it is important to consider optimizing the O-binding requirement of a catalyst surface to steer the reaction pathway as desired.

In an interesting work by He et al., CO₂ gas with minor O₂ partial pressures were used for co-electrolysis and demonstrated a promotion of CO₂ reduction activity compared to the pure CO₂ case.¹²² Compared to the pure CO₂ gas feed and experiments using H₂O₂, a distinct band at 706 cm⁻¹ was observed using SERS when the potential was stepped negatively and O₂ was present (Figure 8E and F). They assigned this band to surface hydroxyl species and concluded that oxygen followed a 4e⁻ reduction mechanism. More importantly, they demonstrated that these surface hydroxyls were able to enhance the reduction of CO₂ to C₂₊ products because a certain amount of *OH coverage was able to reduce the activation barrier and free energy change for *CO coupling (Figure 8G). This is an interesting finding given *OH species are

often overlooked during mechanistic discussion of the CRR, yet are nonetheless present in the C₂ pathway.²⁰ Other spectroscopic investigations into the C₂ pathway have mainly focused on the surface *CO speciation, rather than oxygen-bound intermediates.¹²³⁻¹²⁵ In one study, it was proposed that an oxide layer on copper grows as the potential is decreased due to observation of increasing band intensity around 550 cm⁻¹ (near T_{2g} vibrational mode of Cu₂O), as shown in Figure 8H-J.¹²⁴ This band was considered a poisoning oxide species in an early SERS work.⁸⁸ Therefore, it is also essential for overall mechanism determination to investigate *in situ* any surface or compositional changes that may occur on the catalyst surface during transient events.

4. Summary and Outlook

To date, tremendous efforts have been devoted to the identification of key intermediates in the CRR pathway and their role in directing selectivity. However, the complexity of CO₂ reduction impedes the development of efficient electrocatalysts with specific selectivity to desired products. In the past, it was generally recognized that the interaction between surface-bound species and the catalyst surface has a significant effect on controlling the product distribution. Specifically, we find that oxygen-bound species are crucial for determining selectivity among branching reaction pathways for the CRR. In this Review, we have summarized how oxygen-bound intermediates modify the selectivity trend from both computational and experimental aspects.

From the computational perspective, these techniques greatly facilitate our understanding of the reaction mechanism and pathway selection at the atomic level. In the past, the elementary steps at the initial stages of the CRR pathway have been thoroughly studied, taking into consideration the reaction thermodynamics and kinetics. At different stages of the C₁ pathway, the evolution of various oxygen-containing intermediates (e.g. *OCHO, *CHO, CH₂O*, CH₃O*) leads to diverse reaction energetics and resultant selectivity distribution for C₁ products.^{19, 26, 32, 35, 47, 48, 81} Regarding C₂/C₃ pathways, less progress has been made to

understand the reaction energetics of intermediates in the later stages. Nevertheless, in some theoretical studies, oxygen-bound intermediates play an important role in regulating selectivity to certain C₂ products.^{20, 27} The breakage or preservation of the C-O bonds in oxygen-bound C₂ intermediates (e.g. CH₂CHO*, CH₃CH₂O*) can influence the selectivity for C₂ hydrocarbon versus oxygenate production.^{46, 104, 115} Further, it has been suggested that the oxygen binding strength of the catalyst can affect the adsorption behaviour of oxygen-containing intermediates and product selectivity.³³ Therefore, optimizing the adsorption behaviour and energetics of oxygen-bound species is likely useful for increasing catalyst selectivity for specific products. To achieve higher selectivity, many materials engineering strategies were proposed in computational works. Some of the strategies suggested the introduction of a doping element for regulating the adsorption energies of reaction intermediates and resultant selectivity. Other approaches like interface engineering, alloying, hybridizing, surface reconstruction all have their place in directing CRR selectivity. In addition, operando computations under real catalytic conditions, including solvation effects, ion effects, local pH, would advance our understanding of selectivity trends in CO₂ reduction.

From the experimental perspective, similar conclusions were drawn about the importance of oxygen bound intermediates. While many spectroscopy studies have investigated the early reaction pathway, relatively few have been devoted to study of the late reaction pathway. As outlined in this Review, the reaction pathway to deeply reduced products contains various oxygen-bound intermediates, which is a topic worthy of study in the future. Based on the summaries in this Review paper, the design of catalyst materials for the CRR should consider a balanced adsorption of oxygen-bound and carbon-bound species.

Acknowledgements

The authors acknowledge financial support from the Australian Research Council (DP190103472, FT190100636, and FL170100154).

Conflicts of Interest

The authors have no conflicts of interest to declare.

References

1. Q. Lu and F. Jiao, *Nano Energy*, 2016, **29**, 439-456.
2. J. H. Montoya, L. C. Seitz, P. Chakthranont, A. Vojvodic, T. F. Jaramillo and J. K. Nørskov, *Nat. Mater.*, 2017, **16**, 70-81.
3. O. S. Bushuyev, P. De Luna, C. T. Dinh, L. Tao, G. Saur, J. van de Lagemaat, S. O. Kelley and E. H. Sargent, *Joule*, 2018, **2**, 825-832.
4. A. Vasileff, Y. Zheng and S. Z. Qiao, *Adv. Energy. Mater.*, 2017, **7**, 1700759.
5. R. Kortlever, J. Shen, K. J. Schouten, F. Calle-Vallejo and M. T. M. Koper, *J. Phys. Chem. Lett.*, 2015, **6**, 4073-4082.
6. L. R. L. Ting and B. S. Yeo, *Curr. Opin. Electrochem.*, 2018, **8**, 126-134.
7. Q. Fan, M. Zhang, M. Jia, S. Liu, J. Qiu and Z. Sun, *Mater. Today Energy*, 2018, **10**, 280-301.
8. Y. Hori, A. Murata and R. Takahashi, *J. Chem. Soc., Faraday Trans. 1*, 1989, **85**, 2309-2326.
9. Y. Hori, R. Takahashi, Y. Yoshinami and A. Murata, *J. Phys. Chem. B*, 1997, **101**, 7075-7081.
10. J. J. Kim, D. P. Summers and K. W. Frese, *J. Electroanal. Chem. Interfacial Electrochem.*, 1988, **245**, 223-244.
11. D. W. DeWulf, T. Jin and A. J. Bard, *J. Electrochem. Soc.*, 1989, **136**, 1686-1691.
12. Y. Hori, A. Murata, R. Takahashi and S. Suzuki, *J. Am. Chem. Soc.*, 1987, **109**, 5022-5023.
13. Y. Hori, A. Murata, T. Tsukamoto, H. Wakebe, O. Koga and H. Yamazaki, *Electrochim. Acta*, 1994, **39**, 2495-2500.
14. Y. Hori, O. Koga, H. Yamazaki and T. Matsuo, *Electrochim. Acta*, 1995, **40**, 2617-2622.
15. A. Wuttig, C. Liu, Q. Peng, M. Yaguchi, C. H. Hendon, K. Motobayashi, S. Ye, M. Osawa and Y. Surendranath, *ACS Cent. Sci.*, 2016, **2**, 522-528.

16. C. M. Gunathunge, X. Li, J. Li, R. P. Hicks, V. J. Ovalle and M. M. Waegele, *J. Phys. Chem. C*, 2017, **121**, 12337-12344.
17. M. B. Ross, C. T. Dinh, Y. Li, D. Kim, P. De Luna, E. H. Sargent and P. Yang, *J. Am. Chem. Soc.*, 2017, **139**, 9359-9363.
18. C. M. Gunathunge, V. J. Ovalle, Y. Li, M. J. Janik and M. M. Waegele, *ACS Catal.*, 2018, **8**, 7507-7516.
19. A. A. Peterson, F. Abild-Pedersen, F. Studt, J. Rossmeisl and J. K. Nørskov, *Energy Environ. Sci.*, 2010, **3**, 1311-1315.
20. F. Calle-Vallejo and M. T. M. Koper, *Angew. Chem. Int. Ed.*, 2013, **52**, 7282-7285.
21. X. Nie, M. R. Esopi, M. J. Janik and A. Asthagiri, *Angew. Chem. Int. Ed.*, 2013, **52**, 2459-2462.
22. J. H. Montoya, A. A. Peterson and J. K. Nørskov, *ChemCatChem*, 2013, **5**, 737-742.
23. H. Xiao, T. Cheng, W. A. Goddard and R. Sundararaman, *J. Am. Chem. Soc.*, 2016, **138**, 483-486.
24. T. Cheng, H. Xiao and W. A. Goddard, *Proc. Natl. Acad. Sci. U. S. A.*, 2017, **114**, 1795-1800.
25. H. Xiao, T. Cheng and W. A. Goddard, *J. Am. Chem. Soc.*, 2017, **139**, 130-136.
26. A. Bagger, W. Ju, A. S. Varela, P. Strasser and J. Rossmeisl, *Chemphyschem*, 2017, **18**, 3266-3273.
27. S. Hanselman, M. T. M. Koper and F. Calle-Vallejo, *ACS Energy Lett.*, 2018, **3**, 1062-1067.
28. A. Vasileff, C. Xu, Y. Jiao, Y. Zheng and S. Z. Qiao, *Chem*, 2018, **4**, 1809-1831.
29. A. Bagger, W. Ju, A. S. Varela, P. Strasser and J. Rossmeisl, *ACS Catal.*, 2019, **9**, 7894-7899.
30. X. Zhi, Y. Jiao, Y. Zheng, A. Vasileff and S.-Z. Qiao, *Nano Energy*, 2020, **71**, 104601.
31. M. T. Tang, H. Peng, P. S. Lamoureux, M. Bajdich and F. Abild-Pedersen, *Appl. Catal., B*, 2020, **279**, 119384.
32. A. A. Peterson and J. K. Nørskov, *J. Phys. Chem. Lett.*, 2012, **3**, 251-258.

33. K. P. Kuhl, T. Hatsukade, E. R. Cave, D. N. Abram, J. Kibsgaard and T. F. Jaramillo, *J. Am. Chem. Soc.*, 2014, **136**, 14107-14113.
34. X. Liu, J. Xiao, H. Peng, X. Hong, K. Chan and J. K. Nørskov, *Nat. Commun.*, 2017, **8**, 15438.
35. J. T. Feaster, C. Shi, E. R. Cave, T. Hatsukade, D. N. Abram, K. P. Kuhl, C. Hahn, J. K. Nørskov and T. F. Jaramillo, *ACS Catal.*, 2017, **7**, 4822-4827.
36. A. D. Handoko, F. Wei, Jenndy, B. S. Yeo and Z. W. Seh, *Nat. Catal.*, 2018, **1**, 922-934.
37. S. Zhu, B. Jiang, W.-B. Cai and M. Shao, *J. Am. Chem. Soc.*, 2017, **139**, 15664-15667.
38. N. J. Firet and W. A. Smith, *ACS Catal.*, 2017, **7**, 606-612.
39. I. Oda, H. Ogasawara and M. Ito, *Langmuir*, 1996, **12**, 1094-1097.
40. I. V. Chernyshova, P. Somasundaran and S. Ponnurangam, *Proc. Natl. Acad. Sci. U. S. A.*, 2018, **115**, E9261-E9270.
41. D. Bohra, I. Ledezma-Yanez, G. Li, W. de Jong, E. A. Pidko and W. A. Smith, *Angew. Chem. Int. Ed.*, 2019, **58**, 1345-1349.
42. Z. Pan, K. Wang, K. Ye, Y. Wang, H.-Y. Su, B. Hu, J. Xiao, T. Yu, Y. Wang and S. Song, *ACS Catal.*, 2020, **10**, 3871-3880.
43. D.-Y. Wu, J.-F. Li, B. Ren and Z.-Q. Tian, *Chem. Soc. Rev.*, 2008, **37**, 1025-1041.
44. Y. Zheng, A. Vasileff, X. Zhou, Y. Jiao, M. Jaroniec and S. Z. Qiao, *J. Am. Chem. Soc.*, 2019, **141**, 7646-7659.
45. Y. Zhou, F. Che, M. Liu, C. Zou, Z. Liang, P. De Luna, H. Yuan, J. Li, Z. Wang, H. Xie, H. Li, P. Chen, E. Bladt, R. Quintero-Bermudez, T.-K. Sham, S. Bals, J. Hofkens, D. Sinton, G. Chen and E. H. Sargent, *Nat. Chem.*, 2018, **10**, 974-980.
46. A. Vasileff, Y. Zhu, X. Zhi, Y. Zhao, L. Ge, H. M. Chen, Y. Zheng and S.Z. Qiao, *Angew. Chem. Int. Ed.*, 2020, **59**, 19649-19653.
47. X. Nie, W. Luo, M. J. Janik and A. Asthagiri, *J. Catal.*, 2014, **312**, 108-122.
48. Y. J. Zhang and A. A. Peterson, *Phys. Chem. Chem. Phys.*, 2015, **17**, 4505-4515.
49. J. H. Montoya, C. Shi, K. Chan and J. K. Nørskov, *J. Phys. Chem. Lett.*, 2015, **6**, 2032-2037.

50. E. Pérez-Gallent, M. C. Figueiredo, F. Calle-Vallejo and M. T. M. Koper, *Angew. Chem. Int. Ed.*, 2017, **56**, 3621-3624.
51. K. D. Yang, C. W. Lee, K. Jin, S. W. Im and K. T. Nam, *J. Phys. Chem. Lett.*, 2017, **8**, 538-545.
52. E. Bertheussen, A. Verdaguier-Casadevall, D. Ravasio, J. H. Montoya, D. B. Trimarco, C. Roy, S. Meier, J. Wendland, J. K. Nørskov, I. E. L. Stephens and I. Chorkendorff, *Angew. Chem. Int. Ed.*, 2016, **55**, 1450-1454.
53. E. L. Clark and A. T. Bell, *J. Am. Chem. Soc.*, 2018, **140**, 7012-7020.
54. D. Ren, B. S.-H. Ang and B. S. Yeo, *ACS Catal.*, 2016, **6**, 8239-8247.
55. S. Ma, M. Sadakiyo, R. Luo, M. Heima, M. Yamauchi and P. J. A. Kenis, *J. Power Sources*, 2016, **301**, 219-228.
56. S. Lee, G. Park and J. Lee, *ACS Catal.*, 2017, **7**, 8594-8604.
57. Y. Lum and J. W. Ager, *Energy Environ. Sci.*, 2018, **11**, 2935-2944.
58. J. Huang, M. Mensi, E. Oveisi, V. Mantella and R. Buonsanti, *J. Am. Chem. Soc.*, 2019, **141**, 2490-2499.
59. C. G. Morales-Guio, E. R. Cave, S. A. Nitopi, J. T. Feaster, L. Wang, K. P. Kuhl, A. Jackson, N. C. Johnson, D. N. Abram, T. Hatsukade, C. Hahn and T. F. Jaramillo, *Nat. Catal.*, 2018, **1**, 764-771.
60. Y. Zheng, Y. Jiao, Y. H. Zhu, L. H. Li, Y. Han, Y. Chen, A. J. Du, M. Jaroniec and S. Z. Qiao, *Nat. Commun.*, 2014, **5**, 3783.
61. J. K. Nørskov, J. Rossmeisl, A. Logadottir, L. Lindqvist, J. R. Kitchin, T. Bligaard and H. Jonsson, *J. Phys. Chem. B*, 2004, **108**, 17886-17892.
62. I. C. Man, H.-Y. Su, F. Calle-Vallejo, H. A. Hansen, J. I. Martínez, N. G. Inoglu, J. Kitchin, T. F. Jaramillo, J. K. Nørskov and J. Rossmeisl, *ChemCatChem*, 2011, **3**, 1159-1165.
63. Y. Jiao, Y. Zheng, K. Davey and S. Z. Qiao, *Nat. Energy*, 2016, **1**, 16130.
64. X. Liu, Y. Jiao, Y. Zheng, K. Davey and S. Z. Qiao, *J. Mater. Chem. A*, 2019, **7**, 3648-3654.
65. M. R. Singh, J. D. Goodpaster, A. Z. Weber, M. Head-Gordon and A. T. Bell, *Proc. Natl. Acad. Sci. U. S. A.*, 2017, **114**, E8812-E8821.

66. T. K. Todorova, M. W. Schreiber and M. Fontecave, *ACS Catal.*, 2020, **10**, 1754-1768.
67. J. S. Yoo, R. Christensen, T. Vegge, J. K. Nørskov and F. Studt, *ChemSusChem*, 2016, **9**, 358-363.
68. X. Bai, W. Chen, C. Zhao, S. Li, Y. Song, R. Ge, W. Wei and Y. Sun, *Angew. Chem. Int. Ed.*, 2017, **56**, 12219-12223.
69. Y. Deng, Y. Huang, D. Ren, A. D. Handoko, Z. W. Seh, P. Hirunsit and B. S. Yeo, *ACS Appl. Mater. Interfaces*, 2018, **10**, 28572-28581.
70. K. Ye, Z. Zhou, J. Shao, L. Lin, D. Gao, N. Ta, R. Si, G. Wang and X. Bao, *Angew. Chem. Int. Ed.*, 2020, **59**, 4814-4821.
71. X. Zheng, P. De Luna, F. P. García de Arquer, B. Zhang, N. Becknell, M. B. Ross, Y. Li, M. N. Banis, Y. Li, M. Liu, O. Voznyy, C. T. Dinh, T. Zhuang, P. Stadler, Y. Cui, X. Du, P. Yang and E. H. Sargent, *Joule*, 2017, **1**, 794-805.
72. W. Luc, C. Collins, S. W. Wang, H. L. Xin, K. He, Y. J. Kang and F. Jiao, *J. Am. Chem. Soc.*, 2017, **139**, 1885-1893.
73. B. Jiang, X.-G. Zhang, K. Jiang, D.-Y. Wu and W.-B. Cai, *J. Am. Chem. Soc.*, 2018, **140**, 2880-2889.
74. A. Klinkova, P. De Luna, C.-T. Dinh, O. Voznyy, E. M. Larin, E. Kumacheva and E. H. Sargent, *ACS Catal.*, 2016, **6**, 8115-8120.
75. K. Fan, Y. Jia, Y. Ji, P. Kuang, B. Zhu, X. Liu and J. Yu, *ACS Catal.*, 2020, **10**, 358-364.
76. P. Deng, H. Wang, R. Qi, J. Zhu, S. Chen, F. Yang, L. Zhou, K. Qi, H. Liu and B. Y. Xia, *ACS Catal.*, 2020, **10**, 743-750.
77. C. Cao, D.-D. Ma, J.-F. Gu, X. Xie, G. Zeng, X. Li, S.-G. Han, Q.-L. Zhu, X.-T. Wu and Q. Xu, *Angew. Chem. Int. Ed.*, 2020, **59**, 15014-15020.
78. Q. Gong, P. Ding, M. Xu, X. Zhu, M. Wang, J. Deng, Q. Ma, N. Han, Y. Zhu, J. Lu, Z. Feng, Y. Li, W. Zhou and Y. Li, *Nat. Commun.*, 2019, **10**, 2807.
79. J. H. Koh, D. H. Won, T. Eom, N.-K. Kim, K. D. Jung, H. Kim, Y. J. Hwang and B. K. Min, *ACS Catal.*, 2017, **7**, 5071-5077.
80. N. Han, Y. Wang, H. Yang, J. Deng, J. Wu, Y. Li and Y. Li, *Nat. Commun.*, 2018, **9**, 1320.

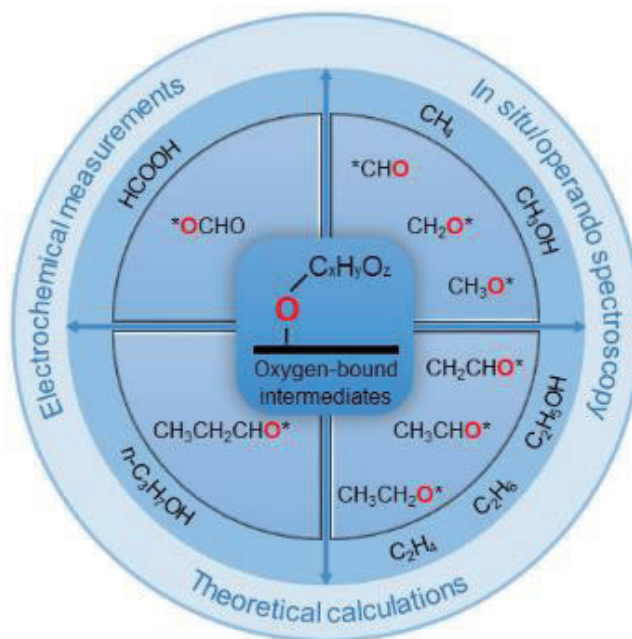
81. A. Vasileff, X. Zhi, C. Xu, L. Ge, Y. Jiao, Y. Zheng and S. Z. Qiao, *ACS Catal.*, 2019, **9**, 9411-9417.
82. A. Vasileff, C. C. Xu, L. Ge, Y. Zheng and S. Z. Qiao, *Chem. Commun.*, 2018, **54**, 13965-13968.
83. M. Dunwell, W. Luc, Y. Yan, F. Jiao and B. Xu, *ACS Catal.*, 2018, **8**, 8121-8129.
84. A. Javier, B. Chmielowiec, J. Sanabria-Chinchilla, Y.-G. Kim, J. H. Baricuatro and M. P. Soriaga, *Electrocatalysis*, 2015, **6**, 127-131.
85. K. J. P. Schouten, Y. Kwon, C. J. M. van der Ham, Z. Qin and M. T. M. Koper, *Chem. Sci.*, 2011, **2**, 1902-1909.
86. H. A. Hansen, C. Shi, A. C. Lausche, A. A. Peterson and J. K. Nørskov, *Phys. Chem. Chem. Phys.*, 2016, **18**, 9194-9201.
87. S. Back, H. Kim and Y. Jung, *ACS Catal.*, 2015, **5**, 965-971.
88. B. D. Smith, D. E. Irish, P. Kedzierzawski and J. Augustynski, *J. Electrochem. Soc.*, 1997, **144**, 4288-4296.
89. Y. Ichinohe, T. Wadayama and A. Hatta, *J. Raman Spectrosc.*, 1995, **26**, 335-340.
90. Y. Katayama, F. Nattino, L. Giordano, J. Hwang, R. R. Rao, O. Andreussi, N. Marzari and Y. Shao-Horn, *J. Phys. Chem. C*, 2019, **123**, 5951-5963.
91. W. J. Durand, A. A. Peterson, F. Studt, F. Abild-Pedersen and J. K. Nørskov, *Surf. Sci.*, 2011, **605**, 1354-1359.
92. M. Umeda, Y. Niitsuma, T. Horikawa, S. Matsuda and M. Osawa, *ACS Appl. Energy Mater.*, 2020, **3**, 1119-1127.
93. Z. Weng, Y. Wu, M. Wang, J. Jiang, K. Yang, S. Huo, X.-F. Wang, Q. Ma, G. W. Brudvig, V. S. Batista, Y. Liang, Z. Feng and H. Wang, *Nat. Commun.*, 2018, **9**, 415.
94. K. J. P. Schouten, Z. Qin, E. Pérez Gallent and M. T. M. Koper, *J. Am. Chem. Soc.*, 2012, **134**, 9864-9867.
95. J. D. Goodpaster, A. T. Bell and M. Head-Gordon, *J. Phys. Chem. Lett.*, 2016, **7**, 1471-1477.
96. A. J. Garza, A. T. Bell and M. Head-Gordon, *ACS Catal.*, 2018, **8**, 1490-1499.
97. K. Jiang, R. B. Sandberg, A. J. Akey, X. Liu, D. C. Bell, J. K. Nørskov, K. Chan and H. Wang, *Nat. Catal.*, 2018, **1**, 111-119.

98. D. Gao, R. M. Arán-Ais, H. S. Jeon and B. Roldan Cuenya, *Nat. Catal.*, 2019, **2**, 198-210.
99. L. Fan, C. Xia, F. Yang, J. Wang, H. Wang and Y. Lu, *Sci. Adv.*, 2020, **6**, eaay3111.
100. I. Ledezma-Yanez, E. P. Gallent, M. T. M. Koper and F. Calle-Vallejo, *Catal. Today*, 2016, **262**, 90-94.
101. A. Dutta, M. Rahaman, N. C. Luedi, M. Mohos and P. Broekmann, *ACS Catal.*, 2016, **6**, 3804-3814.
102. C. S. Chen, J. H. Wan and B. S. Yeo, *J. Phys. Chem. C*, 2015, **119**, 26875-26882.
103. A. D. Handoko, K. W. Chan and B. S. Yeo, *ACS Energy Lett.*, 2017, **2**, 2103-2109.
104. M. Ma, K. Djanashvili and W. A. Smith, *Angew. Chem. Int. Ed.*, 2016, **55**, 6680-6684.
105. J. Li, F. Che, Y. Pang, C. Zou, J. Y. Howe, T. Burdyny, J. P. Edwards, Y. Wang, F. Li, Z. Wang, P. De Luna, C.-T. Dinh, T.-T. Zhuang, M. I. Saidaminov, S. Cheng, T. Wu, Y. Z. Finfrock, L. Ma, S.-H. Hsieh, Y.-S. Liu, G. A. Botton, W.-F. Pong, X. Du, J. Guo, T.-K. Sham, E. H. Sargent and D. Sinton, *Nat. Commun.*, 2018, **9**, 4614.
106. T.-T. Zhuang, Y. Pang, Z.-Q. Liang, Z. Wang, Y. Li, C.-S. Tan, J. Li, C. T. Dinh, P. De Luna, P.-L. Hsieh, T. Burdyny, H.-H. Li, M. Liu, Y. Wang, F. Li, A. Proppe, A. Johnston, D.-H. Nam, Z.-Y. Wu, Y.-R. Zheng, A. H. Ip, H. Tan, L.-J. Chen, S.-H. Yu, S. O. Kelley, D. Sinton and E. H. Sargent, *Nat. Catal.*, 2018, **1**, 946-951.
107. Y. Pang, J. Li, Z. Wang, C.-S. Tan, P.-L. Hsieh, T.-T. Zhuang, Z.-Q. Liang, C. Zou, X. Wang, P. De Luna, J. P. Edwards, Y. Xu, F. Li, C.-T. Dinh, M. Zhong, Y. Lou, D. Wu, L.-J. Chen, E. H. Sargent and D. Sinton, *Nat. Catal.*, 2019, **2**, 251-258.
108. X. Wang, Z. Wang, T.-T. Zhuang, C.-T. Dinh, J. Li, D.-H. Nam, F. Li, C.-W. Huang, C.-S. Tan, Z. Chen, M. Chi, C. M. Gabardo, A. Seifitokaldani, P. Todorović, A. Proppe, Y. Pang, A. R. Kirmani, Y. Wang, A. H. Ip, L. J. Richter, B. Scheffel, A. Xu, S.-C. Lo, S. O. Kelley, D. Sinton and E. H. Sargent, *Nat. Commun.*, 2019, **10**, 5186.
109. K. J. P. Schouten, E. Pérez Gallent and M. T. M. Koper, *J. Electroanal. Chem.*, 2014, **716**, 53-57.
110. Y. Kim, S. Park, S.-J. Shin, W. Choi, B. K. Min, H. Kim, W. Kim and Y. J. Hwang, *Energy Environ. Sci.*, 2020, **13**, 4301-4311.
111. W. Luo, X. Nie, M. J. Janik and A. Asthagiri, *ACS Catal.*, 2016, **6**, 219-229.

112. T.-T. Zhuang, Z.-Q. Liang, A. Seifitokaldani, Y. Li, P. De Luna, T. Burdyny, F. Che, F. Meng, Y. Min, R. Quintero-Bermudez, C. T. Dinh, Y. Pang, M. Zhong, B. Zhang, J. Li, P.-N. Chen, X.-L. Zheng, H. Liang, W.-N. Ge, B.-J. Ye, D. Sinton, S.-H. Yu and E. H. Sargent, *Nat. Catal.*, 2018, **1**, 421-428.
113. Y. Jiao, Y. Zheng, P. Chen, M. Jaroniec and S. Z. Qiao, *J. Am. Chem. Soc.*, 2017, **139**, 18093-18100.
114. K. P. Kuhl, E. R. Cave, D. N. Abram and T. F. Jaramillo, *Energy Environ. Sci.*, 2012, **5**, 7050-7059.
115. L. Wang, D. C. Higgins, Y. Ji, C. G. Morales-Guio, K. Chan, C. Hahn and T. F. Jaramillo, *Proc. Natl. Acad. Sci. U. S. A.*, 2020, **117**, 12572-12575.
116. C. W. Li and M. W. Kanan, *J. Am. Chem. Soc.*, 2012, **134**, 7231-7234.
117. W. Tang, A. A. Peterson, A. S. Varela, Z. P. Jovanov, L. Bech, W. J. Durand, S. Dahl, J. K. Nørskov and I. Chorkendorff, *Phys. Chem. Chem. Phys.*, 2012, **14**, 76-81.
118. S. Sen, D. Liu and G. T. R. Palmore, *ACS Catal.*, 2014, **4**, 3091-3095.
119. K. D. Yang, W. R. Ko, J. H. Lee, S. J. Kim, H. Lee, M. H. Lee and K. T. Nam, *Angew. Chem. Int. Ed.*, 2017, **56**, 796-800.
120. M. R. Gonçalves, A. Gomes, J. Condeço, T. R. C. Fernandes, T. Pardal, C. A. C. Sequeira and J. B. Branco, *Electrochim. Acta*, 2013, **102**, 388-392.
121. R. Kas, R. Kortlever, A. Milbrat, M. T. M. Koper, G. Mul and J. Baltrusaitis, *Phys. Chem. Chem. Phys.*, 2014, **16**, 12194-12201.
122. M. He, C. Li, H. Zhang, X. Chang, J. G. Chen, W. A. Goddard, M.-j. Cheng, B. Xu and Q. Lu, *Nat. Commun.*, 2020, **11**, 3844.
123. J. Gao, H. Zhang, X. Guo, J. Luo, S. M. Zakeeruddin, D. Ren and M. Grätzel, *J. Am. Chem. Soc.*, 2019, **141**, 18704-18714.
124. X. Chen, D. A. Henckel, U. O. Nwabara, Y. Li, A. I. Frenkel, T. T. Fister, P. J. A. Kenis and A. A. Gewirth, *ACS Catal.*, 2020, **10**, 672-682.
125. T.-C. Chou, C.-C. Chang, H.-L. Yu, W.-Y. Yu, C.-L. Dong, J.-J. Velasco-Vélez, C.-H. Chuang, L.-C. Chen, J.-F. Lee, J.-M. Chen and H.-L. Wu, *J. Am. Chem. Soc.*, 2020, **142**, 2857-2867.

Table of Contents:

Role of Oxygen-Bound Reaction Intermediates in Selective Electrochemical CO₂ Reduction



Chapter 3: Impact of Interfacial Electron Transfer on Electrochemical CO₂ Reduction on Graphitic Carbon Nitride/Doped Graphene

3.1 Introduction and Significance

In recent years, metal-free materials have emerged as promising alternatives to metal catalysts for efficient CO₂ reduction reaction (CRR). However, the factors that can impact their catalytic activity are yet to be uncovered. In Chapter 3, we chose graphitic carbon nitride (g-C₃N₄) to investigate the feasibility of regulating its CRR catalytic activity through interfacial electron transfer. The unique functional species in g-C₃N₄ framework exhibit potential activity for CO₂ electrocatalysis, while a conductive substrate of graphene can introduce the essential charge transfer to modify the electronic properties of the hybrid structures.

In this Chapter, a series of g-C₃N₄/graphene hybrid structures with and without heteroatom doping in graphene substrate (C₃N₄/XG, XG = BG, NG, OG, PG, G) were designed and evaluated as electrocatalysts for CRR by DFT calculations. The detailed thermodynamic and charge analyses showed tuneable adsorption energetics and electronic structures among different doping cases. The linear scaling relationships of binding free energies of carbon-bound species (i.e. *COOH, *CO, *CHO) on C₃N₄/XG were observed, providing a baseline to estimate the smallest applied potentials to make corresponding CRR elementary steps become exergonic. Further, a CRR activity trend was obtained on all investigated models and displayed by a volcano type plot, which indicated the best catalytic activity for CRR to CH₄ on C₃N₄/XG with an overpotential of 0.45 V (i.e. -0.28 V vs RHE). Such a low overpotential has yet to be achieved on all previously reported metallic CRR electrocatalysts. The charge transfer analysis revealed that increased interfacial electron charge transfer from doped graphene to g-C₃N₄ could facilitate CO₂ reduction on C₃N₄/XG. The atom-level activity origin suggested the best CRR catalytic performance with more electron transfer of 0.34 e⁻. The computational studies in this Chapter sheds light on catalyst engineering strategy through doping modulation and interfacial construction, leading to the favorable modification of electronic properties and catalytic activities.

3.2 Impact of interfacial electron transfer on electrochemical CO₂ reduction on graphitic carbon nitride/doped graphene

This chapter is included as it appears as a journal paper published by Xing Zhi, Yan Jiao, Yao Zheng, Shi-Zhang Qiao, Impact of interfacial electron transfer on electrochemical CO₂ reduction on graphitic carbon nitride/doped graphene, *Small*, **2019**, 15, 1804224.

Statement of Authorship

Title of Paper	Impact of Interfacial Electron Transfer on Electrochemical CO ₂ Reduction on Graphitic Carbon Nitride/Doped Graphene
Publication Status	<input checked="" type="checkbox"/> Published <input type="checkbox"/> Accepted for Publication <input type="checkbox"/> Submitted for Publication <input type="checkbox"/> Unpublished and Unsubmitted work written in manuscript style
Publication Details	Xing Zhi, Yan Jiao, Yao Zheng, Shi-Zhang Qiao, Impact of interfacial electron transfer on electrochemical CO ₂ reduction on graphitic carbon nitride/doped graphene, <i>Small</i> , 2019 , 15, 1804224.

Principal Author

Name of Principal Author (Candidate)	Xing Zhi		
Contribution to the Paper	Conducted all the computations, carried out data analysis and wrote the paper		
Overall percentage (%)	70%		
Certification:	This paper reports on original research I conducted during the period of my Higher Degree by Research candidature and is not subject to any obligations or contractual agreements with a third party that would constrain its inclusion in this thesis. I am the primary author of this paper.		
Signature		Date	14 Dec. 2020

Co-Author Contributions

By signing the Statement of Authorship, each author certifies that:

- i. the candidate's stated contribution to the publication is accurate (as detailed above);
- ii. permission is granted for the candidate to include the publication in the thesis; and
- iii. the sum of all co-author contributions is equal to 100% less the candidate's stated contribution.

Name of Co-Author	Yan Jiao		
Contribution to the Paper	Discussed computational results and findings, supervised the project, and revised the paper.		
Signature		Date	14 Dec. 2020

Name of Co-Author	Yao Zheng		
Contribution to the Paper	Discussed the research plan, supervised the project, and revised the paper.		
Signature		Date	14 Dec. 2020

Name of Co-Author	Shi-Zhang Qiao		
Contribution to the Paper	Discussed the research plan, supervised the project, and revised the paper.		
Signature		Date	16 Dec. 2020



Impact of Interfacial Electron Transfer on Electrochemical CO₂ Reduction on Graphitic Carbon Nitride/Doped Graphene

Xing Zhi, Yan Jiao,* Yao Zheng, and Shi-Zhang Qiao*

Effective electrocatalysts are required for the CO₂ reduction reaction (CRR), while the factors that can impact their catalytic activity are yet to be discovered. In this article, graphitic carbon nitride (g-C₃N₄) is used to investigate the feasibility of regulating its CRR catalytic performance by interfacial electron transfer. A series of g-C₃N₄/graphene with and without heteroatom doping (C₃N₄/XG, XG = BG, NG, OG, PG, G) is comprehensively evaluated for CRR through computational methods. Variable adsorption energetics and electronic structures are observed among different doping cases, demonstrating that a higher catalytic activity originates from more interfacial electron transfer. An activity trend is obtained to show the best catalytic performance of CRR to methane on C₃N₄/XG with an overpotential of 0.45 V (i.e., -0.28 V vs reverse hydrogen electrode [RHE]). Such a low overpotential has never been achieved on any previously reported metallic CRR electrocatalysts, therefore indicating the availability of C₃N₄/XG for CO₂ reduction and the applicability of electron transfer modulation to improve CRR catalytic performance.

Electrochemical CO₂ reduction plays an important role in producing valuable green fuels and chemicals as commodities to store intermittent clean energy such as solar and wind.^[1] Due to the stability of CO₂ molecule, the CO₂ reduction reaction (CRR) proceeds with sluggish rate and therefore requires efficient electrocatalysts to facilitate the CO₂ conversion.^[2] In order to improve the efficiency of CO₂ reduction and promote the production of valuable hydrocarbons, some characteristics are required for the CRR catalysts, such as tunable electron distribution on the active sites to modulate the adsorption strength of reaction intermediates and reduce reaction barriers. In recent years, numerous metal-free nanostructured materials have emerged as alternatives to traditional metallic catalysts for electrochemical CRR due to their variable chemical compositions and adjustable electronic properties.^[3] The electron distribution of metal-free CRR catalysts, especially carbon-based materials, is facile to be regulated, therefore leading to desired CRR electrocatalytic activity. To this end, it is compelling to explore the underlying CRR activity origin and detailed catalytic mechanism on the metal-free materials.

X. Zhi, Dr. Y. Jiao, Dr. Y. Zheng, Prof. S.-Z. Qiao
School of Chemical Engineering
The University of Adelaide
Adelaide, South Australia 5005, Australia
E-mail: yan.jiao@adelaide.edu.au; s.qiao@adelaide.edu.au

The ORCID identification number(s) for the author(s) of this article can be found under <https://doi.org/10.1002/sml.201804224>.

DOI: 10.1002/sml.201804224

Very recently, graphitic carbon nitride (g-C₃N₄) has been investigated as an applicable metal-free nanomaterial for CO₂ catalysis.^[4] The abundant pyridinic nitrogen species in g-C₃N₄ show strong adsorption capacity to CO₂, which is crucial to activate CRR process.^[5] In addition, the carbon species in g-C₃N₄ exhibit high affinity to oxygen-bound intermediates (*OCH_x, *O, and *OH) in the reaction pathways toward deeply reduced products, such as methane (CH₄).^[6] Moreover, the electronic properties of g-C₃N₄ can be effectively modified by metal-free carbon materials and therefore provide improved electrocatalytic performance on the hybrid catalysts.^[7] These hybrid materials based on g-C₃N₄ have shown their promising capability in energy-related catalytic reactions, such as hydrogen evolution, oxygen evolution, and oxygen reduction reactions, mainly due to their highly exposed active

sites, improved electrical conductivity, and tuneable electron transfer.^[8] Among available carbon materials, the heteroatom-doped graphene has shown extraordinary properties to regulate the electronic structures of g-C₃N₄.^[9] One of the benefits from doped graphene substrates is their contribution toward good electrical conductivity of the hybrid materials. Meanwhile, the electron distribution of g-C₃N₄ can be easily adjusted by doping atoms with different electronegativity on the graphene layer. In this regard, this group of versatile g-C₃N₄/doped graphene hybrid materials might function as metal-free catalysts for electrochemical CO₂ conversion and is worthy to be investigated. Based on comprehensive understanding of these hybrid catalytic materials for CRR, such as exploration of reaction mechanisms, identification of active sites, and search of activity origin, we can unravel the feasibility of these hybrid catalysts for electrochemical CO₂ reduction and predict the best achievable catalytic performance.

In this work, we investigated the electrochemical CO₂ reduction on a series of g-C₃N₄/doped graphene hybrid structures with and without heteroatom doping in graphene substrate (C₃N₄/XG, XG = BG, NG, OG, PG, G) by using density functional theory (DFT) calculations. Through thermodynamic analysis of various possible reaction intermediates, C₃N₄/NG showed the most favorable electrocatalytic performance for CO₂ reduction, and a carbon atom (denoted as C1) in the g-C₃N₄ layer was identified as the active site. In the exploration of reduction pathways, we found that the free energies of three key carbon-bound intermediates (*COOH, *CO, *CHO) were

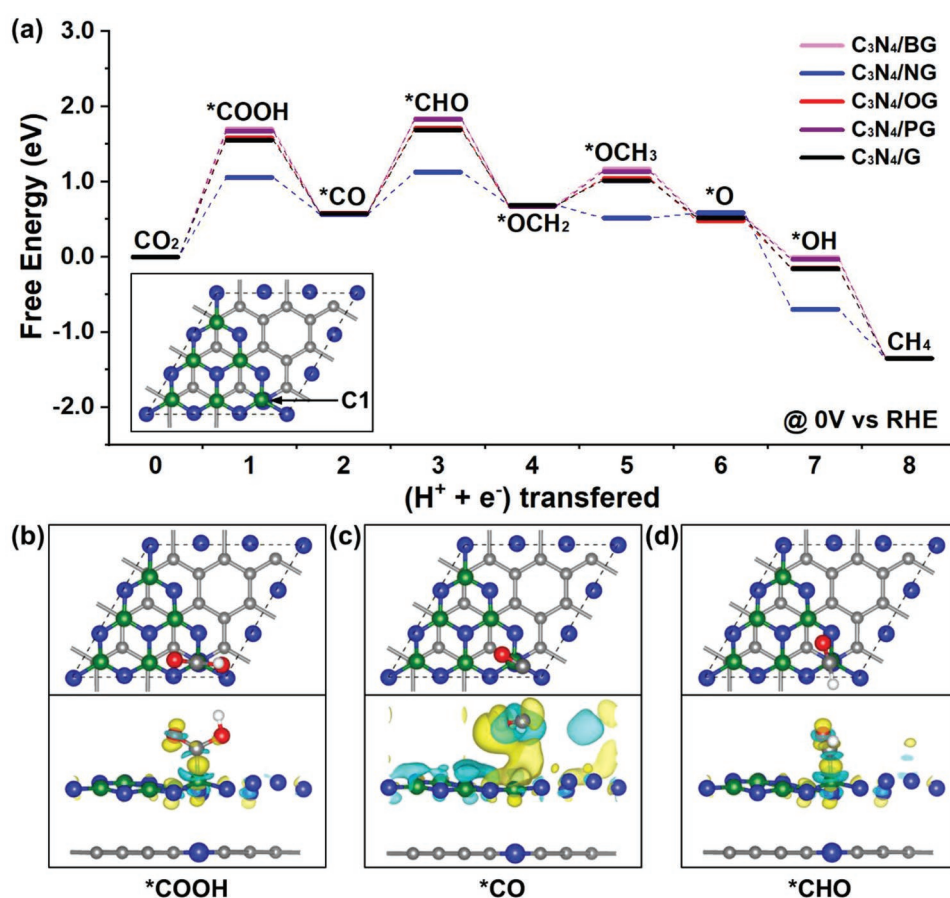


Figure 1. a) Free energy diagrams of CO_2 reduction pathways to CH_4 on C1 site of $\text{C}_3\text{N}_4/\text{XG}$ (XG = BG, NG, OG, PG, G). The inset shows the C1 site. Bottom panels show the optimized geometries and electron transfer of carbon-bound intermediates b) $^*\text{COOH}$, c) $^*\text{CO}$, and d) $^*\text{CHO}$ adsorbed on C1 site of $\text{C}_3\text{N}_4/\text{NG}$. Carbon in graphene layer and adsorbates, carbon in g- C_3N_4 layer, nitrogen, oxygen, and hydrogen atoms are gray, green, blue, red, and white, respectively. Yellow and cyan isosurface represent electron accumulation and electron depletion, respectively. The isosurface value for $^*\text{COOH}$ and $^*\text{CHO}$ is $5 \times 10^{-2} \text{ e } \text{\AA}^{-3}$. The isosurface value for $^*\text{CO}$ is $5 \times 10^{-4} \text{ e } \text{\AA}^{-3}$.

linearly correlated by scaling relations, providing a volcano-type CRR activity trend based on all investigated models. Based on this, it was able to estimate the smallest overpotential of 0.45 V (i.e., a potential of -0.28 V vs reverse hydrogen electrode [RHE]) for CO_2 reduction to CH_4 on this group of catalytic materials. Such a low overpotential has never been observed on so far reported metallic CRR electrocatalysts. The charge distribution analyses revealed that the nitrogen dopant in graphene layer led to the increased electron transfer from heteroatom-doped graphene to g- C_3N_4 , therefore facilitating the protonation of CO_2 and decreasing the free energy barrier toward CRR. In order to reach the best performance, further enhanced electron transfer of 0.34 e^- is required for CH_4 production. This study indicates the feasibility of regulating electron transfer for hybrid catalysts to improve CRR catalytic performance through doping modulation and interfacial construction.

The free energies of elementary steps on electrochemical CO_2 reduction pathway to CH_4 were explored by using DFT calculations. Very recently, the critical impact of varying charge on electrochemistry of 2D materials has been demonstrated by using the grand canonical DFT calculations.^[10] Nevertheless, the conventional DFT method was applied in this study without

incorporating the charge effects. Since g- C_3N_4 is semiconducting with a wide bandgap, it is possible that the applied potential is located within the bandgap, leading to trivial impact of charge on $\text{C}_3\text{N}_4/\text{XG}$. Further details can be found in the Supporting Information. By analyzing the CO_2 binding positions, three different atoms (C1, C2, and N) in g- C_3N_4 were tested as potential active sites (Figures S1–S6, Supporting Information). The free energy diagrams at $U = 0 \text{ V}$ versus RHE with optimal free energy changes toward CH_4 on C1 site are illustrated in Figure 1a. The x axis indicates the number of transferred proton/electron pairs to the catalyst surfaces, including five hybrid structures of $\text{C}_3\text{N}_4/\text{XG}$ (XG = BG, NG, OG, PG, G). At the beginning, the first proton/electron pair transfers to an adsorbed CO_2 to form $^*\text{COOH}$. This hydrogenation step is uphill in energy change for all five $\text{C}_3\text{N}_4/\text{XG}$ catalysts, followed by the OH desorption to form adsorbed $^*\text{CO}$. The next elementary step involves the protonation of $^*\text{CO}$ to $^*\text{CHO}$. When the fourth proton/electron pair is transferred to the metal-free electrocatalysts, the hydrogenation of $^*\text{CHO}$ occurs to form $^*\text{OCH}_2$, with oxygen becoming a connecting atom to the hybrid surfaces. This phenomenon is in good accordance with previously identified reaction mechanisms on metal

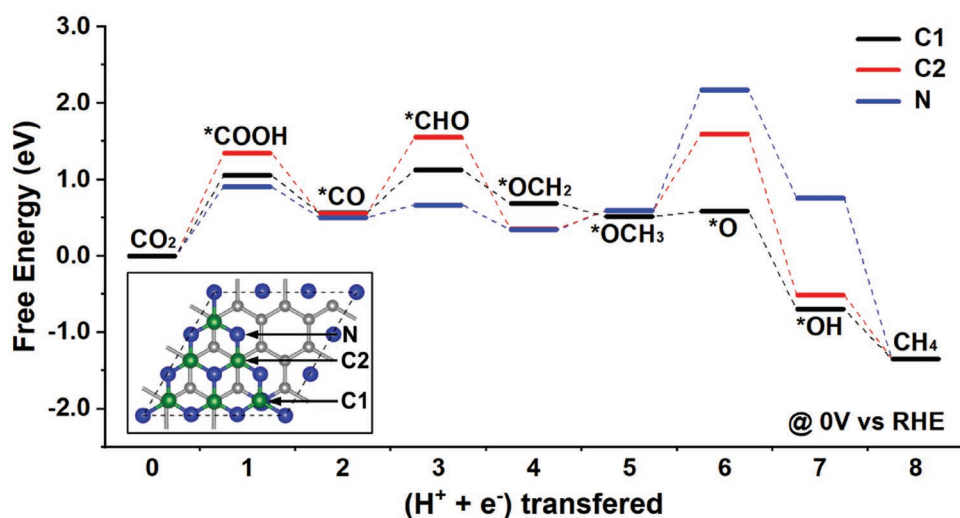


Figure 2. Free energy diagrams of CO_2 reduction to CH_4 on different sites of $\text{C}_3\text{N}_4/\text{NG}$. The inset shows the C1, C2, and N sites on $\text{C}_3\text{N}_4/\text{NG}$. Carbon in graphene layer, carbon in $g\text{-C}_3\text{N}_4$ layer, and nitrogen are gray, green, and blue, respectively.

surfaces and $\text{Cu-C}_3\text{N}_4$ structure.^[6,11] After another hydrogenation step to form $^*\text{OCH}_3$, the sixth proton/electron pair takes the $^*\text{CH}_3$ group off to produce CH_4 . The adsorbed $^*\text{O}$ left on the surface is subsequently desorbed as H_2O . For all five metal-free catalysts, the first hydrogenation process of CO_2 to $^*\text{COOH}$ on C1 site displays the highest uphill free energy change, and therefore becomes the rate-determining step. The free energy change to form $^*\text{COOH}$ is notably lower on $\text{C}_3\text{N}_4/\text{NG}$ with 1.05 eV than that on the other four hybrid surfaces, which indicates better CRR catalytic performance for $\text{C}_3\text{N}_4/\text{NG}$.

The catalytic performances of C2 and N active sites on five $\text{C}_3\text{N}_4/\text{XG}$ catalysts are also studied and compared in the following discussion. For the C2 active site (Figure S7a, Supporting Information), $\text{C}_3\text{N}_4/\text{NG}$ remains better catalytic performance toward CH_4 production than the other four hybrid surfaces, with the same rate-determining step as the first hydrogenation process to form $^*\text{COOH}$. However, for each hybrid catalyst, the free energy levels of reaction intermediates on C2 site are generally higher than those on C1 site. We also conducted the density of state (DOS) analyses of different active sites. As shown in Figure S8f in the Supporting Information, the highest peak of the active site DOS (E_p) shows an overall linear trend against the free energy of $^*\text{COOH}$. The C1 active site displays closer E_p position to the Fermi level (E_F) than the C2 site for all five investigated models (Figure S8a–e, Supporting Information), which indicates stronger adsorption capacity of C1 site to $^*\text{COOH}$. For the N active site (Figure S7b, Supporting Information), the free energy levels of carbon-bound intermediates are generally lower than those on C1 and C2 sites. This behavior is in agreement with the strong adsorption capacity of the nitrogen content in $g\text{-C}_3\text{N}_4$ to carbon-bound intermediates (e.g., $^*\text{COOH}$, $^*\text{CO}$, $^*\text{CHO}$), in good accordance with the previous study.^[6] However, the oxygen-bound intermediates (e.g., $^*\text{OCH}_3$, $^*\text{O}$, $^*\text{OH}$) show higher free energy levels on N site compared with C1 site, therefore leading to an overall poorer catalytic activity toward CRR.

In the exploration of the lowest free energy pathway toward CH_4 production on five $\text{C}_3\text{N}_4/\text{XG}$ catalysts with different

active sites, $\text{C}_3\text{N}_4/\text{NG}$ generally shows favorable catalytic performance. Meanwhile, the free energy levels of elementary steps in the reaction pathways of CH_4 production on $\text{C}_3\text{N}_4/\text{NG}$ vary with different active sites (C1, C2, and N), as shown in Figure 2. For the C2 site, the free energy changes of the protonation steps to form $^*\text{COOH}$ and $^*\text{CHO}$ are both higher than that on C1 site. For the N site, although the free energy levels of $^*\text{COOH}$ and $^*\text{CHO}$ intermediates are lower than that on C1 and C2 sites, the elementary step to produce CH_4 molecule from the adsorbed $^*\text{OCH}_3$ on N site shows much more uphill free energy change, which is thermodynamically unfavorable for CH_4 production. As for the other four hybrid materials, the CRR reaction pathway to CH_4 proceeds with relatively higher free energy changes. In summary, among all C1, C2, and N active sites on $\text{C}_3\text{N}_4/\text{XG}$ ($\text{XG} = \text{BG}, \text{NG}, \text{OG}, \text{PG}, \text{G}$), the C1 site of $\text{C}_3\text{N}_4/\text{NG}$ exhibits the highest catalytic activity for CO_2 electroreduction to CH_4 .

In the reaction process of electrochemical CO_2 reduction to valuable hydrocarbons, the binding free energies of some intermediates (i.e., $^*\text{COOH}$, $^*\text{CO}$, $^*\text{CHO}$) are linearly correlated with each other, because they bind to the catalyst surface through a similar surface–adsorbate bond. As an important concept in the research area of heterogeneous catalysis, linear scaling relationship has been widely applied to describe the CRR catalytic activity trends for metallic materials.^[11b,12] The scaled affinity correlation is beneficial in reducing the dimensionality of eight-electron reaction pathway toward CH_4 and searching for catalytic trends of CO_2 reduction, although the scaling relationships between various carbon-bound intermediates impose restrictions on CRR performance of different catalysts. Herein, we found the similar linear scaling relations in the metal-free hybrid catalysts. As shown in Figure 3a,b, the binding free energies on C1 site for $^*\text{COOH}$, $^*\text{CO}$, and $^*\text{CHO}$ are generally correlated with each other in a linear relationship for the five $\text{C}_3\text{N}_4/\text{XG}$ catalysts. These linear scaling relationships are induced by the fact that all carbon-bound adsorbates bind to the catalyst surfaces through a carbon atom, as shown in Figure 1b–d. The scaling relations of binding free energies

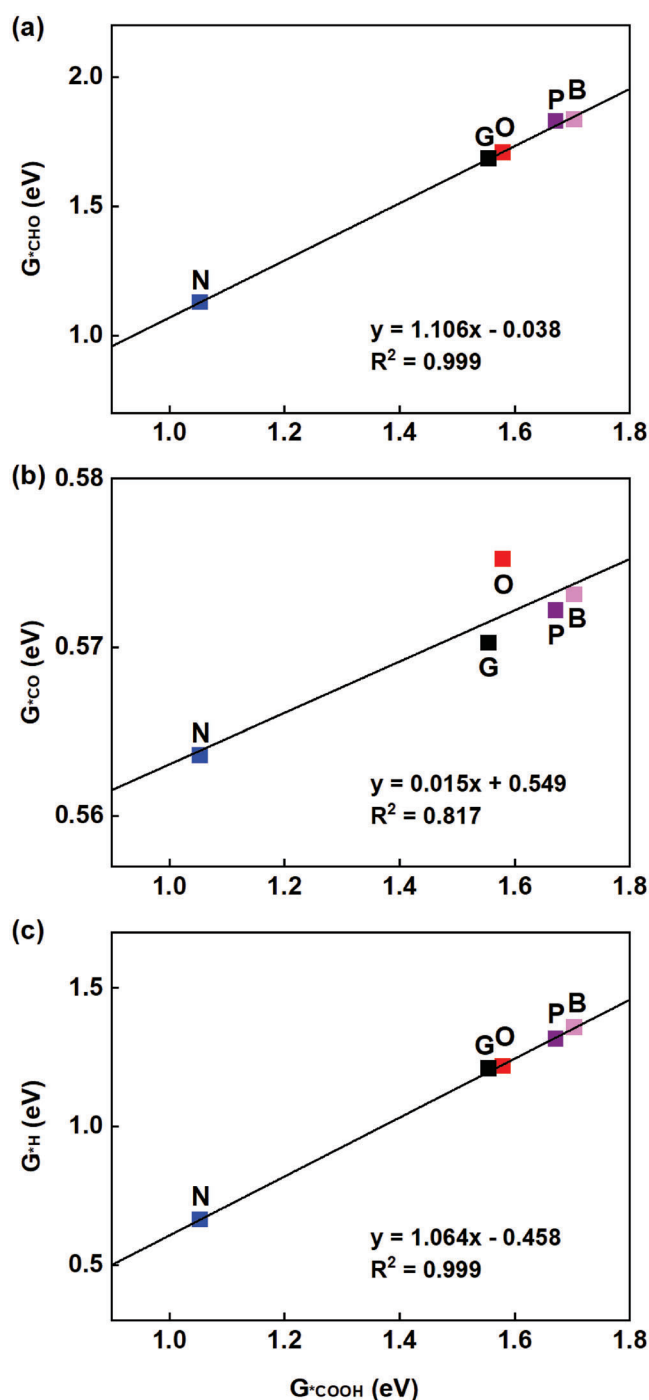


Figure 3. Linear scaling relations for binding free energies of a) *CHO , b) *CO , and c) *H as a function of *COOH free energy on C1 site of $\text{C}_3\text{N}_4/\text{XG}$ (XG = BG, NG, OG, PG, G).

between carbon-containing species on $\text{C}_3\text{N}_4/\text{XG}$ (XG = BG, NG, OG, PG, G) were observed for the first time.

As a main competing reaction to the CRR, hydrogen evolution reaction (HER) is also considered in this study. The major activity indicator, free energies of adsorbed *H , shows a positive linear correlation with *COOH on C1 site (Figure 3c), suggesting the similar trends in catalytic activities for both CRR

and HER on C1 active site. The detailed free energy diagrams of HER are shown in Figure S9a in the Supporting Information. Based on the previous studies,^[13] the HER reaction pathway can be indicated by a diagram involving three states, which are an initial state of $\text{H}^+ + \text{e}^-$, an intermediate of adsorbed *H , and a final product of $1/2 \text{H}_2$. The free energy change to form adsorbed *H is expected to be zero for an optimal HER catalytic activity. However, all five $\text{C}_3\text{N}_4/\text{XG}$ hybrid catalysts show positive free energy levels of adsorbed *H , which are much higher than zero on C1 site. Given this, the *H adsorption is relatively weak on C1 site of $\text{C}_3\text{N}_4/\text{XG}$, although there is still a competition between *COOH adsorption in CRR and *H adsorption in HER.

Some other potential products, such as formic acid (HCOOH) and methane (CH_3OH), are also investigated. The detailed free energy diagrams to form HCOOH are shown in Figure S10 in the Supporting Information. An alternative reaction pathway is demonstrated, in which the first proton/electron pair transfers to an adsorbed CO_2 to form *OCHO with uphill free energy change. The adsorbed *OCHO prefers O binding to C1 site on all five $\text{C}_3\text{N}_4/\text{XG}$ catalysts. However, the adsorption free energy of *OCHO is higher than that of *COOH for each catalyst, suggesting the favorable thermodynamics of *COOH formation toward CH_4 instead of *OCHO adsorption to HCOOH . As shown in Figure S11 in the Supporting Information, the first five elementary steps in the reaction pathway toward CH_3OH are the same as CH_4 . The adsorbed *OCH_3 would form either CH_4 or CH_3OH when the sixth proton/electron pair is transferred to the electrocatalysts. Although the calculation results show that the free energy change to CH_3OH is thermodynamically favored, the electrochemical reduction proceeds in solution with protons free to react with the methyl end of *OCH_3 to form CH_4 . The previous study indicates that CH_3OH would be formed in gas-phase chemistry with adsorbed hydrogen adding to the oxygen end of *OCH_3 .^[11a] Therefore, as a potential product, methanol may be produced in gas-phase reaction, whereas methane is more likely to be formed in electrochemistry.

Based on the computational hydrogen electrode (CHE) model,^[11a,14] the calculated smallest negative potential at which all elementary steps in a reaction pathway become exergonic is called limiting potential (U_l), giving an appropriate measure of the potential-dependent electrochemical rate. It has been reported that the theoretical prediction matches well with the onset potential for CO_2 reduction to various products on Cu surfaces.^[11a,15] According to the preceding discussion, the linear scaling relationships within the carbon-bound adsorbates provide a baseline to estimate the limiting potentials for the corresponding CRR elementary steps. Thus, a volcano relation between energetics of key intermediates (i.e., *COOH in this study) and the limiting potentials could be obtained to display the trend in CRR catalytic activity on $\text{C}_3\text{N}_4/\text{XG}$ (XG = BG, NG, OG, PG, G).

The CO_2 reduction limiting potentials for key elementary steps are correlated with *COOH free energies on C1 site of $\text{C}_3\text{N}_4/\text{XG}$ (Figure 4). Each black solid line on this figure shows the limiting potential of the first three CRR elementary steps in the reaction pathway of Figure 1a, while the black dash line shows the equilibrium potential of 0.17 V versus RHE for CH_4

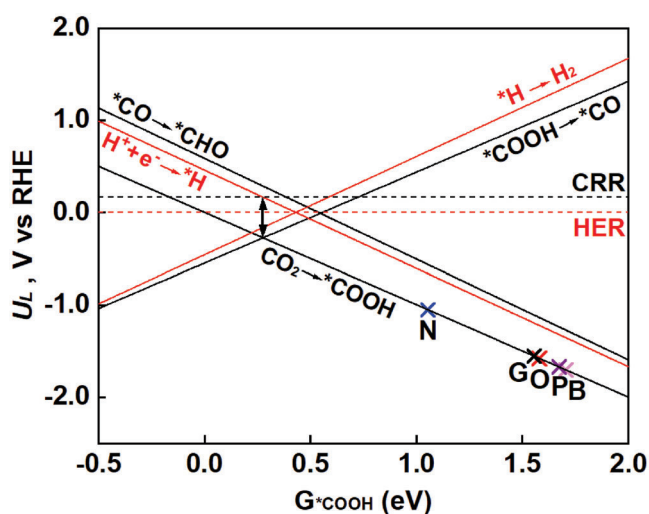


Figure 4. Limiting potentials for key elementary steps of CRR (black solid lines) and two elementary steps of HER (red solid lines) as a function of $G^{\ast}\text{COOH}$ free energy. The black and red dash lines represent the equilibrium potentials for CO_2 reduction to CH_4 and hydrogen evolution, respectively.

production. The difference between the equilibrium potential and each limiting potential reveals the required overpotential for that corresponding elementary step. Therefore, the overall overpotential to produce CH_4 at a proposed $\ast\text{COOH}$ adsorption free energy is indicated by the most negative U_L line. The two U_L lines of $\text{CO}_2 \rightarrow \ast\text{COOH}$ and $\ast\text{COOH} \rightarrow \ast\text{CO}$ with the most negative limiting potentials form a volcano-type plot, describing the trend in catalytic activity of metal-free $\text{C}_3\text{N}_4/\text{XG}$ catalysts for the CRR. The nitrogen doping case is shown to be the closest to the top of volcano-type relation, which agrees with the superior catalytic performance of the C1 site on $\text{C}_3\text{N}_4/\text{NG}$ as mentioned in the previous discussion. The summit of volcano plot shows the best performance of $\text{C}_3\text{N}_4/\text{XG}$ for CH_4 production with the smallest negative limiting potential. At this point, the limiting potentials for CO_2 activation to $\ast\text{COOH}$ and $\ast\text{COOH}$ hydrogenation to $\ast\text{CO}$ become equal, suggesting the overpotential of 0.45 V (i.e., a potential of -0.28 V vs RHE), which is shown by the distance between the volcano top and the CRR equilibrium potential. Such a low overpotential has not been achieved on all previously reported metallic CRR electrocatalysts, for example, a large overpotential of ≈ 1 V is required for copper to produce CH_4 from CO_2 .^[11a,15] Therefore, this group of metal-free $\text{C}_3\text{N}_4/\text{XG}$ catalysts possesses highly promising application prospect in efficient CO_2 electrocatalysis to deeply reduced products.

In concert with the above discussion, the HER limiting potentials for two elementary steps (red solid lines) are derived from the scaling relation of free energies of $\ast\text{H}$ and $\ast\text{COOH}$, and compared with the equilibrium potential for hydrogen evolution (red dash line). The overall limiting potentials toward H_2 and CH_4 produced on C1 site are summarized in Figure S9b in the Supporting Information. The $\text{C}_3\text{N}_4/\text{NG}$ exhibits better catalytic activity for both CH_4 production and hydrogen evolution than the other four hybrid materials. Because the limiting potential offers an estimation of the onset potential,

the different trends of the limiting potentials for HER and CRR are expected to dictate the tendency in selectivity for two reactions. As the binding free energy of $\ast\text{COOH}$ decreases from 0.43 to 0.28 eV, the limiting potential difference between HER and CRR reduces rapidly, thus indicating a rising preference for CRR over HER on this group of metal-free catalysts when the optimum $\ast\text{COOH}$ affinity at the volcano top is reached.

The catalytic property of a catalyst is intrinsically influenced by its electron charge distribution.^[16] To investigate such impact on the five $\text{C}_3\text{N}_4/\text{XG}$ catalysts, we have conducted Bader charge analysis to find the relationship between inherent electron distribution and apparent catalytic activity. As shown in Figure 5a, electron transfer from graphene layer to g- C_3N_4 layer on $\text{C}_3\text{N}_4/\text{XG}$ catalysts was plotted against the free energy of $\ast\text{COOH}$ on C1 active site, which shows an excellent linear relation. A stronger $\ast\text{COOH}$ adsorption was observed with more electron transfer to g- C_3N_4 layer, and vice versa. For example, in the nitrogen doping case, the electron transfer amount is much higher than that in the other four cases, therefore leading to the strongest $\ast\text{COOH}$ adsorption to the C1 site on $\text{C}_3\text{N}_4/\text{NG}$ ($\Delta G = 1.05$ eV). We have also explored the work function of $\text{C}_3\text{N}_4/\text{XG}$ catalysts to indicate the degree of electron transfer. As shown in Figure S12 in the Supporting

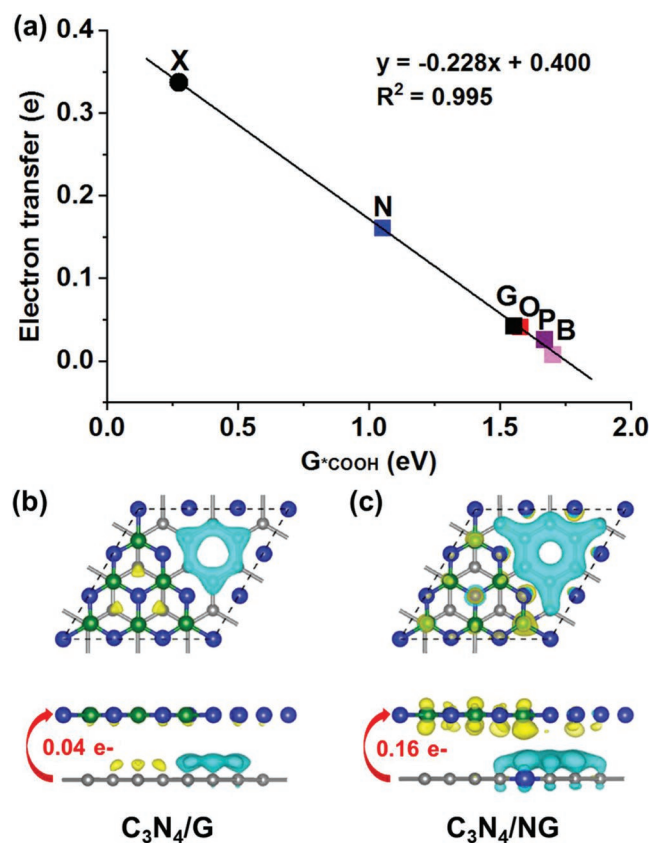


Figure 5. a) Relationship between electron transfer and $\ast\text{COOH}$ free energy on $\text{C}_3\text{N}_4/\text{XG}$ ($\text{XG} = \text{BG}, \text{NG}, \text{OG}, \text{PG}, \text{G}$). Bottom panel shows the interfacial electron transfer in b) $\text{C}_3\text{N}_4/\text{G}$ and c) $\text{C}_3\text{N}_4/\text{NG}$, correspondingly. Yellow isosurface represents electron accumulation and cyan isosurface refers to electron depletion. The isosurface value is $5 \times 10^{-3} \text{ e} \text{ \AA}^{-3}$. The red arrow shows the electron transfer from the supporting layer to the g- C_3N_4 layer.

Information, the work function of C_3N_4/XG was correlated to the free energy of *COOH on C1 active site in a proper linear relation. A stronger *COOH adsorption was generally obtained with smaller work function, which indicates higher degree of electron transfer from C_3N_4/XG catalysts. The work function for the nitrogen doping case is the lowest, matching well with the strongest *COOH adsorption to C1 site on C_3N_4/NG . A similar relationship between adsorption energy and electron transfer has also been reported in recent years.^[17] Through first-principle calculations, electron transfer-based adsorption activity was uncovered in these previous studies, suggesting stronger binding with higher degree of electron transfer. The charge density difference plots are constructed by subtracting the electron charge of independent graphene and $g-C_3N_4$ layers from that of C_3N_4/XG , to visualize the interfacial electron charge transfer. By compositing $g-C_3N_4$ with pure graphene support, the charge density of C_3N_4/G is redistributed with slight electron transfer of $0.04 e^-$ from graphene to $g-C_3N_4$ layer (Figure 5b). After doping one nitrogen atom in graphene, the charge density in the interlayer of C_3N_4/NG shows an apparently increased electron transfer of $0.16 e^-$ from nitrogen-doped graphene to $g-C_3N_4$, resulting in an enhanced electron-rich region on the $g-C_3N_4$ layer and an expanded hole-rich region on the nitrogen-doped graphene layer (Figure 5c). The localized electron accumulation leads to increased electron conductivity on the $g-C_3N_4$ layer, which is significant for the electrocatalysis of CO_2 conversion. This observation suggests that a higher catalytic activity originates from more interfacial electron transfer. According to the above discussions around electron charge transfer amount and adsorption strength, and combining the volcano-type activity trend, it is able to determine that a hybrid catalyst with $0.34 e^-$ interfacial electron transfer (as shown by the X dot in Figure 5a) can achieve the best catalytic performance. Our results show that increasing the interfacial electron transfer from the supporting graphene layer to the $g-C_3N_4$ layer is able to improve the catalytic activity of the hybrid catalysts. Methods for increasing the interfacial electron charge transfer could include the introduction of a secondary element to induce a synergistic effect,^[18] creation of vacancies to modify the substrate layer,^[19] or combination with functional groups to enhance the interaction of the two layers.^[20] By applying these engineering strategies, the electron transfer to the $g-C_3N_4$ layer can be modulated, therefore leading to improved CRR thermodynamics and activity.

In summary, we have conducted comprehensive DFT computations for C_3N_4/XG ($XG = BG, NG, OG, PG, G$) electrocatalysts to investigate their catalytic performance for CO_2 reduction toward the production of deeply reduced hydrocarbons. Our study reveals that the eight-electron reduction processes to CH_4 are thermodynamically preferred on C_3N_4/NG with lower overall free energy change. The linear scaling relationships of carbon-bound intermediates' free energies on C1 site of five C_3N_4/XG catalysts are uncovered, which leads to a volcano type of trend in CRR catalytic activity versus the free energy of key intermediate, i.e., *COOH . This activity trend predicts the best performance for CRR to produce CH_4 on this group of metal-free catalytic materials, which has not been achieved on all previously reported metallic CRR electrocatalysts. In addition, their activity origin can be explained by

interfacial electron transfer, where a higher activity is associated with more electron transfer. Therefore, the catalytic activity can be improved by substrate engineering methods to increase interfacial electron transfer amount on catalysts for CRR. Our findings suggest that interfacial electron transfer modulating is an effective method to enhance the catalytic performance of $g-C_3N_4$ for CO_2 reduction. This study also sheds light on materials engineering strategy for other electrochemical conversion processes with multi-electron transfer steps.

Supporting Information

Supporting Information is available from the Wiley Online Library or from the author.

Acknowledgements

The authors acknowledge the financial support by the Australian Research Council (DP170104464, DP160104866, DE160101163, and FL170100154) and the University of Adelaide Fellowship. DFT computations within this work were undertaken with the assistance of resources and services from the National Computational Infrastructure (NCI) supported by the Australian Government, as well as the Phoenix High Performance Compute (HPC) Service at the University of Adelaide.

Conflict of Interest

The authors declare no conflict of interest.

Keywords

density functional theory, doped graphene, electrocatalytic CO_2 reduction, graphitic carbon nitride, metal-free catalysts

Received: October 11, 2018

Revised: January 14, 2019

Published online: February 4, 2019

- [1] a) Z. W. Seh, J. Kibsgaard, C. F. Dickens, I. Chorkendorff, J. K. Nørskov, T. F. Jaramillo, *Science* **2017**, *355*, eaad4998; b) Q. Lu, F. Jiao, *Nano Energy* **2016**, *29*, 439.
- [2] a) A. Vasileff, Y. Zheng, S. Z. Qiao, *Adv. Energy Mater.* **2017**, *7*, 1700759; b) X. W. Mao, T. A. Hatton, *Ind. Eng. Chem. Res.* **2015**, *54*, 4033.
- [3] a) S. Liu, H. Yang, X. Huang, L. Liu, W. Cai, J. Gao, X. Li, T. Zhang, Y. Huang, B. Liu, *Adv. Funct. Mater.* **2018**, *28*, 1800499; b) J. J. Wu, M. J. Liu, P. P. Sharma, R. M. Yadav, L. L. Ma, Y. C. Yang, X. L. Zou, X. D. Zhou, R. Vajtai, B. I. Yakobson, J. Lou, P. M. Ajayan, *Nano Lett.* **2016**, *16*, 466; c) H. X. Wang, Y. B. Chen, X. L. Hou, C. Y. Ma, T. W. Tan, *Green Chem.* **2016**, *18*, 3250; d) J. J. Wu, R. M. Yadav, M. J. Liu, P. P. Sharma, C. S. Tiwary, L. L. Ma, X. L. Zou, X. D. Zhou, B. I. Yakobson, J. Lou, P. M. Ajayan, *ACS Nano* **2015**, *9*, 5364; e) N. Sreekanth, M. A. Nazrulla, T. V. Vineesh, K. Sailaja, K. L. Phani, *Chem. Commun.* **2015**, *51*, 16061.
- [4] L. M. Azofra, D. R. MacFarlane, C. H. Sun, *Phys. Chem. Chem. Phys.* **2016**, *18*, 18507.
- [5] a) X. Tan, H. A. Tahini, S. C. Smith, *Curr. Opin. Electrochem.* **2017**, *4*, 118; b) Y. Jiao, Y. Zheng, S. C. Smith, A. J. Du, Z. H. Zhu, *ChemSusChem* **2014**, *7*, 435.

- [6] Y. Jiao, Y. Zheng, P. Chen, M. Jaroniec, S. Z. Qiao, *J. Am. Chem. Soc.* **2017**, *139*, 18093.
- [7] a) A. Du, S. Sanvito, Z. Li, D. Wang, Y. Jiao, T. Liao, Q. Sun, Y. H. Ng, Z. Zhu, R. Amal, S. C. Smith, *J. Am. Chem. Soc.* **2012**, *134*, 4393; b) X. Y. Lu, T. H. Tan, Y. H. Ng, R. Amal, *Chem. - Eur. J.* **2016**, *22*, 11991.
- [8] a) X. Tan, H. A. Tahini, S. C. Smith, *ACS Catal.* **2016**, *6*, 7071; b) J. Q. Tian, Q. Liu, A. M. Asiri, K. A. Alamry, X. P. Sun, *ChemSusChem* **2014**, *7*, 2125; c) S. B. Yang, X. L. Feng, X. C. Wang, K. Müllen, *Angew. Chem., Int. Ed.* **2011**, *50*, 5339.
- [9] a) Y. Zheng, Y. Jiao, Y. H. Zhu, L. H. Li, Y. Han, Y. Chen, A. J. Du, M. Jaroniec, S. Z. Qiao, *Nat. Commun.* **2014**, *5*, 3783; b) S. S. Shinde, A. Sami, J. H. Lee, *ChemCatChem* **2015**, *7*, 3873.
- [10] D. Kim, J. Shi, Y. Liu, *J. Am. Chem. Soc.* **2018**, *140*, 9127.
- [11] a) A. A. Peterson, F. Abild-Pedersen, F. Studt, J. Rossmeisl, J. K. Nørskov, *Energy Environ. Sci.* **2010**, *3*, 1311; b) A. A. Peterson, J. K. Nørskov, *J. Phys. Chem. Lett.* **2012**, *3*, 251.
- [12] a) C. Shi, H. A. Hansen, A. C. Lausche, J. K. Nørskov, *Phys. Chem. Chem. Phys.* **2014**, *16*, 4720; b) C. Liu, H. He, P. Zapol, L. A. Curtiss, *Phys. Chem. Chem. Phys.* **2014**, *16*, 26584.
- [13] a) J. K. Nørskov, T. Bligaard, J. Rossmeisl, C. H. Christensen, *Nat. Chem.* **2009**, *1*, 37; b) J. K. Nørskov, T. Bligaard, A. Logadottir, J. R. Kitchin, J. G. Chen, S. Pandalov, U. Stimming, *J. Electrochem. Soc.* **2005**, *152*, j23.
- [14] J. K. Nørskov, J. Rossmeisl, A. Logadottir, L. Lindqvist, J. R. Kitchin, T. Bligaard, H. Jonsson, *J. Phys. Chem. B* **2004**, *108*, 17886.
- [15] W. J. Durand, A. A. Peterson, F. Studt, F. Abild-Pedersen, J. K. Nørskov, *Surf. Sci.* **2011**, *605*, 1354.
- [16] Y. Zheng, Y. Jiao, S. Z. Qiao, *Adv. Mater.* **2015**, *27*, 5372.
- [17] a) Y. Liu, J. Wu, K. P. Hackenberg, J. Zhang, Y. M. Wang, Y. Yang, K. Keyshar, J. Gu, T. Ogitsu, R. Vajtai, J. Lou, P. M. Ajayan, B. C. Wood, B. I. Yakobson, *Nat. Energy* **2017**, *2*, 17127; b) Y. Liu, Y. M. Wang, B. I. Yakobson, B. C. Wood, *Phys. Rev. Lett.* **2014**, *113*, 028304.
- [18] a) J. T. Zhang, Z. H. Zhao, Z. H. Xia, L. M. Dai, *Nat. Nanotechnol.* **2015**, *10*, 444; b) Y. Zheng, Y. Jiao, L. Ge, M. Jaroniec, S. Z. Qiao, *Angew. Chem., Int. Ed.* **2013**, *52*, 3110.
- [19] a) H. Li, C. Tsai, A. L. Koh, L. L. Cai, A. W. Contryman, A. H. Fragapane, J. H. Zhao, H. S. Han, H. C. Manoharan, F. Abild-Pedersen, J. K. Nørskov, X. L. Zheng, *Nat. Mater.* **2016**, *15*, 48; b) S. Gao, Z. T. Sun, W. Liu, X. C. Jiao, X. L. Zu, Q. T. Hu, Y. F. Sun, T. Yao, W. H. Zhang, S. Q. Wei, Y. Xie, *Nat. Commun.* **2017**, *8*, 14503.
- [20] a) J. Yang, D. Voiry, S. J. Ahn, D. Kang, A. Y. Kim, M. Chhowalla, H. S. Shin, *Angew. Chem., Int. Ed.* **2013**, *52*, 13751; b) J. A. Yan, M. Y. Chou, *Phys. Rev. B* **2010**, *82*, 125403.



Supporting Information

for *Small*, DOI: 10.1002/sml.201804224

Impact of Interfacial Electron Transfer on Electrochemical
CO₂ Reduction on Graphitic Carbon Nitride/Doped Graphene

Xing Zhi, Yan Jiao, Yao Zheng, and Shi-Zhang Qiao**

Supporting Information

**Impact of Interfacial Electron Transfer to Electrochemical CO₂
Reduction on Graphitic Carbon Nitride/Doped Graphene**

Xing Zhi, Yan Jiao,* Yao Zheng, Shi-Zhang Qiao*

School of Chemical Engineering, The University of Adelaide, Adelaide, South Australia

5005, Australia

Computational Parameters and Models.

All calculations in this study were carried out using density functional theory (DFT). The Perdew-Burke-Ernzerhof (PBE) functional was employed for electron exchange-correlation within the generalized gradient approximation (GGA), as implemented in the VASP code.^[1] The ionic cores were described by the projector-augmented wave (PAW) method. The cut-off energy for plane wave expansion was set to be 550 eV, optimized from a range of cut-off energies. During geometry optimization, the structures were relaxed to forces on all atoms smaller than 0.01 eV/Å. A Gaussian smearing was employed with 0.20 eV width for free energy calculations. A $5 \times 5 \times 1$ Monkhorst-Pack k-point grid was applied. The DFT-D2 method of Grimme was employed in all calculations to address van der Waals (vdW) interactions between atoms.^[2]

The nanocomposite model of g-C₃N₄ and graphene (C₃N₄/G), using a 3×3 graphene supercell to match the 1×1 g-C₃N₄ cell, was built with optimized lattice constant $a = b = 7.314$ Å and 20 Å of vacuum space. The angle between the two lattice vectors a and b was 120°. Based on the C₃N₄/G model, four other models of g-C₃N₄ and heteroatom-doped graphene (C₃N₄/XG, X = B, N, O, P) were designed with one carbon atom in the graphene layer substituted by the heteroatom (B or N) or with the heteroatom (O or P) added to the graphene layer. The optimized atomic configurations and distances between the two layers of these models are shown in Figure S1. The electron transfers from graphene layer to g-C₃N₄ layer on C₃N₄/XG (XG = BG, NG, OG, PG, G) were studied through Bader charge and charge density difference analyses.^[3]

Reaction Intermediates.

The five nanocomposite models of C₃N₄/XG (XG = BG, NG, OG, PG, G) were investigated as electrocatalysts for the CRR. First, various possible positions both in g-C₃N₄ layer and doped graphene layer were explored to address the CO₂ binding sites, since the CRR starts

with the adsorption of CO₂ molecule. As shown in Figure S1-S5, site 1 (denoted as C1), site 2 (denoted as C2), and site 5 (denoted as N) generally displayed favorable adsorption energies. Therefore, these three positions (C1, C2, and N) in the g-C₃N₄ layer were optimized to be potential active sites for the CRR (Figure S6). The electronic energies of possible intermediates, such as *COOH, *CO, *CHO, *CH, etc., were calculated on C₃N₄/XG (XG = BG, NG, OG, PG, G) with various initial configurations. The optimized geometry and energies were summarized in Tables S1-S5 for five models, respectively. The free energy corrections to all intermediates, reactants and products were presented in Table S6 (for intermediates) and Table S7 (for gas molecules) in SI.

Free Energy Calculation.

The free energies of intermediate states were determined according to $G = E + \text{ZPE} - \text{TS}$. The zero point energy (ZPE) and entropy correction (TS) were calculated from vibration analysis by standard methods and used to convert electronic energies (E) into free energies (G) at 298.15 K (Table S6). The vibrational frequencies were computed by treating all 3N degrees of the adsorbates as vibrational within the harmonic oscillator approximation, and assuming that any changes in the vibrations of the nanocomposite surface were minimal, in concert with earlier studies.^[4] Gas-phase free energies were also obtained by standard methods (Table S7). The gaseous species, CO₂ and CH₄, were calculated at 101,325 Pa, while the liquid water was treated with pressure correction at a fugacity of 3534 Pa corresponding to the vapor pressure of water.^[5] The solvation effects were considered approximately the same as previous studies: hydroxyl adsorbate (*OH), hydroxyl functional groups (*R-OH), and intermediates containing adsorbed CO (*CO, *CHO, etc.) were stabilized by 0.5 eV, 0.25 eV, and 0.10 eV, respectively.^[4b, 5] The free energy of CO₂ and HCOOH were compensated with 0.23 eV and 0.15 eV respectively to match the experimental values.

To include the effect of electrode potential, the computational hydrogen electrode (CHE) model was used to treat the free energy change of each state involving a proton-electron pair transfer as a function of the applied electrical potential.^[6] In this model, the free energy of a proton-electron pair at 0 V vs RHE is by definition equal to half of the free energy of gaseous hydrogen at 101,325 Pa. The application of the CHE model provides a method to predict the electrode potential at which all elementary steps in a certain CO₂ reduction pathway becomes exergonic. This potential is referred to as the limiting potential and used to decide the potential-dependent reaction step. In this study, the relative free energies of intermediates were taken to indicate the starting point of different CO₂ electroreduction pathways, and reaction barriers were not calculated. The barriers for proton transfers to adsorbates are normally small enough to be surmountable at room temperature as reported in previous publications.^[7]

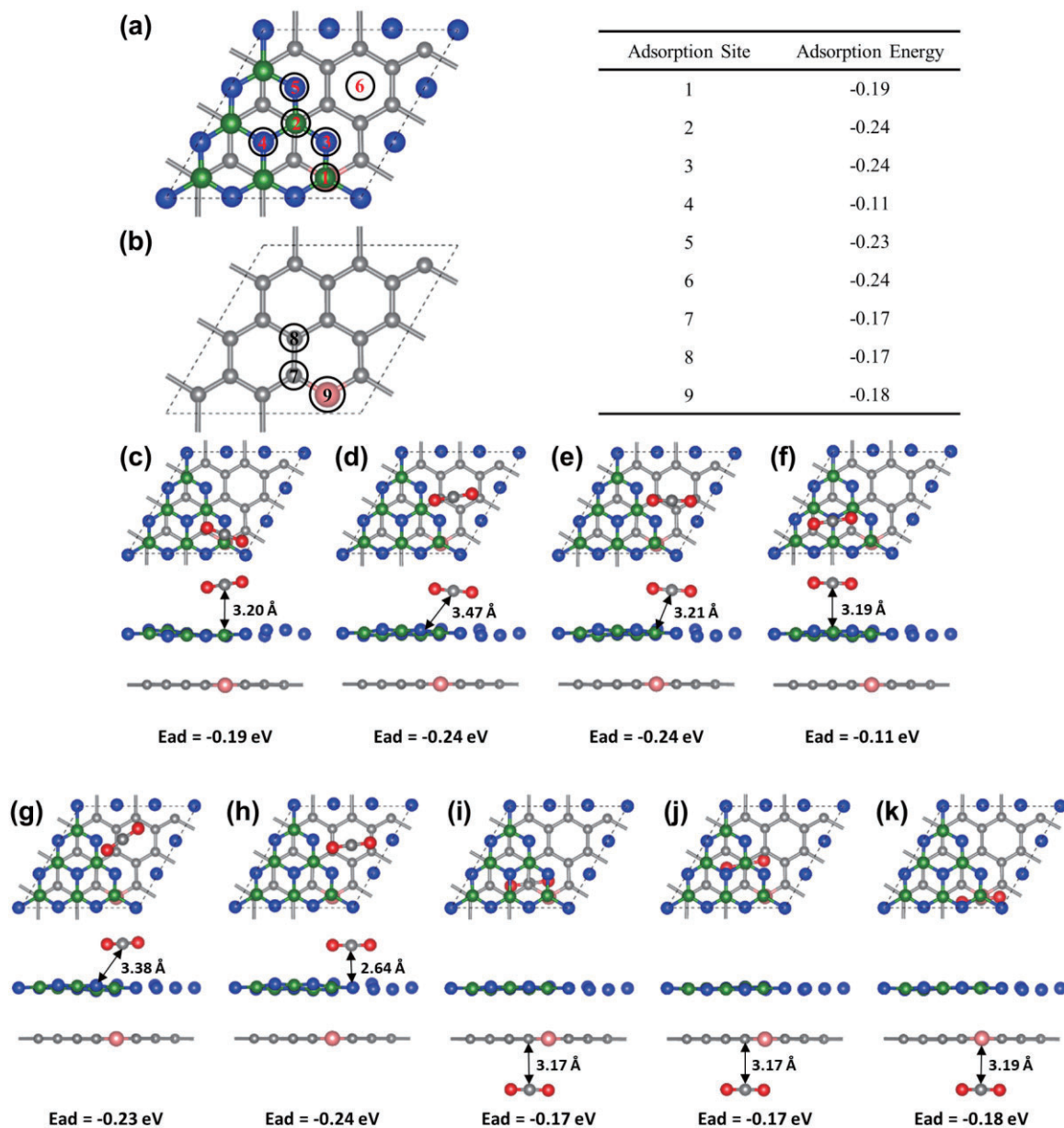


Figure S1. CO₂ adsorption summary in (a) g-C₃N₄ layer and (b) XG layer of C₃N₄/BG. Black circle indicates the adsorption sites that have been considered in this study. The adsorption energy for each site is shown in the table. The corresponding configurations are shown in (c) – (k).

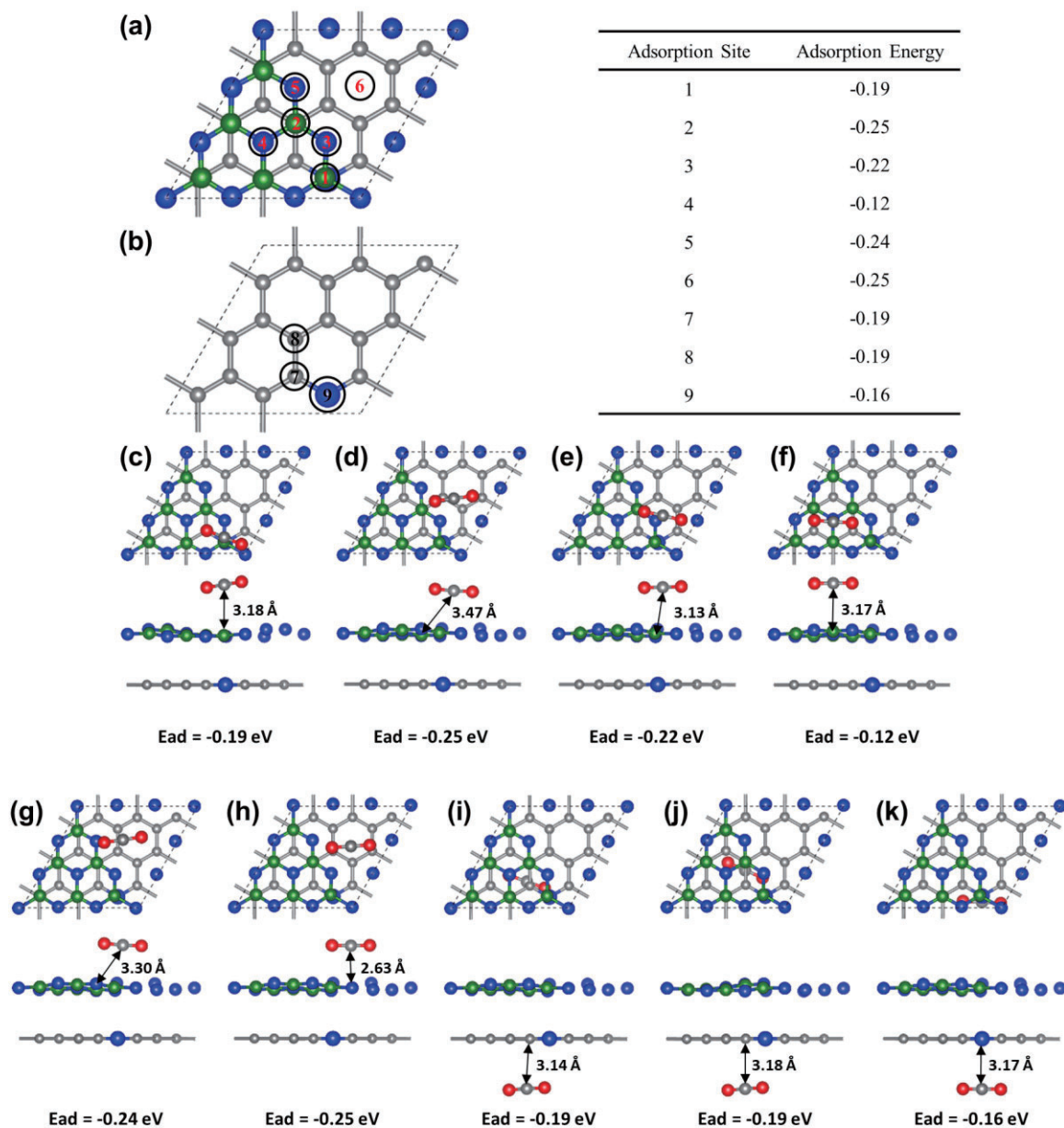


Figure S2. CO₂ adsorption summary in (a) g-C₃N₄ layer and (b) XG layer of C₃N₄/NG. Black circle indicates the adsorption sites that have been considered in this study. The adsorption energy for each site is shown in the table. The corresponding configurations are shown in (c) – (k).

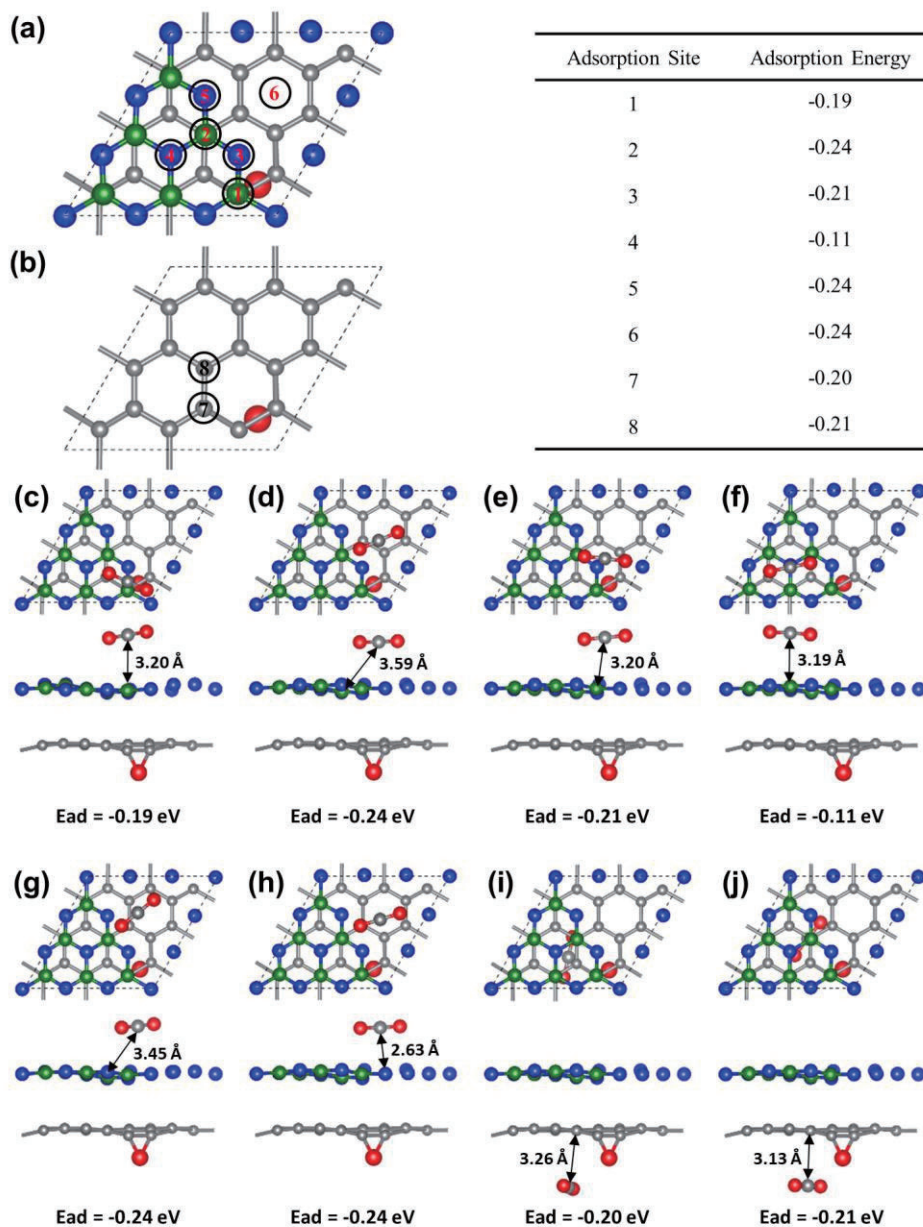


Figure S3. CO₂ adsorption summary in (a) g-C₃N₄ layer and (b) XG layer of C₃N₄/OG. Black circle indicates the adsorption sites that have been considered in this study. The adsorption energy for each site is shown in the table. The corresponding configurations are shown in (c) – (j).

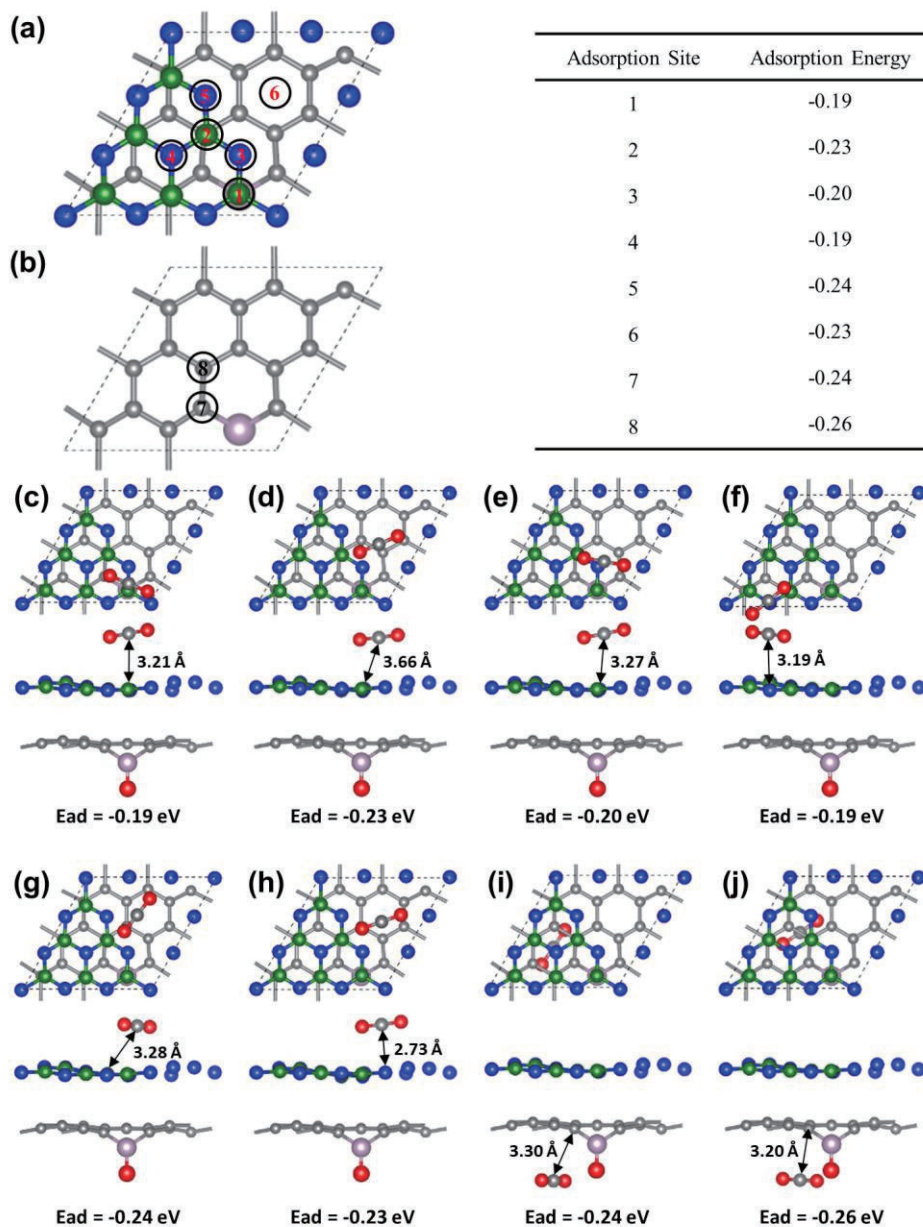


Figure S4. CO₂ adsorption summary in (a) g-C₃N₄ layer and (b) XG layer of C₃N₄/PG. Black circle indicates the adsorption sites that have been considered in this study. The adsorption energy for each site is shown in the table. The corresponding configurations are shown in (c) – (j).

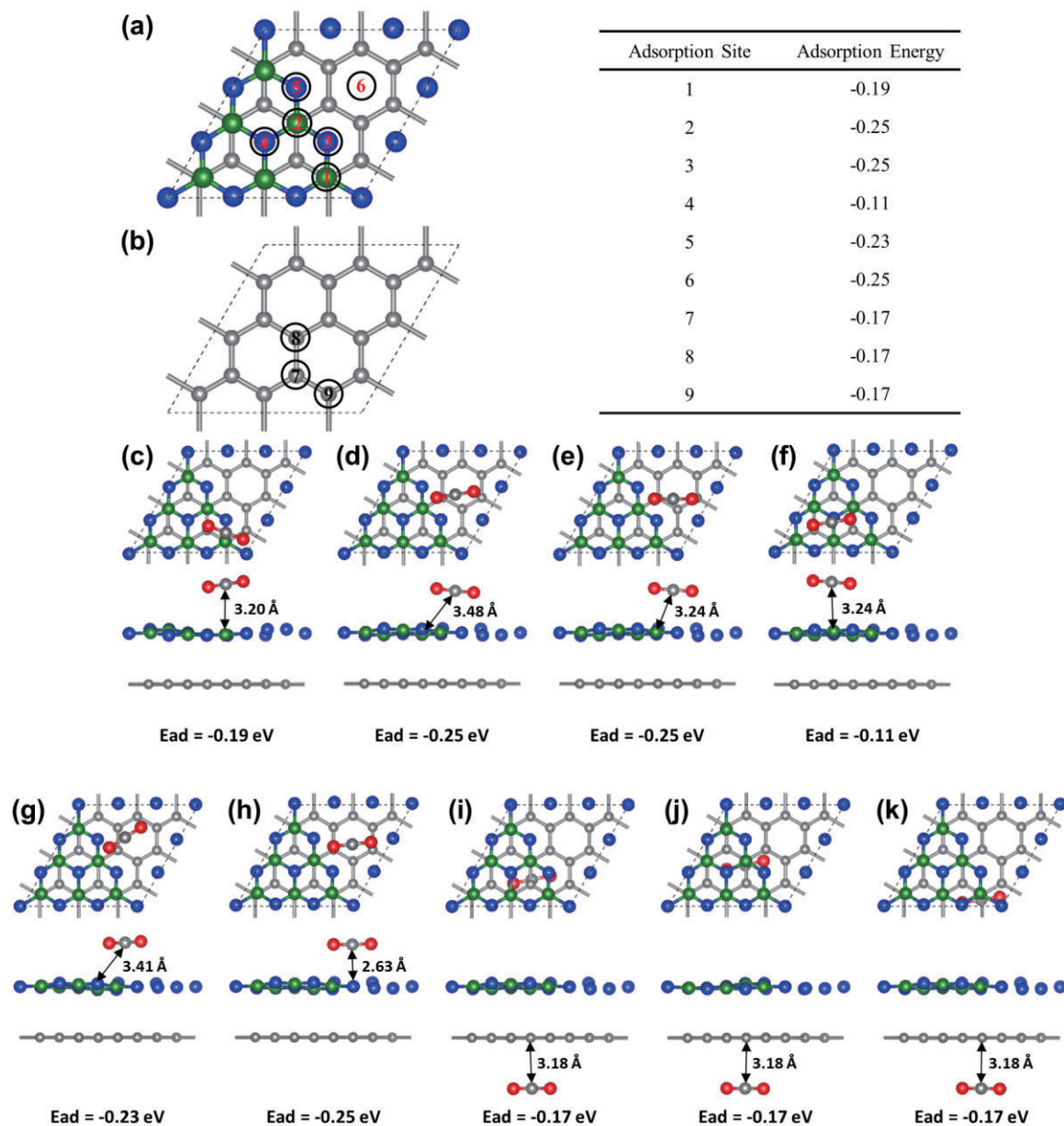


Figure S5. CO₂ adsorption summary in (a) g-C₃N₄ layer and (b) XG layer of C₃N₄/G. Black circle indicates the adsorption sites that have been considered in this study. The adsorption energy for each site is shown in the table. The corresponding configurations are shown in (c) – (k).

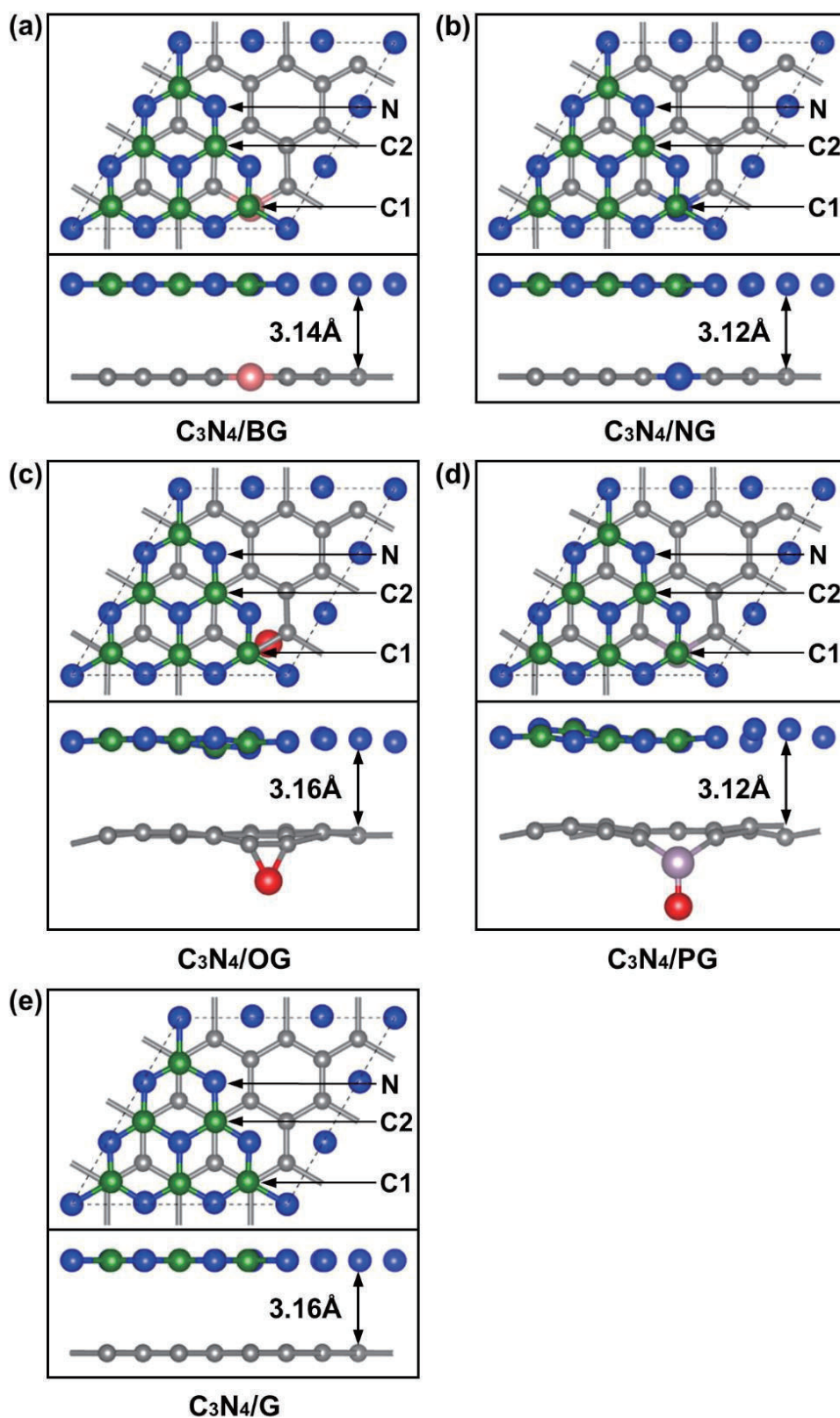


Figure S6. The optimized atomic configurations and three active sites (C1, C2, N) of C_3N_4/XG ($XG = BG, NG, OG, PG, G$). Carbon in graphene layer, carbon in g- C_3N_4 layer, nitrogen, boron, oxygen, phosphorus atoms are grey, green, blue, light magenta, red, and purple, respectively.

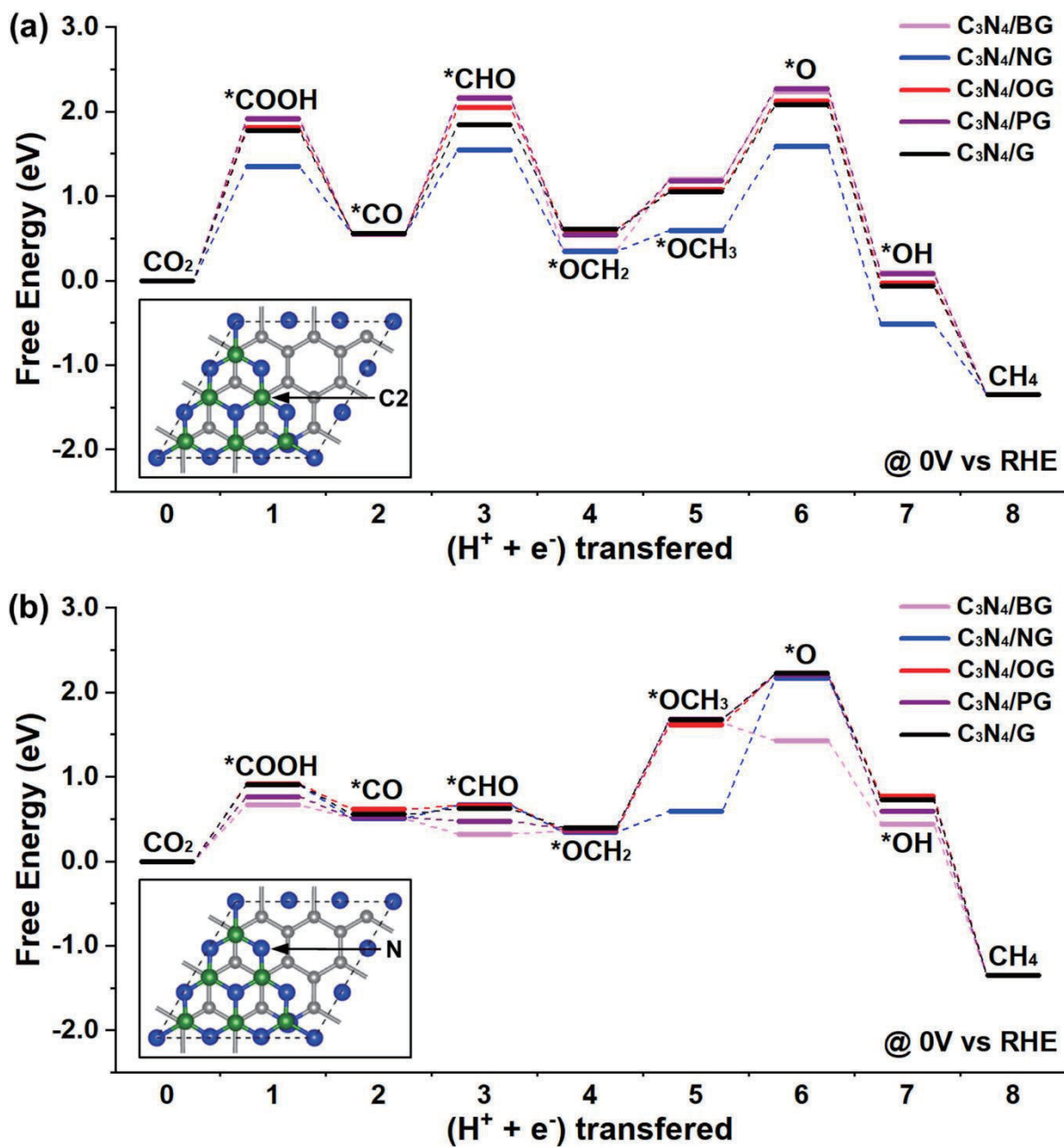


Figure S7. Free energy diagrams of the CO₂ reduction pathway to CH₄ on (a) C2 and (b) N sites of C₃N₄/XG (XG = BG, NG, OG, PG, G). The insets show the corresponding C2 and N sites, respectively.

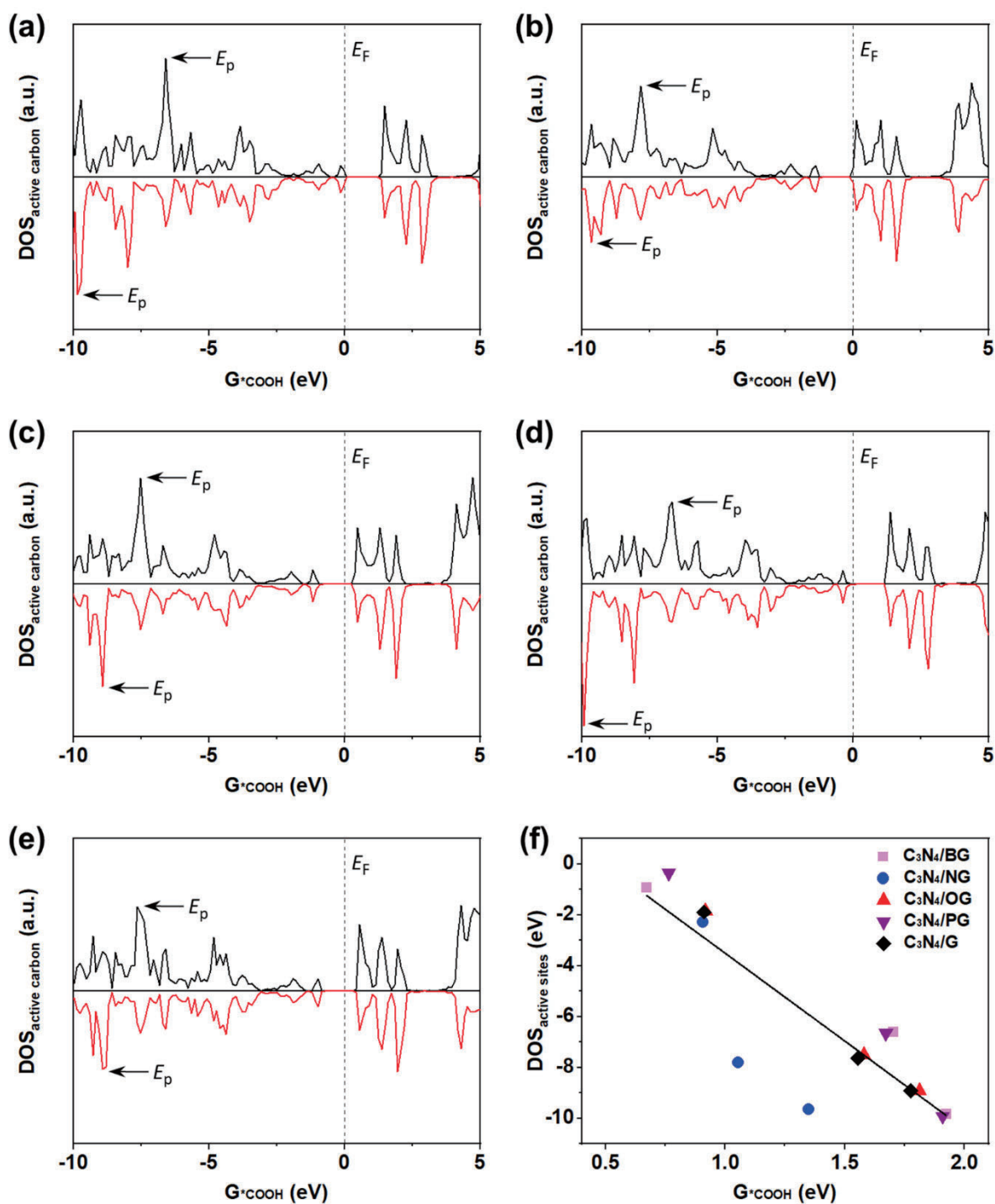


Figure S8. (a-e) The DOS for active carbon sites of C₃N₄/XG (XG = BG, NG, OG, PG, and G, respectively). The black and red lines show the corresponding DOS for C1 and C2 sites. (f) The relationship between *COOH free energy and the highest peak position of active site DOS.

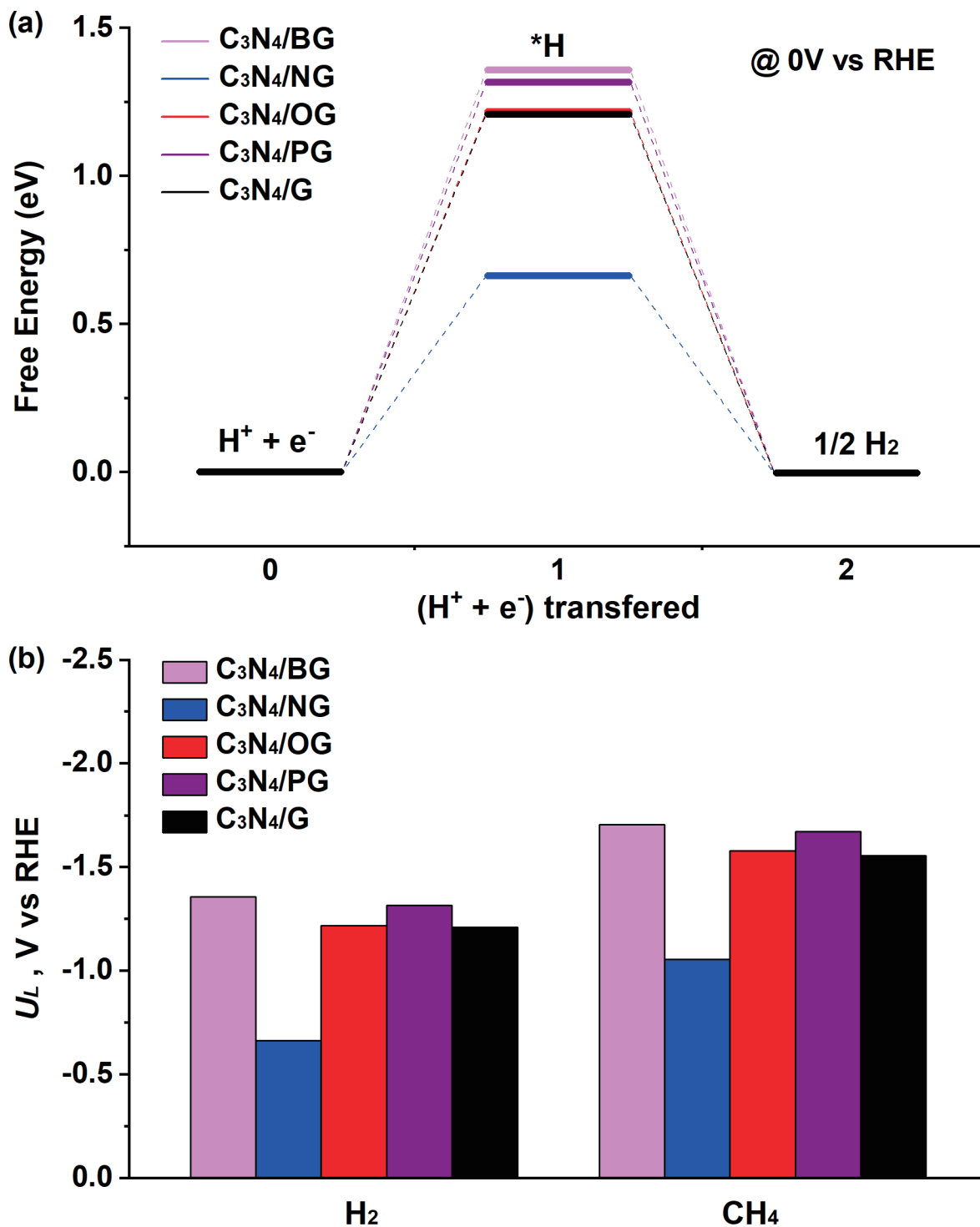


Figure S9. (a) Free energy diagram of hydrogen evolution reaction (HER). (b) The overall limiting potentials for hydrogen evolution and CO_2 reduction to CH_4 on C1 site of $\text{C}_3\text{N}_4/\text{XG}$ (XG = BG, NG, OG, PG, G).

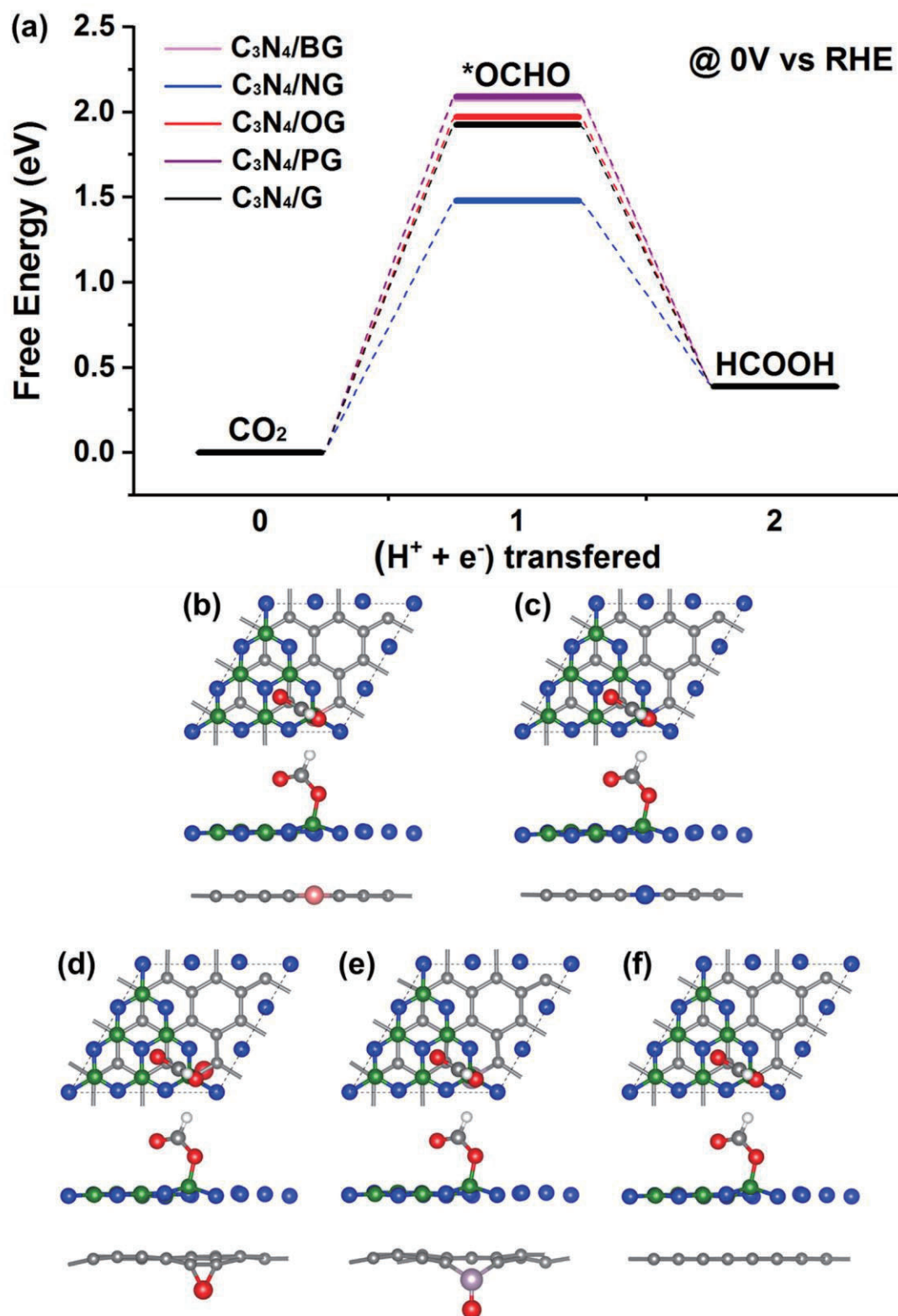


Figure S10. (a) Free energy diagrams of the CO₂ reduction pathway to HCOOH on C₃N₄/XG (XG = BG, NG, OG, PG, G). The corresponding optimized configurations of adsorbed *OCHO are shown in (b) – (f), respectively.

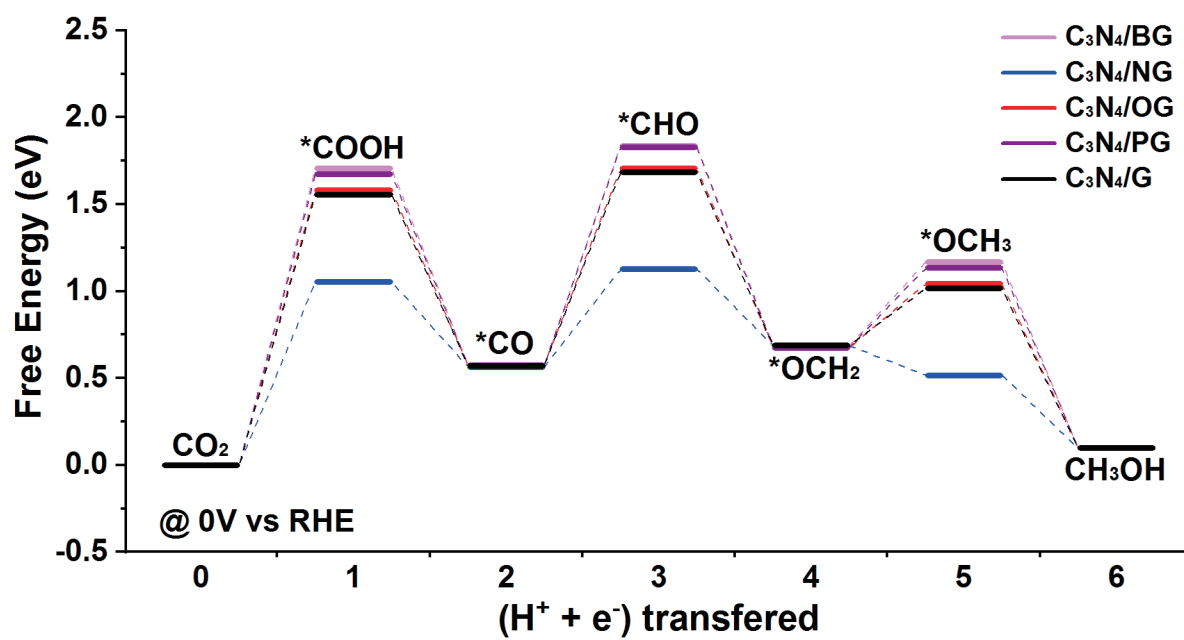


Figure S11. Free energy diagrams of the CO₂ reduction pathway to CH₃OH on C1 site of C₃N₄/XG (XG = BG, NG, OG, PG, G).

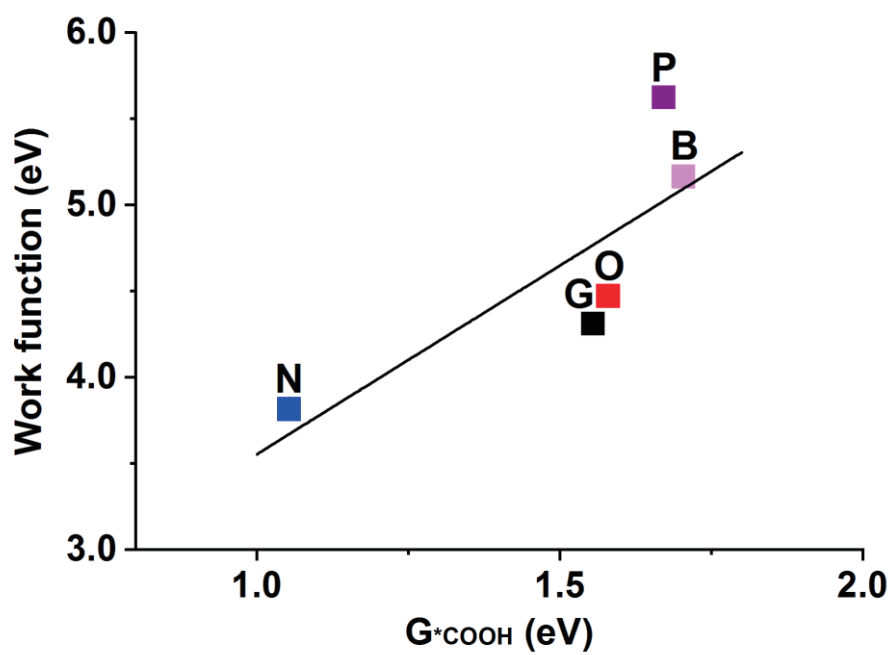
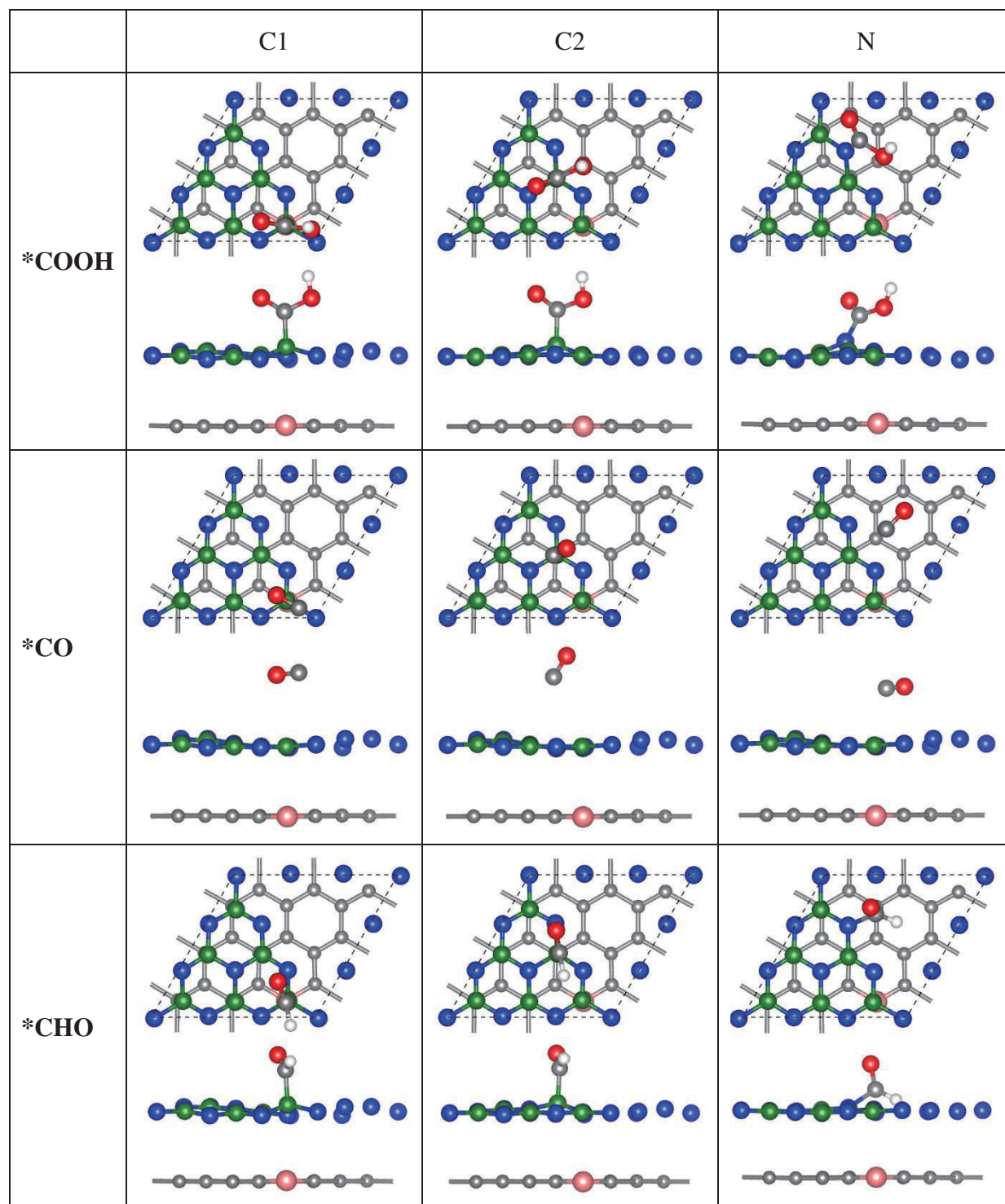
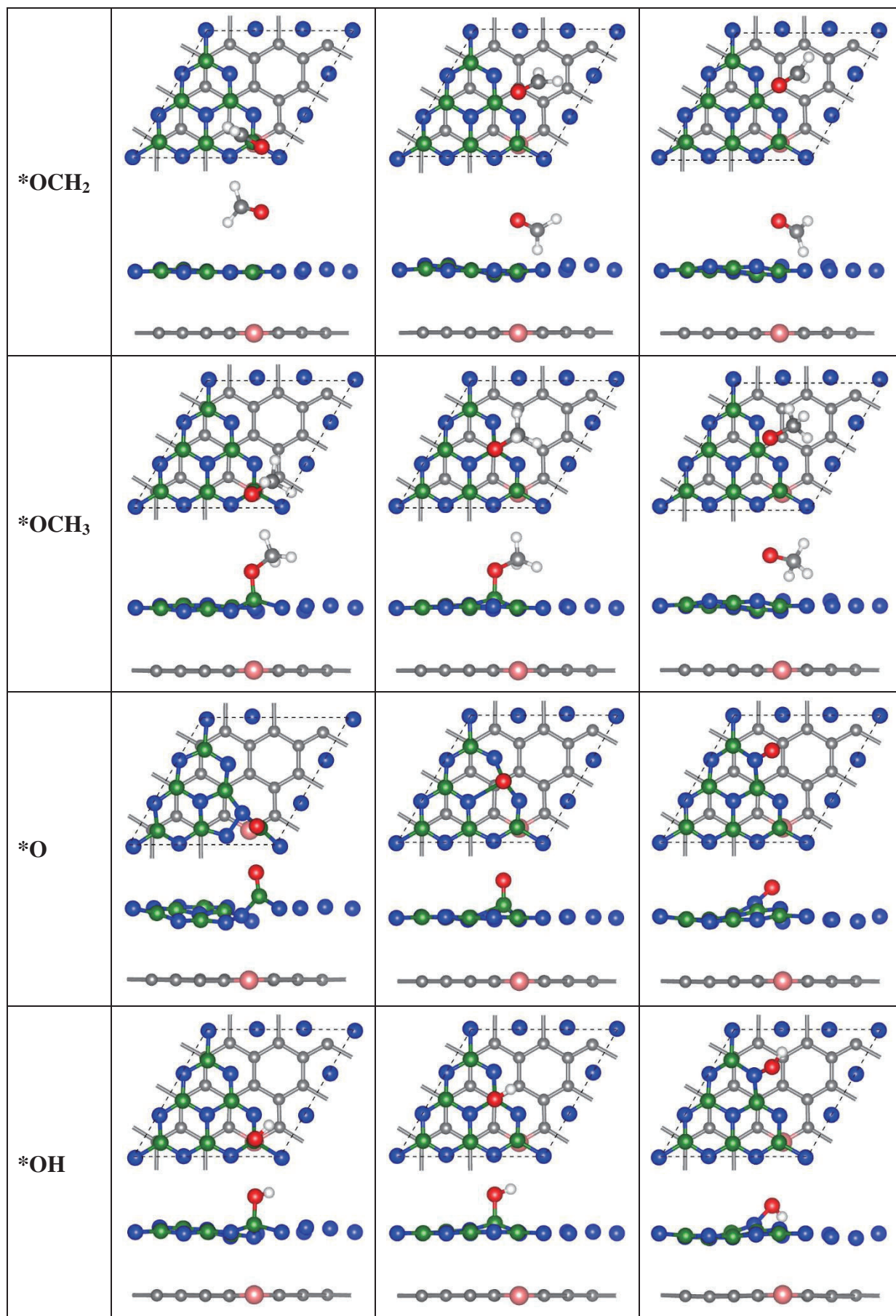


Figure S12. Relationship between work function and *COOH free energy on C_3N_4/XG (XG = BG, NG, OG, PG, G).

Table S1 Summary of optimized configurations of possible reaction intermediates on three active sites (C1, C2, and N) of C_3N_4/BG explored in this study.





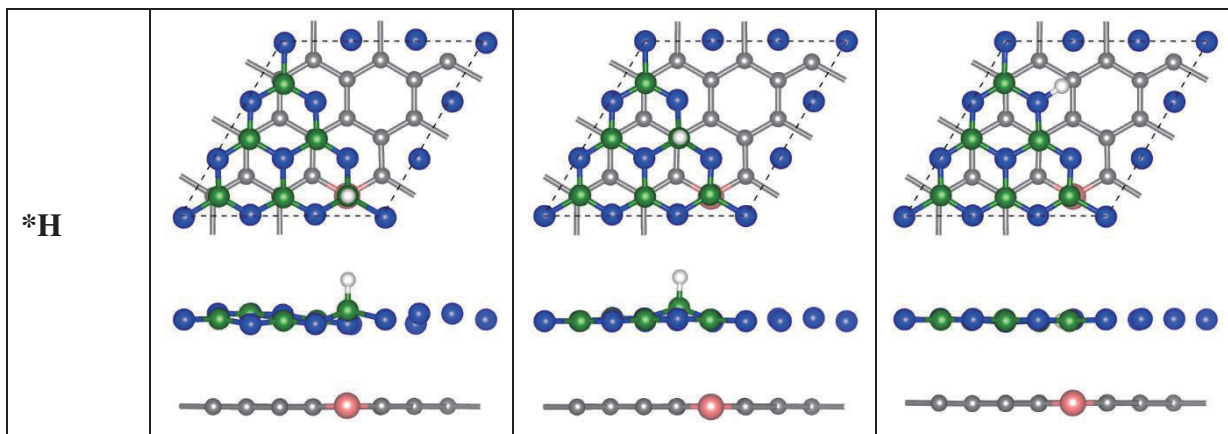
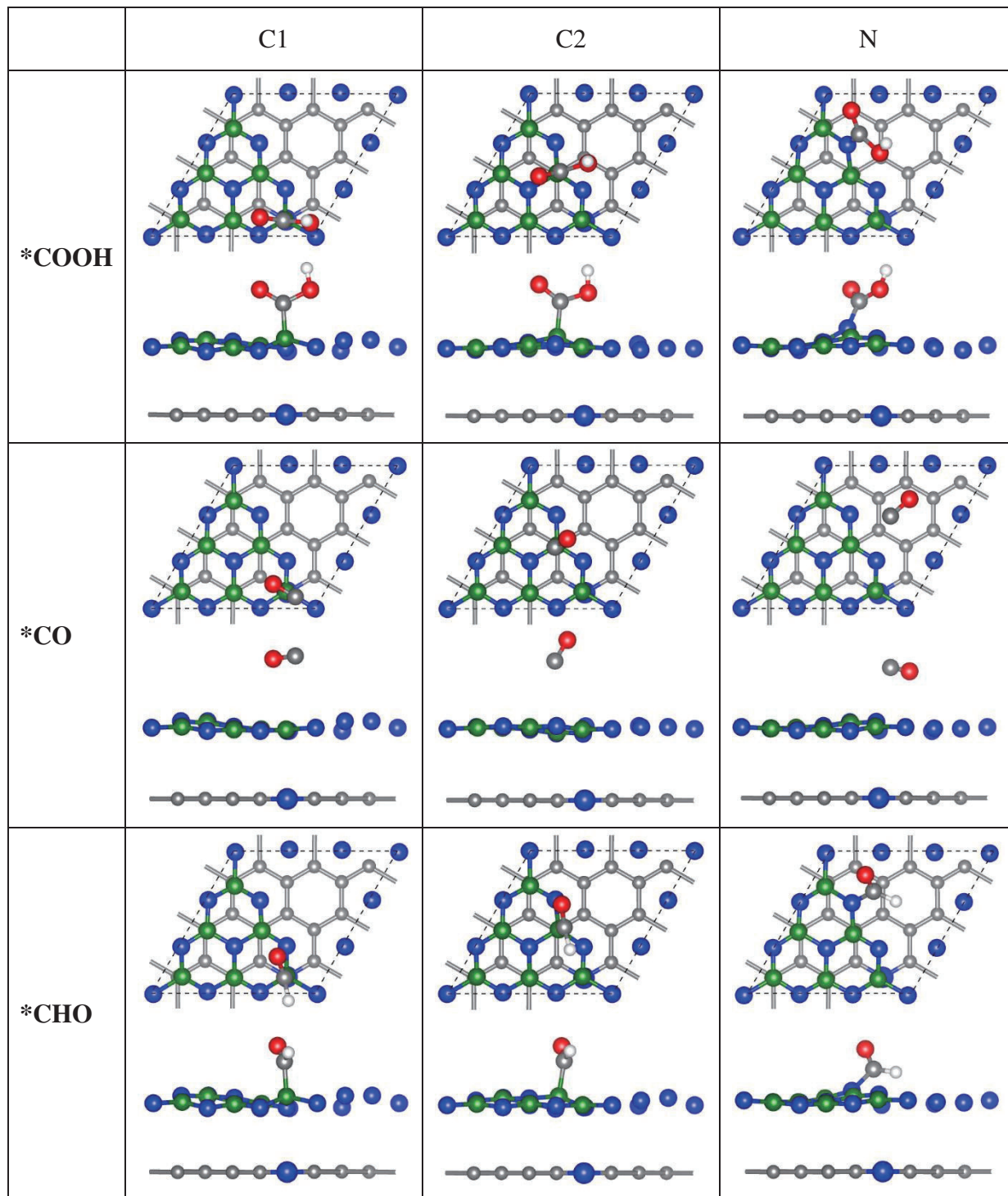
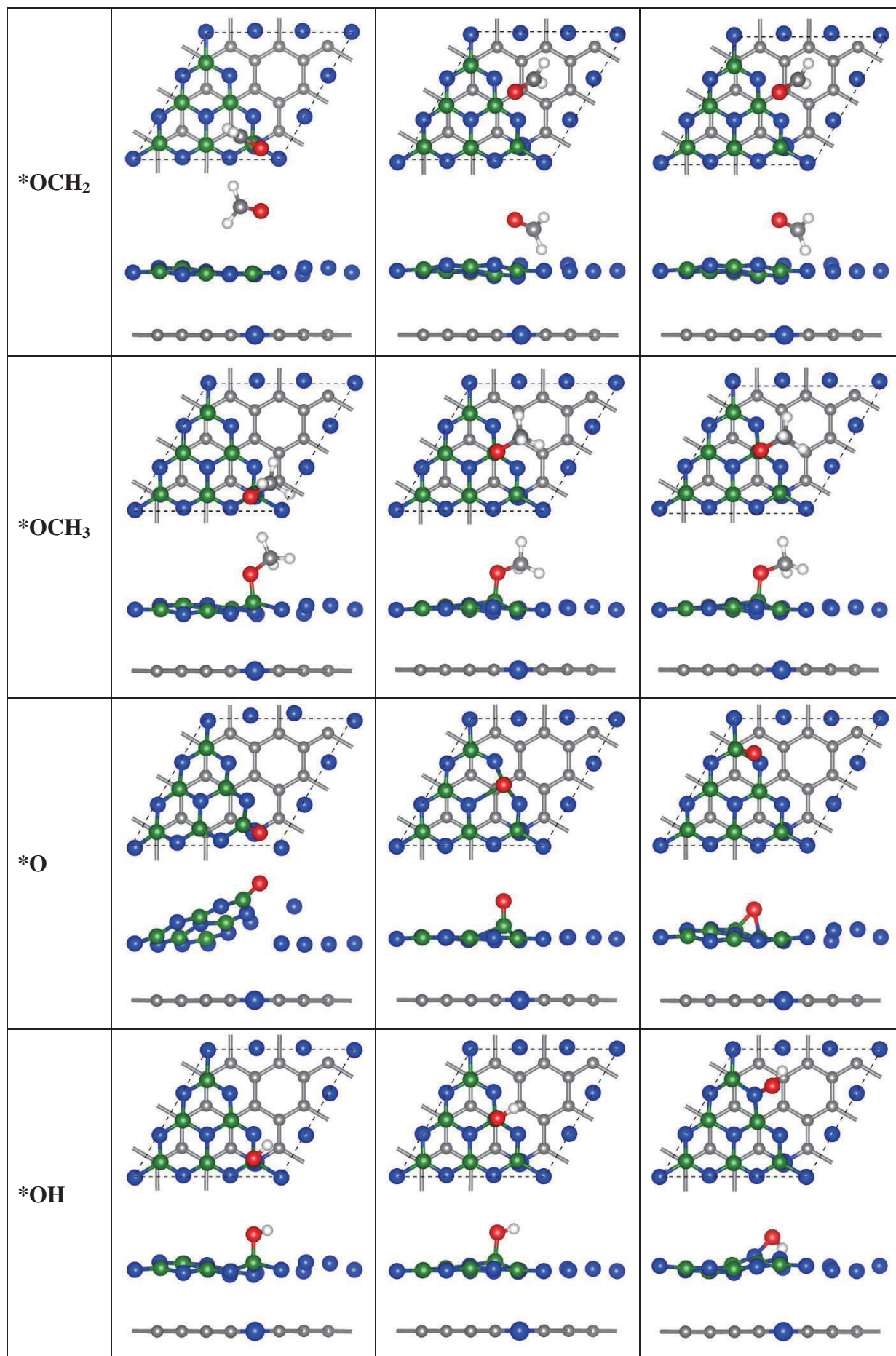


Table S2 Summary of optimized configurations of possible reaction intermediates on three active sites (C1, C2, and N) of C_3N_4/NG explored in this study.





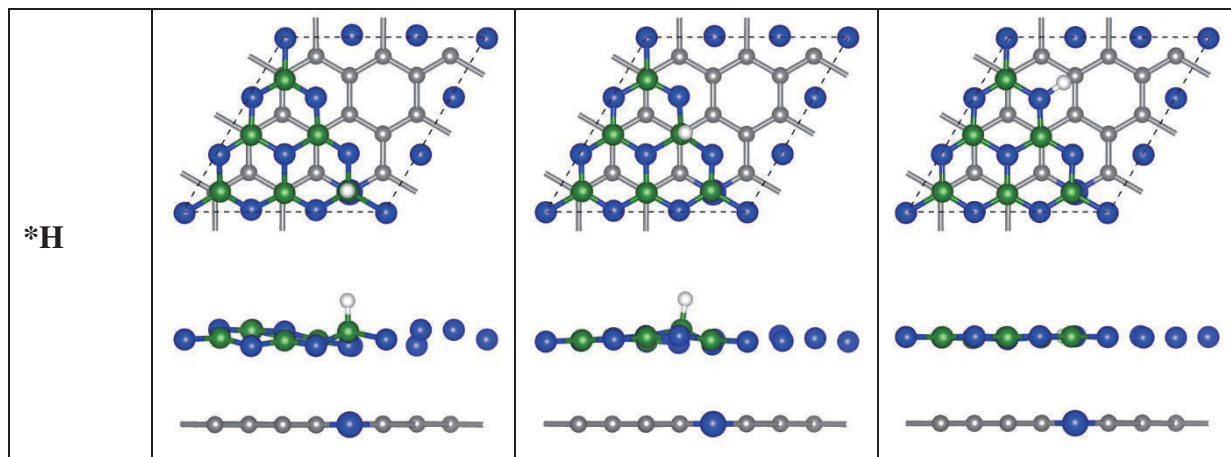
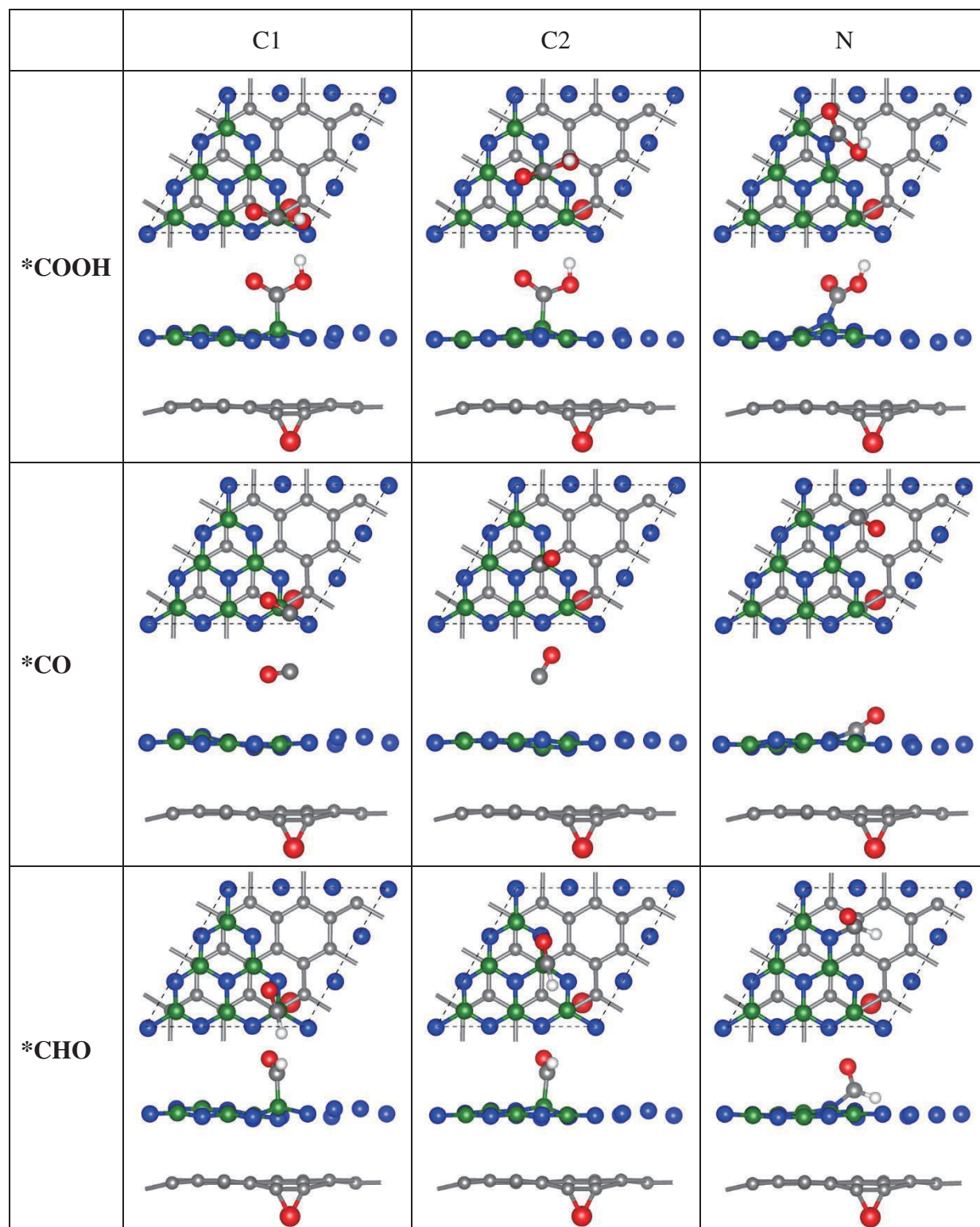
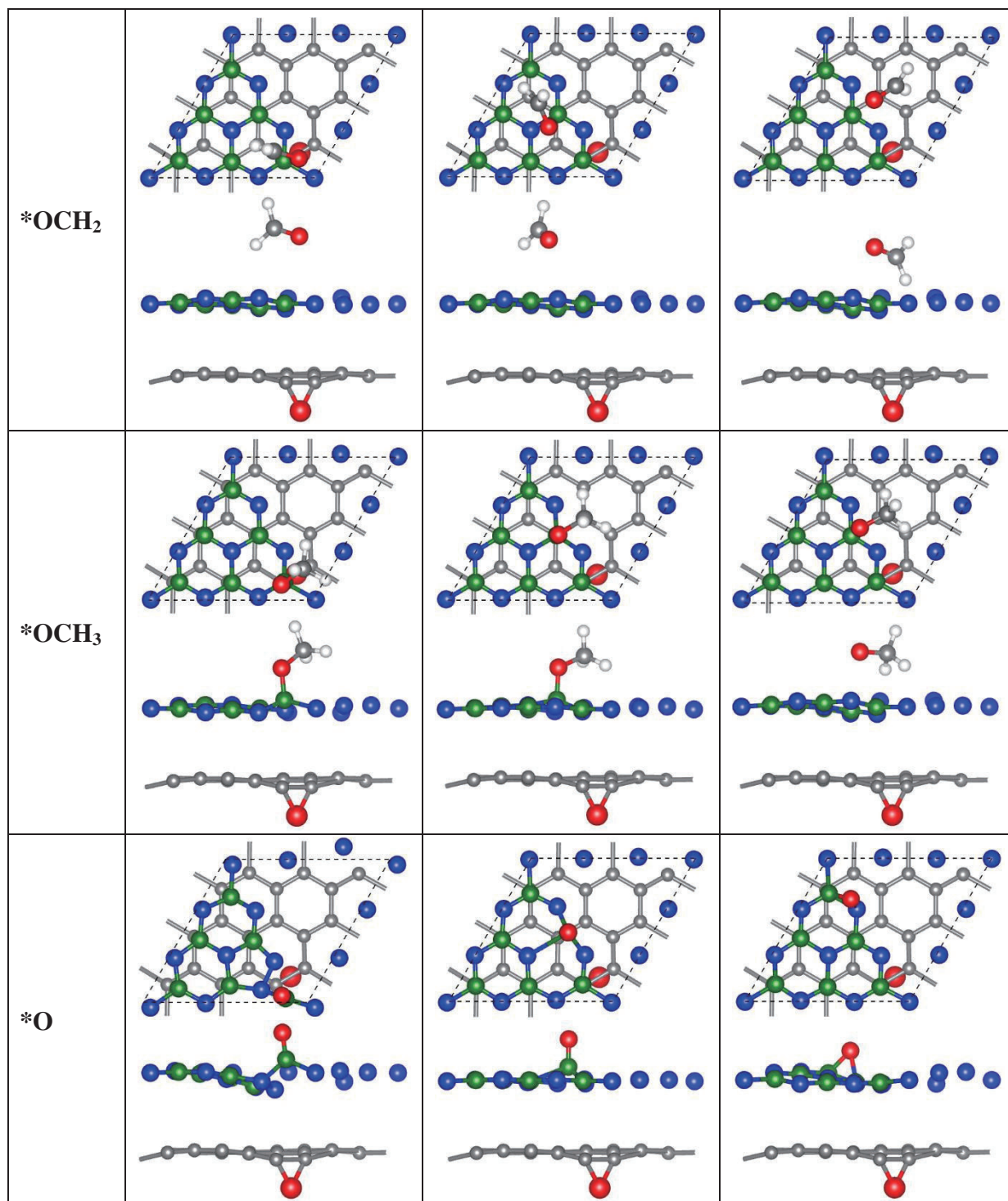


Table S3 Summary of optimized configurations of possible reaction intermediates on three active sites (C1, C2, and N) of C_3N_4/OG explored in this study.





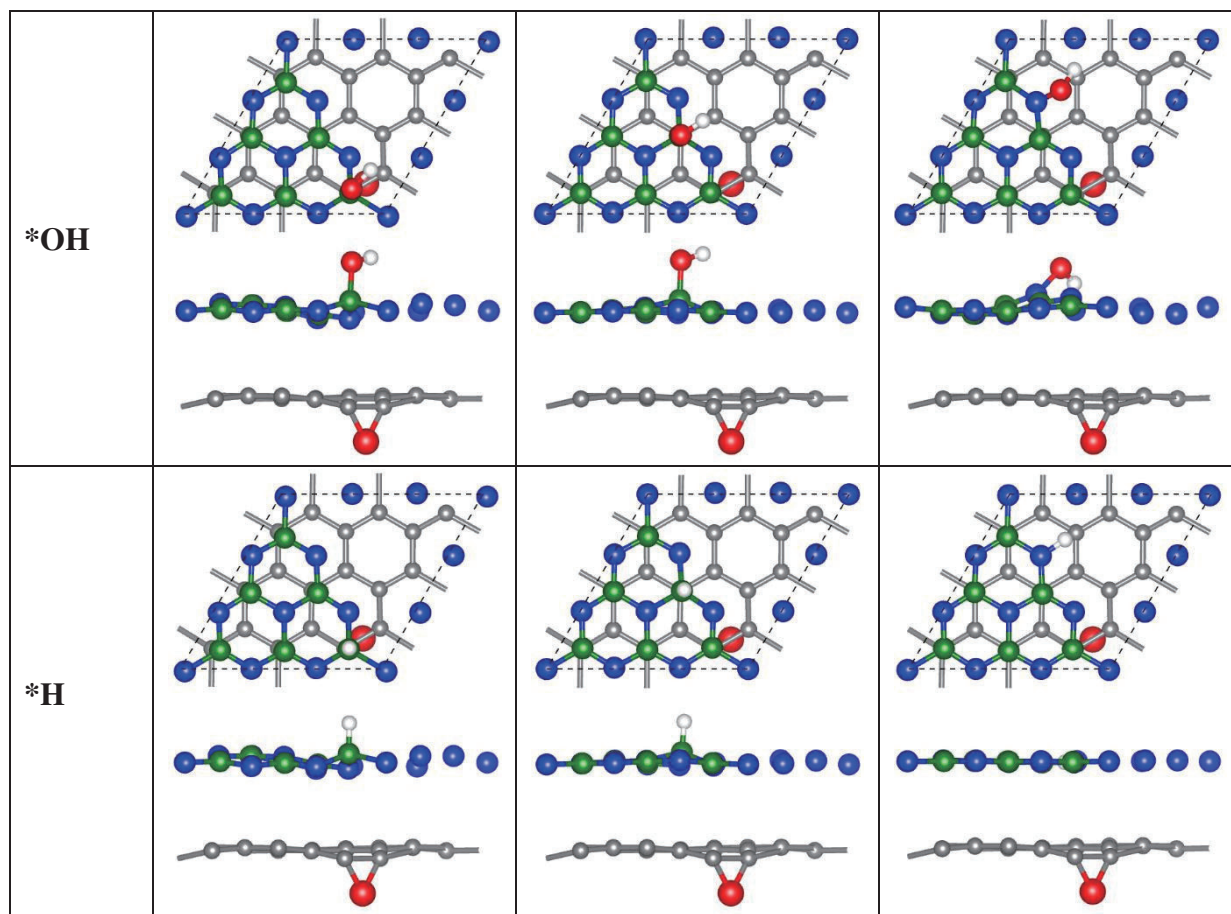
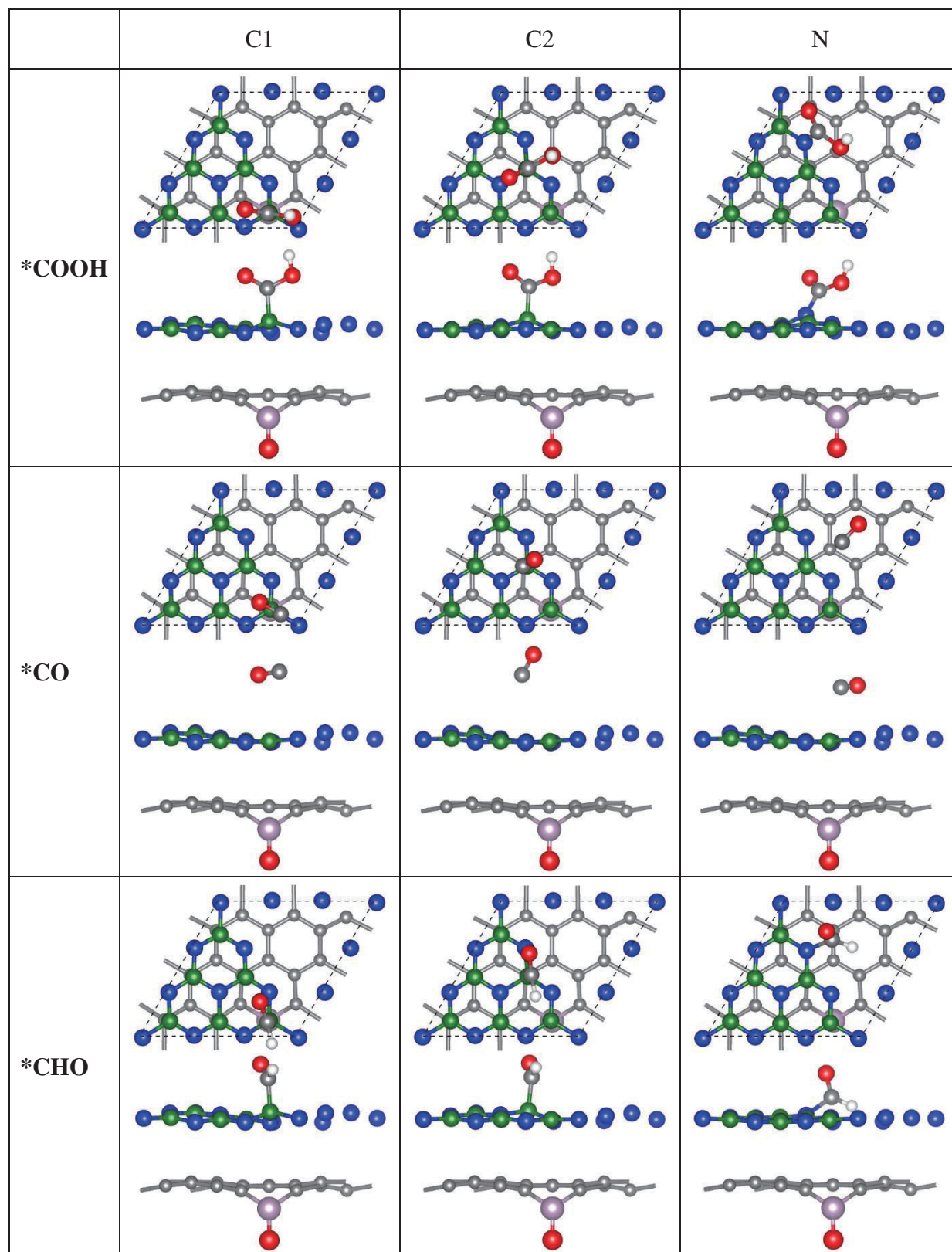
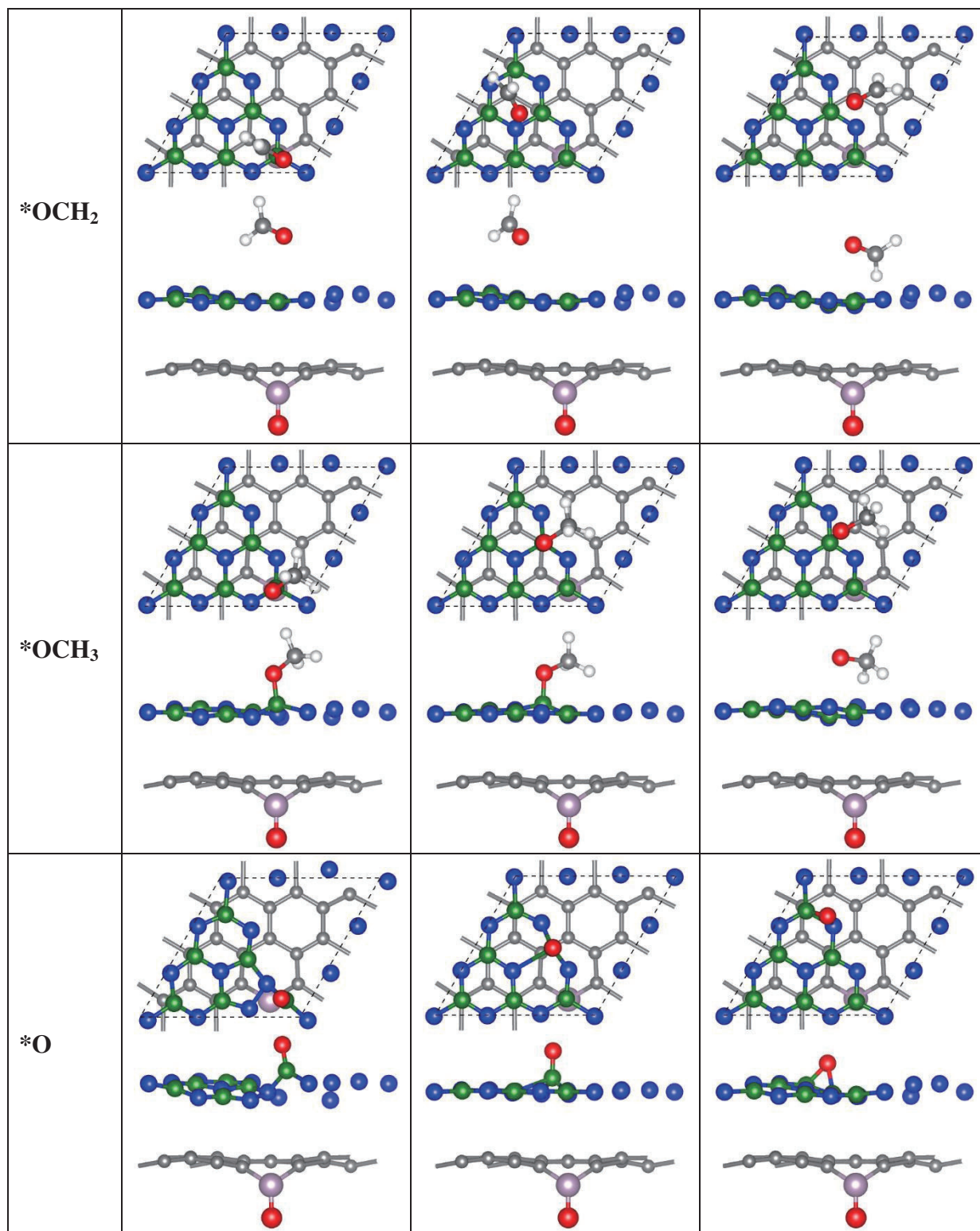


Table S4 Summary of optimized configurations of possible reaction intermediates on three active sites (C1, C2, and N) of C_3N_4/PG explored in this study.





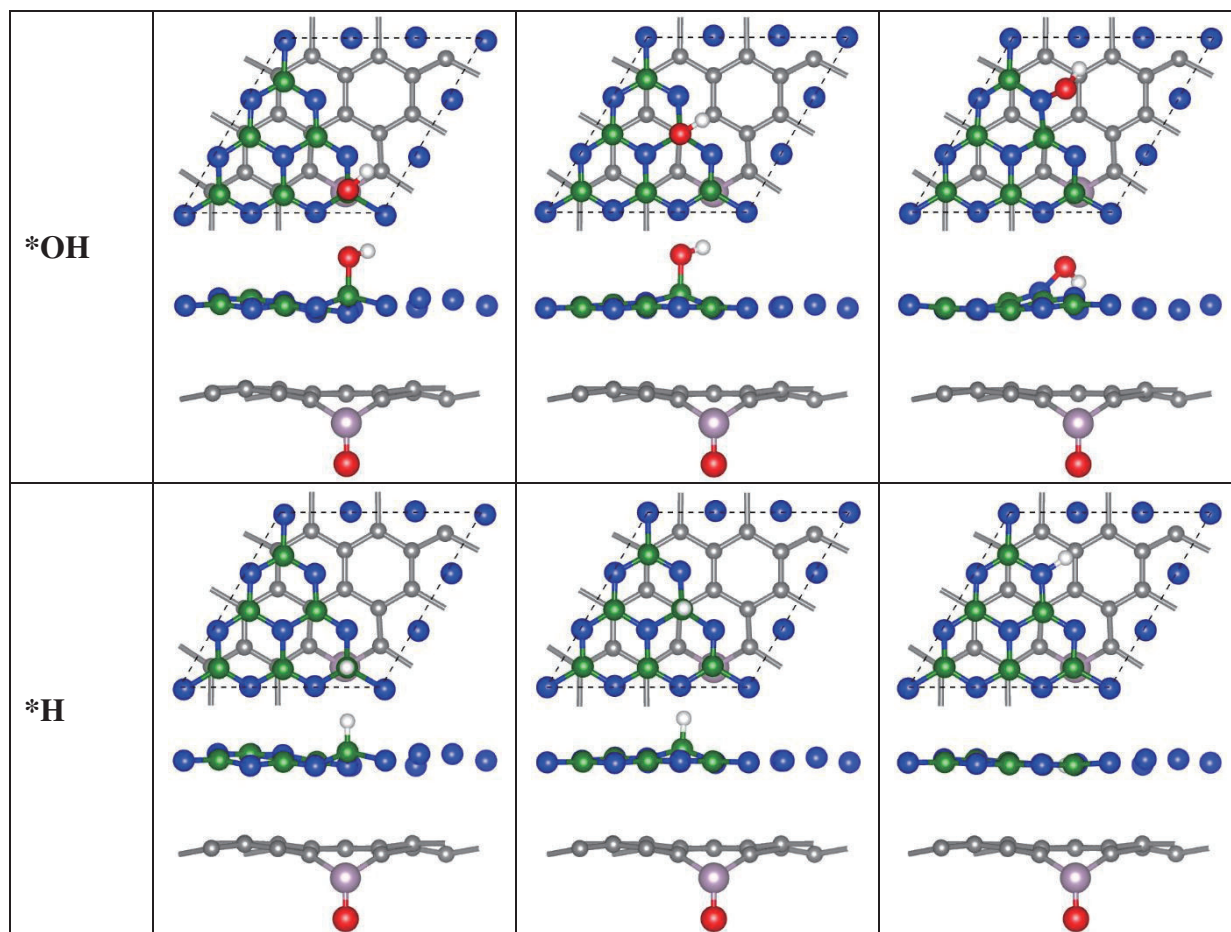
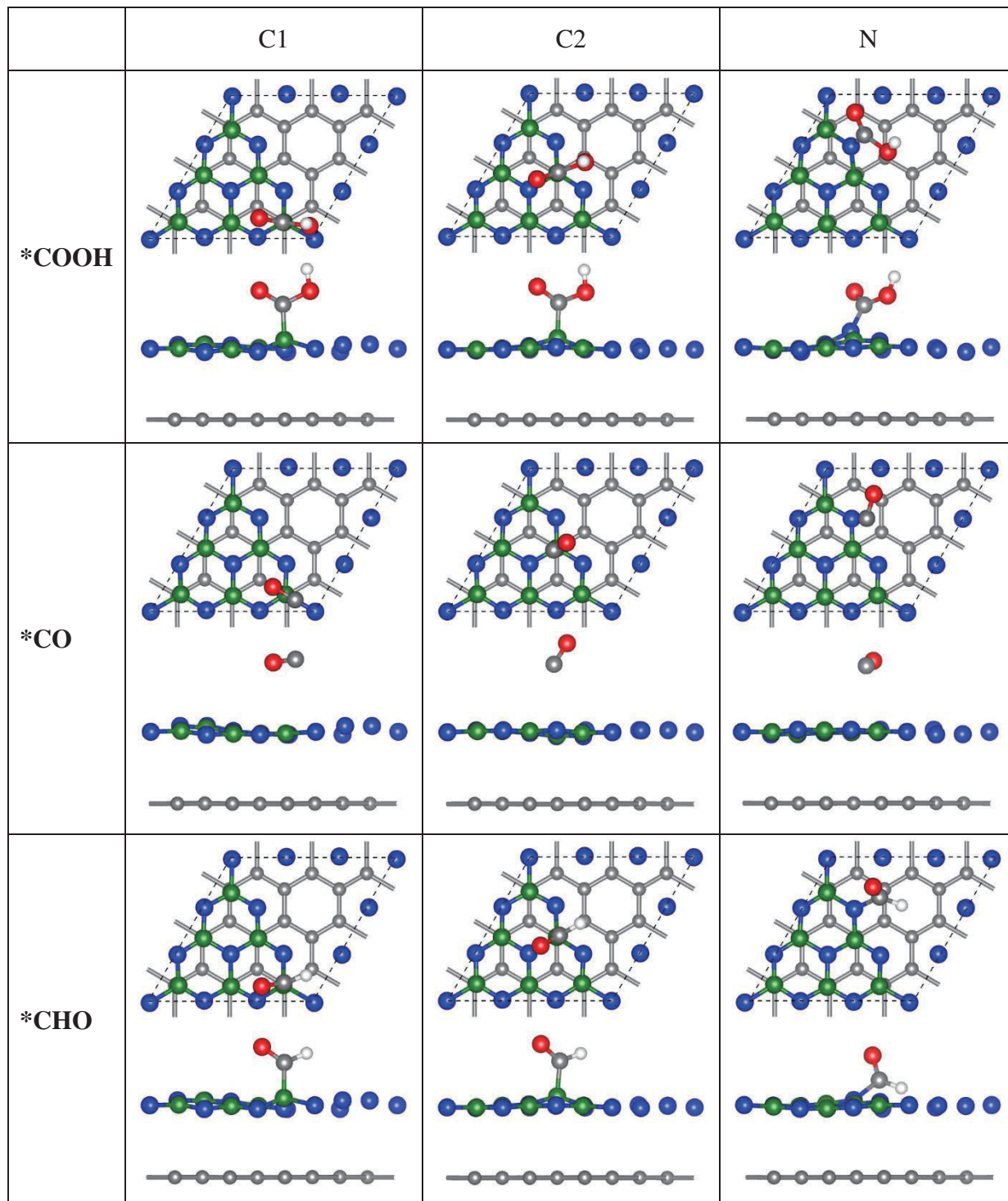
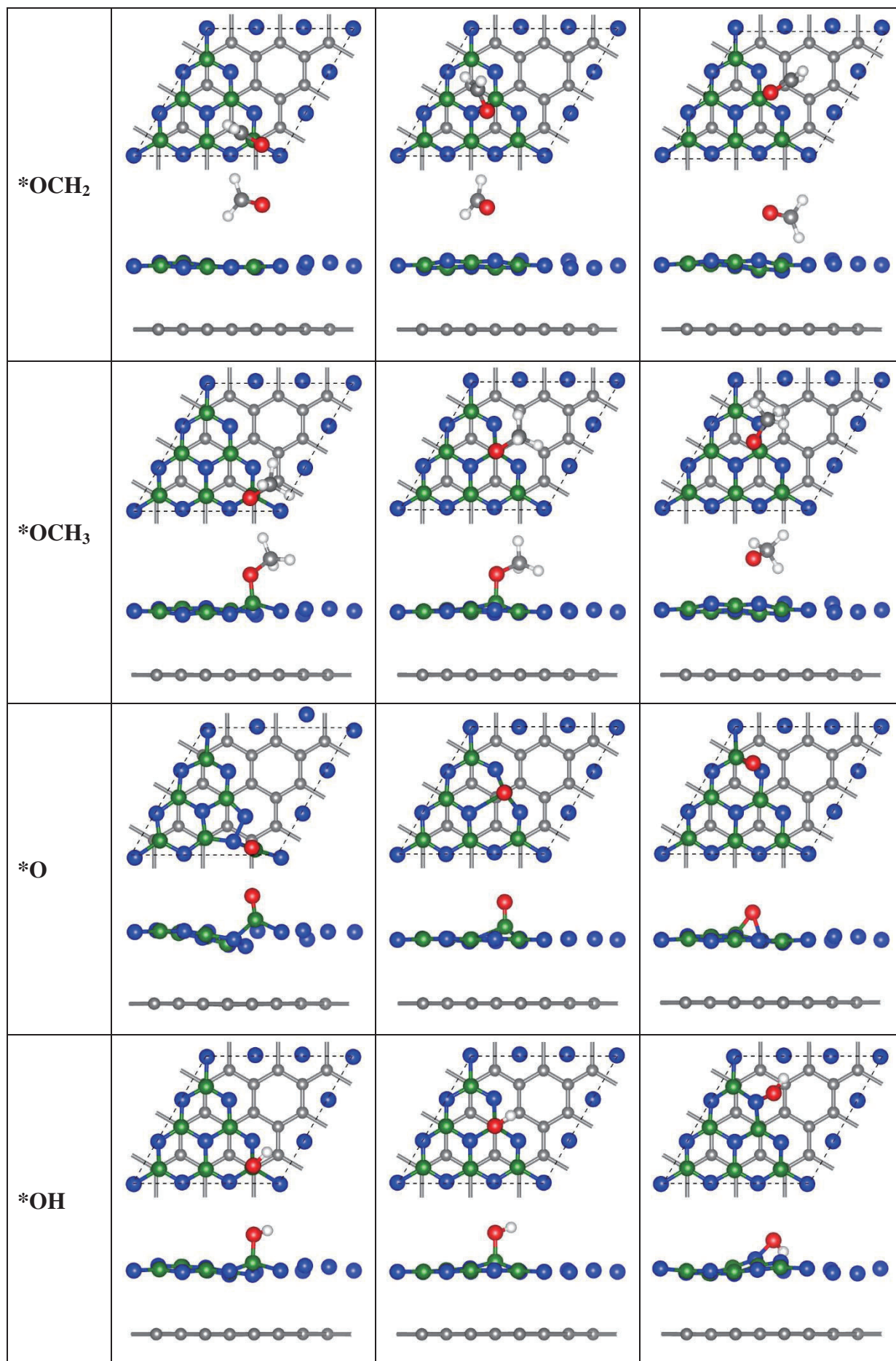


Table S5 Summary of optimized configurations of possible reaction intermediates on three active sites (C1, C2, and N) of C_3N_4/G explored in this study.





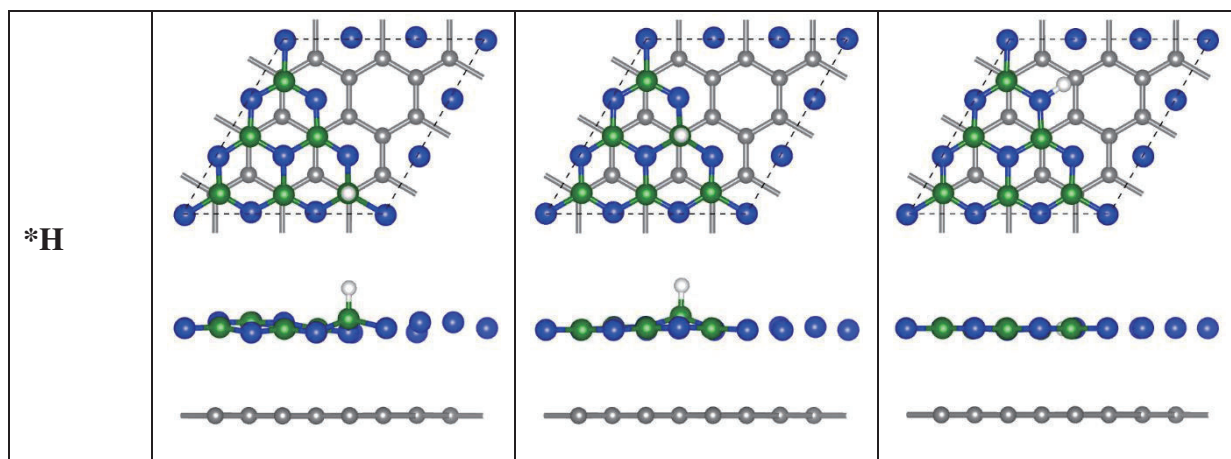


Table S6 Corresponding thermodynamic energy corrections (in eV) for intermediates.

Adsorbate	ZPE	-TS
*COOH	0.677	-0.178
*CO	0.154	-0.282
*CHO	0.541	-0.121
*OCH ₂	0.753	-0.268
*OCH ₃	0.978	-0.267
*O	0.093	-0.041
*OH	0.377	-0.046
*H	0.302	-0.002
*OCHO	0.639	-0.173

Table S7 Corresponding thermodynamic energy corrections (in eV) for gas phase molecules.

Gas molecule	ZPE	-TS
H ₂	0.269	-0.402
CO ₂	0.306	-0.662
CH ₄	1.182	-0.575
H ₂ O(g)	0.568	-0.536
CH ₃ OH(g)	1.350	-0.458

Reference

- [1] a) G. Kresse, J. Furthmuller, *Phys. Rev. B: Condens. Matter Mater. Phys.* **1996**, 54, 11169; b) G. Kresse, D. Joubert, *Phys. Rev. B: Condens. Matter Mater. Phys.* **1999**, 59, 1758; c) J. P. Perdew, K. Burke, M. Ernzerhof, *Phys. Rev. Lett.* **1996**, 77, 3865.
- [2] S. Grimme, *J. Comput. Chem.* **2006**, 27, 1787.
- [3] a) G. Henkelman, A. Arnaldsson, H. Jonsson, *Comput. Mater. Sci.* **2006**, 36, 354; b) E. Sanville, S. D. Kenny, R. Smith, G. Henkelman, *J. Comput. Chem.* **2007**, 28, 899.
- [4] a) G. Jones, J. G. Jakobsen, S. S. Shim, J. Kleis, M. P. Andersson, J. Rossmeisl, F. Abild-Pedersen, T. Bligaard, S. Helveg, B. Hinnemann, J. R. Rostrup-Nielsen, I. Chorkendorff, J. Sehested, J. K. Nørskov, *J. Catal.* **2008**, 259, 147; b) A. A. Peterson, F. Abild-Pedersen, F. Studt, J. Rossmeisl, J. K. Nørskov, *Energy Environ. Sci.* **2010**, 3, 1311.
- [5] W. J. Durand, A. A. Peterson, F. Studt, F. Abild-Pedersen, J. K. Nørskov, *Surf. Sci.* **2011**, 605, 1354.
- [6] a) J. K. Nørskov, J. Rossmeisl, A. Logadottir, L. Lindqvist, J. R. Kitchin, T. Bligaard, H. Jonsson, *J. Phys. Chem. B* **2004**, 108, 17886; b) Y. Jiao, Y. Zheng, M. Jaroniec, S. Z. Qiao, *J. Am. Chem. Soc.* **2014**, 136, 4394.
- [7] C. Shi, K. Chan, J. S. Yoo, J. K. Nørskov, *Org. Process Res. Dev.* **2016**, 20, 1424.

Chapter 4: Selectivity Roadmap for Electrochemical CO₂ Reduction on Copper-based Alloy Catalysts

4.1 Introduction and Significance

The electrochemical CO₂ reduction reaction (CRR) involves a complex reaction network with multiple competing steps, making the development of selective electrocatalysts for CO₂ conversion to desired products a major challenge. Copper (Cu) can uniquely yield a wide range of products beyond CO (e.g. C₁-C₃ hydrocarbon/oxygenate), but suffers from poor selectivity. Given this, engineering of Cu-based electrocatalysts is of great importance in order to address this selectivity issue.

In this Chapter, a novel descriptor-based approach was demonstrated to predict CRR selectivity of catalysts, by extensively modelling a series of Cu-based single atom alloys (M@Cu; M = Co, Ni, Ru, Rh, Ir, Pt, Pd, Au, Ag, Zn, In, Sn) and analysing their adsorption configurations and energetics. From this, the different hydrogen (H) and oxygen (O) affinities of the M atoms were shown to be feasible descriptors in determining CRR selectivity, leading to a practical engineering strategy by alloying metal elements with different H and O affinity for selective CO₂ reduction. The observed product distribution provided valid computational explanation for available reports of CRR selectivity trends in Cu-based bimetallic catalysts; it also gave extended mechanistic insights into the selectivity roadmap for an extensive range of Cu-based alloys. The inherent properties of catalysts were effectively correlated to their selectivity, therefore resulting in a feasible design strategy for highly selective CRR electrocatalysts. The descriptor-based selectivity trends also offered a practicable route to explore the catalytic performance for a wider range of CRR electrocatalysts.

4.2 Selectivity roadmap for electrochemical CO₂ reduction on copper-based alloy catalysts

This chapter is included as it appears as a journal paper published by Xing Zhi, Yan Jiao, Yao Zheng, Anthony Vasileff, Shi-Zhang Qiao, Selectivity roadmap for electrochemical CO₂ reduction on copper-based alloy catalysts, *Nano Energy*, **2020**, 71, 104601.

Statement of Authorship

Title of Paper	Selectivity Roadmap for Electrochemical CO ₂ Reduction on Copper-based Alloy Catalysts
Publication Status	<input checked="" type="checkbox"/> Published <input type="checkbox"/> Accepted for Publication <input type="checkbox"/> Submitted for Publication <input type="checkbox"/> Unpublished and Unsubmitted work written in manuscript style
Publication Details	Xing Zhi, Yan Jiao, Yao Zheng, Anthony Vasileff, Shi-Zhang Qiao, Selectivity roadmap for electrochemical CO ₂ reduction on copper-based alloy catalysts, <i>Nano Energy</i> , 2020 , 71, 104601.

Principal Author

Name of Principal Author (Candidate)	Xing Zhi		
Contribution to the Paper	Conducted all the computations, carried out data analysis and wrote the paper		
Overall percentage (%)	75%		
Certification:	This paper reports on original research I conducted during the period of my Higher Degree by Research candidature and is not subject to any obligations or contractual agreements with a third party that would constrain its inclusion in this thesis. I am the primary author of this paper.		
Signature		Date	14 Dec. 2020

Co-Author Contributions

By signing the Statement of Authorship, each author certifies that:

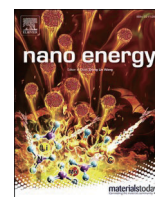
- i. the candidate's stated contribution to the publication is accurate (as detailed above);
- ii. permission is granted for the candidate to include the publication in the thesis; and
- iii. the sum of all co-author contributions is equal to 100% less the candidate's stated contribution.

Name of Co-Author	Yan Jiao		
Contribution to the Paper	Discussed computational results and findings, supervised the project, and revised the paper.		
Signature		Date	14 Dec. 2020

Name of Co-Author	Yao Zheng		
Contribution to the Paper	Discussed the research plan, supervised the project, and revised the paper.		
Signature		Date	14 Dec. 2020

Name of Co-Author	Anthony Vasileff		
Contribution to the Paper	Discussed the paper and helped to revise the paper.		
Signature		Date	15 Dec. 2020

Name of Co-Author	Shi-Zhang Qiao		
Contribution to the Paper	Discussed the research plan, supervised the project, and revised the paper.		
Signature		Date	16 Dec. 2020



Full paper

Selectivity roadmap for electrochemical CO₂ reduction on copper-based alloy catalysts

Xing Zhi, Yan Jiao^{**}, Yao Zheng, Anthony Vasileff, Shi-Zhang Qiao^{*}

Centre for Materials in Energy and Catalysis, School of Chemical Engineering and Advanced Materials, The University of Adelaide, Adelaide, South Australia, 5005, Australia



ARTICLE INFO

Keywords:

Alloys
Density functional theory
Electrochemical CO₂ reduction
Product selectivity
Electrocatalysis

ABSTRACT

Due to the complex reaction network of the electrochemical CO₂ reduction reaction (CRR), developing highly selective electrocatalysts for desired products remains a major challenge. In this study, a series of Cu-based single atom alloys (M@Cu) with multiple active sites are modelled to investigate their CRR selectivity trends by evaluating various adsorption configurations and energetics. The hydrogen (H) and oxygen (O) affinity of the secondary metals in the M@Cu model catalysts are found to be effective descriptors in determining CRR selectivity. The observed product grouping offers valid theoretical elucidation for available reports of CRR selectivity trends for Cu-based alloy catalysts. It also provides further mechanistic insight into the CRR product selectivity for an extensive range of Cu-based bimetallic materials. The selectivity trend based on the intrinsic catalyst properties provides a rational design strategy for highly selective CRR electrocatalysts.

1. Introduction

Electrochemical CO₂ reduction is a promising approach for converting CO₂ to value-added fuels and chemicals by using renewable electricity [1]. This process can store energy from intermittent resources in a sustainable manner and lead to an eco-friendly carbon-neutral cycle [2–4]. The CO₂ reduction reaction (CRR) is complex in nature with a wide variety of products, making the development of highly selective electrocatalysts for desired products a major challenge. Compared with two-electron (2e⁻) transfer products (e.g. CO and HCOOH), more reduced hydrocarbons and alcohols with higher energy density are more suitable for energy storage and transportation in chemical industries [5]. Copper (Cu) has shown unique ability to yield energy dense products via the CRR [6]. However, Cu possesses moderate adsorption strength of key reaction intermediates from a microscopic viewpoint, giving rise to its poor catalyst selectivity in CO₂ electroreduction [7,8]. Therefore, engineering Cu-based catalysts with modified active sites and further understanding of the reaction mechanisms are important to address selectivity issues for the CRR.

Currently, Cu-based alloys which incorporate a secondary metal with different catalytic properties have been widely studied for selective CRR

electrocatalysis [9,10]. These Cu-based bimetallic materials have emerged as effective CRR catalysts through both experimental and computational investigation. For example, the incorporation of In or Sn in Cu-based bimetallic nanoparticles selectively yielded 2e⁻ products with high efficiency [11–13]. Meanwhile, the alloying of Pt, Pd, or Au with Cu in nanostructured Cu-based alloy catalysts exhibited significantly improved product selectivity toward more reduced hydrocarbons and alcohols [14–17]. Despite these case studies, a comprehensive understanding of the CRR selectivity trends for Cu-based alloys is still lacking. Therefore, constructing the CRR selectivity roadmap for an extensive range of Cu-based alloy catalysts is crucial for rational design strategies with the help of in-depth mechanistic exploration.

Various efforts have been undertaken to explore the selectivity of catalysts for CO₂ reduction. For example, the binding energy of the oxygen-bound *OCHO intermediate has been suggested as a feasible indicator for increasing the selectivity of metal catalysts toward HCOOH [18,19]. With regards to highly reduced C1 products (e.g. methane and methanol), catalyst selectivity has been effectively explained by analysing the thermodynamics and kinetics of the *CO protonation step [20–24]. Meanwhile, the reaction barrier to the C–C coupling process involving *CO adsorbate has shown a big influence on the C2 products

* Corresponding author.

** Corresponding author.

E-mail addresses: xing.zhi@adelaide.edu.au (X. Zhi), yan.jiao@adelaide.edu.au (Y. Jiao), yao.zheng01@adelaide.edu.au (Y. Zheng), anthony.vasileff@adelaide.edu.au (A. Vasileff), s.qiao@adelaide.edu.au (S.-Z. Qiao).

<https://doi.org/10.1016/j.nanoen.2020.104601>

Received 30 October 2019; Received in revised form 7 February 2020; Accepted 7 February 2020

Available online 11 February 2020

2211-2855/© 2020 Elsevier Ltd. All rights reserved.

selectivity of Cu surfaces [25–30]. However, there has been limited success in developing generally applicable selectivity descriptors to identify target products of a given CRR electrocatalyst. In addition, the product selectivity of a catalyst is influenced by reaction conditions like local pH and applied overpotentials [31–36]. Hence, the search for more effective selectivity descriptors by considering the intrinsic electrocatalyst properties (which can be tuned independently and obtained with sufficient accuracy) are highly required.

For different catalytic reactions, it has been reported that the inherent metal hydrogen (H) and oxygen (O) affinities play critical roles in determining the activity and selectivity of catalysts by influencing the adsorption energetics of key reaction intermediates [37,38]. Regarding the CRR, the O affinity of metal surfaces is suggested to have an impact on *OCHO binding energy [18]. Further, the oxophilicity of catalytic surfaces is found to have an effect on selectivity between methane and methanol [39]. Given this, the intrinsic H and O affinity of catalysts could serve as promising descriptors for designing highly selective CRR electrocatalysts.

In this study, density functional theory (DFT) calculations are used to explore selectivity trends in 12 Cu-based alloy models (M@Cu) as catalysts for electrochemical CO_2 reduction. The M@Cu alloy models are composed of single metal atoms M (M = Co, Ni, Ru, Rh, Ir, Pt, Pd, Au, Ag, Zn, In, Sn) embedded into the Cu(111) surface. The introduction of single metal atom offers a unique platform to tailor diverse active sites and tune adsorption behaviour of reaction intermediates, thus optimizing the electrocatalytic activity and selectivity. Previously, the DFT calculations have been applied to other bimetallic alloy models for selective CO_2 reduction, suggesting the great potential of computational chemistry for designing high performance CRR catalysts [40–42]. According to extensive thermodynamic analysis, the CRR selectivity in M@Cu catalysts can be rationally tuned by alloying various secondary metals with different metal hydrogen (M-H) and metal oxygen (M-O) affinities, which stem from varying d-orbital positions of the M atoms. The product grouping categorized by intrinsic M-H and M-O affinity in M@Cu alloys provides solid computational explanation for available reports of CRR selectivity trends in Cu-based bimetallic catalysts. It also gives extended theoretical prediction of the selectivity roadmap for a wide range of Cu-based alloys. The inherent properties of the catalyst materials are effectively correlated to their selectivity, leading to a feasible design strategy for highly selective CRR electrocatalysts.

2. Results and discussion

2.1. Selectivity via the first hydrogenation step

Due to the complexity of the CRR process, we focus on several key reaction steps and analyze competition from a thermodynamic viewpoint along different reaction pathways (Fig. S1). The optimized configurations of M@Cu alloy surfaces and Cu(111) surface are shown in Fig. S2. For key reaction intermediates, their optimized configurations are summarized in Table S1. Minor geometrical deformation was observed for both pure catalyst surfaces and various reaction intermediates, indicating their thermodynamic stability. The adhesion energy of metal atom M was also calculated to show the general stability of single metal atom on the Cu surface (Table S2). The free energy corrections are presented in Table S3 (for intermediates) and Table S4 (for molecules). The effect of solvation is included approximately the same as previous studies [21,43]. The effect of ions is another factor influencing product selectivity in CO_2 reduction. The alkali metal cations were identified to affect the distribution of products in electrochemical CO_2 reduction [44,45]. Additionally, effects of electrolyte anions on product selectivity in CO_2 reduction were investigated on Cu surfaces. It was found that Cl^- and Br^- enhanced CO selectivity while I^- had a positive effect on methane formation [46]. Another study reported that the electrolyte anion played a critical role in the formation enhancement of C2 products by facilitating a higher *CO population on

the catalyst surface [47]. However, this study mainly focuses on the impact of intrinsic catalyst properties in determining CRR selectivity, assuming the reaction conditions are identical for various M@Cu alloy models. Therefore, the effect of ions is not considered in this work. Further computational details can be found in the Supporting Information.

The initial hydrogenation of CO_2 leads to the formation of either C-bound *COOH or O-bound *OCHO intermediates; the formation of these two intermediates mainly influences the selectivity toward HCOOH. As shown in Fig. 1a, the hydrogenation of CO_2 toward *COOH on Ag, Zn, In, Sn, Pd and Au doped M@Cu surfaces are endothermic, while other M@Cu alloys show downhill free energy changes for *COOH formation. For Ag, Zn, In and Sn doped M@Cu surfaces with weak M-H affinity, HCOOH production via the *COOH intermediate is preferred on these surfaces for overpotentials smaller than 0.26 V (Fig. 1c). Along the *COOH reaction pathway, the limiting step on Ag, Zn, In, Sn and Au doped M@Cu surfaces is *COOH formation. For other M@Cu alloy catalysts which strongly bind *COOH , the limiting step changes to HCOOH desorption, mostly at high overpotential. In the case of the *OCHO intermediate, the free energy changes (ΔG) of *OCHO on all M@Cu surfaces are thermodynamically downhill (Fig. 1b), indicating the preferred stability of *OCHO . However, high free energy barriers are required for subsequent HCOOH formation. As shown in Fig. 1d, all investigated catalysts are located in the strong *OCHO binding region, causing HCOOH desorption to be the limiting step. The thermochemistry of the CRR is also compared with reaction energetics of the hydrogen evolution reaction (HER). Generally, either *COOH or *OCHO (or both) exhibit stronger adsorption energies than *H on M@Cu surfaces, therefore suggesting the preference for the CRR in the early stages of the reaction pathways (Fig. S3).

Different M-H and M-O affinities in M@Cu alloys have a significant impact on the intermediate adsorption configurations, therefore leading to distinct adsorption energies. As summarized in Fig. 1e, the *COOH intermediate prefers to be adsorbed on the M atom in M@Cu alloys with strong M-H affinity. Strongly bound *COOH is thermodynamically unfavorable for HCOOH production, but prone to form adsorbed *CO after OH desorption. As for M@Cu catalysts with weak M-H affinity, *COOH weakly binds to Cu atoms next to the M atom and is thermodynamically favoured for HCOOH formation. The adsorption condition of the *OCHO intermediate is closely related to M-O affinity (Fig. 1f). On the M@Cu surfaces with weak M-O affinity, the O-bound *OCHO tends to be adsorbed on the Cu atoms around the M atom, while strong M-O affinity leads to *OCHO interaction with the alloy surfaces via a M-O and a Cu-O bond. Generally, the adsorption strength of the *OCHO intermediate decreases in M@Cu alloys with lower M-O affinity and therefore the formation of HCOOH via *OCHO is facilitated.

2.2. Selectivity via *CO intermediate adsorption strength

After OH desorption from *COOH , *CO is formed for further protonation toward highly reduced products or desorption to CO. The free energy changes of *CO protonation to *CHO and CO desorption are compared to demonstrate product selectivity, using M-H and M-O affinity in the M@Cu alloys as a grouping criterion. As shown in Fig. 2a and b, the Ag, Zn, In and Sn doped M@Cu surfaces in the regions with both weak M-H and M-O affinities show their preference for CO generation with lower free energy changes for CO desorption; while higher free energy changes are required for *CO protonation to *CHO . These four alloy catalysts are also demonstrated to be thermodynamically favorable for HCOOH production in the previous discussion. Therefore, M@Cu alloys with both weak M-H and M-O affinities prefer to yield $2e^-$ transfer products. Meanwhile, the Co, Ni, Ru, Rh, Ir and Pt doped M@Cu surfaces located in the regions with both strong M-H and M-O affinities show strong *CO binding and hence high barrier to CO desorption. Thus, the general product favorability on this group of alloy catalysts are highly reduced C1 products via hydrogenation of *CO . However, the

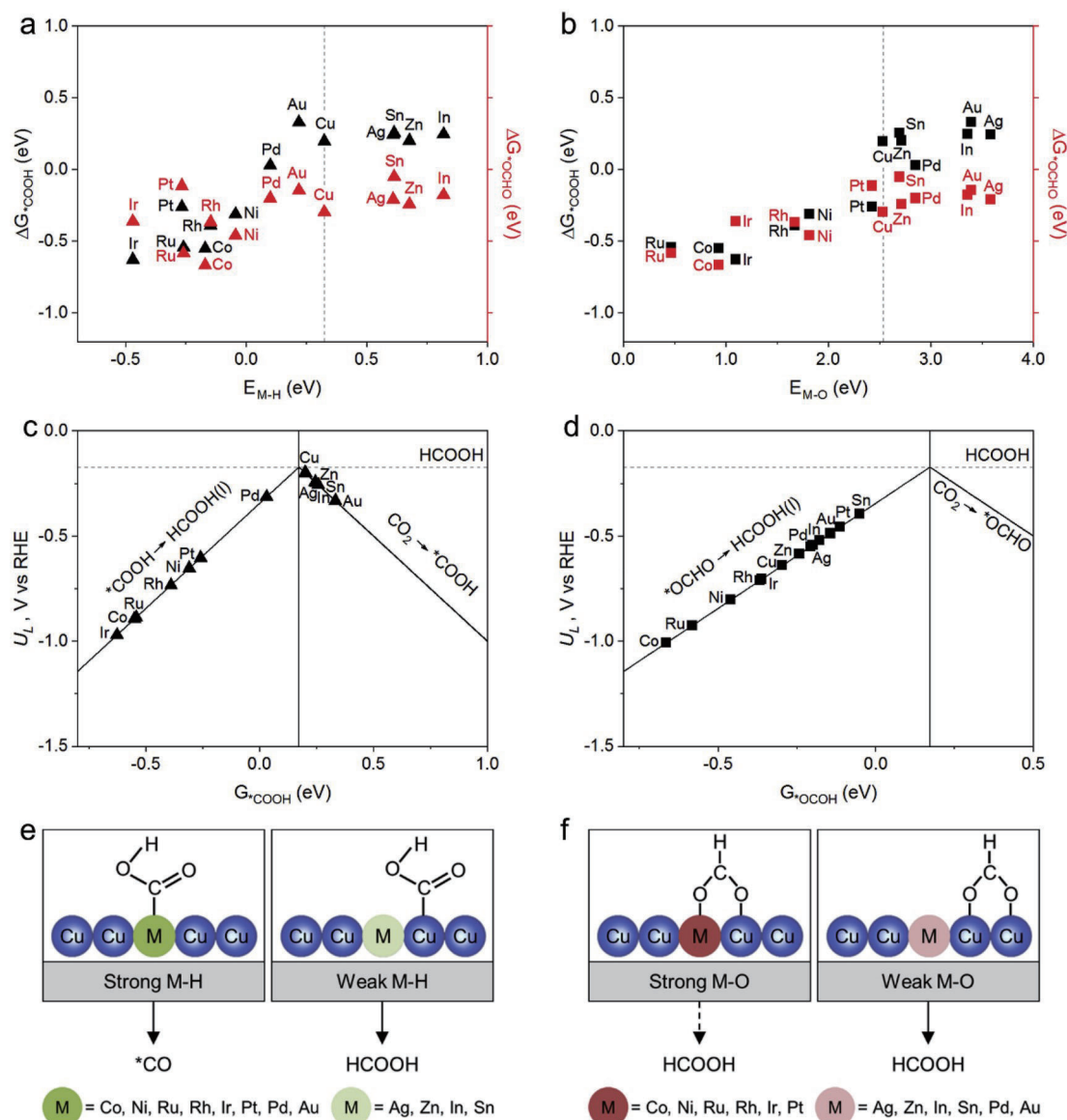


Fig. 1. The free energy changes of *COOH and *OCHO on $M@Cu$ alloy surfaces plotted against (a) M-H affinity and (b) M-O affinity, respectively. Theoretical activity volcano plots for HCOOH via (c) *COOH and (d) *OCHO intermediate, respectively. Summary of the optimized adsorption configurations of (e) *COOH and (f) *OCHO intermediates and selectivity trends to HCOOH and other reduced products based on different M-H and M-O affinities of the $M@Cu$ catalysts. Dashed arrow indicates elementary reaction step that can occur simultaneously yet with less favorable thermodynamics.

overall activity is limited on these six alloys (except for Pt@Cu) due to high free energy changes for the following step. The Pt@Cu alloy shows the lowest free energy change for *CO protonation to *CHO among all investigated catalyst models in this study, suggesting its high selectivity toward deeply reduced C1 products via the *CHO intermediate. As for the Pd and Au doped alloy surfaces, they exhibit moderately strong M-H but weak M-O affinities. Experimentally it has been shown that C2 products were generated on Cu-Pd and Cu-Au alloys [15–17]. In this regard, further understanding of C2 product selectivity induced by M-H and M-O affinity in $M@Cu$ alloys is vital for completing the whole roadmap for selective CO_2 electroreduction. This will be discussed later in greater detail. The thermodynamic energetics of *COH formation from adsorbed *CO on $M@Cu$ surfaces are also evaluated. As shown in Fig. S4, the free energy changes of *CO protonation to *CHO and *COH are compared based on varying M-H and M-O affinities in $M@Cu$ alloys. Generally, *CO hydrogenation to *CHO is thermodynamically favoured relative to *COH , although both reaction pathways via *CHO or *COH are available for further reduction steps.

In the exploration of CRR catalytic activity and selectivity trends, linear scaling relationships have been widely reported for various metallic and metal-free electrocatalysts [8,48–51]. The linear scaling relations within carbon-bound adsorbates (i.e. *CO , *COOH , *CHO , *COH) are also observed on the investigated $M@Cu$ alloy catalysts (Fig. 2c). Based on this, the limiting potentials (U_L) for key elementary steps of CO_2 reduction to highly reduced C1 products can be obtained to estimate the thermodynamically preferred reaction pathway. As can be seen in Fig. 2d, the elementary limiting potentials are correlated with *CO free energies in this series of alloy catalysts. The two most negative U_L lines display the limiting potentials required to protonate *CO to *CHO or *COH , indicative of the potential-limiting *CO protonation step. The U_L line of $^*CO \rightarrow ^*CHO$ exhibits a steeper slope and a more positive position than the line of $^*CO \rightarrow ^*COH$, suggesting better sensitivity and activity of the reaction energetics for *CHO formation by regulating the adsorption energy of *CO . Therefore, for C1 hydrocarbons and alcohols, the U_L line of *CO protonation to *CHO is selected to estimate the overall theoretical overpotential and *CHO is rationalized

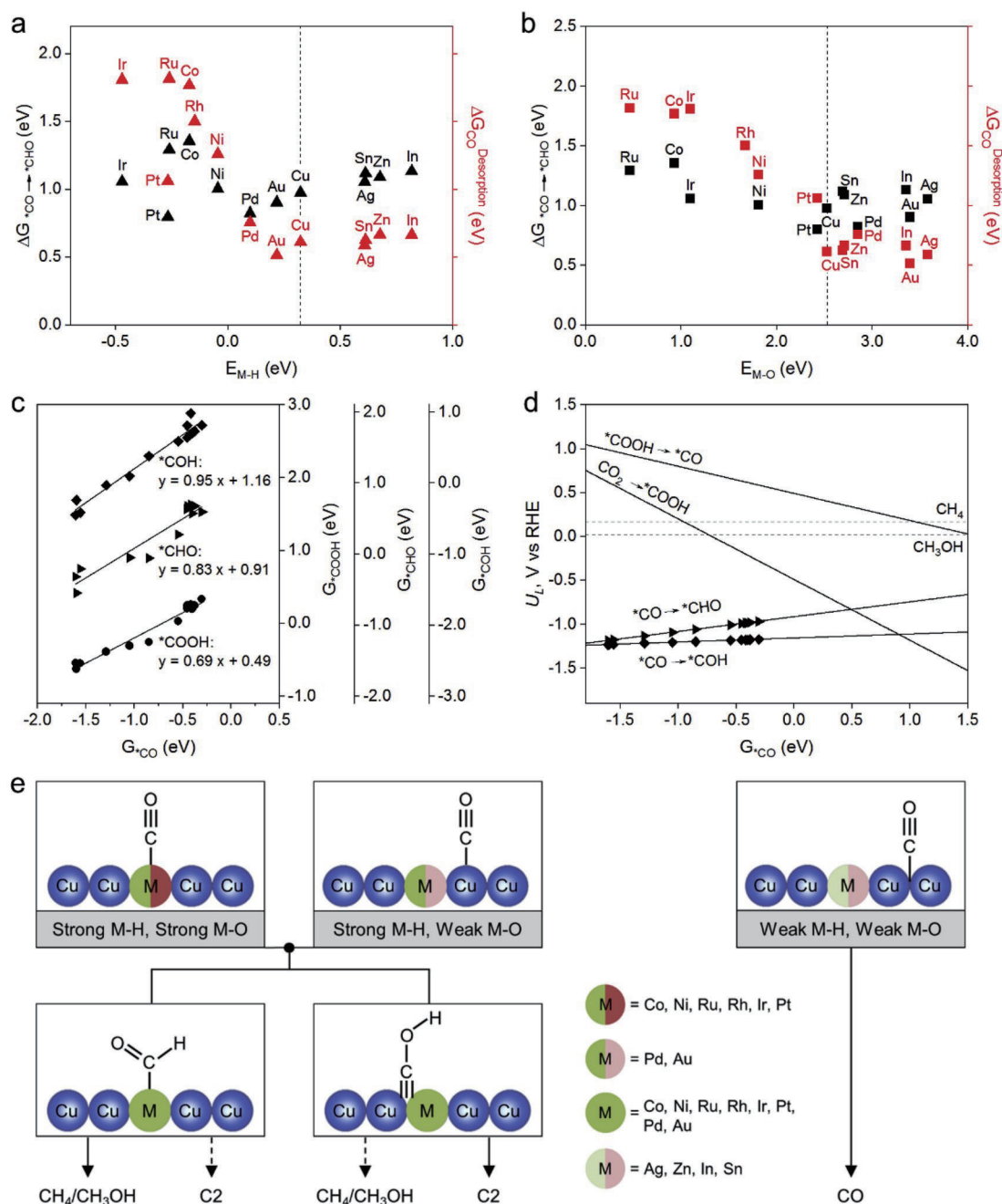


Fig. 2. The free energy changes of *CO protonation to *CHO and CO desorption on M@Cu alloy surfaces plotted against (a) M-H affinity and (b) M-O affinity, respectively. The ΔG value of *CO protonation to *CHO on Rh@Cu is missing due to geometric instability of *CHO on Rh@Cu . (c) Scaling relations for the free energies of *COOH , *CHO and *COH as a function of *CO free energy on various M@Cu catalysts. (d) Limiting potentials for key elementary steps of CO_2 reduction to highly reduced C1 products as a function of *CO free energy. The black dashed lines represent the equilibrium potential for CO_2 reduction to CH_4 and CH_3OH . (e) Summary of the optimized adsorption configurations of *CO , *CHO and *COH intermediates and selectivity trends to CO and highly reduced products according to various M-H and M-O affinities of the M@Cu catalysts. Dashed arrows have the same meaning as Fig. 1.

as the dominant intermediate.

The optimized adsorption configurations of *CO , *CHO and *COH on the M@Cu surfaces and the preferred reaction pathways induced by different M-H and M-O affinities in M@Cu alloys are summarized in Fig. 2e. The adsorbed *CO moves away from the M atom with decreasing M-H and M-O binding strength and therefore the selectivity for CO is separated for M@Cu alloys with both weak M-H and M-O affinities. For other M@Cu surfaces with strong M-H affinity, the *CO intermediate is prone to further protonation to *CHO or *COH . The formation of *CHO is thermodynamically preferred for highly reduced C1 products (e.g. CH_4 and CH_3OH), while the *COH intermediate plays an important role

in producing C_2 products via the C-C coupling process (discussed further later).

2.3. Selectivity for C-C coupling

From the preceding discussion, Pd and Au doped M@Cu catalysts possess strong M-H but weak M-O affinities, suggesting their distinct catalytic properties for selective CO_2 electroreduction. In particular, the free energy change difference between *CO protonation to *CHO and CO desorption on Pd@Cu is the lowest among all investigated catalyst models, indicating the coexistence of CO and adsorbed *CHO near the

catalyst surface (Fig. 2a and b). Therefore, we examine the potential C–C coupling process through a CO insertion mechanism toward C2 products, which has been suggested by various computational studies [27–29,33]. Since Ag, Zn, In and Sn doped M@Cu catalysts preferentially generate $2e^-$ products, they are not included in the study of reaction mechanisms for C2 products. After *CO protonation, either *CHO or *COH can be formed on M@Cu surfaces, such that both OC-CHO and OC-COH coupling mechanisms are considered in this study. As shown in Fig. 3a and b, the free energy changes of OC-COH coupling scale linearly with M-H and M-O affinity respectively for various M@Cu alloy catalysts. This suggests that M-H and M-O affinity in M@Cu alloys can also be used as the descriptor to illustrate selectivity for C2 products. The Pd and Au doped M@Cu catalysts show lower free energy changes for OC-COH coupling, indicating their preference for C2 product selectivity. When the free energy changes of OC-CHO coupling are plotted against M-H affinity on M@Cu surfaces, a relatively strong linear correlation is observed (Fig. S5a). However, a worse linear fit is observed between the free energy changes of OC-CHO coupling and M-O affinity (Fig. S5b). In thermodynamic terms, the free energy changes of OC-COH coupling are generally lower than that of OC-CHO coupling, indicating the favorability of *COCOHO formation along the reaction pathway to C2 products.

As summarized in Fig. 3c, the different M-H and M-O affinities of M@Cu alloys impact the CO_2 reduction selectivity by affecting the intermediate adsorption configurations. The optimized configurations of the *COCHO intermediate are divided into two groups. The CHO moiety

in *COCHO generally shows horizontal geometry on M@Cu surfaces with strong M-O affinity. On the other hand, M@Cu catalysts with weak M-O affinity display vertical adsorption geometry of *COCHO . For the *COCOHO intermediate, the optimized configurations are analogous on various M@Cu surfaces with either strong or weak M-O affinity. The *COCOHO intermediate adsorbs to catalyst surfaces via two carbon atoms, suggesting its stronger interaction with the catalysts. Herein, M-H and M-O affinities in M@Cu alloys are rationalized to be useful indicators for C2 product selectivity.

2.4. Selectivity roadmap of M@Cu alloy surfaces

After extensive calculation of different M@Cu alloy catalysts for CO_2 reduction, Fig. 4a summarizes the product grouping established using M-H and M-O affinity. These M@Cu catalysts are classified into 3 groups targeting different products. Specifically, the Ag, Zn, In and Sn doped M@Cu alloys with both weak M-H and M-O affinities are grouped together for their preferential formation of two electron transfer products (i.e. CO and HCOOH). The Co, Ni, Ru, Rh, Ir and Pt doped M@Cu alloys show potential toward C1 products with higher electron transfer numbers (e.g. CH_4 and CH_3OH); these alloy catalysts possess both strong M-H and M-O affinities. Meanwhile, the Pd and Au doped M@Cu surfaces with weak M-H but strong M-O affinities are classified as another group with potential toward C2 products. This calculated product grouping determined by the M-H and M-O affinity in the M@Cu alloys is

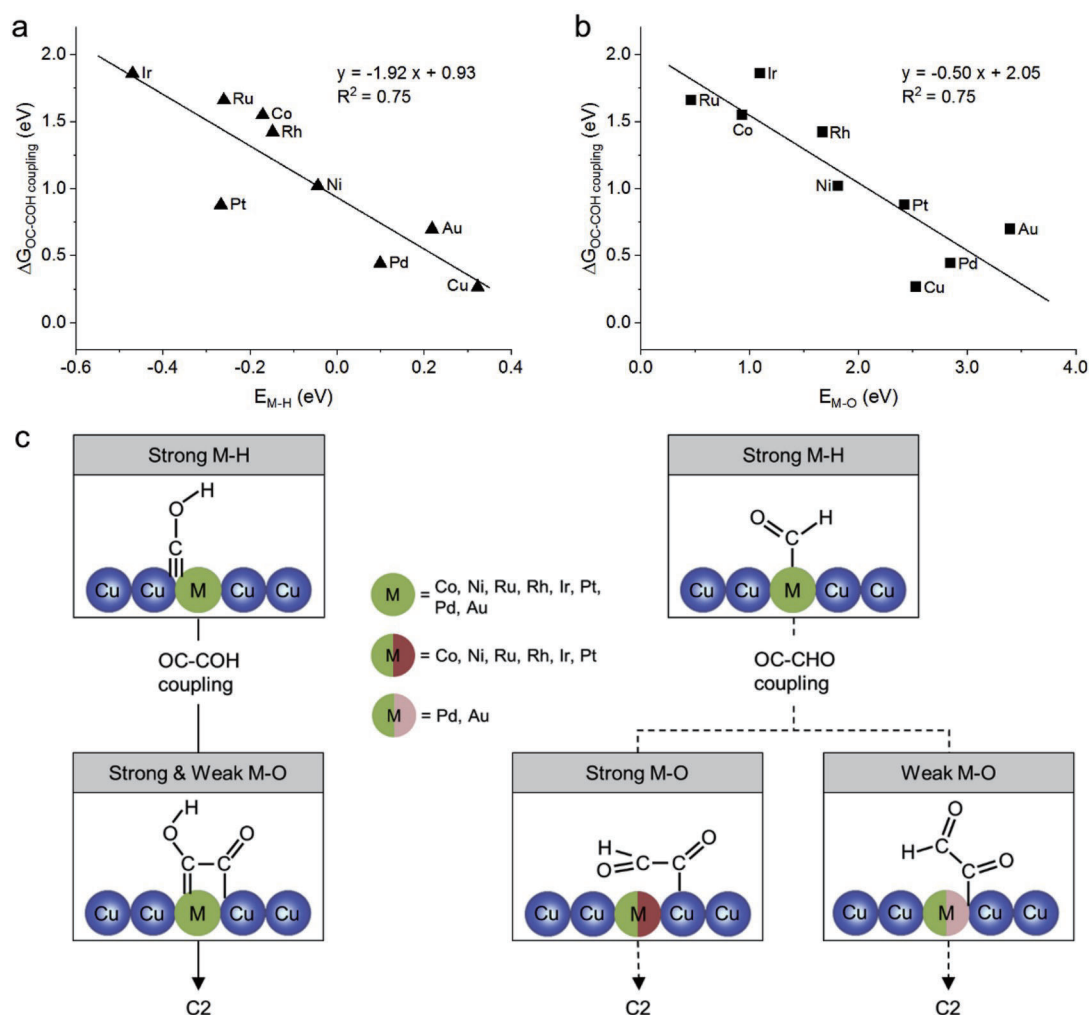


Fig. 3. Relationship of the free energy changes of OC-COH coupling on M@Cu alloy surfaces with (a) M-H and (b) M-O affinity, respectively. (c) Summary of the optimized configurations of *COCOHO and *COCHO intermediates and selectivity preference to C2 products based on different M-H and M-O affinities of the M@Cu catalysts. Dashed arrows have the same meaning as Fig. 1.

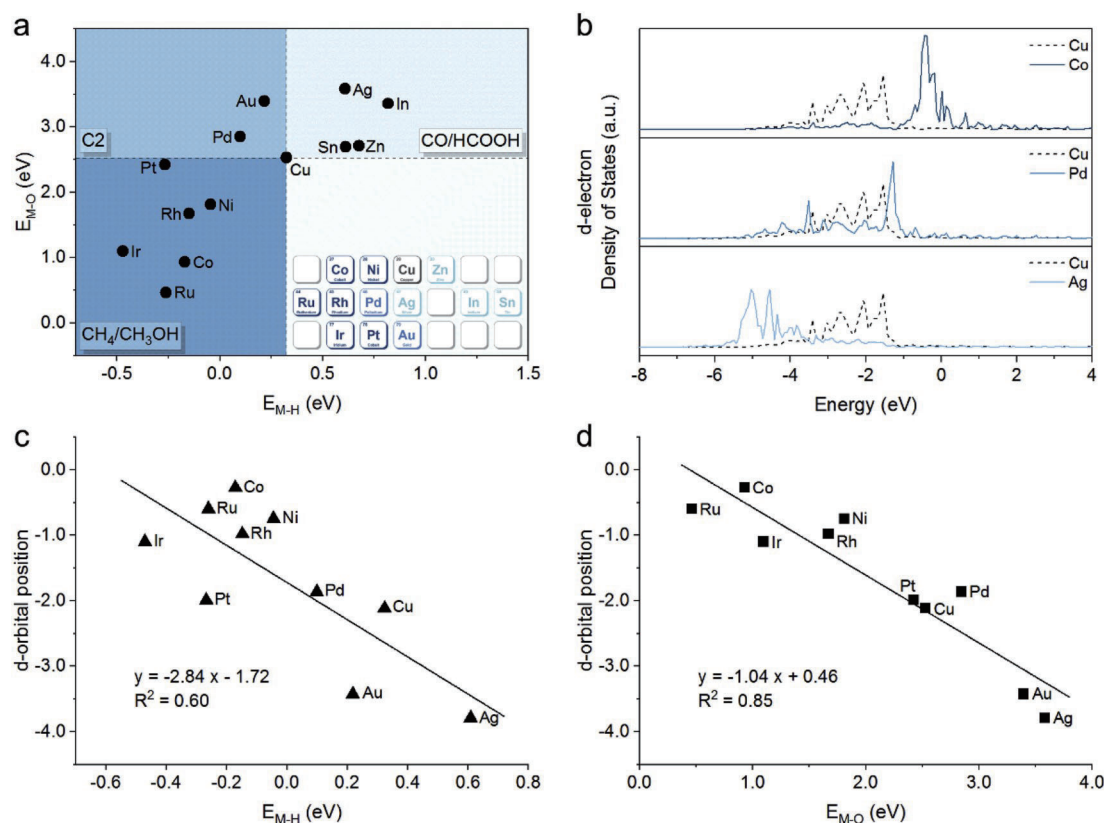


Fig. 4. (a) Product grouping of the M@Cu catalysts according to their M-H and M-O affinities. The inset shows the investigated metal elements on the periodic table. (b) d-electron Density of States (DOS) for M atoms in Co, Pd, and Ag doped M@Cu alloys. Relationship between the d-band centre of d-block M atoms with their (c) M-H affinity and (d) M-O affinity, respectively.

in good accordance with previously reported CRR selectivity trends in Cu-based bimetallic materials [9]. For example, Cu–In and Cu–Sn bimetallic electrocatalysts showed high selectivity toward two electron transfer products [11–13,52]. Cu–Pt nanocrystals with controlled Cu/Pt atomic ratios exhibited high faradic efficiency for CH_4 [14]. In addition, Cu–Pd and Cu–Au alloy catalysts performed appreciable selectivity for C_2 products [15–17]. Therefore, utilization of H and O affinities as descriptors provides a feasible route to address issues with CRR selectivity by influencing the adsorption geometry and strength of reaction intermediates. It should be noted that the doped metal atoms in our studied M@Cu alloys exhibit differing H- and O-affinities compared to their corresponding bulk forms (Table S5). Therefore, a comprehensive selectivity trend is established for directing effective design strategies of selective CRR catalysts.

The underlying reason of the different M-H and M-O affinities in M@Cu alloys is possibly explained by density of states (DOS) analysis. Fig. 4b shows varying d-electron density of states of the M atoms in three representative M@Cu alloys from different product groups. The d-orbital position is considered to play a significant role in determining the adsorption strength of key reaction intermediates. The d-band positions of d-block M atoms show a linear relationship with M-H and M-O affinity in M@Cu alloys respectively in Fig. 4c and d. A higher d-band position generally results in stronger M-H and M-O affinities. Therefore, the M-H and M-O affinities in M@Cu alloys are suggested to be influenced by electronic structures.

3. Conclusion

In summary, we conducted extensive DFT calculations for the electrochemical CO_2 reduction using M@Cu (M = Co, Ni, Ru, Rh, Ir, Pt, Pd, Au, Ag, Zn, In, Sn) alloy surfaces as catalysts to investigate their product

selectivity trends. Through thermodynamic analysis of various key reaction intermediates, the M-H and M-O affinities in M@Cu alloys are found to be useful descriptors in determining CRR selectivity. Therefore, practical catalyst design strategies can be developed using the concept of H and O affinities of the secondary metal in alloy catalysts. The observed product distribution for M@Cu alloys matches well with previously reported CRR product selectivity trends for Cu-based bimetallic electrocatalysts. It also provides further mechanistic insights into the selectivity roadmap for a wider range of Cu-based alloys. Our findings suggest that the intrinsic properties of the catalysts can effectively describe their products selectivity. This descriptor-based approach to explore selectivity trend could also be extended to other CRR electrocatalysts, like alloys with interfacial sites, single atom catalysts, nanoparticles, and hybrid materials.

Declaration of competing interest

The authors declare no conflict of interest.

Acknowledgements

The authors acknowledge financial support by the Australian Research Council (DP160104866, DP170104464, DP190103472, DE160101163, and FL170100154) and the University of Adelaide Fellowship. DFT computations within this work were undertaken with the assistance of resources and services from the National Computational Infrastructure (NCI) supported by the Australian Government, as well as the Phoenix High Performance Compute (HPC) Service at the University of Adelaide.

Appendix A. Supplementary data

Supplementary data to this article can be found online at <https://doi.org/10.1016/j.nanoen.2020.104601>.

References

- [1] D.T. Whipple, P.J.A. Kenis, *J. Phys. Chem. Lett.* 1 (2010) 3451–3458.
- [2] M. Gattrell, N. Gupta, A. Co, *J. Electroanal. Chem.* 594 (2006) 1–19.
- [3] N.S. Lewis, *Science* 351 (2016) aad1920.
- [4] Q. Lu, F. Jiao, *Nano Energy* 29 (2016) 439–456.
- [5] C.F. Shih, T. Zhang, J. Li, C. Bai, *Joule* 2 (2018) 1925–1949.
- [6] Y. Hori, H. Wakebe, T. Tsukamoto, O. Koga, *Electrochim. Acta* 39 (1994) 1833–1839.
- [7] A. Bagger, W. Ju, A.S. Varela, P. Strasser, J. Rossmeisl, *ChemPhysChem* 18 (2017) 3266–3273.
- [8] A.A. Peterson, J.K. Nørskov, *J. Phys. Chem. Lett.* 3 (2012) 251–258.
- [9] A. Vasileff, C. Xu, Y. Jiao, Y. Zheng, S.Z. Qiao, *Chem* 4 (2018) 1809–1831.
- [10] C.W. Lee, K.D. Yang, D.H. Nam, J.H. Jang, N.H. Cho, S.W. Im, K.T. Nam, *Adv. Mater.* 30 (2018) 1704717.
- [11] S. Rasul, D.H. Anjum, A. Jedidi, Y. Minenkov, L. Cavallo, K. Takanebe, *Angew. Chem. Int. Ed.* 54 (2015) 2146–2150.
- [12] S. Sarfraz, A.T. Garcia-Esparza, A. Jedidi, L. Cavallo, K. Takanebe, *ACS Catal.* 6 (2016) 2842–2851.
- [13] A. Vasileff, C.C. Xu, L. Ge, Y. Zheng, S.Z. Qiao, *Chem. Commun.* 54 (2018) 13965–13968.
- [14] X. Guo, Y.X. Zhang, C. Deng, X.Y. Li, Y.F. Xue, Y.M. Yan, K.N. Sun, *Chem. Commun.* 51 (2015) 1345–1348.
- [15] S. Ma, M. Sadakiyo, M. Heima, R. Luo, R.T. Haasch, J.I. Gold, M. Yamauchi, P.J. A. Kenis, *J. Am. Chem. Soc.* 139 (2017) 47–50.
- [16] F. Jia, X. Yu, L. Zhang, *J. Power Sources* 252 (2014) 85–89.
- [17] J. Monzó, Y. Malewski, R. Kortlever, F.J. Vidal-Iglesias, J. Solla-Gullón, M.T. M. Koper, P. Rodriguez, *J. Mater. Chem. A* 3 (2015) 23690–23698.
- [18] J.T. Feaster, C. Shi, E.R. Cave, T. Hatsukade, D.N. Abram, K.P. Kuhl, C. Hahn, J. K. Nørskov, T.F. Jaramillo, *ACS Catal.* 7 (2017) 4822–4827.
- [19] J.S. Yoo, R. Christensen, T. Vegge, J.K. Nørskov, F. Studt, *ChemSusChem* 9 (2016) 358–363.
- [20] X.W. Nie, M.R. Esopi, M.J. Janik, A. Asthagiri, *Angew. Chem. Int. Ed.* 52 (2013) 2459–2462.
- [21] A.A. Peterson, F. Abild-Pedersen, F. Studt, J. Rossmeisl, J.K. Nørskov, *Energy Environ. Sci.* 3 (2010) 1311–1315.
- [22] X. Liu, J. Xiao, H. Peng, X. Hong, K. Chan, J.K. Nørskov, *Nat. Commun.* 8 (2017) 15438.
- [23] F. Calle-Vallejo, M.T.M. Koper, *ACS Catal.* 7 (2017) 7346–7351.
- [24] J. Hussain, H. Jónsson, E. Skúlason, *ACS Catal.* 8 (2018) 5240–5249.
- [25] F. Calle-Vallejo, M.T.M. Koper, *Angew. Chem. Int. Ed.* 52 (2013) 7282–7285.
- [26] J.H. Montoya, C. Shi, K. Chan, J.K. Nørskov, *J. Phys. Chem. Lett.* 6 (2015) 2032–2037.
- [27] J.H. Montoya, A.A. Peterson, J.K. Nørskov, *ChemCatChem* 5 (2013) 737–742.
- [28] A.J. Garza, A.T. Bell, M. Head-Gordon, *ACS Catal.* 8 (2018) 1490–1499.
- [29] X. Liu, P. Schlexer, J. Xiao, Y. Ji, L. Wang, R.B. Sandberg, M. Tang, K.S. Brown, H. Peng, S. Ringe, C. Hahn, T.F. Jaramillo, J.K. Nørskov, K. Chan, *Nat. Commun.* 10 (2019) 32.
- [30] A. Bagger, W. Ju, A.S. Varela, P. Strasser, J. Rossmeisl, *ACS Catal.* 9 (2019) 7894–7899.
- [31] Y. Hori, A. Murata, R. Takahashi, *J. Chem. Soc., Faraday Trans. 1* 85 (1989) 2309–2326.
- [32] K.J.P. Schouten, E. Pérez Gallent, M.T.M. Koper, *J. Electroanal. Chem.* 716 (2014) 53–57.
- [33] H. Xiao, T. Cheng, W.A. Goddard, R. Sundararaman, *J. Am. Chem. Soc.* 138 (2016) 483–486.
- [34] J.D. Goodpaster, A.T. Bell, M. Head-Gordon, *J. Phys. Chem. Lett.* 7 (2016) 1471–1477.
- [35] T. Cheng, H. Xiao, W.A. Goddard, *Proc. Natl. Acad. Sci. U. S. A.* 114 (2017) 1795–1800.
- [36] Y. Zheng, A. Vasileff, X. Zhou, Y. Jiao, M. Jaroniec, S.Z. Qiao, *J. Am. Chem. Soc.* 141 (2019) 7646–7659.
- [37] J.K. Nørskov, F. Abild-Pedersen, F. Studt, T. Bligaard, *Proc. Natl. Acad. Sci. U. S. A.* 108 (2011) 937–943.
- [38] J. Greeley, T.F. Jaramillo, J. Bonde, I.B. Chorkendorff, J.K. Nørskov, *Nat. Mater.* 5 (2006) 909–913.
- [39] K.P. Kuhl, T. Hatsukade, E.R. Cave, D.N. Abram, J. Kibsgaard, T.F. Jaramillo, *J. Am. Chem. Soc.* 136 (2014) 14107–14113.
- [40] M.J. Cheng, E.L. Clark, H.H. Pham, A.T. Bell, M. Head-Gordon, *ACS Catal.* 6 (2016) 7769–7777.
- [41] K. Sun, T. Cheng, L.N. Wu, Y.F. Hu, J.G. Zhou, A. MacLennan, Z.H. Jiang, Y.Z. Gao, W.A. Goddard, Z.J. Wang, *J. Am. Chem. Soc.* 139 (2017) 15608–15611.
- [42] S. Zhu, Q. Wang, X. Qin, M. Gu, R. Tao, B.P. Lee, L. Zhang, Y. Yao, T. Li, M. Shao, *Adv. Energy Mater.* 8 (2018) 1802238.
- [43] W.J. Durand, A.A. Peterson, F. Studt, F. Abild-Pedersen, J.K. Nørskov, *Surf. Sci.* 605 (2011) 1354–1359.
- [44] A. Murata, Y. Hori, *Bull. Chem. Soc. Jpn.* 64 (1991) 123–127.
- [45] J. Resasco, L.D. Chen, E. Clark, C. Tsai, C. Hahn, T.F. Jaramillo, K. Chan, A.T. Bell, *J. Am. Chem. Soc.* 139 (2017) 11277–11287.
- [46] A.S. Varela, W. Ju, T. Reier, P. Strasser, *ACS Catal.* 6 (2016) 2136–2144.
- [47] Y. Huang, C.W. Ong, B.S. Yeo, *ChemSusChem* 11 (2018) 3299–3306.
- [48] X. Zhi, Y. Jiao, Y. Zheng, S.Z. Qiao, *Small* 15 (2019) 1804224.
- [49] C. Shi, H.A. Hansen, A.C. Lausche, J.K. Nørskov, *Phys. Chem. Chem. Phys.* 16 (2014) 4720–4727.
- [50] P. Hirunsit, W. Soodsawang, J. Limtrakul, *J. Phys. Chem. C* 119 (2015) 8238–8249.
- [51] A. Vasileff, Y. Zheng, S.Z. Qiao, *Adv. Energy Mater.* 7 (2017) 1700759.
- [52] A. Vasileff, X. Zhi, C. Xu, L. Ge, Y. Jiao, Y. Zheng, S.Z. Qiao, *ACS Catal.* 9 (2019) 9411–9417.



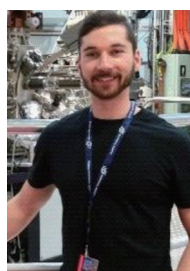
Xing Zhi received her BE degree in Pharmaceutical Engineering from Central South University in 2013 and ME degree in Biochemical Engineering from Tianjin University in 2016, respectively. She is currently a Ph. D. candidate in School of Chemical Engineering and Advanced Materials under the supervision of Prof. Shi-Zhang Qiao at The University of Adelaide. Her current research focuses on computational studies of catalyst materials for electrochemical CO₂ reduction reaction.



Yan Jiao received her PhD degree in 2012 from the University of Queensland, Australia. She is currently a Senior Lecturer in the University of Adelaide working with Professor Shi-Zhang Qiao. Her current research focuses on design of catalyst materials for clean energy conversion reactions by computer simulation and development of computational electrochemistry theory.



Yao Zheng received his PhD degree in 2014 from the University of Queensland, Australia. Currently he is a Senior Research Fellow in the University of Adelaide working with Professor Shi-Zhang Qiao. His current research focuses on fundamental studies of some key electrocatalysis processes by combining experiments and theoretical computations, and development of advanced electrocatalysts for energy conversion processes like hydrogen evolution reaction, CO₂ reduction reaction, and nitrogen reduction reaction at ambient conditions.



Anthony Vasileff received his Bachelors in Chemical Engineering at the University of Adelaide in 2014. He is currently a Ph.D. candidate under the supervision of Prof. Shi-Zhang Qiao in the School of Chemical Engineering and Advanced Materials at the University of Adelaide. His current research involves mechanistic studies to determine factors affecting product selectivity for electrochemical CO₂ reduction on a range of catalyst materials.



Shi-Zhang Qiao received his PhD degree in Chemical Engineering from the Hong Kong University of Science and Technology in 2000, and is currently a Chair Professor and ARC Lureate Fellow at the School of Chemical Engineering and Advanced Materials of the University of Adelaide, Australia. His research interests include synthesis and characterisation of nanomaterials as well as their applications in catalysis, energy storage and conversion (fuel cell, batteries, electrocatalysis and photocatalysis).

Supporting Information

Selectivity Roadmap for Electrochemical CO₂ Reduction on Copper-Based Alloy Catalysts

Xing Zhi, Yan Jiao,^{*} Yao Zheng, Anthony Vasileff, Shi-Zhang Qiao^{*}

Centre for Materials in Energy and Catalysis

School of Chemical Engineering and Advanced Materials

The University of Adelaide

Adelaide, South Australia 5005, Australia

^{*} Correspondence: s.qiao@adelaide.edu.au; yan.jiao@adelaide.edu.au

Computational Parameters and Models.

All calculations were performed using density functional theory (DFT) method. The Perdew-Burke-Ernzerhof (PBE) functional of the generalized gradient approximation (GGA) was employed for electron exchange-correlation, as implemented in the Vienna Ab initio Simulation Package (VASP).[1-3] The ionic cores were described by the projector-augmented wave (PAW) method. A plane-wave cutoff energy was set to 550 eV. During geometry optimization, the structures were relaxed to a force on the atoms smaller than 0.01 eV Å⁻¹. A 0.18 eV width of the smearing and (4 × 4 × 1) Gamma k-point grid were applied. The Tkatchenko-Scheffler method was adopted in all calculations to address van der Waals (vdW) interactions between atoms.

The Cu (111) surface was modeled with a three-layered slab of a (3 × 3) supercell with 15 Å of vacuum space. The M@Cu single atom alloy models were built by substituting one Cu surface atom with one dopant metal atom M (M = Co, Ni, Ru, Rh, Ir, Pt, Pd, Au, Ag, Zn, In, Sn), respectively. The optimized configurations of Cu and M@Cu structures are shown in Figure S2. Adsorption of reaction intermediates on the Cu and M@Cu surfaces was calculated with the bottom two layers fixed and the top layer relaxed. The adhesion energy of the dopant metal atom M was calculated as

$$E_{\text{ad}} = E_{\text{M@Cu}} - E_{\text{Cu-v}} - E_{\text{M}}$$

where $E_{\text{M@Cu}}$ is the energy of M@Cu surface, $E_{\text{Cu-v}}$ is the energy of Cu (111) surface with one Cu surface atom vacancy, and E_{M} is the energy of M atom (Table S2).

Free Energy Calculation.

The free energies of the reaction intermediates were calculated according to $G = E + \text{ZPE} - \text{TS}$. The zero point energy (ZPE) and entropy correction (TS) were calculated from vibration analysis by standard methods and used to convert electronic energies (E) into free energies (G) at 298.15 K (Table S3). The vibrational frequencies were computed by treating all 3N degrees of the adsorbates as vibrational within the harmonic oscillator approximation, and assuming that any changes in the vibrations of the M@Cu surfaces were minimal, in concert with earlier studies.[4, 5] The free energies of molecules were also obtained by standard methods (Table S4). The gaseous species, CO₂ and CO, were calculated at 101,325 Pa, while H₂O and HCOOH were treated with pressure correction at a fugacity of 3534 Pa and 19 Pa respectively, corresponding to the vapour pressure of water and 1M HCOOH.[6] The solvation effects were considered approximately the same as previous studies: *COOH and other related intermediates were stabilized by 0.25 eV and 0.10 eV, respectively.[5, 6] The effect of ions were not included. The free energies of CO₂, CO and HCOOH were compensated with 0.32 eV, -0.17 eV and 0.19 eV respectively to match the experimental values.

To include the effect of electrode potential, the computational hydrogen electrode (CHE) model was used to treat the free energy change of each state involving a proton-electron pair transfer as a function of the applied electrical potential.[7, 8] In this model, the free energy of a proton-electron pair at 0 V vs RHE is by definition equal to half of the free energy of gaseous hydrogen at 101,325 Pa. The application of the CHE model provides a method to predict the electrode potential at which all elementary steps in a certain CO₂ reduction pathway become exergonic. This potential is referred to as the limiting potential and used to decide the potential-dependent reaction step. In this study, the relative free energies of intermediates were taken to indicate the starting point of different CO₂ electroreduction pathways, and reaction barriers were not calculated. The barriers for proton transfers to adsorbates are normally small enough to be surmountable at room temperature as reported in previous publications.[9]

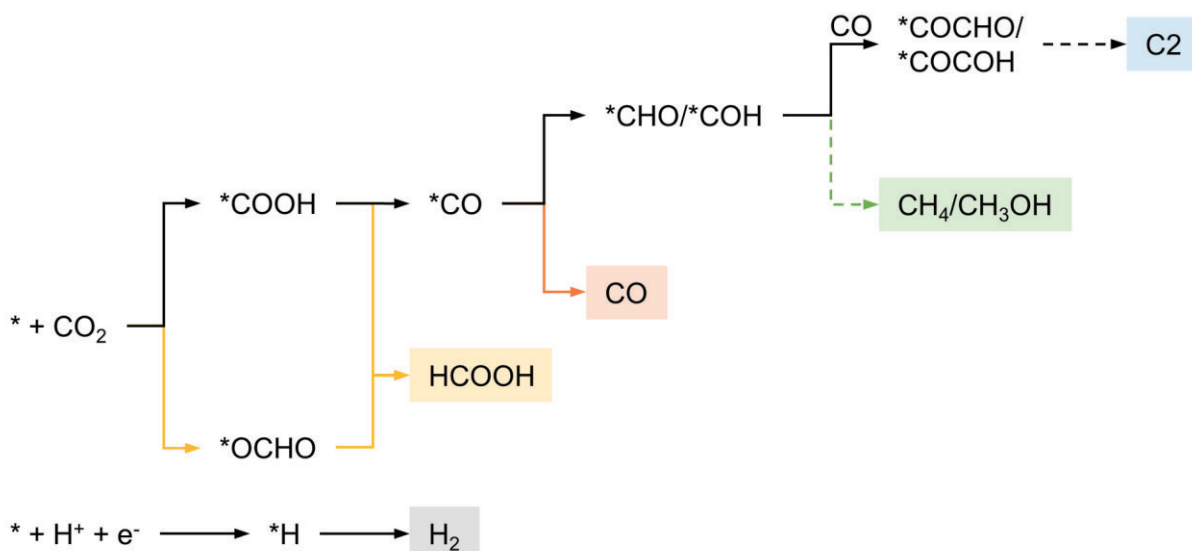


Figure S1. Reaction pathways to various products through key intermediates in this study. Dashed arrows indicate multiple proton/electron transfer steps.

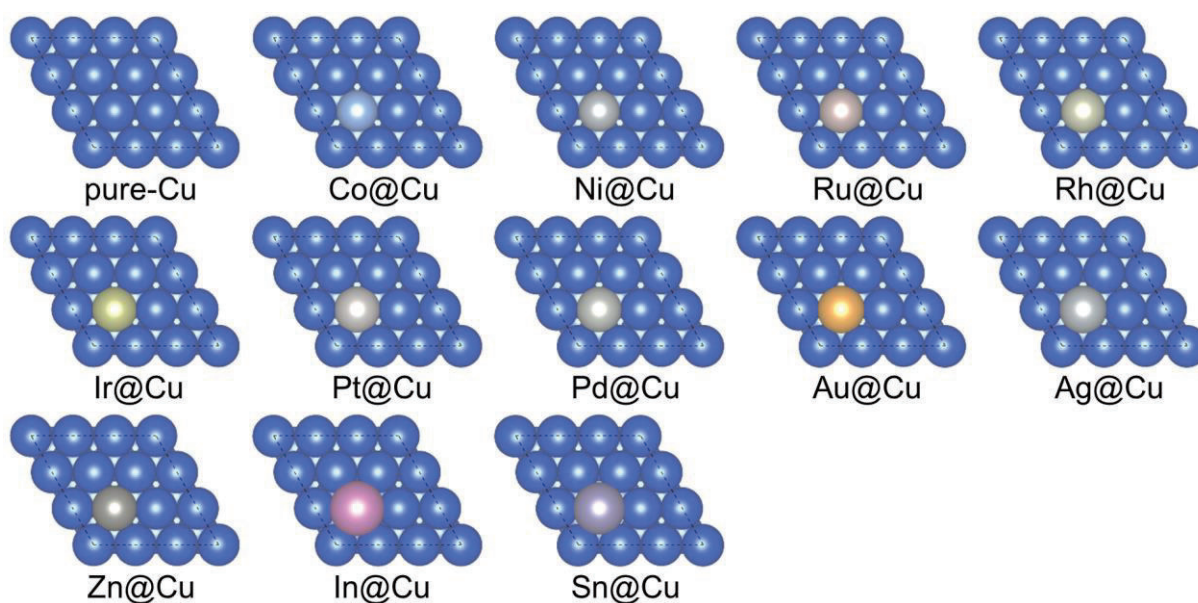


Figure S2. The optimized configurations of the M@Cu alloy surfaces and the pure Cu surface. Copper atoms are blue and other metal atoms are labelled for each structure.

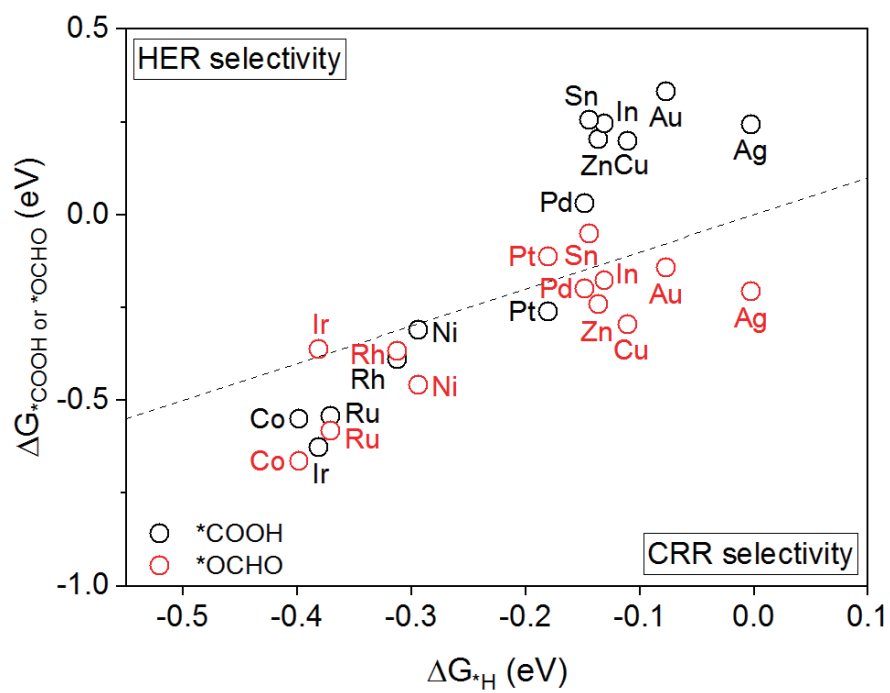


Figure S3. Selectivity analysis between the hydrogen evolution reaction and CO₂ reduction reaction based on the free energy changes of the first hydrogenation intermediates.

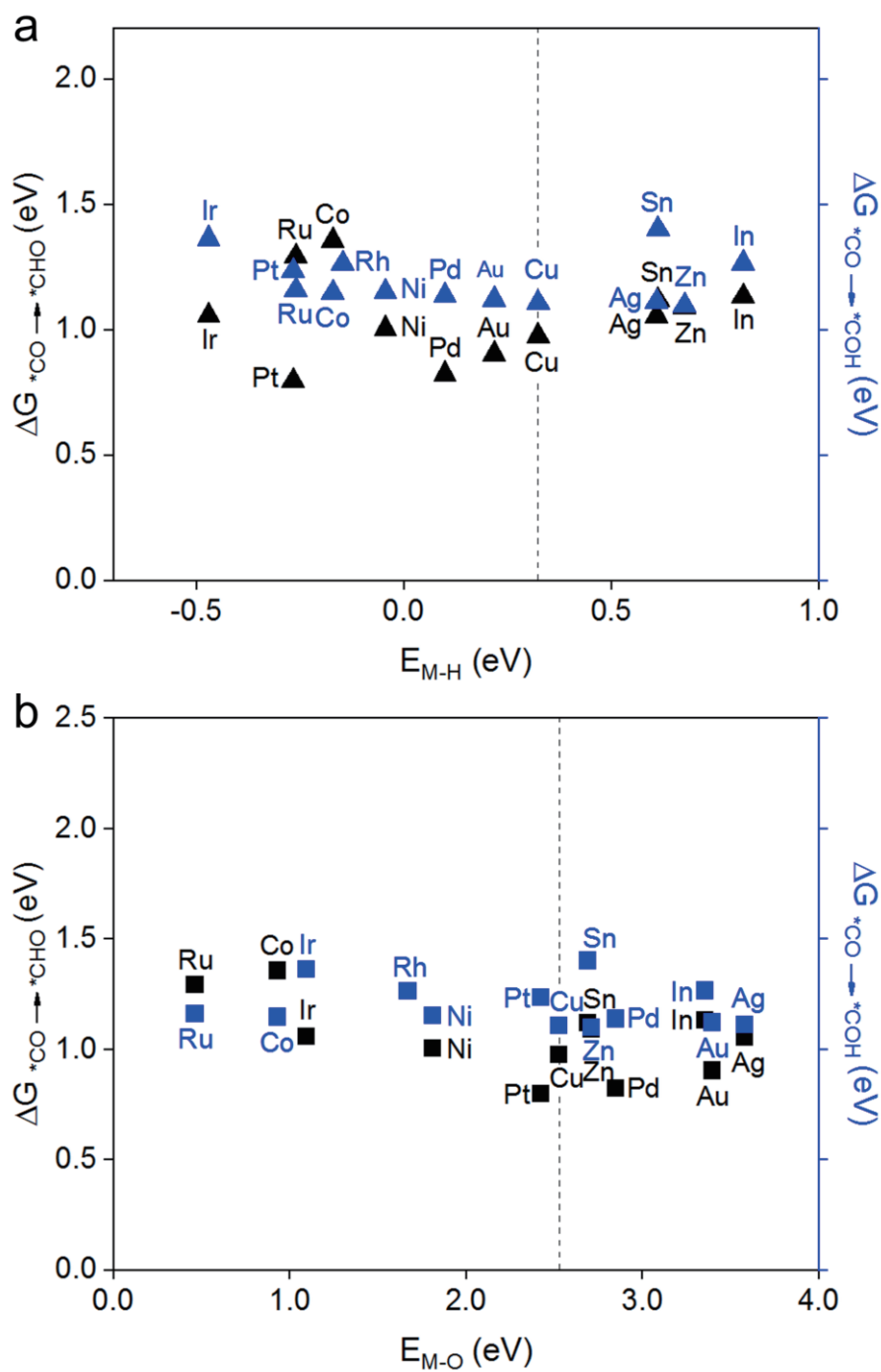


Figure S4. The free energy changes of $*CO$ protonation to $*CHO$ and $*COH$ on $M@Cu$ alloy surfaces plotted against (a) M-H affinity and (b) M-O affinity, respectively. The ΔG value of $*CO$ protonation to $*CHO$ on $Rh@Cu$ is missing due to geometric instability of $*CHO$ on $Rh@Cu$.

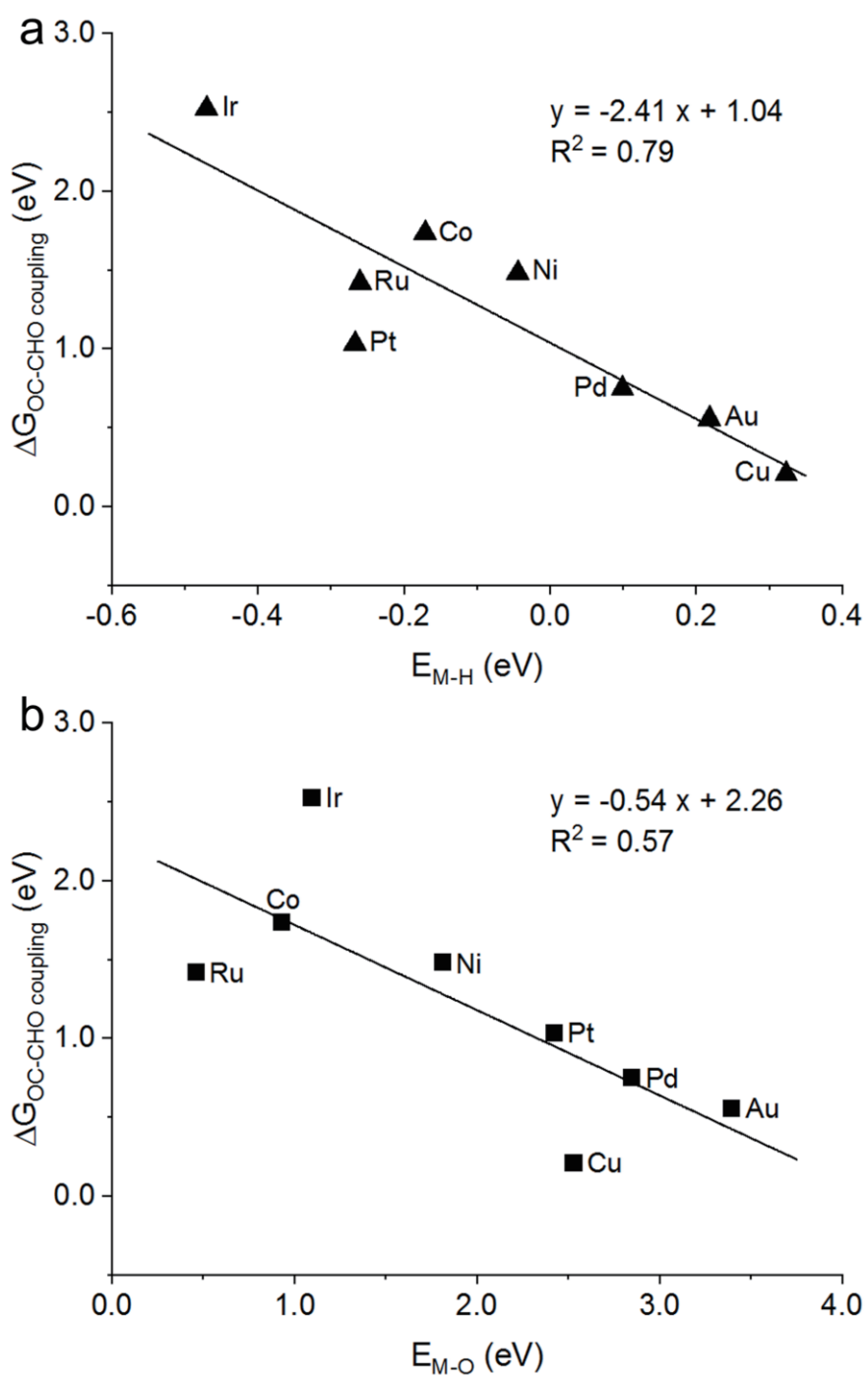
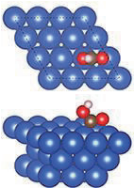
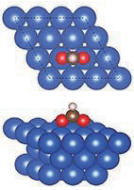
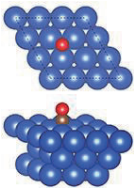
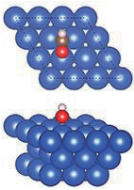
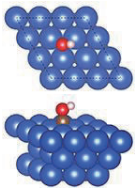
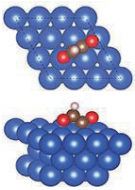
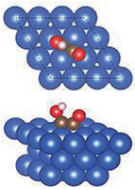
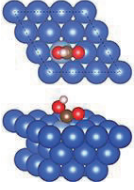
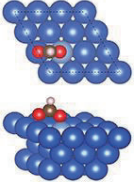
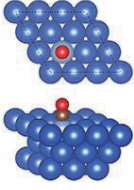
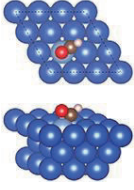
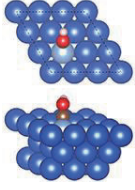
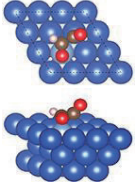
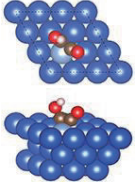
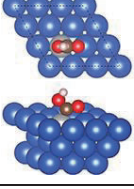
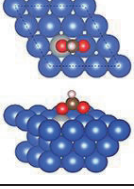
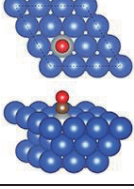
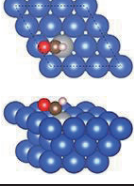
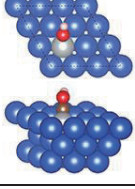
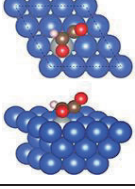
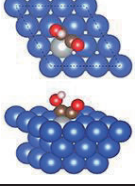
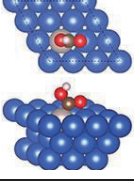
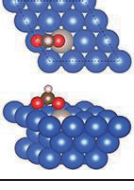
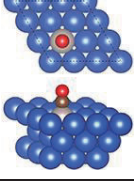
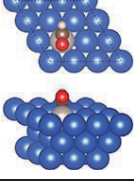
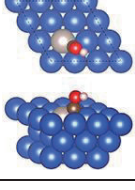
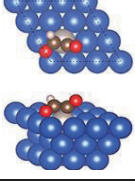
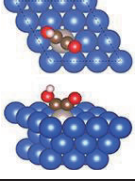
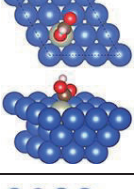
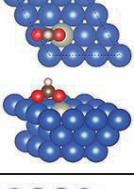
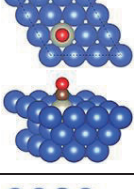
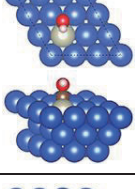
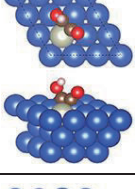
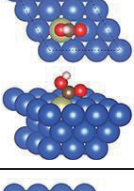
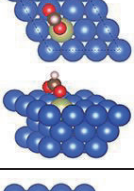
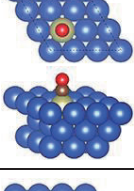
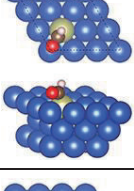
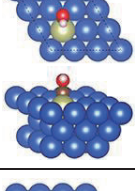
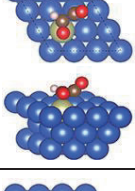
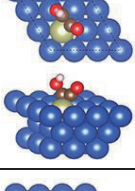
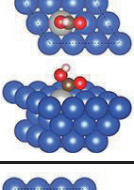
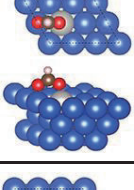
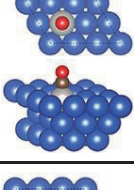
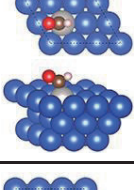
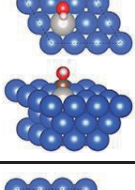
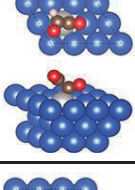
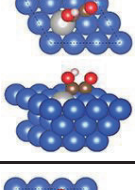
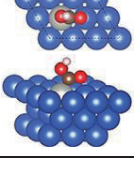
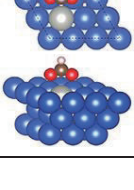
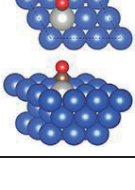
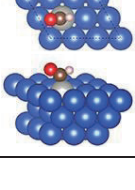
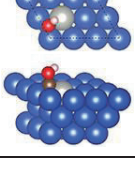
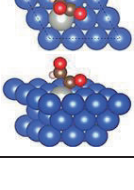
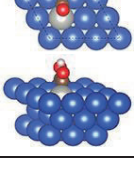
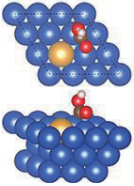
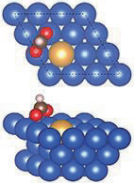
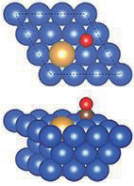
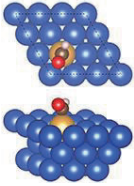
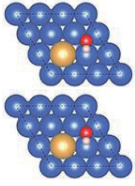
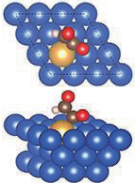
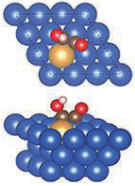
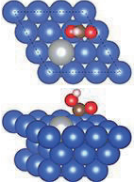
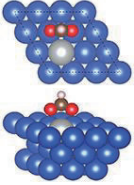
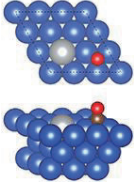
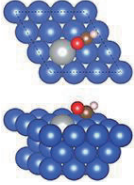
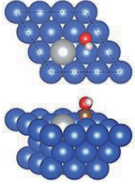
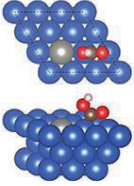
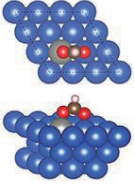
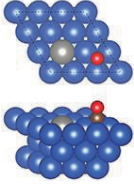
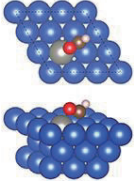
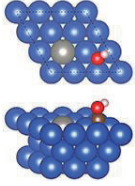
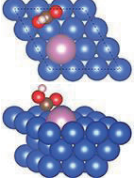
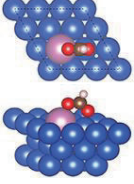
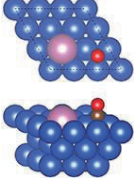
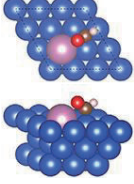
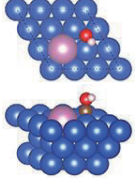
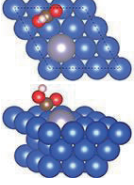
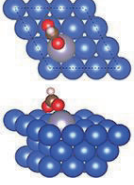
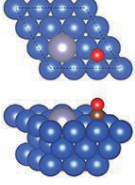
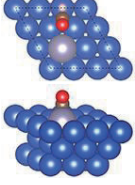
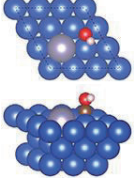


Figure S5. Relationship of the free energy changes of OC-CHO coupling on M@Cu alloy surfaces with (a) M-H affinity and (b) M-O affinity, respectively. The ΔG value of OC-CHO coupling on Rh@Cu is missing due to geometric instability of *CHO on Rh@Cu.

Table S1. Summary of optimized configurations of key reaction intermediates in this study.

	*COOH	*OCHO	*CO	*CHO	*COH	*COCHO	*COCO
Cu							
Co@Cu							
Ni@Cu							
Ru@Cu							
Rh@Cu				<i>a</i>		<i>b</i>	
Ir@Cu							
Pt@Cu							
Pd@Cu							

Au@Cu							
Ag@Cu						<i>c</i>	<i>c</i>
Zn@Cu						<i>c</i>	<i>c</i>
In@Cu						<i>c</i>	<i>c</i>
Sn@Cu						<i>c</i>	<i>c</i>

^{a,b} The optimized configuration is missing due to geometric instability of *CHO on Rh@Cu alloy surface.

^c The optimized configurations are missing because the Ag, Zn, In, and Sn doped M@Cu alloy surfaces prefer to yield 2e- products. Therefore, the C2 reaction intermediates are not included for these catalyst models.

Table S2. The adhesion energy (in eV) of metal atom M on Cu (111) surface.

M@Cu	E_{ad}
Co@Cu	0.179
Ni@Cu	-0.438
Ru@Cu	0.591
Rh@Cu	-0.607
Ir@Cu	-0.409
Pt@Cu	-1.472
Pd@Cu	-1.303
Au@Cu	-1.394
Ag@Cu	-0.853
Zn@Cu	-1.477
In@Cu	-1.857
Sn@Cu	-2.189

Table S3. Corresponding thermodynamic energy corrections (in eV) for intermediates.

Adsorbate	ZPE	-TS
*COOH	0.604	-0.223
*OCHO	0.616	-0.219
*CO	0.181	-0.132
*CHO	0.439	-0.166
*COH	0.464	-0.161
*H	0.175	-0.005
*O	0.065	-0.057

Table S4. Corresponding thermodynamic energy corrections (in eV) for molecules.

Gas molecule	ZPE	-TS
H ₂	0.269	-0.402
CO	0.132	-0.610
CO ₂	0.307	-0.662
H ₂ O	0.571	-0.536
HCOOH	0.890	-0.502

Table S5. H and O affinities of metals in their bulk form and as embedded single atoms in the Cu(111) surface.

Metal elements	In bulk		In Cu(111) surface	
	E_{M-H} (eV) ^a	$D_{O(M)}$ (eV) ^b	E_{M-H} (eV)	E_{M-O} (eV)
Cu	1.88	2.97	0.32	2.53
Co	2.01(strong)	4.11(strong)	-0.17(strong)	0.93(strong)
Ni	2.05(strong)	3.79(strong)	-0.05(strong)	1.81(strong)
Ru	(strong)	5.47(strong)	-0.26(strong)	0.47(strong)
Rh	2.59(strong)	4.20(strong)	-0.15(strong)	1.67(strong)
Ir	2.61(strong)	4.29(strong)	-0.47(strong)	1.10(strong)
Pt	2.59(strong)	4.34(strong)	-0.27(strong)	2.42(strong)
Pd	(strong)	2.47(weak)	0.10(strong)	2.85(weak)
Au	1.97(weak)	2.31(weak)	0.22(strong)	3.40(weak)
Ag	1.67(weak)	2.29(weak)	0.61(weak)	3.58(weak)
Zn	1.42(weak)	2.59(weak)	0.68(weak)	2.71(weak)
In	1.34(weak)	3.59(strong)	0.82(weak)	3.36(weak)
Sn	1.42(weak)	5.47(strong)	0.61(weak)	2.69(weak)

^a E_{M-H} values are measured from Figure 3, Trasatti, S.[10] The values for Ru and Pd are missing in the reference. Therefore we use the M-H bond strength values from [Comprehensive Handbook of Chemical Bond Energies, CRC Press, Boca Raton, FL, 2007] to decide the relative hydrogen adsorption strength on these metals.

^b $D_{O(M)}$ is the dissociation enthalpy of metal oxides. The original values are presented in kJ/mol and converted to eV here.[11]

Reference

- [1] G. Kresse, J. Furthmuller, *Phys. Rev. B: Condens. Matter Mater. Phys.*, 54 (1996) 11169-11186.
- [2] G. Kresse, D. Joubert, *Phys. Rev. B: Condens. Matter Mater. Phys.*, 59 (1999) 1758-1775.
- [3] J.P. Perdew, K. Burke, M. Ernzerhof, *Phys. Rev. Lett.*, 77 (1996) 3865-3868.
- [4] G. Jones, J.G. Jakobsen, S.S. Shim, J. Kleis, M.P. Andersson, J. Rossmeisl, F. Abild-Pedersen, T. Bligaard, S. Helveg, B. Hinnemann, J.R. Rostrup-Nielsen, I. Chorkendorff, J. Sehested, J.K. Nørskov, *J. Catal.*, 259 (2008) 147-160.
- [5] A.A. Peterson, F. Abild-Pedersen, F. Studt, J. Rossmeisl, J.K. Nørskov, *Energy Environ. Sci.*, 3 (2010) 1311-1315.
- [6] W.J. Durand, A.A. Peterson, F. Studt, F. Abild-Pedersen, J.K. Nørskov, *Surf. Sci.*, 605 (2011) 1354-1359.
- [7] J.K. Nørskov, J. Rossmeisl, A. Logadottir, L. Lindqvist, J.R. Kitchin, T. Bligaard, H. Jonsson, *J. Phys. Chem. B*, 108 (2004) 17886-17892.
- [8] Y. Jiao, Y. Zheng, M. Jaroniec, S.Z. Qiao, *J. Am. Chem. Soc.*, 136 (2014) 4394-4403.
- [9] C. Shi, K. Chan, J.S. Yoo, J.K. Nørskov, *Org. Process Res. Dev.*, 20 (2016) 1424-1430.
- [10] S. Trasatti, *J. Electroanal. Chem.*, 39 (1972) 163-184.
- [11] K.P. Kepp, *Inorg. Chem.*, 55 (2016) 9461-9470.

Chapter 5: Kinetic Insights into Selective C-C Coupling for Electrochemical CO₂ Reduction on Copper Alloy Surfaces

5.1 Introduction and Significance

In the electrochemical CO₂ reduction reaction (CRR), the C-C coupling is an essential step for producing multi-carbon products, yet shows large kinetic barriers. Despite the advances of CO dimerization mechanism, the mechanistic elucidation for OC-COH and OC-CHO coupling is far from settled. Hence, greater understanding of C-C coupling reaction kinetics is required to permit the efficient conversion of CO₂ toward C₂₍₊₎ products.

In this Chapter, a kinetic investigation of C-C coupling between *CO and *COH/*CHO on Cu alloy surfaces (M@Cu, M = Pt, Pd, Au) was conducted using DFT computations. The reaction kinetics and thermodynamics for OC-COH and OC-CHO coupling steps were evaluated on Cu and M@Cu surfaces. Based on the variation trend of activation barriers, we demonstrated the kinetic preference of OC-COH coupling compared to OC-CHO coupling among different C₂ pathways. Linear energy relations were observed describing correlations between activation barriers and reaction energies for C-C coupling and reverse C-C dissociation reactions. This provides a practical method for estimating variations of reaction kinetics from thermodynamic analysis and predicting favorable C-C coupling selectivity on a wider range of CRR electrocatalysts.

5.2 Kinetic insights into selective C-C coupling for electrochemical CO₂ reduction on copper alloy surfaces

This chapter is included as it appears as a journal paper in preparation for publication by Xing Zhi, Yan Jiao, Yao Zheng, Shi-Zhang Qiao, Kinetic insights into selective C-C coupling for electrochemical CO₂ reduction on copper alloy surfaces, **2021**, to be submitted.

Statement of Authorship

Title of Paper	Kinetic Insights into Selective C-C Coupling for Electrochemical CO ₂ Reduction on Copper Alloy Surfaces
Publication Status	<input type="checkbox"/> Published <input type="checkbox"/> Accepted for Publication <input type="checkbox"/> Submitted for Publication <input checked="" type="checkbox"/> Unpublished and Unsubmitted work written in manuscript style
Publication Details	Xing Zhi, Yan Jiao, Yao Zheng, Shi-Zhang Qiao, Kinetic insights into selective C-C coupling for electrochemical CO ₂ reduction on copper alloy surfaces, to be submitted .

Principal Author

Name of Principal Author (Candidate)	Xing Zhi		
Contribution to the Paper	Conducted all the computations, carried out data analysis and wrote the paper		
Overall percentage (%)	80%		
Certification:	This paper reports on original research I conducted during the period of my Higher Degree by Research candidature and is not subject to any obligations or contractual agreements with a third party that would constrain its inclusion in this thesis. I am the primary author of this paper.		
Signature		Date	14 Dec. 2020

Co-Author Contributions

By signing the Statement of Authorship, each author certifies that:

- i. the candidate's stated contribution to the publication is accurate (as detailed above);
- ii. permission is granted for the candidate to include the publication in the thesis; and
- iii. the sum of all co-author contributions is equal to 100% less the candidate's stated contribution.

Name of Co-Author	Yan Jiao		
Contribution to the Paper	Discussed computational results and findings, supervised the project, and revised the paper.		
Signature		Date	14 Dec. 2020

Name of Co-Author	Yao Zheng		
Contribution to the Paper	Discussed the research plan, supervised the project, and revised the paper.		
Signature		Date	14 Dec. 2020

Name of Co-Author	Shi-Zhang Qiao		
Contribution to the Paper	Discussed the research plan, supervised the project, and revised the paper.		
Signature		Date	16 Dec. 2020

COMMUNICATION

Kinetic Insights into Selective C-C Coupling for Electrochemical CO₂ Reduction on Copper Alloy Surfaces

Received 00th January 20xx,
Accepted 00th January 20xx

Xing Zhi,^a Yan Jiao,^{*a} Yao Zheng^a and Shi-Zhang Qiao^{*a}

DOI: 10.1039/x0xx00000x

In electrochemical CO₂ reduction reaction, the C-C coupling process is a key elementary step for producing multi-carbon products but suffers from high activation barriers. Therefore, optimizing the energetics of C-C coupling is crucial for efficient conversion of CO₂ to C₂₍₊₎ products. Here, we investigate the kinetic variations for the C-C coupling reactions induced by the heteroatom doping of a secondary metal element (Pt, Pd or Au) in the Cu substrate. The OC-COH coupling is found kinetically more favorable than OC-CHO coupling on copper-based alloy surfaces. The underlying factor that facilitates the OC-COH coupling step originates from the increased reactivity of adsorbed *CO species. Linear energy relations between activation barriers and reaction energies are observed for C-C coupling and reverse C-C dissociation reactions. This provides a useful strategy to estimate kinetic variations for C-C coupling in CO₂ reduction pathways.

The electrochemical reduction of CO₂ to multi-carbon products offers a practical means to energy storage as high-value carbon-based fuels and chemicals.^{1, 2} The C-C bond formation is an essential step for producing C₂₍₊₎ hydrocarbons and oxygenates, in which the *CO and its hydrogenated derivatives *CHO/*COH are known as building blocks.³⁻⁸ However, the C-C coupling is a rate-determining step with large energy barriers in the electrochemical conversion of CO₂ to C₂₍₊₎ products.⁹ In addition, it remains a challenge to identify the dominant C-C coupling step to C₂ intermediates. Despite extensive efforts in developing the CO dimerization mechanism,^{10, 11} the mechanistic elucidation of OC-COH and OC-CHO coupling is still under debate. Therefore, greater understanding is needed regarding reaction kinetics of different C-C coupling steps to promote the CO₂ conversion efficiency to multi-carbon products.

In the development of CRR electrocatalysts with improved activity and selectivity, heteroatom doping presents a practical engineering strategy.¹²⁻¹⁶ Copper is the only known metal that can generate a wide range of C₂₍₊₎ products, but it shows limited product selectivity.¹⁷ Alloying of a secondary metal element with copper is demonstrated as an effective approach for modulating reaction energetics and controlling selectivity distribution.^{18, 19} The dopant metal atoms in the copper-based bimetallic materials exhibit intrinsic effects on adsorption behaviours of key reaction intermediates. For example, in a computational study, we found that the oxygen and hydrogen affinities of the secondary metals in copper-based alloy catalysts can serve as descriptors in determining CRR product selectivity.²⁰ Given this, copper alloy materials present promising catalyst systems to tune the adsorption strength of key intermediates and to achieve a favorable reaction pathway. The adsorbed *CO species has been identified as a key intermediate by both experimental observations and theoretical analysis in the CRR.^{10, 11, 21-23} The *CO also plays an important role in the C-C coupling processes.⁴⁻⁸ It is of interest to control CO adsorption and evaluate its contribution to the kinetic variations of C-C bond formation in generating C₂₍₊₎ products.

In order to simplify the energetic analysis of catalytic reactions, the reaction kinetics can be linearly correlated to reaction energies.²⁴⁻²⁸ This kind of linear relations between the activation barrier and the reaction energy for an elementary reaction step is called the Brønsted-Evans-Polanyi (BEP) relation. Because of the hardness to detect both activation barriers and reaction energies in experiments, the computational methods provide a promising avenue to quantify the BEP relation in heterogeneous catalysis.²⁹ Based on density functional theory (DFT) calculations, the underlying BEP relation is widely used to estimate activation barriers from reaction energies in a range of catalytic reactions, such as ammonia synthesis and hydrogenation/dehydrogenation reactions.²⁹⁻³² In terms of the C-C bond coupling in CO₂ reduction, the transition state barrier is an essential parameter that affects the reaction rate and

^a Centre for Materials in Energy and Catalysis (CMEC), School of Chemical Engineering and Advanced Materials, The University of Adelaide, SA 5005, Australia

Email: yan.jiao@adelaide.edu.au; s.giao@adelaide.edu.au

Electronic Supplementary Information (ESI) available: See DOI: 10.1039/x0xx00000x

associated pathway selection.⁸ A linear energy relation between kinetics and thermodynamics is therefore required to describe variations in catalytic activity and selectivity for the C-C bond coupling process on CRR electrocatalysts.

In this work, we study the reaction kinetics of C-C coupling between *CO and *COH/*CHO on Cu alloy surfaces (M@Cu) by using density functional theory (DFT) calculations. The Pt, Pd and Au elements were selected as potential components in Cu alloys that can affect the catalytic activity and selectivity for C-C bond formation. The Cu(111) and Cu(100) surfaces were used as substrates for alloying. Through evaluation of activation barriers for OC-COH and OC-CHO coupling processes, we demonstrated the kinetic preference and associated C-C coupling selectivity on M@Cu catalysts. The origin of kinetic variations was identified by underlying electronic properties. Linear energy relations were observed between activation barriers and reaction energies for C-C coupling and reverse C-C dissociation reactions, which can be used to estimate variations of reaction kinetics and to predict preferred C-C coupling selectivity for CRR electrocatalysts.

The C-C coupling is a rate-determining process for generating multi-carbon products in electrochemical CO₂ reduction.^{9, 23} Although major research efforts have been devoted to the CO dimerization, less has been done to investigate the coupling between *CO and its hydrogenated derivatives (i.e. *CHO and *COH). It was demonstrated that the *COH was a common intermediate for C₁ and C₂ (C₃) pathways at neutral pH. This enabled a CO-COH pathway for the C-C coupling.⁶ The formation of the *COCO intermediate was evidenced by both experimental and computational observations at low overpotentials during CO reduction on Cu(100) electrodes.²¹ Despite the proposed absence at low potentials, *COH or *CHO are likely formed at a wider range of applied potentials.^{5, 8, 23} Herein, the reaction energetics of OC-COH and OC-CHO coupling processes are studied to illustrate their accessibility in the C₂ pathways on Cu alloy surfaces. Figure 1 shows the reaction pathways of CO₂ reduction toward C₂ products via OC-COH and OC-CHO coupling. The general stability of the dopant metal atom on Cu alloy surfaces was evaluated by calculating the adhesion energy of M atom (Table S1). Due to the dopant

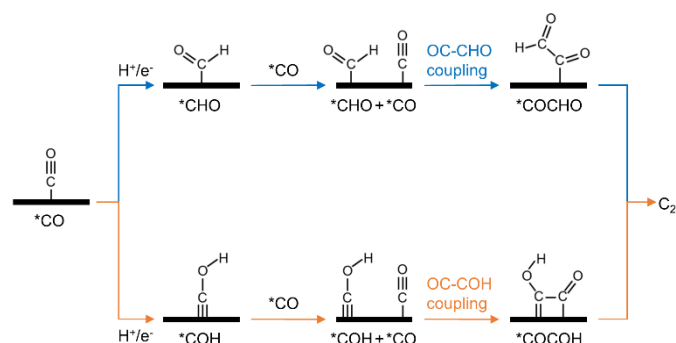


Figure 1. Reaction pathways of CO₂ reduction toward C₂ products via C-C coupling. The blue path represents the C₂ pathway via OC-CHO coupling; the orange path denotes the C₂ pathway via OC-COH coupling.

metal atoms, the Cu-based bimetallic catalysts show varied reaction kinetics for the investigated C-C bond formation steps. By using the nudged elastic band (NEB) method,^{33, 34} the reaction kinetics for OC-COH coupling are calculated with a (4 × 4 × 1) k-point grid. Further computational details are provided in the Supporting Information. As shown in Figure 2a-d, the activation barriers for OC-COH coupling on M@Cu(111) (M = Pt, Pd, Au) surfaces are increased compared to the Cu(111) surface. The Pt and Pd doped Cu(111) surfaces show comparable minimum energy paths with slightly increased activation energies for the C-C association process (Figure 2b and c). On the contrary, the Au@Cu(111) surface exhibits greater activation barrier than the Cu(111) surface (Figure 2d), indicating its unfavorable kinetics for OC-COH coupling. Except for the activation barrier of the OC-COH association ($\Delta E_{a(AS)}$), the corresponding reaction energy ($\Delta E_{(AS)}$) is also summarized in Figure 2e, which is the energy difference between the initial and the final state. The reaction energies of OC-COH coupling on M@Cu(111) surfaces are greater than that on the Cu(111) surface, which corresponds to the energy trend of activation barriers. For the Cu(100) surface, the reaction kinetics for OC-COH association are facilitated by introducing Pt, Pd or Au dopant atoms. As shown in Figure 3a-d, the Pt and Pd doped Cu(100) surfaces exhibit analogous decreased activation

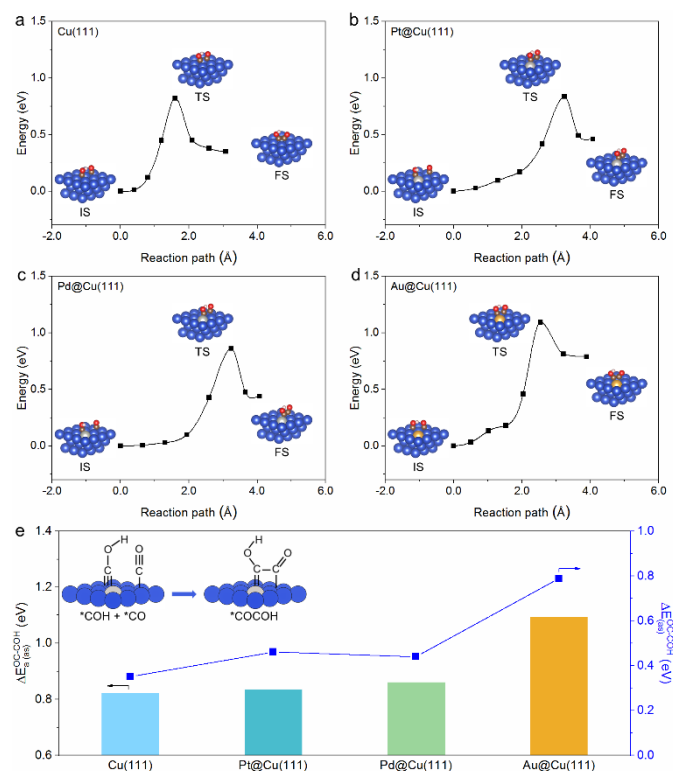


Figure 2. The minimum energy paths for OC-COH coupling on (a) Cu(111), (b) Pt@Cu(111), (c) Pd@Cu(111) and (d) Au@Cu(111) catalyst surfaces, respectively. Insets show the optimized structures of initial state (IS), transition state (TS), and final state (FS). Copper atoms are shown as blue-spheres with other metal atoms labelled for each catalyst surface. Carbon, oxygen, and hydrogen atoms are brown, red, and light pink, respectively. (e) Activation barriers and reaction energies for C-C association between adsorbed *CO and *COH on Cu(111) and M@Cu(111) surfaces. The inset shows the schematic configurations of the initial and final states for the corresponding C-C association reaction. Copper and the dopant metal atoms are blue and grey, respectively.

energies compared to the Cu(100) surface, while the Au doped Cu(100) surface displays the most favorable kinetics for the OC-COH coupling process. The activation barriers and reaction energies for OC-COH coupling on Cu(100) and M@Cu(100) surfaces are summarized in Figure 3e. The reaction energies keep steady after Pt or Pd doping in the Cu(100) surface with energy variations less than 0.015 eV, while the reaction energy on Au@Cu(100) becomes exoergic. In brief, the coupling between *CO and *COH is kinetically favorable on M@Cu(100) surfaces due to the heteroatom doping of a secondary metal element (Pt, Pd or Au) in the Cu substrate.

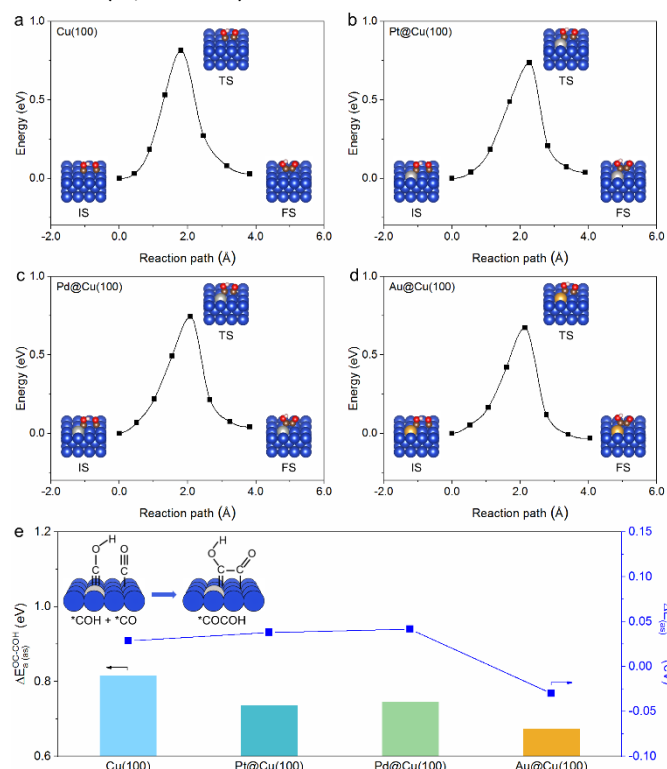


Figure 3. The minimum energy paths for OC-COH coupling on (a) Cu(100), (b) Pt@Cu(100), (c) Pd@Cu(100), and (d) Au@Cu(100) catalyst surfaces, respectively. Insets show the optimized structures of initial state (IS), transition state (TS), and final state (FS). Copper atoms are shown as blue-spheres with other metal atoms labelled for each catalyst surface. Carbon, oxygen, and hydrogen atoms are brown, red, and light pink, respectively. (e) Activation barriers and reaction energies for C-C association between adsorbed *CO and *COH on Cu(100) and M@Cu(100) surfaces. The inset shows the schematic configurations of the initial and final states for the corresponding C-C association reaction. Copper and the dopant metal atoms are blue and grey, respectively.

The *CHO intermediate is another *CO hydrogenated derivative that is involved in the C-C coupling reaction. The activation barriers for OC-CHO coupling are calculated with a $(1 \times 1 \times 1)$ k-point grid because it is computationally demanding to obtain the minimum energy paths with a $(4 \times 4 \times 1)$ k-point grid. This also suggests the less favorable reaction kinetics of OC-CHO coupling compared to OC-COH coupling. Using denser k-point grid can change the activation barriers, but is unlikely to alter the variation trend of reaction energetics on the investigated Cu-based catalyst surfaces. The reaction kinetics for OC-CHO coupling on M@Cu(111) surfaces become less favorable compared to the Cu(111) surface (Figure S1a-d). The same variation trend of activation barriers and reaction energies is

shown in Figure S1e, which indicates the suppressed reaction energetics for OC-CHO coupling on M@Cu(111) surfaces. As shown in Figure S2a-d, the OC-CHO coupling is also kinetically unfavorable on M@Cu(100) surfaces with increased activation barriers compared to the Cu(100) surface. The reaction energies for OC-CHO coupling are correspondingly levelled up on M@Cu(100) surfaces in comparison with the Cu(100) surface (Figure S2e). In general, both activation barriers and reaction energies for OC-CHO coupling on M@Cu(100) surfaces are lower than those on corresponding M@Cu(111) surfaces, indicating more favorable reaction energetics on M@Cu(100) surfaces. Nevertheless, the OC-CHO coupling is impeded after introducing a secondary metal element (Pt, Pd or Au) to the Cu substrate.

To understand the origin of kinetic variations, we investigated the underlying electronic properties. The density of states (DOS) analysis was conducted for the initial state of OC-COH coupling with two separate C_1 adsorbates (i.e. *CO and *COH) on the catalyst surface. The adsorption of *CO leads to the binding states between C atom and the nearby Cu atom in the energy range from -6 to -8 eV on the (100) surfaces (Figure 4a). When the secondary metal element (Pt, Pd or Au) is doped into the Cu(100) surface, a lower overlap is observed among the binding states between p orbital for C atom of the adsorbed *CO and d orbital for the nearby Cu atom on M@Cu(100) surfaces compared to the Cu(100) surface. This finding indicates an improved reactivity of CO during the OC-COH coupling on M@Cu(100) surfaces. The Bader charge analysis shows the tunable charge distribution in the initial state of OC-COH coupling. As shown in Figure 4b, the Bader charge for C atom of adsorbed *CO on each M@Cu(100) surface is less than that on

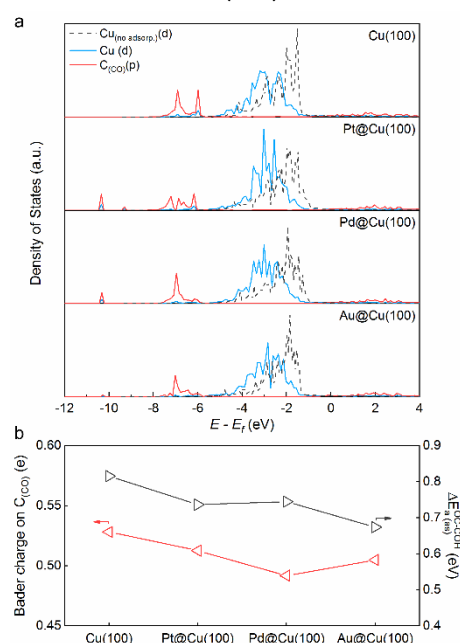


Figure 4. (a) The density of states (DOS) of d-orbital for the nearby Cu atom and p-orbital for C atom of adsorbed *CO in the initial state of OC-COH coupling on Cu(100) and M@Cu(100) surfaces. The d-orbital DOS of the nearby Cu atom without adsorption is also shown in the dashed line. (b) Relationship between the charge distribution on C atom of adsorbed *CO in the initial state of OC-COH coupling and activation barriers for OC-COH coupling on Cu(100) and M@Cu(100) surfaces.

the Cu(100) surface. This is in agreement with the DOS result of the lower binding states overlap on M@Cu(100) surfaces. Therefore, the increased reactivity of adsorbed *CO is rationalized by its decreased interaction with the nearby Cu site on M@Cu(100) surfaces. The activation barriers for OC-COH coupling are compared with the Bader charge analysis to uncover the intrinsic electronic effects on reaction kinetics. The analogous variation trends in Figure 4b indicate that more reactive surface-bound CO on M@Cu(100) surfaces can facilitate the OC-COH coupling. By way of contrast, the unfavorable kinetics for OC-COH coupling on M@Cu(111) surfaces compared to the Cu(111) surface can be explained by the increased interaction between adsorbed *CO and the nearby Cu atom. The DOS analysis of a higher overlap among the binding states (Figure S3a) agrees with the increased Bader charge for C atom of *CO (Figure S3b) on M@Cu(111) surfaces. In summary, optimization of reaction kinetics for OC-COH coupling are enabled by control of CO adsorption.

In the analysis of complex catalytic reactions, linear energy relations have been widely applied to understand the energetic trends related to underlying thermodynamics and kinetics.^{25, 30, 35} The Brønsted-Evans-Polanyi (BEP) relation is known as a linear relationship between the activation barrier and the reaction energy for an elementary reaction step.²⁹ However, it is hard to measure values of these two properties in experiments. Given this, the computational methods based on density functional theory present a solution to quantify the linear relations. In heterogeneous catalysis, the BEP relation can be used to estimate activation barriers from reaction energies and to depict catalytic variations of different catalyst surfaces.²⁶ Based on the C-C coupling energy trend on Cu and M@Cu surfaces, linear energy relations between activation barriers and reaction energies are evaluated. The optimized transition state geometries vary from decoupled states for OC-COH coupling (Figure 2a-d, 3a-d) to associated states for OC-CHO coupling (Figure S1a-d, S2a-d). Due to the final-state-like geometry for transition states in BEP relations, linear energy trends are explored for both C-C coupling and reverse C-C dissociation reactions. Figure 5a shows the description of the reaction energy ($\Delta E_{(as)/(dis)}$) and the activation barrier ($\Delta E_{a (as)/(dis)}$) for C-C association/dissociation processes. A linear energy relation is observed between the activation barrier and reaction energy for the C-C bond dissociation of adsorbed *COCOH on the investigated Cu-based catalyst surfaces (Figure 5b). In addition, the linear scaling relation for OC-COH coupling is also obtained correlating the activation barrier to the reaction energy (Figure 5c). For the OC-COH coupling, the catalyst surfaces with less endoergic reaction energies exhibit lower activation barriers for C-C association between adsorbed *CO and *COH. Specifically, M@Cu(100) surfaces show more favorable reaction energetics and resultant higher selectivity for OC-COH coupling than M@Cu(111) surfaces. Furthermore, the linear relations are also established for OC-CHO dissociation and association processes (Figure S4 and S5). The consistent variation trends of activation barriers and reaction energies are observed for the OC-CHO coupling mechanism. However, the reaction energetics of the OC-CHO coupling process become less favorable after

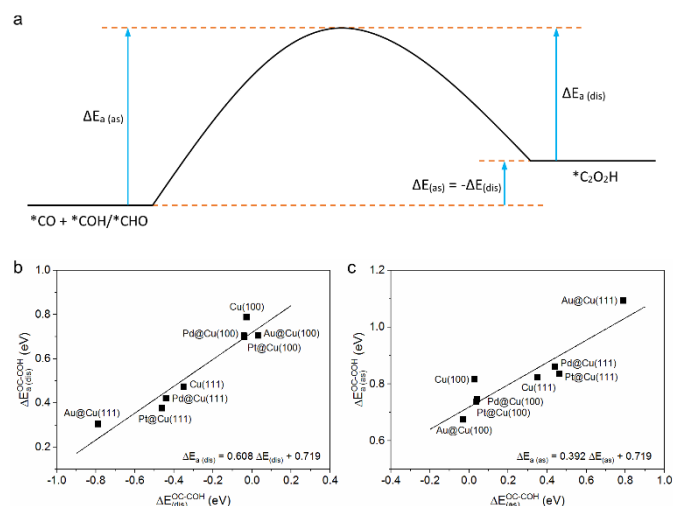


Figure 5. (a) The description of energies for C-C association/dissociation reactions. (b) The activation energy for C-C bond dissociation of adsorbed *COCOH as a function of the corresponding reaction energy. (c) The activation energy for OC-COH coupling as a function of the corresponding reaction energy. A ($4 \times 4 \times 1$) k-point grid is applied.

secondary metal doping in the Cu substrate. To sum up, the linear energy relations provide a feasible method to estimate activation barriers from reaction energies and predict variations in catalytic activity and selectivity for different catalysts.

In terms of thermodynamics, the reaction energies for OC-COH coupling, OC-CHO coupling, and CO dimerization processes are compared on the (111) and (100) surfaces respectively (Figure S6 and S7). The OC-COH coupling on (100) surfaces shows the most favorable reaction energies. By contrast, the CO dimerization is thermodynamically less favorable than OC-COH and OC-CHO coupling. Based on the preceding discussion of linear relations between activation barriers and reaction energies, it is likely that CO dimerization possess higher kinetic barriers than the other two C-C coupling steps. This variation trend is in good agreement with the previous study, demonstrating that higher degree of hydrogenation of reaction adsorbates leads to reduced kinetic barriers for C-C coupling process.³⁵

Conclusions

A kinetic investigation of C-C coupling selectivity in electrochemical CO₂ reduction was conducted using DFT computations. The reaction kinetics for OC-COH and OC-CHO coupling processes were evaluated on Cu and M@Cu catalysts surfaces. Based on the variation trend of activation barriers, we highlight the kinetic favorability of OC-COH coupling compared to OC-CHO coupling on copper-based alloy surfaces. The analysis of electronic properties demonstrates that the increased reactivity of adsorbed *CO species contributes to the favorable reaction energetics of OC-COH coupling. Linear energy relations are established to describe correlations between activation barriers and reaction energy for C-C association/dissociation reactions. This leads to a practical method for estimating kinetic variations from thermodynamic analysis for C-C bond formation on varied CRR electrocatalysts.

Conflicts of interest

The authors have no conflicts of interest to declare.

Acknowledgements

The authors acknowledge financial support from the Australian Research Council (DP190103472, FT190100636, and FL170100154). DFT computations in this work were undertaken with assistance of resources and services from the National Computational Infrastructure (NCI) supported by the Australian Government, and the Phoenix High Performance Computing (HPC) Service at The University of Adelaide.

References

1. Y. Zheng, A. Vasileff, X. Zhou, Y. Jiao, M. Jaroniec and S. Z. Qiao, *J. Am. Chem. Soc.*, 2019, **141**, 7646-7659.
2. K. D. Yang, C. W. Lee, K. Jin, S. W. Im and K. T. Nam, *J. Phys. Chem. Lett.*, 2017, **8**, 538-545.
3. T. K. Todorova, M. W. Schreiber and M. Fontecave, *ACS Catal.*, 2020, **10**, 1754-1768.
4. X. Liu, P. Schlexer, J. Xiao, Y. Ji, L. Wang, R. B. Sandberg, M. Tang, K. S. Brown, H. Peng, S. Ringe, C. Hahn, T. F. Jaramillo, J. K. Nørskov and K. Chan, *Nat. Commun.*, 2019, **10**, 32.
5. A. J. Garza, A. T. Bell and M. Head-Gordon, *ACS Catal.*, 2018, **8**, 1490-1499.
6. H. Xiao, T. Cheng, W. A. Goddard and R. Sundararaman, *J. Am. Chem. Soc.*, 2016, **138**, 483-486.
7. W. Luo, X. Nie, M. J. Janik and A. Asthagiri, *ACS Catal.*, 2016, **6**, 219-229.
8. J. D. Goodpaster, A. T. Bell and M. Head-Gordon, *J. Phys. Chem. Lett.*, 2016, **7**, 1471-1477.
9. R. Kortlever, J. Shen, K. J. Schouten, F. Calle-Vallejo and M. T. M. Koper, *J. Phys. Chem. Lett.*, 2015, **6**, 4073-4082.
10. J. H. Montoya, C. Shi, K. Chan and J. K. Nørskov, *J. Phys. Chem. Lett.*, 2015, **6**, 2032-2037.
11. F. Calle-Vallejo and M. T. M. Koper, *Angew. Chem. Int. Ed.*, 2013, **52**, 7282-7285.
12. W. Ma, S. Xie, T. Liu, Q. Fan, J. Ye, F. Sun, Z. Jiang, Q. Zhang, J. Cheng and Y. Wang, *Nat. Catal.*, 2020, **3**, 478-487.
13. A. Vasileff, Y. Zhu, X. Zhi, Y. Zhao, L. Ge, H. M. Chen, Y. Zheng and S. Qiao, *Angew. Chem. Int. Ed.*, 2020, **59**, 19649-19653.
14. X. Zhi, Y. Jiao, Y. Zheng and S. Z. Qiao, *Small*, 2019, **15**, 1804224.
15. Y. Zhou, F. Che, M. Liu, C. Zou, Z. Liang, P. De Luna, H. Yuan, J. Li, Z. Wang, H. Xie, H. Li, P. Chen, E. Bladt, R. Quintero-Bermudez, T.-K. Sham, S. Bals, J. Hofkens, D. Sinton, G. Chen and E. H. Sargent, *Nat. Chem.*, 2018, **10**, 974-980.
16. M. J. Cheng, E. L. Clark, H. H. Pham, A. T. Bell and M. Head-Gordon, *ACS Catal.*, 2016, **6**, 7769-7777.
17. K. P. Kuhl, E. R. Cave, D. N. Abram and T. F. Jaramillo, *Energy Environ. Sci.*, 2012, **5**, 7050-7059.
18. A. Vasileff, C. Xu, Y. Jiao, Y. Zheng and S. Z. Qiao, *Chem*, 2018, **4**, 1809-1831.
19. A. Vasileff, X. Zhi, C. Xu, L. Ge, Y. Jiao, Y. Zheng and S. Z. Qiao, *ACS Catal.*, 2019, **9**, 9411-9417.
20. X. Zhi, Y. Jiao, Y. Zheng, A. Vasileff and S.-Z. Qiao, *Nano Energy*, 2020, **71**, 104601.
21. E. Pérez-Gallent, M. C. Figueiredo, F. Calle-Vallejo and M. T. M. Koper, *Angew. Chem. Int. Ed.*, 2017, **56**, 3621-3624.
22. A. Wuttig, C. Liu, Q. Peng, M. Yaguchi, C. H. Hendon, K. Motobayashi, S. Ye, M. Osawa and Y. Surendranath, *ACS Cent. Sci.*, 2016, **2**, 522-528.
23. T. Cheng, H. Xiao and W. A. Goddard, *Proc. Natl. Acad. Sci. U. S. A.*, 2017, **114**, 1795-1800.
24. P. Ferrin, D. Simonetti, S. Kandoi, E. Kunkes, J. A. Dumesic, J. K. Nørskov and M. Mavrikakis, *J. Am. Chem. Soc.*, 2009, **131**, 5809-5815.
25. A. Michaelides, Z. P. Liu, C. J. Zhang, A. Alavi, D. A. King and P. Hu, *J. Am. Chem. Soc.*, 2003, **125**, 3704-3705.
26. J. K. Nørskov, T. Bligaard, A. Logadottir, S. Bahn, L. B. Hansen, M. Bollinger, H. Bengaard, B. Hammer, Z. Sljivancanin, M. Mavrikakis, Y. Xu, S. Dahl and C. J. H. Jacobsen, *J. Catal.*, 2002, **209**, 275-278.
27. Z.-P. Liu and P. Hu, *J. Chem. Phys.*, 2001, **114**, 8244-8247.
28. V. Pallassana and M. Neurock, *J. Catal.*, 2000, **191**, 301-317.
29. A. Logadottir, T. H. Rod, J. K. Nørskov, B. Hammer, S. Dahl and C. J. H. Jacobsen, *J. Catal.*, 2001, **197**, 229-231.
30. S. Wang, V. Petzold, V. Tripkovic, J. Kleis, J. G. Howalt, E. Skúlason, E. M. Fernández, B. Hvolbæk, G. Jones, A. Toftelund, H. Falsig, M. Björketun, F. Studt, F. Abild-Pedersen, J. Rossmeisl, J. K. Nørskov and T. Bligaard, *Phys. Chem. Chem. Phys.*, 2011, **13**, 20760-20765.
31. P. Crawford, B. McAllister and P. Hu, *J. Phys. Chem. C*, 2009, **113**, 5222-5227.
32. T. R. Munter, T. Bligaard, C. H. Christensen and J. K. Nørskov, *Phys. Chem. Chem. Phys.*, 2008, **10**, 5202-5206.
33. G. Henkelman, B. P. Uberuaga and H. Jonsson, *J. Chem. Phys.*, 2000, **113**, 9901-9904.
34. G. Henkelman and H. Jonsson, *J. Chem. Phys.*, 2000, **113**, 9978-9985.
35. J. H. Montoya, A. A. Peterson and J. K. Nørskov, *ChemCatChem*, 2013, **5**, 737-742.

Supporting Information

Kinetic Insights into Selective C-C Coupling for Electrochemical CO₂ Reduction on Copper Alloy Surfaces

Xing Zhi, Yan Jiao*, Yao Zheng, Shi-Zhang Qiao*

Centre for Materials in Energy and Catalysis (CMEC)

School of Chemical Engineering and Advanced Materials

The University of Adelaide, SA 5005, Australia

* Correspondence: s.qiao@adelaide.edu.au; yan.jiao@adelaide.edu.au

Computational Methods.

All computations were conducted using density functional theory (DFT) method. The Perdew-Burke-Ernzerhof (PBE) functional was applied for electron exchange correlation within the generalized gradient approximation (GGA), as implemented in the VASP code.^{1,2} The ionic cores were described by the projector-augmented wave (PAW) method.³ The parameter of 500 eV was used for the plane wave cutoff energy with a 0.18 eV width of the smearing.

The Cu(111) and Cu(100) surfaces were modeled with three-layer (3×3) supercells with 15 Å of vacuum space. The M@Cu models were simulated by substituting one Cu surface atom with one dopant metal atom M (M = Pt, Pd, Au), respectively. The adsorption energies were calculated on the Cu and M@Cu surfaces with the bottom two layers fixed. In order to evaluate the stability of the dopant metal atom on Cu alloy surfaces, the adhesion energy of the dopant metal atom M was calculated from the following:

$$E_{\text{ad}} = E_{\text{M@Cu}} - E_{\text{Cu-v}} - E_{\text{M}}$$

where $E_{\text{M@Cu}}$ is the energy of M@Cu(111) or M@Cu(100) surface, $E_{\text{Cu-v}}$ is the corresponding energy of Cu(111) or Cu(100) surface with one Cu surface atom vacancy, and E_{M} is the energy of M atom (Table S1).

Kinetic barriers for C-C coupling processes were evaluated by using the climbing-image nudged elastic band (NEB) method.^{4,5} Transition state energies were calculated with the top layer relaxed and the rest constrained in the three-layer (3×3) supercells. Varied Gamma k-point grids were used for different C-C coupling steps. All structures in geometry optimizations and transition state calculations were relaxed to forces less than 0.05 eV \AA^{-1} .

Table S1. The adhesion energy (in eV) of metal atom M on Cu(111) and Cu(100) surfaces.

Metal atom M	E_{ad}	
	On Cu(111) surface	On Cu(100) surface
Pt	-1.47	-1.04
Pd	-1.17	-0.96
Au	-1.31	-1.10

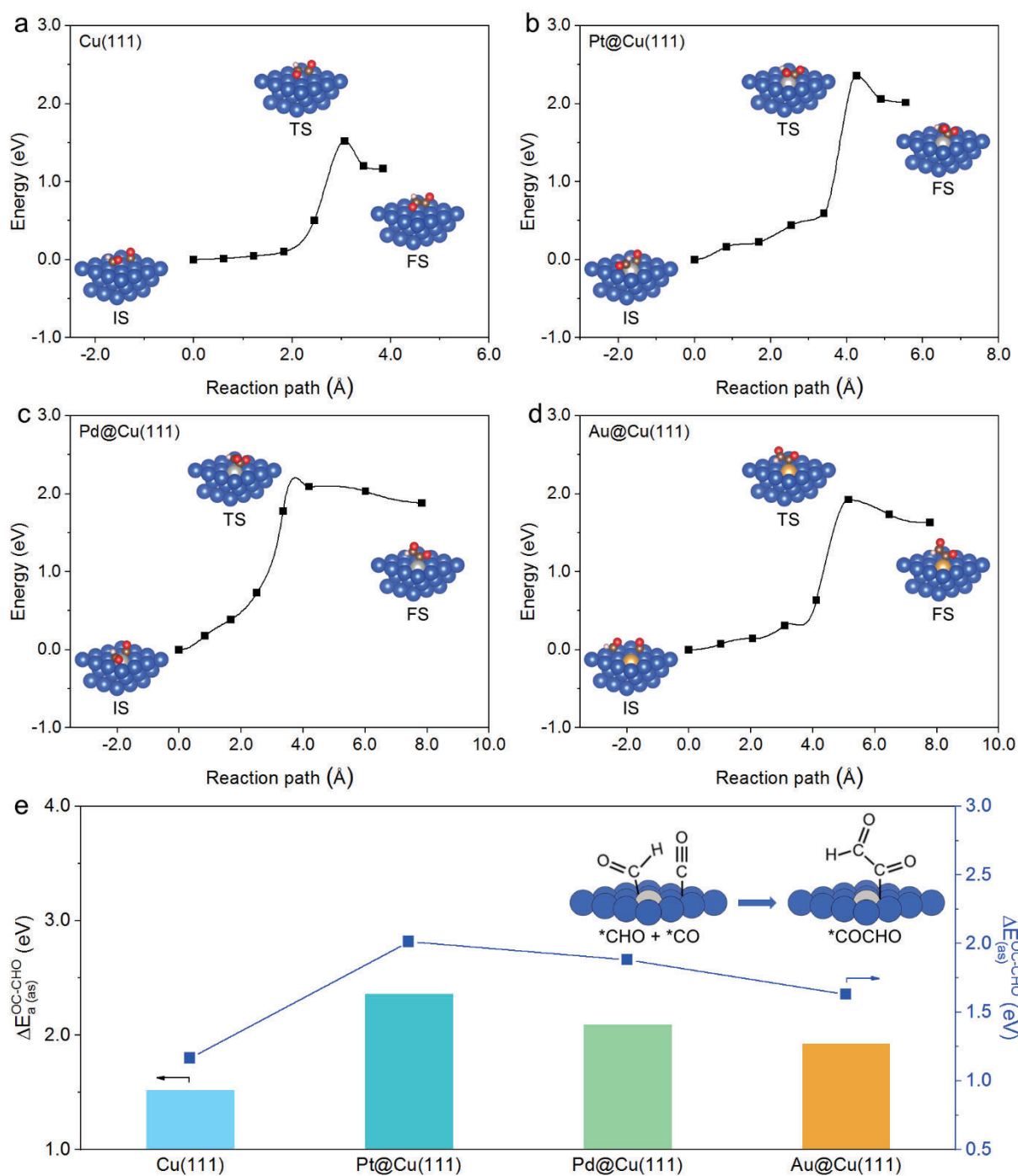


Figure S1. The minimum energy paths for OC-CHO coupling on (a) Cu(111), (b) Pt@Cu(111), (c) Pd@Cu(111) and (d) Au@Cu(111) catalyst surfaces, respectively. Insets show the optimized structures of initial state (IS), transition state (TS), and final state (FS). Copper atoms are shown as blue-spheres with other metal atoms labelled for each catalyst surface. Carbon, oxygen, and hydrogen atoms are brown, red, and light pink, respectively. A $(1 \times 1 \times 1)$ k-point grid is applied. (e) Activation barriers and reaction energies for C-C association between adsorbed *CO and *CHO on Cu(111) and M@Cu(111) surfaces. The inset shows the schematic configurations of the initial and final states for the corresponding C-C association reaction. Copper and the dopant metal atoms are blue and grey, respectively.

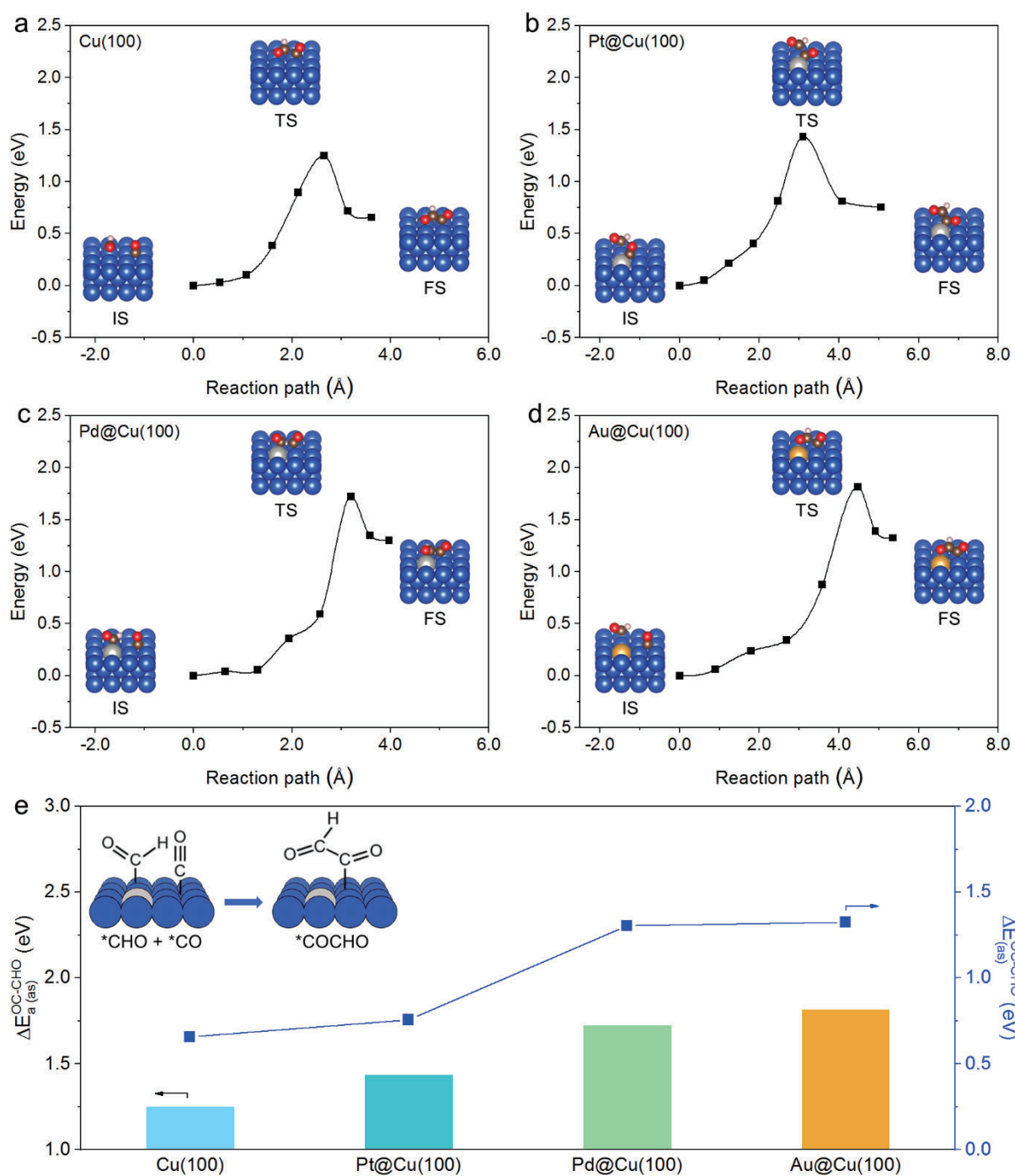


Figure S2. The minimum energy paths for OC-CHO coupling on (a) Cu(100), (b) Pt@Cu(100), (c) Pd@Cu(100), and (d) Au@Cu(100) catalyst surfaces, respectively. Insets show the optimized structures of initial state (IS), transition state (TS), and final state (FS). Copper atoms are shown as blue-spheres with other metal atoms labelled for each catalyst surface. Carbon, oxygen, and hydrogen atoms are brown, red, and light pink, respectively. A $(1 \times 1 \times 1)$ k-point grid is applied. (e) Activation barriers and reaction energies for C-C association between adsorbed *CO and *CHO on Cu(100) and M@Cu(100) surfaces. The inset shows the schematic configurations of the initial and final states for the corresponding C-C association reaction. Copper and the dopant metal atoms are blue and grey, respectively.

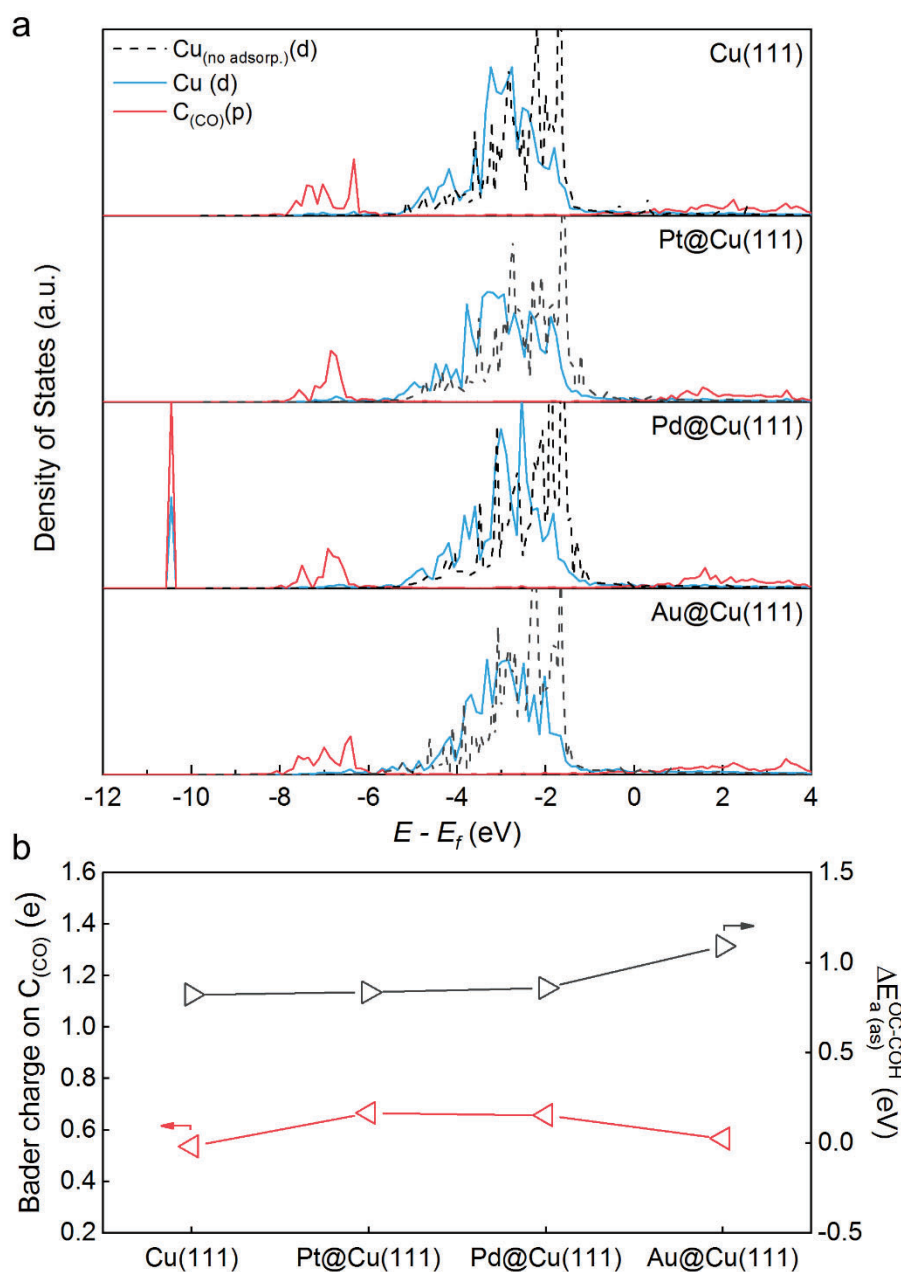


Figure S3. (a) The density of states (DOS) of d-orbital for the nearby Cu atom and p-orbital for C atom of adsorbed *CO in the initial state of OC-COH coupling on Cu(111) and M@Cu(111) surfaces. The d-orbital DOS of the nearby Cu atom without adsorption is also shown in the dashed line. (b) Relationship between the charge distribution on C atom of adsorbed *CO in the initial state of OC-COH coupling and activation barriers for OC-COH coupling on Cu(111) and M@Cu(111) surfaces.

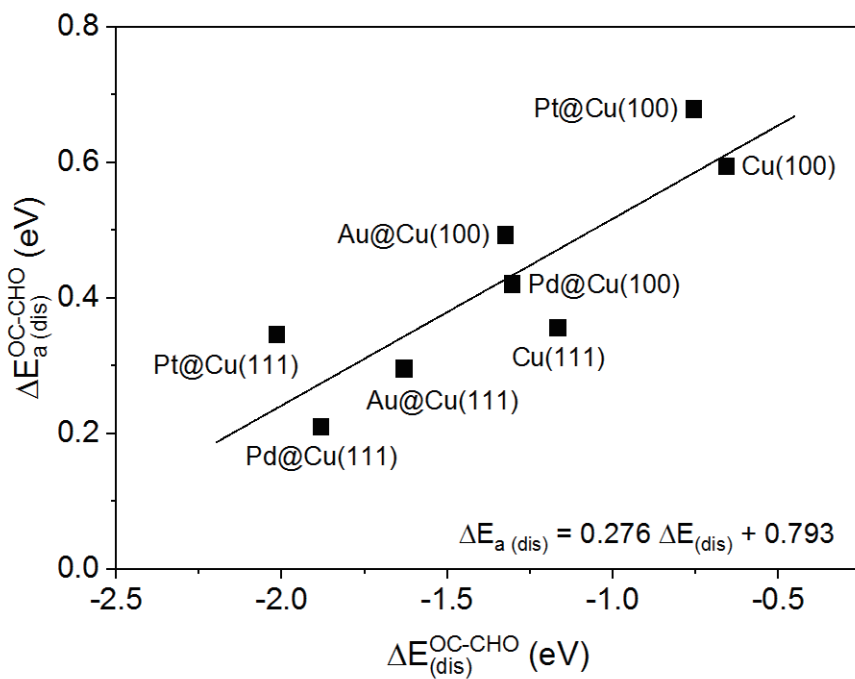


Figure S4. The activation energy for C-C bond dissociation of adsorbed *COCHO as a function of the corresponding reaction energy. A $(1 \times 1 \times 1)$ k-point grid is applied.

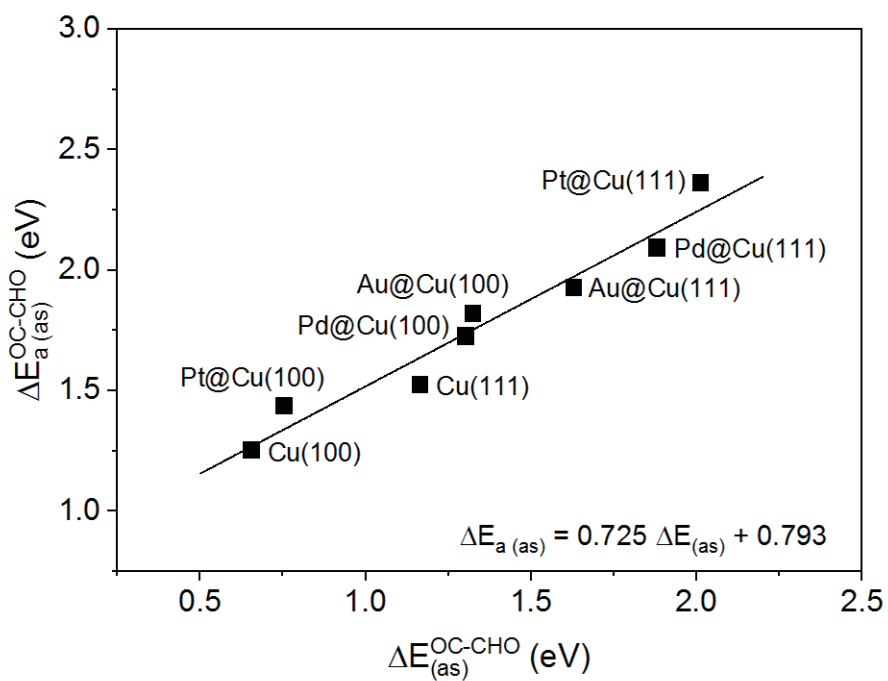


Figure S5. The activation energy for OC-CHO coupling as a function of the corresponding reaction energy. A $(1 \times 1 \times 1)$ k-point grid is applied.

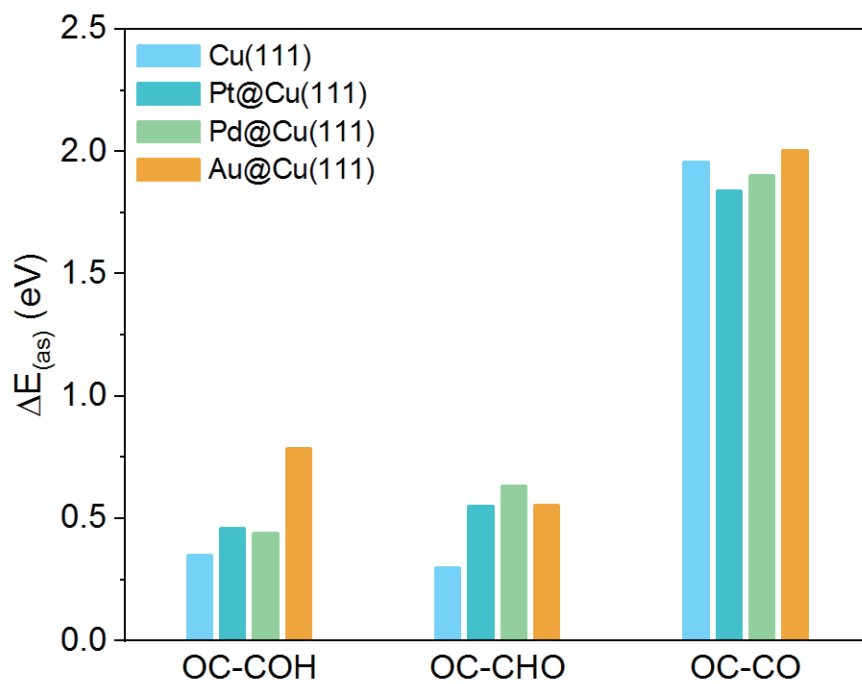


Figure S6. The reaction energies for C-C coupling of OC-COH, OC-CHO, and OC-CO on Cu(111) and M@Cu(111) catalyst surfaces. A $(4 \times 4 \times 1)$ k-point grid is applied.

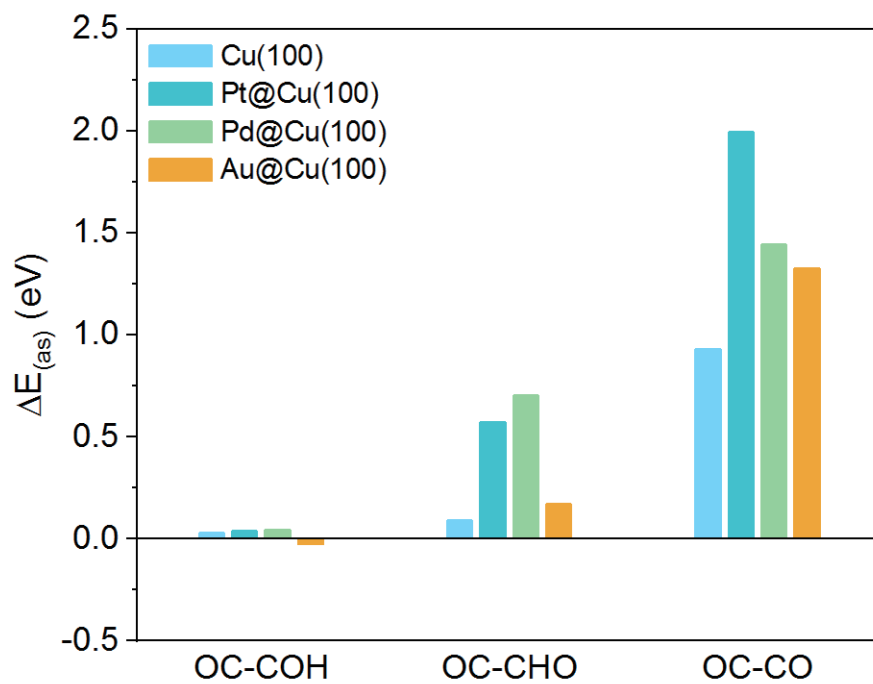


Figure S7. The reaction energies for C-C coupling of OC-COH, OC-CHO, and OC-CO on Cu(100) and M@Cu(100) catalyst surfaces. A $(4 \times 4 \times 1)$ k-point grid is applied.

References

1. J. P. Perdew, K. Burke and M. Ernzerhof, *Phys. Rev. Lett.*, 1996, **77**, 3865-3868.
2. G. Kresse and J. Furthmuller, *Phys. Rev. B: Condens. Matter Mater. Phys.*, 1996, **54**, 11169-11186.
3. G. Kresse and D. Joubert, *Phys. Rev. B: Condens. Matter Mater. Phys.*, 1999, **59**, 1758-1775.
4. G. Henkelman, B. P. Uberuaga and H. Jonsson, *J. Chem. Phys.*, 2000, **113**, 9901-9904.
5. G. Henkelman and H. Jonsson, *J. Chem. Phys.*, 2000, **113**, 9978-9985.

Chapter 6: Directing Selectivity of CO₂ Electroreduction to Target C₂ Products via Non-metal Doping on Cu Surfaces

6.1 Introduction and Significance

The generation of C₂ products during the electrochemical CO₂ reduction reaction (CRR) is of particular importance for clean energy storage. However, selective CO₂ electroreduction to desired C₂ products is presently limited, as most research focus on the C-C coupling step rather than the selectivity after such step. Therefore, the understanding of C₂ reaction mechanism in the late stages of CRR is much needed.

In this Chapter, a strategy of non-metal doping to copper surface (Cu-X; X = B, N, P, S, Cl, Br and I) was applied to modulate C₂ products (including ethylene, ethane and ethanol) selectivity during CRR. Through evaluation of adsorption energetics of post-C₂-coupling intermediates on these models, we demonstrated the thermodynamically derived selectivity amongst competing reaction pathways. The oxygen affinities of the dopant atom site and the Cu site on Cu-X catalysts were identified as descriptors for C₂ product selectivity. Ethylene production was found to be more favoured on Cu-X catalysts doped with strong oxygen-affinity atoms, such as boron dopant atom, despite competing reaction pathways. Ethane selectivity was generally boosted whereas ethanol formation was suppressed by non-metal doping on Cu surfaces. The electron transfer through Bader charge analyses and electronegativity of non-metal dopant atoms were uncovered as the underlying electronic properties that affected oxygen affinities of multiple active sites and associated C₂ product selectivity. The improved understanding of C₂ reaction mechanism at later CRR stages provided a practical strategy to direct C₂ product selectivity for electrocatalytic CO₂ reduction.

6.2 Directing selectivity of CO₂ electroreduction to target C₂ products via non-metal doping on Cu surfaces

This chapter is included as it appears as a journal paper published by Xing Zhi, Yan Jiao, Yao Zheng, Kenneth Davey, Shi-Zhang Qiao, Directing selectivity of CO₂ electroreduction

to target C₂ products via non-metal doping on Cu surfaces, *J. Mater. Chem. A*, **2021**, 9, 6345-6351.

Statement of Authorship

Title of Paper	Directing Selectivity of CO ₂ Electroreduction to Target C ₂ Products via Non-metal Doping on Cu Surfaces
Publication Status	<input checked="" type="checkbox"/> Published <input type="checkbox"/> Accepted for Publication <input type="checkbox"/> Submitted for Publication <input type="checkbox"/> Unpublished and Unsubmitted work written in manuscript style
Publication Details	Xing Zhi, Yan Jiao, Yao Zheng, Kenneth Davey, Shi-Zhang Qiao, Directing selectivity of CO ₂ electroreduction to target C ₂ products via non-metal doping on Cu surfaces, <i>J. Mater. Chem. A</i> , 2021 , 9, 6345-6351.

Principal Author

Name of Principal Author (Candidate)	Xing Zhi		
Contribution to the Paper	Conducted all the computations, carried out data analysis and wrote the paper		
Overall percentage (%)	70%		
Certification:	This paper reports on original research I conducted during the period of my Higher Degree by Research candidature and is not subject to any obligations or contractual agreements with a third party that would constrain its inclusion in this thesis. I am the primary author of this paper.		
Signature	_____	Date	31 Mar. 2021

Co-Author Contributions

By signing the Statement of Authorship, each author certifies that:

- the candidate's stated contribution to the publication is accurate (as detailed above);
- permission is granted for the candidate to include the publication in the thesis; and
- the sum of all co-author contributions is equal to 100% less the candidate's stated contribution.

Name of Co-Author	Yan Jiao		
Contribution to the Paper	Discussed computational results and findings, supervised the project, and revised the paper.		
Signature	_____	Date	31 Mar. 2021

Name of Co-Author	Yao Zheng		
Contribution to the Paper	Discussed the research plan, supervised the project, and revised the paper.		
Signature	_____	Date	31 Mar. 2021

Name of Co-Author	Kenneth Davey		
Contribution to the Paper	Discussed the paper and helped to revise the paper.		
Signature		Date	06 Apr. 2021

Name of Co-Author	Shi-Zhang Qiao		
Contribution to the Paper	Discussed the research plan, supervised the project, and revised the paper.		
Signature		Date	31 Mar. 2021

Cite this: *J. Mater. Chem. A*, 2021, 9, 6345

Directing the selectivity of CO₂ electroreduction to target C₂ products via non-metal doping on Cu surfaces†

Xing Zhi, Yan Jiao, * Yao Zheng,  Kenneth Davey and Shi-Zhang Qiao *

Understanding the late stages of the electrochemical CO₂ reduction reaction (CRR) in the formation of various C₂ products provides great opportunities for fully achieving a selective CRR to target products. Here, we report, for the first time, that C₂ product (including ethylene, ethane and ethanol) selectivity can be directed by the active site's oxygen affinity on a range of non-metal doped copper surfaces (Cu–X). Through theoretical evaluation of adsorption energetics of key post-C₂-coupling intermediates, we demonstrate how branching reaction pathways are competing with each other and how selectivity for different products is achieved. The oxygen affinities of different active sites on Cu–X catalysts, including the dopant atom and Cu sites, are identified as descriptors for C₂ product selectivity. The ethylene pathway is shown to be favored on Cu–X surfaces doped with strong oxygen affinity atoms, such as boron. Ethane selectivity is generally boosted by Cu–X, whereas ethanol generation is suppressed by non-metal doping on Cu surfaces. Bader charge analyses of electron distribution on intermediates and electronegativity analyses of non-metal dopant atoms are integrated to identify the impact of intrinsic electronic properties on adsorption behaviour, together with the resultant C₂ product selectivity on Cu–X catalysts. Our findings shed light on controlling product selectivity by modulating oxygen affinity in complex electrochemical reactions.

Received 30th November 2020
Accepted 29th January 2021

DOI: 10.1039/d0ta11604a

rsc.li/materials-a

Introduction

The electrochemical reduction of CO₂ to multi-carbon products offers a practical means to energy storage as high-value carbon-based fuels and chemicals through using renewable electricity.^{1–3} The production of C₂ hydrocarbons and alcohols, *e.g.* ethylene and ethanol, is of particular interest in the electrochemical CO₂ reduction reaction (CRR). This is because of the high energy densities and economic value of these final products.^{4–6} However, efficient conversion of CO₂ to C₂ products remains challenging because of limited selectivity and activity of existing catalysts.

Among CO₂ reduction electrocatalysts, Cu-based materials appear promising for catalyzing CO₂ to C₂ products.^{3,7–11} Previous studies have shown that introducing modifier elements to Cu can tune the adsorption energetics of key reaction intermediates and result in improved selectivity of target products.^{12–15} However, an improved understanding is needed of Cu surface engineering to optimize C₂ product selectivity. A quantitative understanding of the underlying reaction

mechanism for C₂ product selectivity is necessary for rational design of efficient catalysts.

Significant research efforts were made to understand the initial C–C coupling steps and favorability for C₂ to C₁ products.^{16–22} It is well-known that *CO is a key intermediate for C–C coupling processes at early stages of C₂ pathways. By contrast, less effort has been directed to address reaction pathways at late stages for C₂ product selectivity.^{23–26} Various pathways to C₂ products have been proposed to occur through different intermediates.^{8,27–29} A refinement of intermediate energetics is required therefore to preference target C₂ compounds. It has been proposed that *OCHCH₂ is a key intermediate at which the pathways for ethylene and ethanol bifurcate.^{2,18,25} Hydrogenation of this intermediate leads to either ethylene desorption with *O remaining or *OCHCH₃ formation. In the past, active sites on Cu-based materials exhibit varied free energies for adsorbed oxygen and key C₂ species.³⁰ Hence, the interaction between oxygen and catalyst surfaces would play an important role in regulating the adsorption energies of post C₂ intermediates.

Recently, our group experimentally demonstrated that the formation of ethane shares a common pathway with ethylene and ethanol. The oxygen-bound ethoxy (*OCH₂CH₃) intermediate was observed during ethane production by various *in situ* characterisation techniques, such as X-ray absorption fine-structure and Raman spectroscopy.³¹ Additionally, oxygen

Centre for Materials in Energy and Catalysis (CMEC), School of Chemical Engineering and Advanced Materials, The University of Adelaide, SA 5005, Australia. E-mail: yan.jiao@adelaide.edu.au; s.qiao@adelaide.edu.au

† Electronic supplementary information (ESI) available. See DOI: 10.1039/d0ta11604a

affinity of catalysts has been reported as a selectivity descriptor for CO₂ electroreduction.^{32–35} Therefore, we propose that adsorption energetics of post C₂ intermediates can be regulated *via* oxygen-atom binding to the catalyst surface.

Here, using density functional theory (DFT) calculations, we explore C₂ product selectivity for electrochemical CO₂ reduction on a range of Cu-based catalysts doped with non-metal elements (Cu–X). Based on our findings, we highlight the role of oxygen (O) affinities of different active sites, including the dopant atom and Cu, during this process. The Cu–X catalyst models were simulated with one dopant atom X (X = B, N, P, S, Cl, Br, or I) located on a hollow-site of the Cu(100) surface. The CRR selectivity toward target C₂ products was demonstrated by thermodynamic analyses of three key, post-C₂-coupling reaction intermediates *i.e.* *OCHCH₂, *OCHCH₃ and *OCH₂CH₃. Among the competing reaction pathways, ethylene production was preferred on Cu–X catalysts doped with strong O affinity atoms, such as the B dopant atom. Ethane selectivity exhibited an enhancement, while ethanol formation was relatively suppressed by non-metal doping on Cu surfaces. An applied combination of Bader charge analyses and electronegativity analyses highlighted the underlying impact of electronic properties on adsorption thermochemistry and C₂ product selectivity. Importantly, we provide (1) an improved understanding of the C₂ mechanism for CO₂ electroreduction and (2) a practical strategy to direct CRR selectivity toward target C₂ products.

Methods

All computations were performed using density functional theory (DFT). The Perdew–Burke–Ernzerhof (PBE) functional was employed for the electron exchange correlation within the generalized gradient approximation (GGA), as is implemented in the VASP code.^{36,37} The ionic cores were described by the projector-augmented wave (PAW) method.³⁸ The cut-off energy for plane wave expansion was set to 500 eV. During geometry optimization, the structures were relaxed to forces on the atoms to less than 0.05 eV Å⁻¹. A 0.18 eV width of the smearing and a (4 × 4 × 1) Monkhorst–Pack *k*-point grid was applied. The Tkatchenko–Scheffler method³⁹ was adopted in all computations to address van der Waals (vdW) interactions between atoms. Compared to the vdW methods that are geometry-dependent such as DFT-D3,⁴⁰ the Tkatchenko–Scheffler method describes vdW interactions in correlation with the electron density. This is expedient to capture the complexity of the electronic structure of a system.⁴¹ Due to the high selectivity toward C₂ products, the Cu(100) surface was employed and modeled with a four-layered slab of a (3 × 3) supercell with a 15 Å vacuum space. The optimized configurations of Cu and Cu–X structures are shown in Fig. S1.† Stability of the non-metal doping was confirmed by computing the adhesion energy of the dopant atom on a hollow site, a bridge site, or a top site of the Cu(100) surface (Tables S1 and S2†). It was found that the hollow site was the most favorable for the non-metal doping.

The O affinity of the dopant atom site (E_{X-O}) was characterized by the adsorption energy of an O atom on the dopant atom

site of a Cu–X surface (Fig. S2†) that was calculated from the following:

$$E_{X-O} = E_{O/\text{slab}} - E_{\text{slab}} - E_{\text{O}} \quad (1)$$

where $E_{O/\text{slab}}$ is the energy for an O atom adsorbed on the dopant atom site of a Cu–X surface, E_{slab} is the energy of the Cu–X surface, and E_{O} is the energy of an O atom obtained from $E(\text{H}_2\text{O}-\text{H}_2)$. The more the negative value of the adsorption energy, the more it represents a stronger O affinity of the dopant atom site. The O affinity of the Cu site ($E_{\text{Cu-O}}$) was represented by the adsorption energy of an O atom on a hollow Cu site of the Cu(100) surface, with and without dopant atoms (Fig. S2†). Various Cu sites for O adsorption were investigated. The O atom preferred to adsorb on a hollow site.

During optimization of reaction intermediates, the adsorbates and top two layers were permitted to relax while the bottom two layers were fixed. The reaction pathways up to the formation of the *OCHCH₂ intermediate are considered identical for CO₂ electroreduction to ethylene, ethane and ethanol. The optimized intermediate configurations with dopant atoms or Cu examined as active sites are summarized in Tables S3 and S4,† respectively. The free energy diagrams toward different C₂ products *i.e.* ethylene, ethane and ethanol, starting from *OCHCH₂ adsorbed on the dopant atom site or the Cu site of Cu–X surfaces, are shown in Fig. S3 and S4,† respectively. The free energies of the reaction intermediates were calculated from:

$$G = E + \text{ZPE} - \text{TS} \quad (2)$$

in which the zero-point energy (ZPE) and entropy correction (TS) were computed from standard vibrational frequency analysis and applied to convert DFT-calculated electronic energies (E) to free energies (G) at 298.15 K (Table S5†). The vibrational frequencies were calculated by treating only the adsorbates as vibrational using the harmonic oscillator approximation.⁴²

The free energies of molecules were also computed *via* standard methods (Table S6†). The gaseous species, CO₂, C₂H₄ and C₂H₆, were computed at the standard state pressure of 101 325 Pa, while C₂H₅OH was treated with a pressure correction at a fugacity of 3242.4 Pa in concert with earlier work.⁴³ Solvation corrections for adsorbates were included by using the approximations previously described (Table S7†).^{18,24} Note that different methods were applied in the past to include solvation effects, leading to variations in reaction pathways and onset potentials.^{44–50} Thus, treatment of solvation effects may cause changes in reaction energetics. In this work, we assumed that the solvation corrections were identical for the investigated Cu–X model catalysts. It is notable that ions can play a role in directing the CRR selectivity.^{51–54} We assumed that ions effects were similar for each model catalyst, unlikely to alter the selectivity trends. The kinetic analysis was not included in this study. It was supposed that the kinetic barriers of endergonic reaction steps were not much greater than the reaction energies and that exergonic steps had surmountable barriers.⁴² Nevertheless, it is noteworthy that an alternative reaction pathway to

a target product may become favorable after taking into account the kinetic barriers of elementary electrochemical steps.^{29,50} Future kinetic study will be conducted for advancing the reaction mechanism at late stages of C₂ pathways. The computational hydrogen electrode (CHE) model was used to simulate proton–electron pair transfers.⁵⁵ In this model, the free energy of a proton–electron pair at 0 V vs. RHE is defined as equal to a half of the free energy of gaseous H₂ at 101 325 Pa.

Results and discussion

Electrochemical CO₂ reduction to C₂ products proceeds *via* C–C coupling of *CO–CO, *CO–CHO, or *CO–COH intermediates.^{8,16–19,56} The thermochemistry of the hydrogen evolution reaction (HER) at the initial stage was evaluated. The *H adsorption on the dopant atom site shows a general uphill free energy change for most Cu–X catalysts, indicating unfavorable thermodynamics of the HER (Table S8†). It has been proposed that C₂ products such as ethylene and ethanol share the same reaction pathway at the early stages of CO₂ electroreduction.⁵⁷ Following consecutive proton/electron transfer steps, the *OCHCH₂ intermediate is formed at a later stage. It is widely regarded as the selectivity determining intermediate (SDI) for C₂ products.^{2,25,58} Therefore the focus is on the adsorption energetics of post C₂ intermediates – beginning with adsorbed *OCHCH₂ on various active sites of Cu–X catalyst surfaces and exploration of selectivity competition for C₂ products along the branching reaction pathways.

Hydrogenation of *OCHCH₂ leads to either the formation of adsorbed acetaldehyde (*OCHCH₃) or desorption of ethylene (C₂H₄) with *O remaining on the catalyst surface. The production of the acetaldehyde molecule (CH₃CHO) from *OCHCH₂ hydrogenation was also evaluated. The free energy difference between two states of acetaldehyde indicates favorable formation of adsorbed *OCHCH₃ on each active site of Cu–X catalyst surfaces (Table S9†). The dopant atoms were initially investigated as active sites for *OCHCH₂ adsorption. As is shown in Fig. 1a and b, the free energy changes for C₂H₄ production and *OCHCH₃ formation exhibit opposing trends, based on varying O affinity of the dopant atom site (E_{X-O}) in various Cu–X catalysts. It is seen that the hydrogenation of *OCHCH₂ to C₂H₄ is thermodynamically more favorable on Cu–X surfaces with greater E_{X-O} , while *OCHCH₃ formation is preferred with decreasing E_{X-O} . For the Cu–B surface, a low, uphill free energy change (0.11 eV) for C₂H₄ desorption is observed and free energy change to form *OCHCH₃ is 0.5 eV higher than that to produce C₂H₄. This finding indicates therefore, a preference for C₂H₄ desorption on the Cu–B catalyst. The preferred C₂H₄ production is in good agreement with previous experimental observations that boron-doped copper catalysts exhibited high faradaic efficiency (F.E.) for C₂ products, mainly ethylene (52 ± 2% F.E.).¹⁴ For the other Cu–X catalysts, the free energy change (ΔG) for *OCHCH₂ hydrogenation to *OCHCH₃ is lower than that for C₂H₄ desorption on each catalyst. Specifically, the N, S, I, Br and Cl doped Cu–X surfaces show downhill free energy changes for *OCHCH₃ formation, while C₂H₄ desorption on these catalyst surfaces is endothermic. The Cu–P surface

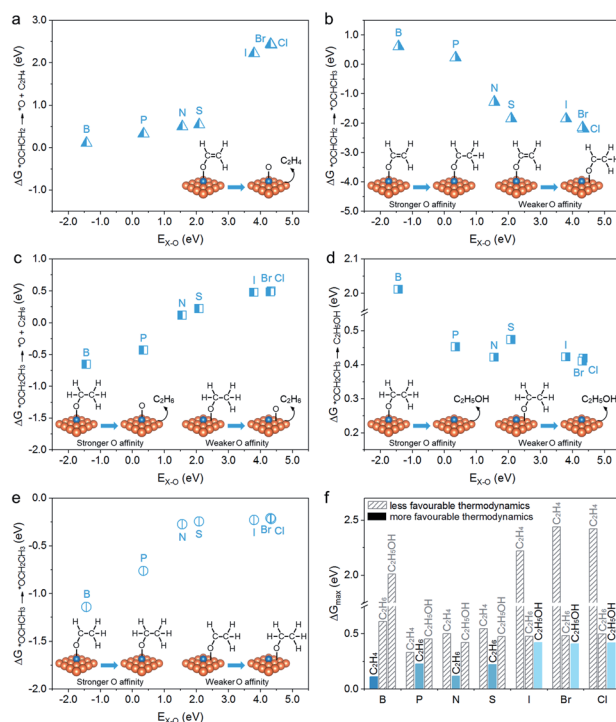


Fig. 1 Free energy changes of *OCHCH₂ hydrogenation to (a) C₂H₄ production or (b) *OCHCH₃ intermediate plotted against O affinity of the dopant atom site. The free energy changes of *OCHCH₂ hydrogenation to (c) C₂H₆ or (d) C₂H₅OH production plotted against O affinity of the dopant atom site. (e) The free energy changes of *OCHCH₂ hydrogenation to the *OCH₂CH₃ intermediate plotted against O affinity of the dopant atom site. Inset shows the predisposed adsorption configurations with dopant atoms examined as active sites. Cu and dopant atoms are, respectively, in orange and blue. (f) The maximum uphill free energy changes for C₂ products with dopant atoms examined as active sites. Lower free energy changes represent more favorable thermodynamics. The C₂ products with more favorable thermodynamics are labelled with solid bars, while the C₂ products with less favorable thermodynamics are labelled with shaded bars.

exhibits a thermodynamic preference for *OCHCH₃ formation with a lower free energy barrier compared with the two competing reaction steps. The figure inset shows the preferred adsorption configurations of related intermediates. It is notable that *OCHCH₃ remains on the dopant atom site of Cu–X surfaces with stronger E_{X-O} while *OCHCH₃ prefers to adsorb on adjacent Cu site of Cu–X surfaces with weaker E_{X-O} .

The varying O affinity of the dopant atom site on Cu–X catalysts has a significant influence on the reaction thermodynamics for C₂ products. Production of C₂H₄ is more favored on Cu–X surfaces that facilitate C–O bond-breaking in adsorbed *OCHCH₂; these surfaces are doped with atoms with stronger O affinity and therefore weaker C–O bonds. Additionally, the *OCHCH₂ intermediate is prone to be protonated on the α -carbon and moved toward *OCHCH₃ generation on Cu–X surfaces doped with weaker O affinity atoms. It is concluded, based on the O affinity of the dopant atom site on Cu–X catalyst, that Cu–B has high C₂H₄ selectivity owing to the strongest O affinity of the B atom on the catalyst surface. Other Cu–X catalysts show a preference for *OCHCH₃ formation.

The *OCHCH_3 electroreduction step leads to the formation of an ethoxy (*OCH_2CH_3) intermediate. Previous work using differential electrochemical mass spectrometry (DEMS) identified acetaldehyde as a precursor for ethanol formation.⁵⁹ This was also reported in a combined experimental-computational study in which acetaldehyde reduction proceeded *via* an ethoxy intermediate toward ethanol on Cu catalysts.²⁵ From Fig. 1e, it can be seen that the free energy changes with *OCHCH_3 hydrogenation to *OCH_2CH_3 on Cu-X surfaces are downhill. This finding indicates favorable thermodynamics for this elementary step. The adsorption preference of *OCH_2CH_3 is similar to that for *OCHCH_3 (Table S3†). For Cu-X surfaces doped with stronger O affinity atoms *i.e.* X = B and P, *OCH_2CH_3 adsorbs on the dopant atom site. For other Cu-X surfaces doped with weaker O affinity atoms, *OCH_2CH_3 is stabilized on the adjacent Cu site. Following the formation of *OCH_2CH_3 , the reaction pathways proceed with an additional bifurcation toward either ethane (C_2H_6) or ethanol (C_2H_5OH). As is seen in Fig. 1c and d, the free energy changes with *OCH_2CH_3 hydrogenation to C_2H_6 or C_2H_5OH are compared. This is to highlight the selectivity toward these two C_2 products on different Cu-X catalyst surfaces doped with varying O affinity atoms. The Cu-B and Cu-P surfaces doped with strong O affinity atoms preferably generate C_2H_6 with downhill free energy changes, while uphill free energy changes are required for C_2H_5OH . The Cu-N and Cu-S surfaces doped with moderate O affinity atoms display lower free energy barriers for C_2H_6 formation than that for C_2H_5OH generation. The Cu-I, Cu-Br and Cu-Cl surfaces doped with weak O affinity atoms exhibit a preference for C_2H_5OH production with lower uphill free energy changes than those for C_2H_6 formation. In general, product selectivity to C_2H_6 is more favored on Cu-X catalysts with increasing O affinity of the dopant atom site, whereas C_2H_5OH production becomes preferable with decreasing O affinity of the dopant atom site.

The selectivity toward different C_2 products on Cu-X catalysts using the thermodynamic analyses of O affinity of the dopant atom site (E_{X-O}) as a descriptor is summarized as Fig. 1f, which compares the maximum uphill free energy changes (ΔG_{max}) of elementary steps for the three C_2 products on each Cu-X catalyst surface. Lower free energy changes lead to less applied potentials at which the reaction pathway becomes exergonic. Advantageously, this can be practically used to evaluate C_2 product selectivity. The Cu-X catalysts with stronger E_{X-O} predispose selective reactions toward C_2 hydrocarbons *i.e.* ethylene and ethane, leaving an adsorbed *O remaining on the catalyst surface. The Cu-X catalysts with weaker O affinity predispose selectivity to ethanol, with the C-O bond maintained in the ethanol-forming pathway. Among the non-metal doping elements on Cu surfaces, B exhibits the strongest O affinity. The result is that this leads to selectivity toward C_2H_4 . The P, N and S doping elements result in a medium O affinity and a predisposed selectivity to C_2H_6 . For I, Br and Cl doped Cu-X catalysts with weak O affinity of the dopant atom site, an optimized predisposition for C_2H_5OH selectivity is seen.

The surface Cu atoms in the Cu-X model catalysts as active sites for intermediate adsorption were investigated for impact on CRR catalytic activity and selectivity. As is shown in Fig. 2a-e,

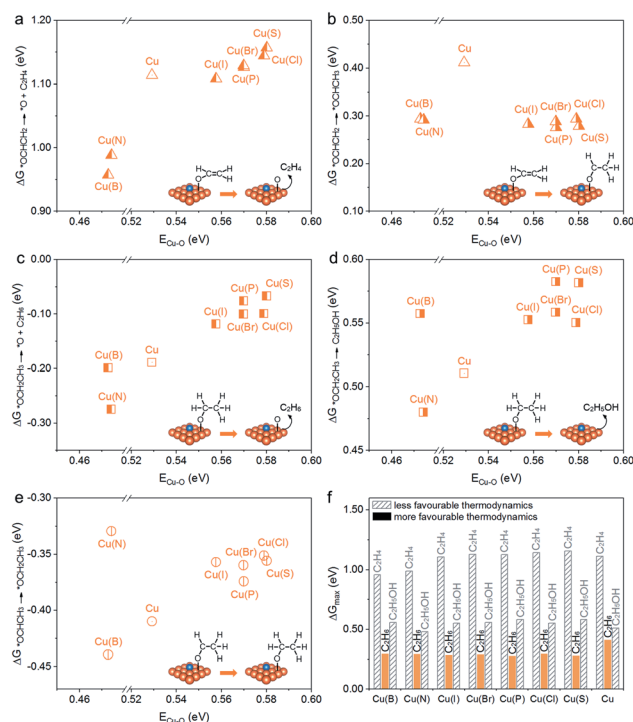


Fig. 2 Free energy changes of *OCHCH_2 hydrogenation to (a) C_2H_4 production or (b) *OCHCH_3 intermediate plotted against O affinity of the Cu site. The free energy changes of *OCH_2CH_3 hydrogenation to (c) C_2H_6 or (d) C_2H_5OH production plotted against O affinity of the Cu site. (e) The free energy changes of *OCHCH_3 hydrogenation to the *OCH_2CH_3 intermediate plotted against O affinity of the Cu site. Inset shows the predisposed adsorption configurations with Cu atoms examined as active sites. Cu and dopant atoms are, respectively, in orange and blue. (f) The maximum uphill free energy changes for C_2 products with Cu atoms examined as active sites. Lower free energy changes represent more favorable thermodynamics. The C_2 products with more favorable thermodynamics are labelled with solid bars, while the C_2 products with less favorable thermodynamics are labelled with shaded bars.

the varying O affinity of a hollow Cu site (E_{Cu-O}) on Cu(100) surfaces with and without dopant atoms was evaluated as an additional, confirmatory descriptor to target selectivity of C_2 products. The *OCHCH_2 was observed to have a horizontal configuration on the Cu site (Table S4†). Along the bifurcating pathways from *OCHCH_2 hydrogenation, *OCHCH_3 formation is thermodynamically more favorable than C_2H_4 production on the Cu site of each Cu-X or pure Cu catalyst (Fig. 2a and b). The high free energy change for *OCHCH_2 hydrogenation to C_2H_4 on the Cu site is likely due to the stable configuration of the *OCHCH_2 intermediate, which requires more energy input to break the C-O bond. The following *OCHCH_3 protonation to *OCH_2CH_3 on the Cu site is exothermic. This suggests greater stabilization of the ethoxy intermediate (Fig. 2e). The reaction pathways thereafter bifurcate toward ethane or ethanol production *via* *OCH_2CH_3 hydrogenation. As is shown in Fig. 2c and d, C_2H_6 formation is thermodynamically predisposed with downhill free energy changes on the Cu site, while C_2H_5OH production is less favorable with uphill free energy changes.

In conclusion, the non-metal doping on Cu–X surfaces leads to varying O affinity of a hollow Cu site ($E_{\text{Cu-O}}$) across a narrow range. The Cu–X catalysts show a predisposition to ethane on the Cu site with lower free energy changes (Fig. 2f). In contrast, less favorable thermodynamics are seen for ethylene and ethanol generation on the Cu site of Cu–X surfaces because of greater free energy changes. It is noteworthy that the free energy change of $^*\text{OCHCH}_2$ hydrogenation to $^*\text{OCHCH}_3$ on the Cu site of Cu–X surfaces is lowered compared with the pure Cu surface (Fig. 2b). This suggests the practical feasibility of directing CRR selectivity along desired reaction pathways by doping non-metal elements. The energetics of $^*\text{OH}$ adsorption were evaluated to indicate the feasibility for $^*\text{O}$ removal on Cu–X surfaces (Table S10†). The adsorbed $^*\text{O}$ is hydrogenated to $^*\text{OH}$ and then removed as a water molecule. It is worth noting that high O affinity may induce limited efficiency for $^*\text{O}$ and $^*\text{OH}$ removal. However, for Cu–X catalysts in this study, different active sites with varied O affinity would take effect together for clearing the $^*\text{O}$ species.

To investigate an underlying reason for varying C_2 product selectivity on Cu–X catalysts, Bader charge analyses, together with the evaluation of intrinsic properties for various doping elements were carried out. Bader charge analyses were conducted for the $^*\text{O}$ and $^*\text{OCHCH}_2$ species to study electron charge distribution on the adsorbates. This can be impacted by varying properties of dopant atoms. Electronegativity (χ) was introduced as an intrinsic property for doping elements to highlight possible electronic effects on oxygen affinity and associated selectivity toward C_2 products (Table S11†).⁶⁰ The

difference in electronegativity between two atoms offers a useful measure of the ionic character and polarity of the bond between them.⁶¹ Given this, the electronegativity difference ($\Delta\chi$) between the doping element and oxygen was used to assess the electron charge transfer tendency of oxygen interaction with the Cu–X catalyst surfaces.

As is shown in Fig. 3a–c, linear relationships were observed amongst calculated electronegativity differences, the oxygen affinity of the dopant atom site, and the electron charge on the $^*\text{OCHCH}_2$ intermediate adsorbed on the dopant atom site. A stronger O affinity of the dopant atom site is associated with greater electronegativity difference and more electron charge on $^*\text{OCHCH}_2$. Note that the deviation of Cu–N can be ascribed to the high electronegativity of the N doping element, leading to electron accumulation on the N dopant atom.⁶¹ The plots of charge density differences for the $^*\text{OCHCH}_2$ intermediate adsorbed on the dopant atom sites of three representative Cu–X (X = B, S and I) surfaces are shown as Fig. 3d. This figure aids visualization of the varying electron charge transfer induced by different doping elements. Together with decreasing O affinity of the dopant atom site, the electron charge transferred to adsorbed $^*\text{OCHCH}_2$ decreases. Similar relationships among O affinity of the dopant atom site, electron charge on $^*\text{O}$ adsorbed on the dopant atom site, and electronegativity difference between the doping element and oxygen are highlighted in Fig. S5a–c.† The plots of charge density differences for $^*\text{O}$ adsorption on the dopant atom sites of Cu–B, Cu–S, and Cu–I are shown as Fig. S5d.† The electron charge distribution was also investigated for $^*\text{OCHCH}_2$ (or $^*\text{O}$) adsorbed on the Cu site.

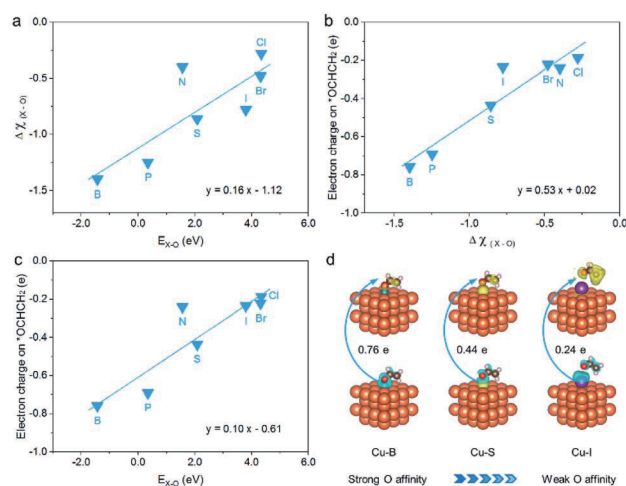


Fig. 3 (a) Electronegativity difference between the doping element and oxygen plotted against O affinity of the dopant atom site ($E_{\text{X-O}}$). (b) Electron charge on $^*\text{OCHCH}_2$ adsorbed on the dopant atom site plotted against the electronegativity difference between the doping element and oxygen. (c) Relationship between electron charge on $^*\text{OCHCH}_2$ adsorbed on the dopant atom site and O affinity of the dopant atom site ($E_{\text{X-O}}$). (d) Electron charge transfer of $^*\text{OCHCH}_2$ adsorbed on the dopant atom site of Cu–B (left), Cu–S (middle) and Cu–I (right) with decreasing $E_{\text{X-O}}$. Yellow and cyan isosurface represents, respectively, electron accumulation and electron depletion. The isosurface value for Cu–B and Cu–S is $2 \times 10^{-2} \text{ e}\text{\AA}^{-3}$ and that for Cu–I is $2 \times 10^{-3} \text{ e}\text{\AA}^{-3}$.

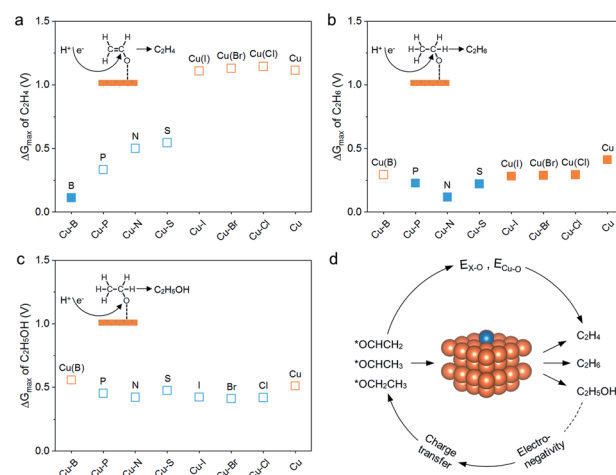


Fig. 4 Optimized overall maximum free energy changes for (a) C_2H_4 , (b) C_2H_6 , and (c) $\text{C}_2\text{H}_5\text{OH}$ on multiple active sites of Cu–X catalysts. The blue symbols represent C_2 product selectivity predisposed by the dopant atom site, while the orange symbols represent C_2 product selectivity predisposed by the Cu site. For each Cu–X catalyst surface, the most favorable selectivity toward the target C_2 product is labelled by the filled square, while less favorable C_2 product selectivity is labelled by the open square. Inset shows the reaction mechanism for CO_2 electroreduction to C_2H_4 , C_2H_6 and $\text{C}_2\text{H}_5\text{OH}$. (d) Schematic for directing selectivity of electrochemical CO_2 reduction toward target C_2 products.

As is shown in Fig. S6 and S7,[†] greater electronegativity difference between the doping element and oxygen results in more electron charge transfer to the adsorbate, indicating stronger interaction between the adsorbate and the Cu site. Therefore it is concluded that the selectivity of apparent C₂ products on Cu–X catalysts is influenced by inherent properties of the doping elements, in particular, electronegativity.

Overall selectivity toward different C₂ products *i.e.* ethylene, ethane and ethanol, on Cu–X catalysts, based on the extensive computation of thermochemistry and electronic properties of post C₂ intermediates on various active sites, is summarized in Fig. 4a–c. It is seen that the Cu–B catalyst exhibits predisposed selectivity toward ethylene formation, with the B dopant atom acting as the selectivity determining active site. For other Cu–X catalysts, ethane production is thermodynamically more disposed than ethylene and ethanol, with varying selectivity determining active sites. Notably, the maximum free energy changes for ethane production on Cu–X catalysts are lower than those on the pure Cu catalyst surface (Fig. 4b).

Through non-metal doping on Cu surfaces, selectivity toward target C₂ products on Cu–X catalysts is demonstrated by using oxygen affinities of the dopant atom site and Cu site as descriptors (Fig. 4d). The charge distribution on C₂ adsorbates is influenced by electronegativity of doping elements. This leads therefore to varying adsorption energetics of the post C₂ intermediates.

Conclusions

A new investigation of electrochemical CO₂ reduction to target C₂ products on a series of Cu–X (X = B, N, P, S, Cl, Br, or I) catalysts was conducted using DFT calculations. Thermodynamic analyses of key, post C₂ intermediates were conducted, based on which we theoretically confirmed that the selectivity toward C₂ hydrocarbons and alcohols is linked with O affinities of the dopant atom site and Cu site. An ethylene pathway becomes predisposed on Cu–X catalysts doped with strong O affinity atoms, namely the Cu–B catalyst. Ethane selectivity exhibits a general enhancement, whereas ethanol selectivity is relatively repressed by non-metal doping on Cu surfaces. The impact of electronic properties on intermediate adsorption and predisposed selectivity is underscored by Bader charge analyses of electron transfer to adsorbates and electronegativity analyses of non-metal dopant atoms. It is concluded that this new understanding of the C₂ reaction mechanism will provide a practically rational basis to direct C₂ product selectivity for the electrochemical CO₂ reduction.

Conflicts of interest

The authors have no conflicts of interest to declare.

Acknowledgements

The authors acknowledge financial support from the Australian Research Council (DP160104866, DP190103472, FT190100636, and FL170100154). DFT computations were undertaken with

assistance of resources and services from the National Computational Infrastructure (NCI) supported by the Australian Government, together with the Phoenix High Performance Computing (HPC) Service at The University of Adelaide.

References

- Z. W. Seh, J. Kibsgaard, C. F. Dickens, I. Chorkendorff, J. K. Nørskov and T. F. Jaramillo, *Science*, 2017, **355**, eaad4998.
- K. D. Yang, C. W. Lee, K. Jin, S. W. Im and K. T. Nam, *J. Phys. Chem. Lett.*, 2017, **8**, 538–545.
- Y. Zheng, A. Vasileff, X. Zhou, Y. Jiao, M. Jaroniec and S. Z. Qiao, *J. Am. Chem. Soc.*, 2019, **141**, 7646–7659.
- K. J. P. Schouten, F. Calle-Vallejo and M. T. M. Koper, *Angew. Chem., Int. Ed.*, 2014, **53**, 10858–10860.
- A. E. Farrell, R. J. Plevin, B. T. Turner, A. D. Jones, M. Hare and D. M. Kammen, *Science*, 2006, **311**, 506.
- O. S. Bushuyev, P. De Luna, C. T. Dinh, L. Tao, G. Saur, J. van de Lagemaat, S. O. Kelley and E. H. Sargent, *Joule*, 2018, **2**, 825–832.
- P. De Luna, R. Quintero-Bermudez, C.-T. Dinh, M. B. Ross, O. S. Bushuyev, P. Todorović, T. Regier, S. O. Kelley, P. Yang and E. H. Sargent, *Nat. Catal.*, 2018, **1**, 103–110.
- A. J. Garza, A. T. Bell and M. Head-Gordon, *ACS Catal.*, 2018, **8**, 1490–1499.
- K. P. Kuhl, E. R. Cave, D. N. Abram and T. F. Jaramillo, *Energy Environ. Sci.*, 2012, **5**, 7050–7059.
- T. K. Todorova, M. W. Schreiber and M. Fontecave, *ACS Catal.*, 2020, **10**, 1754–1768.
- S. Nitopi, E. Bertheussen, S. B. Scott, X. Liu, A. K. Engstfeld, S. Horch, B. Seger, I. E. L. Stephens, K. Chan, C. Hahn, J. K. Nørskov, T. F. Jaramillo and I. Chorkendorff, *Chem. Rev.*, 2019, **119**, 7610–7672.
- W. Ma, S. Xie, T. Liu, Q. Fan, J. Ye, F. Sun, Z. Jiang, Q. Zhang, J. Cheng and Y. Wang, *Nat. Catal.*, 2020, **3**, 478–487.
- T.-T. Zhuang, Z.-Q. Liang, A. Seifitokaldani, Y. Li, P. De Luna, T. Burdyny, F. Che, F. Meng, Y. Min, R. Quintero-Bermudez, C. T. Dinh, Y. Pang, M. Zhong, B. Zhang, J. Li, P.-N. Chen, X.-L. Zheng, H. Liang, W.-N. Ge, B.-J. Ye, D. Sinton, S.-H. Yu and E. H. Sargent, *Nat. Catal.*, 2018, **1**, 421–428.
- Y. Zhou, F. Che, M. Liu, C. Zou, Z. Liang, P. De Luna, H. Yuan, J. Li, Z. Wang, H. Xie, H. Li, P. Chen, E. Bladt, R. Quintero-Bermudez, T.-K. Sham, S. Bals, J. Hofkens, D. Sinton, G. Chen and E. H. Sargent, *Nat. Chem.*, 2018, **10**, 974–980.
- Y. Deng, Y. Huang, D. Ren, A. D. Handoko, Z. W. Seh, P. Hirunsit and B. S. Yeo, *ACS Appl. Mater. Interfaces*, 2018, **10**, 28572–28581.
- E. Pérez-Gallent, M. C. Figueiredo, F. Calle-Vallejo and M. T. M. Koper, *Angew. Chem., Int. Ed.*, 2017, **56**, 3621–3624.
- X. Liu, P. Schlexer, J. Xiao, Y. Ji, L. Wang, R. B. Sandberg, M. Tang, K. S. Brown, H. Peng, S. Ringe, C. Hahn, T. F. Jaramillo, J. K. Nørskov and K. Chan, *Nat. Commun.*, 2019, **10**, 32.
- F. Calle-Vallejo and M. T. M. Koper, *Angew. Chem., Int. Ed.*, 2013, **52**, 7282–7285.

- 19 H. Xiao, T. Cheng, W. A. Goddard and R. Sundararaman, *J. Am. Chem. Soc.*, 2016, **138**, 483–486.
- 20 J. H. Montoya, A. A. Peterson and J. K. Nørskov, *ChemCatChem*, 2013, **5**, 737–742.
- 21 J. H. Montoya, C. Shi, K. Chan and J. K. Nørskov, *J. Phys. Chem. Lett.*, 2015, **6**, 2032–2037.
- 22 K. Jiang, R. B. Sandberg, A. J. Akey, X. Liu, D. C. Bell, J. K. Nørskov, K. Chan and H. Wang, *Nat. Catal.*, 2018, **1**, 111–119.
- 23 E. Bertheussen, A. Verdaguer-Casadevall, D. Ravasio, J. H. Montoya, D. B. Trimarco, C. Roy, S. Meier, J. Wendland, J. K. Nørskov, I. E. L. Stephens and I. Chorkendorff, *Angew. Chem., Int. Ed.*, 2016, **55**, 1450–1454.
- 24 S. Hanselman, M. T. M. Koper and F. Calle-Vallejo, *ACS Energy Lett.*, 2018, **3**, 1062–1067.
- 25 I. Ledezma-Yanez, E. P. Gallent, M. T. M. Koper and F. Calle-Vallejo, *Catal. Today*, 2016, **262**, 90–94.
- 26 Y. C. Li, Z. Wang, T. Yuan, D.-H. Nam, M. Luo, J. Wicks, B. Chen, J. Li, F. Li, F. P. G. de Arquer, Y. Wang, C.-T. Dinh, O. Voznyy, D. Sinton and E. H. Sargent, *J. Am. Chem. Soc.*, 2019, **141**, 8584–8591.
- 27 W. Luo, X. Nie, M. J. Janik and A. Asthagiri, *ACS Catal.*, 2016, **6**, 219–229.
- 28 H. Xiao, T. Cheng and W. A. Goddard, *J. Am. Chem. Soc.*, 2017, **139**, 130–136.
- 29 T. Cheng, H. Xiao and W. A. Goddard, *Proc. Natl. Acad. Sci. U. S. A.*, 2017, **114**, 1795–1800.
- 30 O. Piqué, F. Viñes, F. Illas and F. Calle-Vallejo, *ACS Catal.*, 2020, **10**, 10488–10494.
- 31 A. Vasileff, Y. Zhu, X. Zhi, Y. Zhao, L. Ge, H. M. Chen, Y. Zheng and S. Qiao, *Angew. Chem., Int. Ed.*, 2020, **59**, 19649–19653.
- 32 X. Zhi, Y. Jiao, Y. Zheng, A. Vasileff and S.-Z. Qiao, *Nano Energy*, 2020, **71**, 104601.
- 33 J. T. Feaster, C. Shi, E. R. Cave, T. Hatsukade, D. N. Abram, K. P. Kuhl, C. Hahn, J. K. Nørskov and T. F. Jaramillo, *ACS Catal.*, 2017, **7**, 4822–4827.
- 34 K. P. Kuhl, T. Hatsukade, E. R. Cave, D. N. Abram, J. Kibsgaard and T. F. Jaramillo, *J. Am. Chem. Soc.*, 2014, **136**, 14107–14113.
- 35 A. Vasileff, C. Xu, Y. Jiao, Y. Zheng and S. Z. Qiao, *Chem*, 2018, **4**, 1809–1831.
- 36 J. P. Perdew, K. Burke and M. Ernzerhof, *Phys. Rev. Lett.*, 1996, **77**, 3865–3868.
- 37 G. Kresse and J. Furthmüller, *Phys. Rev. B: Condens. Matter Mater. Phys.*, 1996, **54**, 11169–11186.
- 38 G. Kresse and D. Joubert, *Phys. Rev. B: Condens. Matter Mater. Phys.*, 1999, **59**, 1758–1775.
- 39 A. Tkatchenko and M. Scheffler, *Phys. Rev. Lett.*, 2009, **102**, 073005.
- 40 S. Grimme, J. Antony, S. Ehrlich and H. Krieg, *J. Chem. Phys.*, 2010, **132**, 154104.
- 41 J. Hermann, R. A. DiStasio and A. Tkatchenko, *Chem. Rev.*, 2017, **117**, 4714–4758.
- 42 A. A. Peterson, F. Abild-Pedersen, F. Studt, J. Rossmeisl and J. K. Nørskov, *Energy Environ. Sci.*, 2010, **3**, 1311–1315.
- 43 Y. Jiao, Y. Zheng, P. Chen, M. Jaroniec and S. Z. Qiao, *J. Am. Chem. Soc.*, 2017, **139**, 18093–18100.
- 44 A. Rendón-Calle, S. Builes and F. Calle-Vallejo, *Appl. Catal., B*, 2020, **276**, 119147.
- 45 M. T. Tang, H. Peng, P. S. Lamoureux, M. Bajdich and F. Abild-Pedersen, *Appl. Catal., B*, 2020, **279**, 119384.
- 46 J. Hussain, H. Jonsson and E. Skulason, *ACS Catal.*, 2018, **8**, 5240–5249.
- 47 K. S. Rawat, A. Mahata and B. Pathak, *J. Catal.*, 2017, **349**, 118–127.
- 48 T. Cheng, H. Xiao and W. A. Goddard, *J. Phys. Chem. Lett.*, 2015, **6**, 4767–4773.
- 49 X. Nie, W. Luo, M. J. Janik and A. Asthagiri, *J. Catal.*, 2014, **312**, 108–122.
- 50 X. Nie, M. R. Esopi, M. J. Janik and A. Asthagiri, *Angew. Chem., Int. Ed.*, 2013, **52**, 2459–2462.
- 51 Y. Huang, C. W. Ong and B. S. Yeo, *ChemSusChem*, 2018, **11**, 3299–3306.
- 52 D. Gao, I. T. McCrum, S. Deo, Y.-W. Choi, F. Scholten, W. Wan, J. G. Chen, M. J. Janik and B. Roldan Cuenya, *ACS Catal.*, 2018, **8**, 10012–10020.
- 53 J. Resasco, L. D. Chen, E. Clark, C. Tsai, C. Hahn, T. F. Jaramillo, K. Chan and A. T. Bell, *J. Am. Chem. Soc.*, 2017, **139**, 11277–11287.
- 54 A. S. Varela, W. Ju, T. Reier and P. Strasser, *ACS Catal.*, 2016, **6**, 2136–2144.
- 55 J. K. Nørskov, J. Rossmeisl, A. Logadottir, L. Lindqvist, J. R. Kitchin, T. Bligaard and H. Jonsson, *J. Phys. Chem. B*, 2004, **108**, 17886–17892.
- 56 J. D. Goodpaster, A. T. Bell and M. Head-Gordon, *J. Phys. Chem. Lett.*, 2016, **7**, 1471–1477.
- 57 R. Kortlever, J. Shen, K. J. Schouten, F. Calle-Vallejo and M. T. M. Koper, *J. Phys. Chem. Lett.*, 2015, **6**, 4073–4082.
- 58 Q. Fan, M. Zhang, M. Jia, S. Liu, J. Qiu and Z. Sun, *Mater. Today Energy*, 2018, **10**, 280–301.
- 59 E. L. Clark and A. T. Bell, *J. Am. Chem. Soc.*, 2018, **140**, 7012–7020.
- 60 A. L. Allred, *J. Inorg. Nucl. Chem.*, 1961, **17**, 215–221.
- 61 L. C. Allen, *J. Am. Chem. Soc.*, 1989, **111**, 9003–9014.

Supporting Information

Directing Selectivity of CO₂ Electroreduction to Target C₂ products via Non-metal Doping on Cu Surfaces

Xing Zhi, Yan Jiao*, Yao Zheng, Kenneth Davey, Shi-Zhang Qiao*

Centre for Materials in Energy and Catalysis (CMEC)

School of Chemical Engineering and Advanced Materials

The University of Adelaide, SA 5005, Australia

*Email: yan.jiao@adelaide.edu.au; s.qiao@adelaide.edu.au

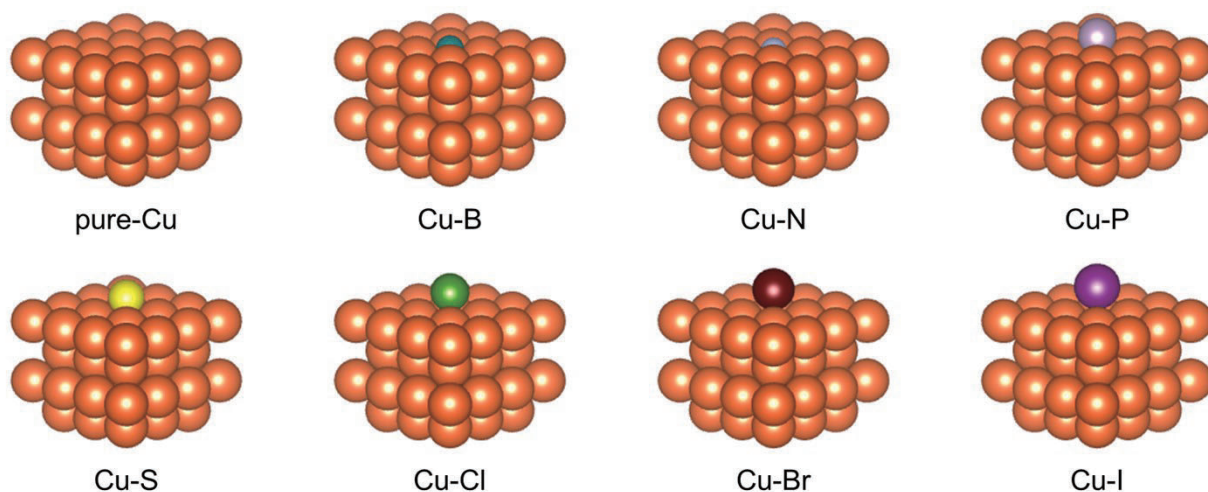


Figure S1. Optimized configurations of Cu-X, and pure Cu, surfaces. Copper atoms are shown as orange-spheres with other non-metal atoms labelled for each structure. Fluorine is not included as a doping element, because after geometry optimization of some reaction intermediates on the Cu-F model, the F atom move away from its original position, which indicates geometric instability of Cu-F model.

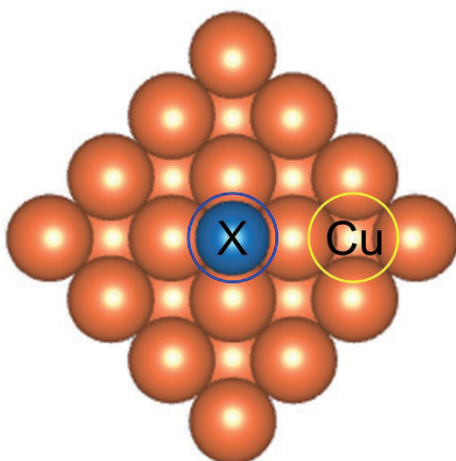


Figure S2. Dopant atom site (blue circle) and Cu site (yellow circle) used to rationalize oxygen affinities as descriptors for C_2 product selectivity on Cu-X catalysts.

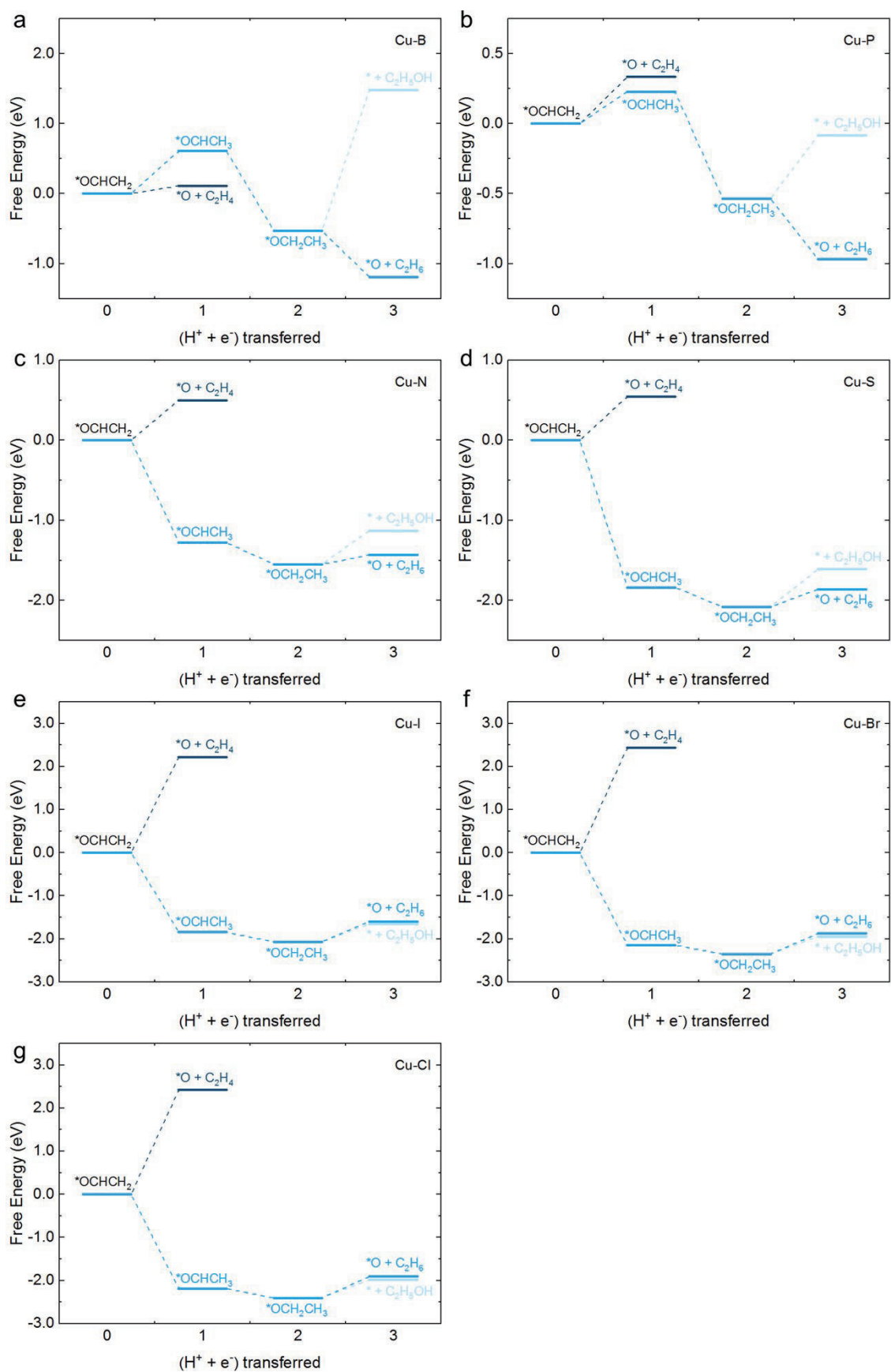


Figure S3. Free energy diagram starting from $*\text{OCHCH}_2$ intermediate adsorbed on the dopant atom site to ethylene (dark blue line), ethane (blue line) and ethanol (light blue line) for each Cu-X surface.

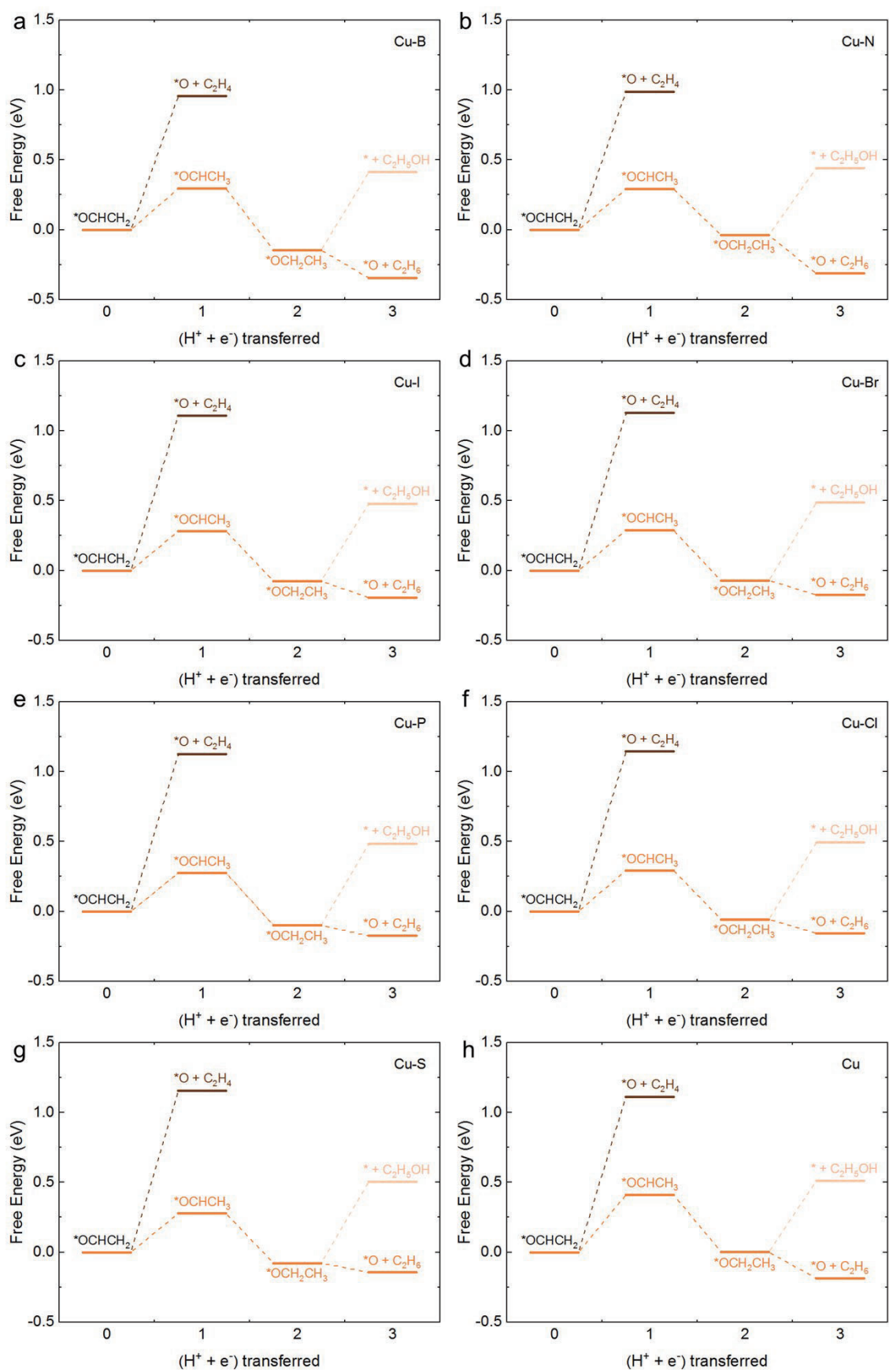


Figure S4. Free energy diagram starting from $*OCHCH_2$ intermediate adsorbed on the Cu site to ethylene (orange-brown line), ethane (orange line) and ethanol (light orange line) for each Cu-X surface and pure Cu surface.

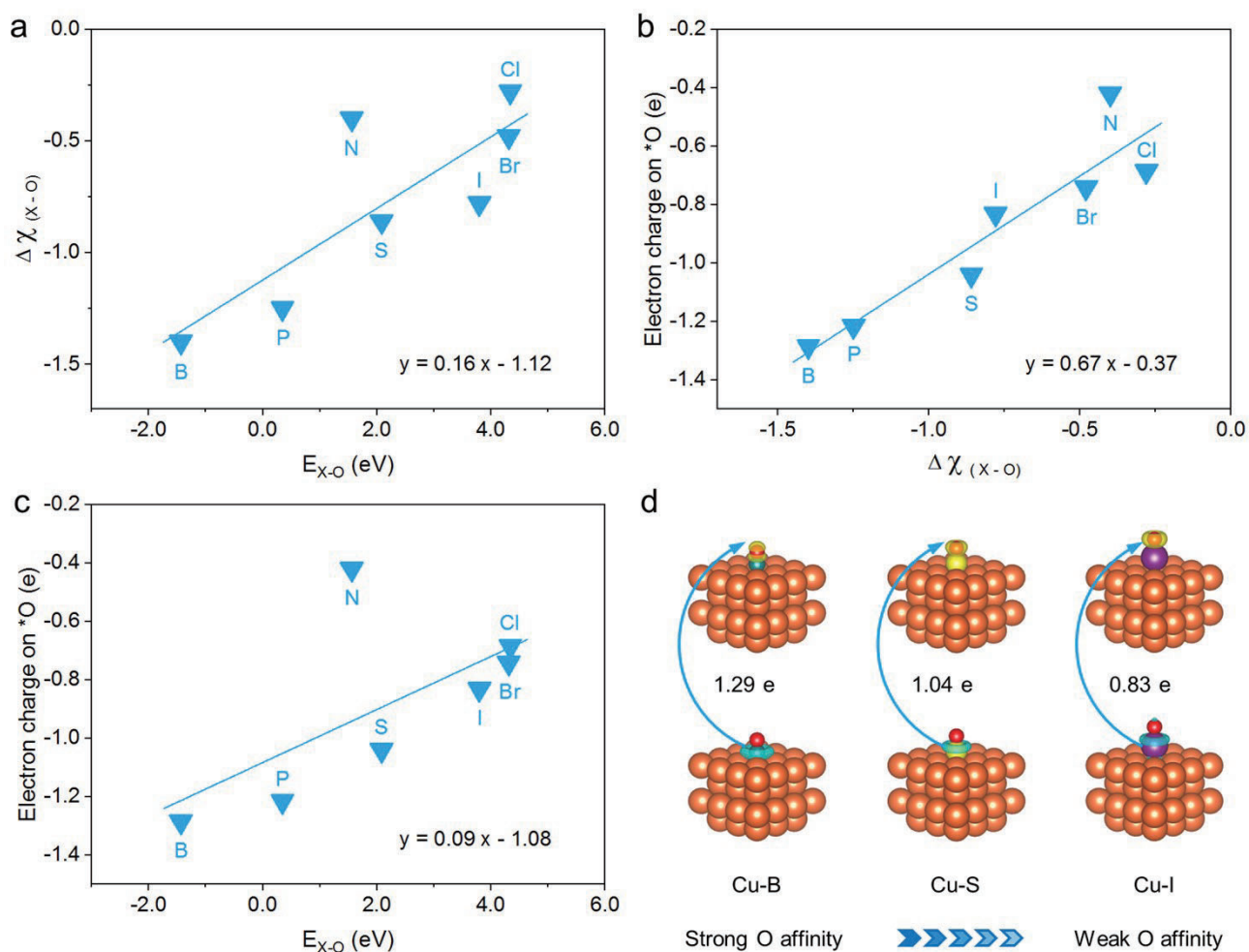


Figure S5. (a) Electronegativity difference between doping element and oxygen plotted against O affinity of the dopant atom site (E_{X-O}). (b) Electron charge on *O adsorbed on the dopant atom site plotted against the electronegativity difference between the doping element and oxygen. (c) Relationship between the electron charge on *O adsorbed on the dopant atom site and O affinity of the dopant atom site (E_{X-O}). (d) Electron charge transfer of *O adsorbed on the dopant atom site of Cu-B (left), Cu-S (middle), and Cu-I (right) with decreasing E_{X-O} . Yellow and cyan isosurface represents electron accumulation and electron depletion, respectively. The isosurface value is $2 \times 10^{-2} e \text{ \AA}^{-3}$.

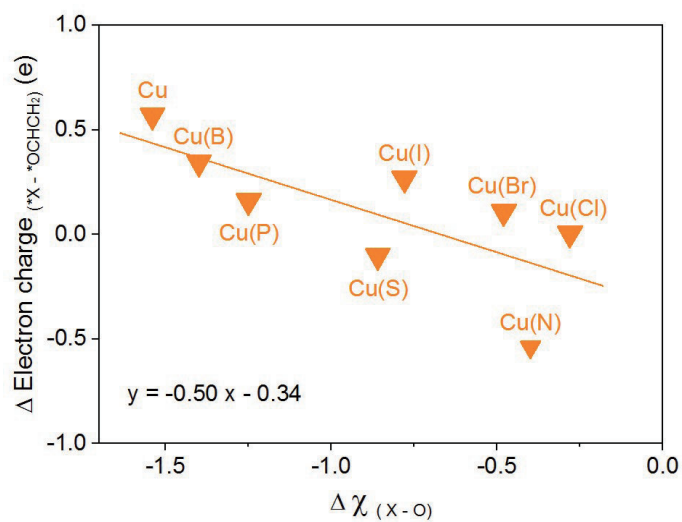


Figure S6. Difference in electron charge between dopant atom and *OCHCH₂ adsorbed on the Cu site plotted against electronegativity difference between doping element and oxygen.

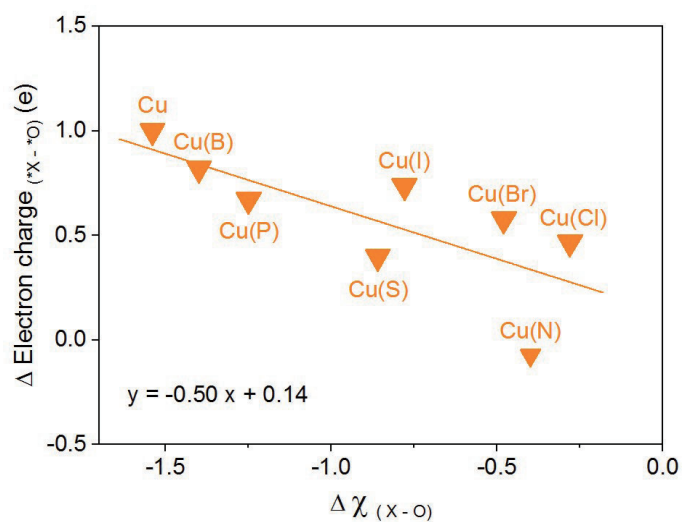


Figure S7. Difference in electron charge between dopant atom and *O adsorbed on the Cu site plotted against electronegativity difference between doping element and oxygen.

Table S1. Adhesion energy (in eV) of dopant atom X on a hollow site of Cu(100) surface.

Model catalyst	E_{ah}^a	E_{X}^b
Cu-B	0.715	-6.704
Cu-P	-1.288	-5.372
Cu-N	0.524	-8.312
Cu-S	-2.071	-4.126
Cu-I	-2.195	-1.316
Cu-Br	-2.168	-1.490
Cu-Cl	-2.194	-1.777

^a E_{ah} values were computed as $E_{\text{ah}} = E_{\text{Cu-X}} - E_{\text{Cu}} - E_{\text{X}}$, where $E_{\text{Cu-X}}$ is the energy of Cu-X surface, E_{Cu} is the energy of Cu(100) surface, and ^b E_{X} is the energy of X atom in its most stable format. For N, Cl, Br and I doped catalysts, the reference energies for E_{X} are based on calculated energies of N_2 , Cl_2 , Br_2 and I_2 gaseous molecules, respectively. For B, P and S doped catalysts, the reference energies for E_{X} are based on calculated energies of corresponding elementary substances, which are B_{12} , P_4 , and S_{32} .

Table S2. Adhesion energy (in eV) of dopant atom X on a bridge site or a top site of Cu(100) surface.

Model catalyst	E_{ah}^a (bridge site)	E_{ah}^a (top site)
Cu-B	2.317	3.168
Cu-P	-0.136	0.580
Cu-N	2.037	3.376
Cu-S	-1.146	-0.358
Cu-I	-1.940	-1.653
Cu-Br	-1.991	-1.682
Cu-Cl	-2.079	-1.743

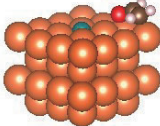
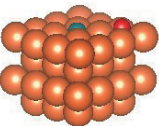
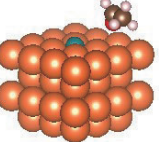
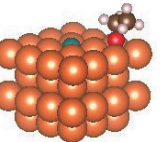
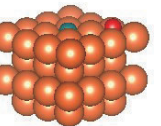
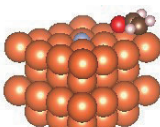
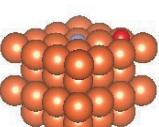
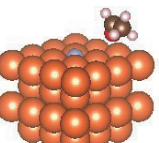
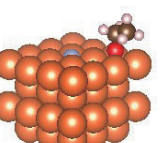
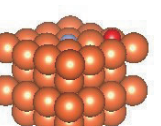
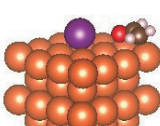
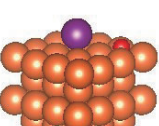
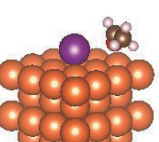
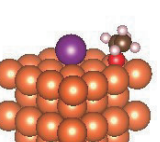
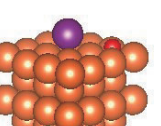
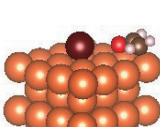
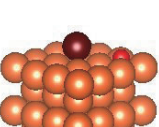
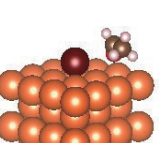
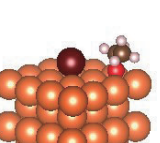
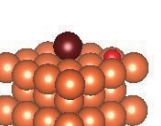
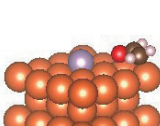
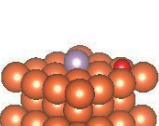
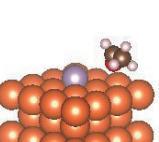
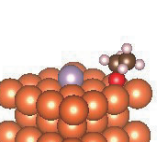
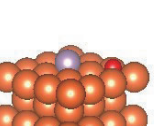
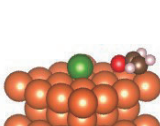
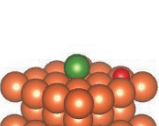
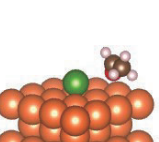
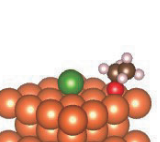
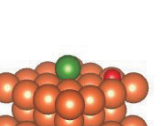
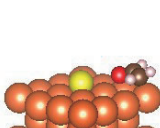
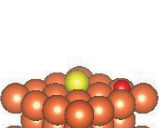
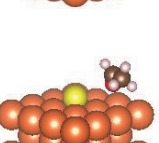
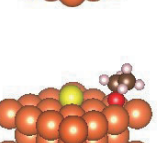
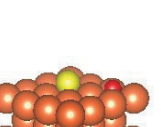


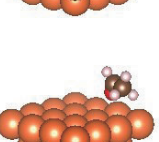
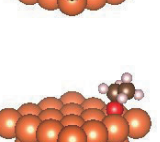
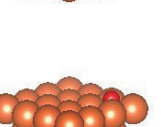
^a E_{ah} values were computed as $E_{\text{ah}} = E_{\text{Cu-X}} - E_{\text{Cu}} - E_{\text{X}}$, where $E_{\text{Cu-X}}$ is the energy of Cu-X surface, E_{Cu} is the energy of Cu(100) surface, and E_{X} is the energy of X atom. E_{X} values are the same as those listed in Table S1.

Table S3. Comparative summary of optimized configurations of key, C₂ reaction intermediates in this research, beginning with *OCHCH₂ adsorbed on the dopant atom site.

Model catalyst	*OCHCH ₂	*O ^a	*OCHCH ₃	*OCH ₂ CH ₃	*O ^b
Cu-B					
Cu-P					
Cu-N					
Cu-S					
Cu-I					
Cu-Br					
Cu-Cl					

^a Optimized *O adsorption configurations after ethylene desorption from *OCHCH₂. ^b Optimized *O adsorption configurations following ethane desorption from *OCH₂CH₃.

Table S4. Comparative summary of optimized configurations of key, C₂ reaction intermediates in this research, beginning with *OCHCH₂ adsorbed on the Cu site.

Model catalyst	*OCHCH ₂	*O ^a	*OCHCH ₃	*OCH ₂ CH ₃	*O ^b
Cu-B					
Cu-N					
Cu-I					
Cu-Br					
Cu-P					
Cu-Cl					
Cu-S					
Cu					

^a Optimized *O adsorption configurations after ethylene desorption from *OCHCH₂. ^b Optimized *O adsorption configurations after ethane desorption from *OCH₂CH₃.

Table S5. Thermodynamic energy corrections (in eV) for reaction intermediates.

Adsorbate	ZPE	-TS
*OCHCH ₂	1.200	-0.274
*OCHCH ₃	1.498	-0.310
*OCH ₂ CH ₃	1.837	-0.281

Table S6. Thermodynamic energy corrections (in eV) for gaseous molecules.

Gas molecule	ZPE	-TS
CO ₂	0.307	-0.661
C ₂ H ₄	1.356	-0.411
C ₂ H ₆	1.805	-0.519
C ₂ H ₅ OH	2.119	-0.572

Table S7. Solvation corrections (in eV) for reaction intermediates.

Adsorbate	Solvation Correction
*OCHCH ₂	0.38
*OCHCH ₃	0.10
*OCH ₂ CH ₃	0.00

Table S8. Free energy change (in eV) of *H adsorption on the dopant atom site of Cu-X surface.

Model catalyst	ΔG_{*H}
Cu-B	-0.473
Cu-P	0.036
Cu-N	-0.935
Cu-S	0.710
Cu-I	1.932 ^a
Cu-Br	1.914 ^a
Cu-Cl	1.874 ^a

^a Free energy change of *H adsorption on the dopant atom site of Cu-I, Cu-Br, and Cu-Cl was calculated with the dopant atom fixed in z direction.

For Cu-X catalysts with positive free energy change of *H adsorption on the dopant atom site, the hydrogen evolution reaction (HER) is not favorable. Regarding the Cu-X catalysts with negative free energy change of *H adsorption, the HER may have an effect on the full product distribution. In experimental studies, the hydrogen evolution also exhibits an inevitable Faradaic efficiency during the electrocatalytic CO₂ reduction [Nat. Chem., 2018, 10, 974-980]. However, for most Cu-X catalysts in this study, the HER is thermodynamically unfavorable.

Table S9. Free energy differences (in eV) between two states of acetaldehyde, i.e. adsorbed *OCHCH₃ and CH₃CHO molecule, with dopant atoms and Cu examined as active sites.

Model catalyst	ΔG_{-X}^a	ΔG_{-Cu}^b
Cu-B	-1.261	-0.509
Cu-P	-0.080	-0.599
Cu-N	-0.540	-0.541
Cu-S	-0.622	-0.617
Cu-I	-0.585	-0.587
Cu-Br	-0.592	-0.589
Cu-Cl	-0.592	-0.590
Cu	^c	-0.492

^a ΔG_{-X} is the free energy difference between adsorbed *OCHCH₃ on the dopant atom site and CH₃CHO molecule with catalyst substrate. ^b ΔG_{-Cu} is the free energy difference between adsorbed *OCHCH₃ on the Cu site and CH₃CHO molecule with catalyst substrate. ^c ΔG_{-X} value for pure Cu model catalyst is missing due to the absence of dopant atom site. The negative values of ΔG indicate favorable thermodynamics for *OCHCH₃ formation.

Table S10. Adsorption energy (in eV) of *OH intermediate on Cu-X and Cu surfaces

Model catalyst	E_{*OH}^a
Cu-B	-1.317
Cu-P	-0.180
Cu-N	-0.159
Cu-S	-0.196
Cu-I	-0.171
Cu-Br	-0.177
Cu-Cl	-0.180
Cu	-0.194

^a E_{*OH} values were obtained by optimizing the *OH adsorption on various active sites of Cu-X and Cu surfaces. The Cu-X catalysts that have very high O affinity to the dopant atom (e.g. Cu-B) exhibit limited efficiency for *OH removal. Along with decreasing O affinity to the dopant atom, the removal of *OH from Cu-X catalysts surfaces is likely to be facilitated.

Table S11. Electronegativity (χ) of doping element, copper and oxygen.

Atomic symbol	χ
B	2.04
P	2.19
N	3.04
S	2.58
I	2.66
Br	2.96
Cl	3.16
Cu	1.90
O	3.44

Chapter 7: Conclusions and Perspectives

This Thesis has demonstrated the application of heteroatom doping as a material engineering strategy for the development of efficient CRR electrocatalysts with improved selectivity toward target products. By using DFT computations, comprehensive understanding of reaction energetics and selectivity roadmap for different products was obtained.

In Chapter 2, a mechanistic evaluation of CRR pathway selectivity was presented by identifying the important role of oxygen-bound intermediates. From both computational and experimental studies, an in-depth understanding of reaction mechanisms provided a framework for directing selectivity toward target products. In Chapter 3, C_3N_4/XG hybrid structures were investigated as CRR electrocatalysts for the conversion of CO_2 to methane. A volcano-type activity trend based on scaling relations of three key intermediates ($*COOH$, $*CO$, $*CHO$) was obtained to estimate the best catalytic performance for methane production on this group of C_3N_4/XG catalysts. It was demonstrated that the improved catalytic activity originated from increased interfacial electron transfer. This activity origin provided insights into catalyst design strategy of doping modulation and interfacial construction

In Chapter 4 and 5, copper-based bimetallic materials were modelled to study their CRR selectivity trends by evaluating the thermodynamics and kinetics of critical elementary steps. Firstly, a descriptor-based approach was developed for product grouping and selectivity prediction. Through evaluating adsorption configurations and thermochemistry for various reaction intermediates, the hydrogen and oxygen affinities of the secondary metals in copper alloy catalysts were found to be effective descriptors in determining CRR selectivity. The intrinsic electronic properties of these alloy catalysts were effectively correlated to their product selectivity, leading to a practical design strategy of alloying in copper for highly selective CRR electrocatalysts. Secondly, activation barriers of C-C coupling steps on copper-based alloy surfaces were calculated by using NEB method. The OC-COH coupling was kinetically more favorable than the OC-CHO coupling on the investigated copper alloy catalysts for the formation of C_2 products. The linear energy

relations for C-C coupling and reverse C-C dissociation reactions provided a means to estimate activation barriers from reaction energies.

Chapter 6 focused on non-metal doped copper surfaces and late stages of CRR pathways to C₂ products (including ethylene, ethane and ethanol). The adsorption energetics of key post-C₂-coupling intermediates were theoretically evaluated to demonstrate how branching reaction pathways were competing with each other. The oxygen affinities of the dopant atom site and the Cu site were identified as descriptors for C₂ product selectivity. Bader charge analyses of electron transfer and electronegativity analyses of non-metal dopant atoms showed that intrinsic electronic properties had a marked effect on oxygen affinities of multiple active sites and associated C₂ product selectivity. As a result, modulation of oxygen affinity to control C₂ product selectivity amongst competing reaction pathways was achieved.

The work presented in this Thesis provides insights into the catalyst engineering strategy of heteroatom doping and demonstrates its importance in directing CRR selectivity. This Thesis also demonstrates the significance of theoretical computations to understand the reaction mechanisms in relation to reaction thermodynamics and kinetics, and intrinsic effects of dopant atoms. Therefore, the development of heteroatom-doped catalysts with tunable electronic properties provides great opportunities for controlling product distribution and achieving a selective CRR to target products.

Although tremendous progress has been made in understanding CRR mechanisms and performance of catalysts at the atomic level using theoretical DFT computations, more efforts are needed to depict a full picture for continued development of electrocatalytic CO₂ reduction. Many material engineering approaches such as interface engineering, alloying, hybridizing, surface defects and imperfections all have their place for achieving higher CRR selectivity. Furthermore, as the CRR pathway selection is affected by the real catalytic conditions and catalyst structural evolution, operando computations are highly required to achieve a more comprehensive understanding of the reaction mechanisms for directing selectivity to the target product. With the development of computational power and techniques, the operando computations under actual catalytic conditions, including solvation effects, ion effects, local pH, would become more achievable. In addition, the

combination of operando computations and operando spectroscopy presents a significant scope for identifying the evolution of reaction intermediates under actual operating conditions.

Appendix I: Publications during PhD Candidature

- [1] **Xing Zhi**, Yan Jiao, Yao Zheng, Shizhang Qiao, Impact of interfacial electron transfer on electrochemical CO₂ reduction on graphitic carbon nitride/doped graphene, *Small*, **2019**, 15, 1804224.
- [2] **Xing Zhi**, Yan Jiao, Yao Zheng, Anthony Vasileff, Shizhang Qiao, Selectivity roadmap for electrochemical CO₂ reduction on copper-based alloy catalysts, *Nano Energy*, **2020**, 71, 104601.
- [3] **Xing Zhi**, Yan Jiao, Yao Zheng, Kenneth Davey, Shizhang Qiao, Directing selectivity of CO₂ electroreduction to target C₂ products via non-metal doping on Cu surfaces, *J. Mater. Chem. A*, **2021**, 9, 6345-6351.
- [4] **Xing Zhi**, Yan Jiao, Yao Zheng, Shizhang Qiao, Kinetic insights into selective C-C coupling for electrochemical CO₂ reduction on copper alloy surfaces, **2021**, to be submitted.
- [5] **Xing Zhi**, Anthony Vasileff, Yao Zheng, Yan Jiao, Shizhang Qiao, Role of oxygen-bound reaction intermediates in selective electrochemical CO₂ reduction, **2021**, submitted for publication.
- [6] Anthony Vasileff⁺, **Xing Zhi**⁺, Chaochen Xu, Lei Ge, Yan Jiao, Yao Zheng, Shizhang Qiao, Selectivity control for electrochemical CO₂ reduction by charge redistribution on the surface of copper alloys, *ACS Catal.*, **2019**, 9, 9411–9417. (+ Equal contribution)
- [7] Chaochen Xu⁺, **Xing Zhi**⁺, Anthony Vasileff, Dan Wang, Bo Jin, Yan Jiao, Yao Zheng, Shizhang Qiao, Highly selective two-electron electrocatalytic CO₂ reduction on single-atom Cu catalysts, *Small Struct.*, **2020**, 2000058. (+ Equal contribution)
- [8] Anthony Vasileff, Yanping Zhu, **Xing Zhi**, Yongqiang Zhao, Lei Ge, Hao Ming Chen, Yao Zheng, Shizhang Qiao, Electrochemical reduction of CO₂ to ethane through stabilization of an ethoxy intermediate, *Angew. Chem. Int. Ed.*, **2020**, 59, 19649-19653.